

Alvaro Cubero Ruiz

Technological solutions and laser
processes for the development of
superconductor-based
applications.

Director/es

Martinez Fernandez, Elena
Angurel Lambán, Luis Alberto

<http://zaguan.unizar.es/collection/Tesis>

© Universidad de Zaragoza
Servicio de Publicaciones

ISSN 2254-7606



Universidad
Zaragoza

Tesis Doctoral

TECHNOLOGICAL SOLUTIONS AND LASER
PROCESSES FOR THE DEVELOPMENT OF
SUPERCONDUCTOR-BASED APPLICATIONS.

Autor

Alvaro Cubero Ruiz

Director/es

Martinez Fernandez, Elena
Angurel Lambán, Luis Alberto

UNIVERSIDAD DE ZARAGOZA
Escuela de Doctorado

2021



TESIS DOCTORAL

Technological solutions and laser
processes
for the development of
superconductor-based applications

Álvaro Cubero Ruiz

Zaragoza, February 2021



Technological solutions and laser
processes
for the development of
superconductor-based applications

Memoria presentada por

Álvaro Cubero Ruiz

para optar al grado de
Doctor en Física

Directores de Tesis

Luis Alberto Angurel Lambán
Elena Martínez Fernández

- ¡Madre!

-Lo de la tesis, que ya está

COMPENDIUM OF PUBLICATIONS

The following thesis is presented as a compendium of publications.

This work comprises four published original research papers and a preprint (submitted):

- A. A. Cubero, R. Navarro, P. Kováč, L. Kopera, M. A. Rindfleisch and E. Martínez, *Quench dynamics in MgB₂ Rutherford cables*. Superconductor Science and Technology vol. 31, (2018) 045009 (9pp).
- B. A. Cubero, A.B. Núñez-Chico, R. Navarro, L.A. Angurel and E. Martínez, *Electromagnetic behaviour and thermal stability of a conduction-cooled, no-insulated 2G-HTS coil at intermediate temperatures*. Cryogenics 108 (2020) 103070 (9pp).
- C. A. Cubero, E. Martínez, G.F. de la Fuente, I. García-Cano, S. Dosta, L.A. Angurel, *Large enhancement of thermal conductance at ambient and cryogenic temperatures by laser remelting of plasma-sprayed Al₂O₃ coatings on Cu*. [Preprint] Submitted to Journal of the European Ceramic Society.
- D. A. Cubero, E. Martínez, L.A. Angurel, G.F. de la Fuente, R. Navarro, H. Legall, J. Krüger and J. Bonse, *Effects of laser-induced periodic surface structures on the superconducting properties of Niobium*. Applied Surface Science 508 (2020) 145140 (7pp)
- E. A. Cubero, E. Martínez, L.A. Angurel, G.F. de la Fuente, R. Navarro, H. Legall, J. Krüger and J. Bonse, *Surface Superconductivity Changes of Niobium Sheets by Femtosecond Laser-Induced Periodic Nanostructures*. Nanomaterials 10 (2020) 2525.

“It don’t mean a thing if it ain’t got that swing”

-Edward Kennedy “Duke” Ellington (1899-1974)

Table of Contents

- Resumen7
 - Principales retos abordados en las publicaciones9
- OBJECTIVES.....13
 - Overall OBJECTIVES of the thesis.....15
 - Main challenges addressed in the publications17
- STATE OF THE ART21
- 1. Superconducting Materials and their applications23
 - 1.1 Phenomena, History and Materials23
 - 1.2 Applied Superconductivity: From the laboratory to the final application29
 - 1.2.1 Wires and tapes fabrication29
 - 1.2.2 Conductors and Coils manufacturing - Technological interest of SC windings33
 - Coils manufacture.....36
 - 1.3 Applications39
 - 1.3.1 High magnetic field applications39
 - 1.3.2 Electric power applications40
 - Cables41

Transformers	42
Superconducting Fault Current Limiters (SFCL).....	43
Energy Storage.....	43
Rotating machines: Locomotion, generators and motors.....	44
1.3.3 SRF Cavities.....	45
1.4 References	48
2. Surface Processing by Laser Technologies	57
2.1. Laser: Fundamentals.....	57
2.1.1. Laser classifications	61
2.1.2. Laser safety.....	63
2.2. Laser-Matter interaction	65
2.2.1. Photon-matter interaction	65
2.2.2. Material optical properties.....	67
2.3. Laser induced surface modifications	69
Ablation	70
2.3.1. Application of melting processes	73
2.3.2. Application of nanostructuring surface processes	77
2.4. Gaussian optics and relevant processing parameters.....	83
2.4.1. Energy distribution within the laser beam	83
2.4.2. Processing parameters. Scanning surfaces	88
2.5. References	92
PUBLICATIONS	99
Publication A.....	101
Quench dynamics in MgB ₂ Rutherford cables.....	101
Publication B.....	117
Electromagnetic behaviour and thermal stability of a conduction-cooled, no-insulated 2G-HTS coil at intermediate temperatures	117

Publication C.....	129
Large enhancement of thermal conductance at ambient and cryogenic temperatures by laser remelting of plasma-sprayed Al ₂ O ₃ coatings on Cu	129
Publication D.....	149
Effects of laser-induced periodic surface structures on the superconducting properties of Niobium	149
Publication E.....	159
Surface Superconductivity Changes of Niobium Sheets by Femtosecond Laser-Induced Periodic Nanostructures.....	159
DISCUSSION	179
Global Discussion.....	181
1. Thermal stability and electromagnetic behaviour of superconducting cables and coils	181
1.1 MgB ₂ Rutherford cables: Quench analysis	181
1.2 2G-HTS coil: Electromagnetic and thermal behaviour.	185
2. Laser melting techniques to improve thermal properties of alumina coatings ..	188
3. Surface laser nanostructuring and superconducting properties.....	191
CONCLUSIONS	199
Thesis Conclusions.....	201
1. Thermal stability and electromagnetic behaviour of superconducting cables and coils	201
2. Laser melting techniques to improve thermal properties of Al ₂ O ₃ coatings	203
3. Surface laser nanostructuring and superconducting properties of Niobium samples.....	204
4. Further, based on the former, research lines.....	205
Conclusiones Generales.....	209
1. Cables y bobinas superconductoras: Estabilidad térmica y comportamiento electromagnético.....	209

2. Procesado láser para la mejora de propiedades térmicas de los recubrimientos de alúmina	211
3. Procesado láser para la nanoestructuración de muestras de Nb y el estudio de sus propiedades superconductoras.....	212
4. Líneas y trabajos futuros	214
Agradecimientos Y Recuerdos	217

Resumen

Desde principios del siglo pasado, la superconductividad ha supuesto un avance espectacular para algunas aplicaciones. Algunas de ellas están muy consolidadas y otras suponen una mejora considerable frente a las alternativas basadas en “materiales tradicionales”, a pesar de que todavía existen ciertas limitaciones que se deben superar. Un buen ejemplo de este último grupo son las aplicaciones de potencia (generación de energía o aquellas relacionadas con la distribución): Máquinas rotativas – generadores o motores –, cables, estabilizadores de red, etc. Para el desarrollo y mejora de estas aplicaciones, la comunidad científica tiene que contar con las restricciones propias de este tipo de materiales. Sus esfuerzos deben centrarse en la mejora de las propiedades superconductoras, en el diseño y fabricación de conductores con arquitecturas que muchas veces son complejas, y en la integración de esos cables y los diferentes componentes en un sistema asegurando su fiabilidad. Es necesario prestar especial atención al estudio y optimización de las propiedades mecánicas, térmicas y electromagnéticas de esos conductores y, por ende, del sistema completo.

Un completo análisis del comportamiento desde el punto de vista térmico es esencial para diseñar el correcto funcionamiento del dispositivo, sobre todo mientras trabaja en régimen superconductor a temperaturas criogénicas. El comportamiento térmico está fuertemente relacionado con las propiedades electromagnéticas de los materiales superconductores, caracterizándose por curvas voltaje-intensidad con una alta no-linealidad y una fuerte dependencia de sus propiedades superconductoras con la temperatura y el campo magnético. En este contexto, una parte importante de esta tesis está relacionada con la estabilidad térmica de distintos dispositivos superconductores y sus necesarios equipos auxiliares.

Desde el punto de vista de los materiales superconductores, su estabilidad térmica es crucial para asegurar las condiciones de operación de todas las partes del sistema. A la hora de diseñar un dispositivo superconductor y asegurar unas condiciones estables de trabajo, se ha de tener especial cuidado con la generación y propagación de inestabilidades térmicas (*quench*). Estas transiciones irreversibles desde el estado superconductor a un estado normal (resistivo) mientras el sistema está en funcionamiento, se pueden inducir aplicando sobrecorrientes o perturbaciones térmicas en el conductor. Estos estudios son muy importantes tanto en el diseño de hilos y cables, como en la configuración de bobinas.

Asimismo, el diseño del sistema criogénico auxiliar, necesario para mantener las condiciones de operación de estos materiales, desempeña un papel importante en la estabilidad térmica del propio dispositivo. La inyección de corriente al dispositivo puede suponer, si no está bien diseñada, un aporte de calor que suponga que el superconductor trabaje por debajo de su potencial. En consecuencia, es importante controlar la generación de calor a lo largo de las barras de alimentación de corriente, así como proporcionar un anclaje térmico a las distintas partes (superconductoras e intermedias) para asegurar las adecuadas condiciones de temperatura.

Otra aplicación para la que la superconductividad ha supuesto una mejora relevante son las cavidades resonantes de radio frecuencia. Estos resonadores se emplean en los aceleradores de partículas y necesitan ser fabricados con materiales con una resistencia muy baja para mejorar su rendimiento. De esta forma, los materiales superconductores suponen una alternativa real que incrementa su eficacia notablemente. Las características superficiales de estos materiales condicionan los fenómenos de superconductividad superficial, por lo que para esta aplicación es necesario disponer de materiales con alta pureza y controlar sus propiedades superficiales.

A lo largo de esta tesis se ha empleado tecnología láser para la modificación de propiedades superficiales con dos finalidades diferentes relacionadas con materiales superconductores y sus aplicaciones. En los láseres pulsados, la duración del pulso está directamente relacionada con el aporte de energía a la superficie procesada. Pulsos más largos que centenares de picosegundos inducen procesos principalmente térmicos por lo que pueden usarse para calentar, fundir o generar ablación del material de la superficie. Por otro lado, la interacción de la materia con láseres de pulsos ultracortos (más cortos que unos picosegundos) se rige por otros mecanismos diferentes y facilita la formación de nanoestructuras en la superficie. En este trabajo se han empleado distintos láseres

(duración de pulso y longitud de onda diferentes) con diversos objetivos. Por un lado, se ha utilizado un láser de infrarrojo cercano con pulsos de 200 ns para fundir, total o parcialmente, un recubrimiento cerámico sobre sustratos metálicos. Por otro lado, se han empleado diferentes láseres de pulsos ultracortos para nanoestructurar la superficie de materiales superconductores: un láser ultravioleta de 300 ps y dos láseres que emiten en el infrarrojo cercano con pulsos en el rango de los femtosegundos.

Esta tesis se ha estructurado de la siguiente manera: Se ha incluido un capítulo de **Estado del arte** en el que se introducen tecnologías asociadas con la superconductividad y con el procesado láser de superficies. En la primera parte, se presta especial atención a las aplicaciones superconductoras relacionadas con el trabajo descrito en esta tesis, en particular aplicaciones de potencia y las cavidades resonantes superconductoras. Conjuntamente, en el apartado de tecnologías láser, se describen los procesos de fusión y de nanoestructuración de superficies. A continuación, se incluye el **compendio de artículos**, que agrupa los principales resultados obtenidos a lo largo de la tesis relacionados con los principales retos abordados. Posteriormente, en la **discusión de resultados** se completan las publicaciones con otros resultados parciales y trabajos paralelos a incluidos en las publicaciones. Por último, se exponen las principales **conclusiones** de la tesis, indicando además varias líneas de investigación que quedan abiertas gracias a este trabajo.

Principales retos abordados en las publicaciones

En la primera parte de esta tesis doctoral, se analiza la estabilidad térmica de cables y bobinas superconductoras. Se ha estudiado la generación y propagación de *quench* en cables de diboruro de magnesio (MgB_2) con geometría Rutherford. Este tipo de cables trenzados aportan varias ventajas sobre otros conductores del tipo “monolítico” (hilos o cintas), ya que suponen un incremento de la capacidad de transporte y la reducción de pérdidas AC, que están relacionadas con la presencia de corrientes o/y campos magnéticos alternos. Típicamente, se emplean dos configuraciones para estudiar los *quench*: la generación de calor localizada, simulando un punto caliente gracias a un calentador externo y, por otro lado, la aplicación de sobrecorrientes (corrientes por encima de la corriente crítica del cable). En la **publicación A** se emplean los dos tipos de experimentos para analizar el comportamiento de cables compuestos por 12 hilos, cada uno de los cuales está formado por un único filamento de MgB_2 rodeado por una barrera de Nb y, todo ello, recubierto por una aleación de cobre-níquel. También se ha estudiado

cómo influyen las propiedades de dicho recubrimiento metálico en el comportamiento global del cable.

Por otro lado, se ha analizado la estabilidad térmica de una bobina tipo doble *pancake* fabricada con cinta de material superconductor de alta temperatura de segunda generación (2G-HTS), la cual se bobinó de forma continua y sin aislamiento entre espiras. La bobina se ancló térmicamente al dedo frío de un criogenerador para ser enfriada por conducción. Este tipo de bobinas sin aislamiento aportan mayor robustez ante inestabilidades térmicas y son más compactas, pero generan un pequeño retraso entre las rampas de corriente y del campo magnético, además de pérdidas adicionales durante los procesos de carga y descarga, que pueden suponer un problema en algunas de las aplicaciones. En la **publicación B** se analizó el comportamiento térmico y electromagnético de esta bobina incluyendo los procesos de carga y de descarga, la medida de la corriente crítica de la bobina, las pérdidas generadas, y sus diferentes contribuciones, durante las rampas de carga y descarga, así como la conductancia térmica que se establece en las diferentes uniones térmicas que se han utilizado para refrigerar la bobina.

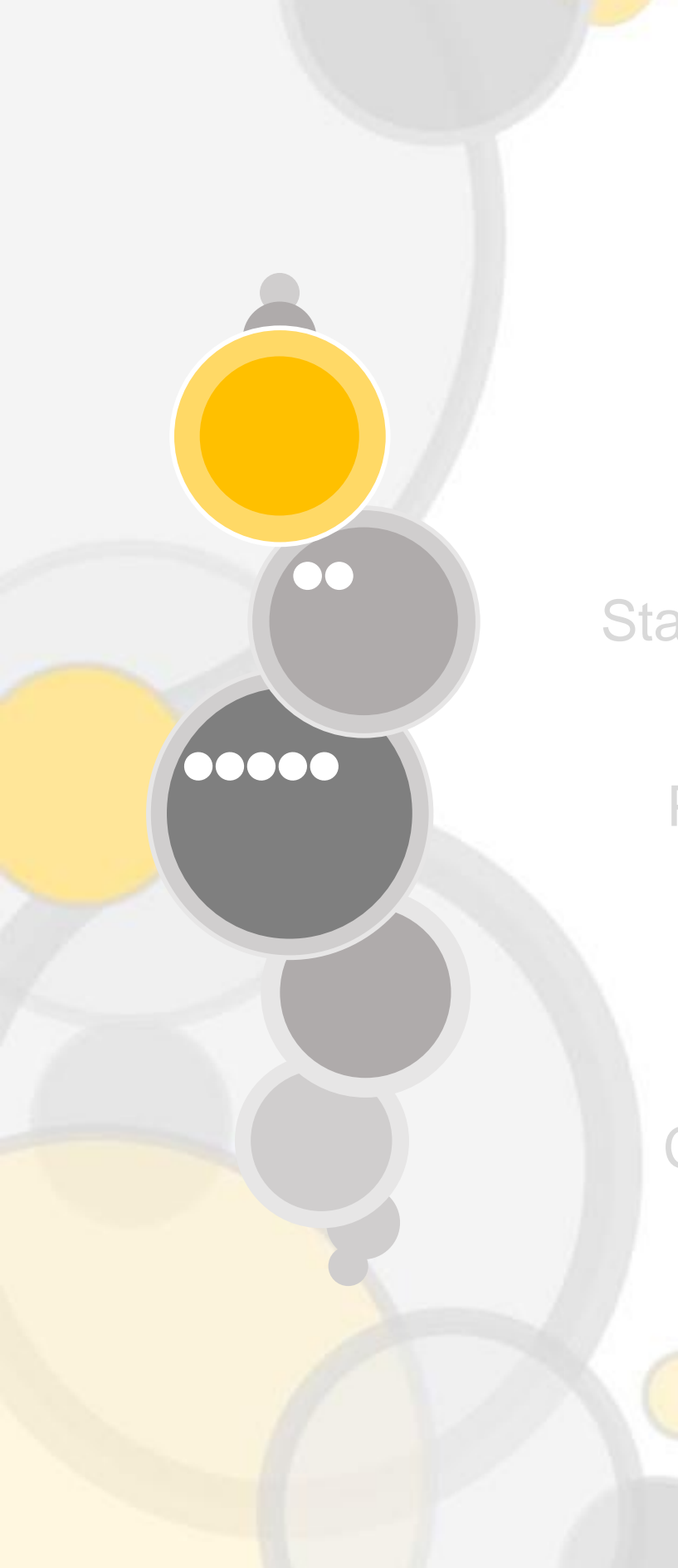
Para poder realizar estos estudios fue necesario inyectar de forma estable corrientes por encima de los 400 A. Esto supuso un reto por el calor generado en el equipo y en las barras de corriente, con un extremo a temperatura ambiente y otro a temperaturas criogénicas con la bobina. Estas barras de corriente se han diseñado con tres partes, conectadas por uniones atornilladas, que a su vez están termalizadas y presentan aislamiento eléctrico. La estabilidad térmica de estas barras también se analiza en la **publicación B**.

Ese anclaje o disipador térmico necesita presentar buena conductancia térmica y aislamiento eléctrico. La solución propuesta fueron piezas de cobre recubiertas por una capa de alúmina proyectada por plasma. Esta capa mantiene el aislamiento eléctrico, pero es necesario mejorar sus propiedades térmicas. En la **publicación C** se estudia cómo, mediante el procesado láser de superficies, se puede densificar y re-fundir la capa de Al_2O_3 mejorando su comportamiento térmico sin que se vea comprometida la unión del recubrimiento con el sustrato. Para ello ha sido necesario optimizar todos los parámetros de procesado láser reduciendo la formación de agujeros y grietas en el fundido frío, así como inducir un cambio microestructural en el recubrimiento que mejore las propiedades térmicas de la unión.

La versatilidad de las tecnologías láser permite facilitar la formación de nanoestructuras. Otro de los objetivos de este trabajo fue estudiar si las propiedades superconductoras

pueden verse modificadas por la interacción con radiación láser. Una estancia de 3 meses en el Bundesanstalt für Materialforschung und –prüfung (BAM, Berlin, Alemania) brindó la posibilidad de emplear láseres de pulsos ultracortos para el procesado de superficies. La utilización de estos láseres facilita la formación de micro y nanoestructuras en la superficie del material con una disposición casi periódica, lo que abre un nuevo camino a la ingeniería de superficies y una gran variedad de nuevas aplicaciones.

Desde el punto de vista de la superconductividad, en particular los superconductores tipo II, una determinada red de defectos puede mejorar las propiedades magnéticas del material, especialmente para campos magnéticos externos entre los campos críticos inferior y superior, H_{C1} y H_{C2} , *respectivamente*. Además de estos estudios que tienen una componente de volumen importante, se han estudiado los efectos en la superconductividad superficial, que persiste en una capa muy fina, incluso con campos magnéticos superiores a H_{C2} . Las **publicaciones D** y **E** son los primeros trabajos que demuestran que estos tratamientos láser pueden modificar las propiedades superconductoras del material. Para estos estudios se han utilizado muestras de niobio por ser el elemento puro superconductor con una temperatura crítica y campos magnéticos críticos más altos. Dichas estructuras han sido generadas con distintos láseres: un láser ultravioleta con pulsos en el rango de cientos de picosegundos, y dos láseres que emiten pulsos en el infrarrojo cercano en el rango de los femtosegundos. Además, se han estudiado tratamientos en diferentes atmósferas. Esta modificación superficial es de gran interés para una aplicación directa del material, como es la construcción de cavidades resonantes de radio frecuencia.



Objectives

State of the Art

Publications

Discussion

Conclusions

Overall objectives of the thesis

Since the beginning of the past century, superconducting technologies have meant a spectacular upgrade in some applications. Some of them are already well established, some others offer some advantages in comparison with those based on “traditional” materials, but challenges still remain. Good examples of the latter type are power generation applications and those related with grid technology: Rotating machines (generators and motors), cables, grid stabilizers, etc. In order to develop and to improve these applications and many others, scientific community has had to deal with intrinsic restrictions of these materials. The development of these devices covers multiple aspects, from those directly related with the improvement of the superconducting properties, through the design and manufacture of complex conductor architectures, to those related to the correct integration of the different components and the reliability of the system. Special attention has to be paid to the study and optimization of the mechanical, thermal and electromagnetic properties of the used conductors and the final device.

Thermal behaviour analysis is essential to a proper functioning of the device in the superconducting operation regime at the required cryogenic temperatures. The thermal performance of the device is directly linked with the electromagnetic properties of the superconducting materials, characterized by highly non-linear current-voltage curves and by the strong dependence of the superconducting properties with temperature and applied magnetic fields. Within this context, a large part of this thesis is connected with thermal stability of different superconducting devices and its required ancillary technologies.

From the superconductor point of view, thermal stability is crucial to ensure every part of the device is working under the adequate operating conditions, whatever the superconducting material used to fabricate it. When designing a superconducting device, special care has to be taken with the generation and propagation of quenches, in order to ensure stable working conditions. An overcurrent or a heat disturbance can trigger a quench, which is the irreversible transition of the whole superconducting device to the normal (resistive) state during operation. These studies are relevant both, in the design of the wire and cable architecture as well as of the coil configuration.

Moreover, the design of the cryogenic system can play a relevant role in improving the thermal stability of the system. Current injection to the superconducting device may represent a heat overload, which can produce the superconductor to work below its potential if it is not properly designed. Therefore, it is important to control the heat propagation along the current leads and other ancillary equipment, as well as to provide the correct thermal anchorage of the superconductor and heat sinks, to ensure the appropriate temperature conditions.

Another application where superconductivity has been a step forward are the radio frequency cavities. These resonators are used in particle accelerators, and thanks to ultralow resistivity of superconducting materials, cavities performance has achieved an extraordinary upgrade. Surface properties determine surface superconductivity in these materials, being relevant their purity and surface control.

In this thesis, laser technology has been applied to modify the surface properties of the materials in two very different requests related with superconducting materials and their applications. Laser pulse duration has a direct relation with the energy delivery, so that near infrared (n-IR) lasers with pulses duration longer than hundreds of picoseconds produce mainly thermal processes that can be used to heat, melt or ablate the material surface. By contrast, the interaction of ultrashort (shorter than few picoseconds) pulse lasers with matter obeys to different mechanisms and eases surface nanostructuring. During this work, different pulsed lasers, which differ in wavelength and pulse duration, have been used with different objectives. In one hand, a laser of wavelength in the n-IR and with pulse duration of about 200 ns has been used to melt, totally or partially, ceramic coatings over metallic substrates. On the other hand, ultrafast laser irradiation has been used to nanostructure the surface of superconducting materials. Different nanostructures have been induced with a 300-ps UV and two fs n-IR laser sources.

This thesis is structured as follows. Next section after referring the thesis objectives is a ***State-of-the-art*** where superconducting and laser technologies are presented. Taking into account the applications of the superconducting materials that have been studied in this work, this description has been centred on power applications and superconducting radio frequency (SRF) cavities. On the other hand, laser technologies and their use in materials processing, based on both, melting and surface nanostructuring treatments, have been described. The following section is the ***compendium of publications*** and all the obtained results related with the main challenges of this thesis. Furthermore, a joint ***discussion*** of the main results of this thesis is exposed. Finally, main ***conclusions*** derived from the presented work are depicted, indicating also some research lines that have been opened as a result of the developed work.

Main challenges addressed in the publications

Opening works presented in this PhD thesis are related with the analysis of thermal stability in superconducting cables and coils. Quench generation and propagation have been studied in a MgB₂ Rutherford cable. This braided-type conductor provides several advantages over other conductors, such as an increase of current transport and a reduction of alternating current (AC) losses. Usually, two different experimental configurations are used to perform these analyses. The first option is to generate a localised hot-spot using a heater. The second one is to induce the quench by overcurrents, i.e., by applying currents higher than the critical current. In **publication A**, both configurations have been used to analyse the behaviour of a cable made with 12 strands of monocoil MgB₂/Nb/Cu10Ni wire during a quench, by measuring the evolution of intra- and inter-strand voltages. The influence of the physical properties of the metallic sheath in the wire performance has been studied.

Thermal stability has also been studied in a double pancake continuous coil. The first objective has been to build a double pancake (DP) continuous coil fabricated with second generation high temperature superconducting (2G-HTS) tape without insulation between turns, being able to withstand high currents. It has been cooled by conduction (anchored to a cryocooler's cold finger). Then, thermal and electromagnetic behaviour of the coil have been analysed. No-insulated coils are proposed to provide more robustness against thermal instabilities than the standard ones. They also reach greater compactness. By contrast, they present a delay between current and magnetic field ramps, together with additional losses during charge and discharge that could be a drawback for some

applications, where ramping should be as fast as possible. In **publication B**, the electromagnetic and thermal properties of a DP coil have been analysed, including: Charge and discharge characteristics, experimentally measured and numerically estimated critical current values, different loss contributions during current ramps and the thermal contact conductance between different parts of the double pancake coil. Their implications on the coil thermal stability have been discussed.

In these studies, electrical currents higher than 400 A in steady conditions have been implemented. This represents a challenge because of the heat generated in the current leads that connect room temperature to the coil. Current leads have been designed in three sections and were connected by bolted junctions that are thermally anchored to heat sinks using electrical insulating junctions. The behaviour of these current leads has been also described in **publication B**.

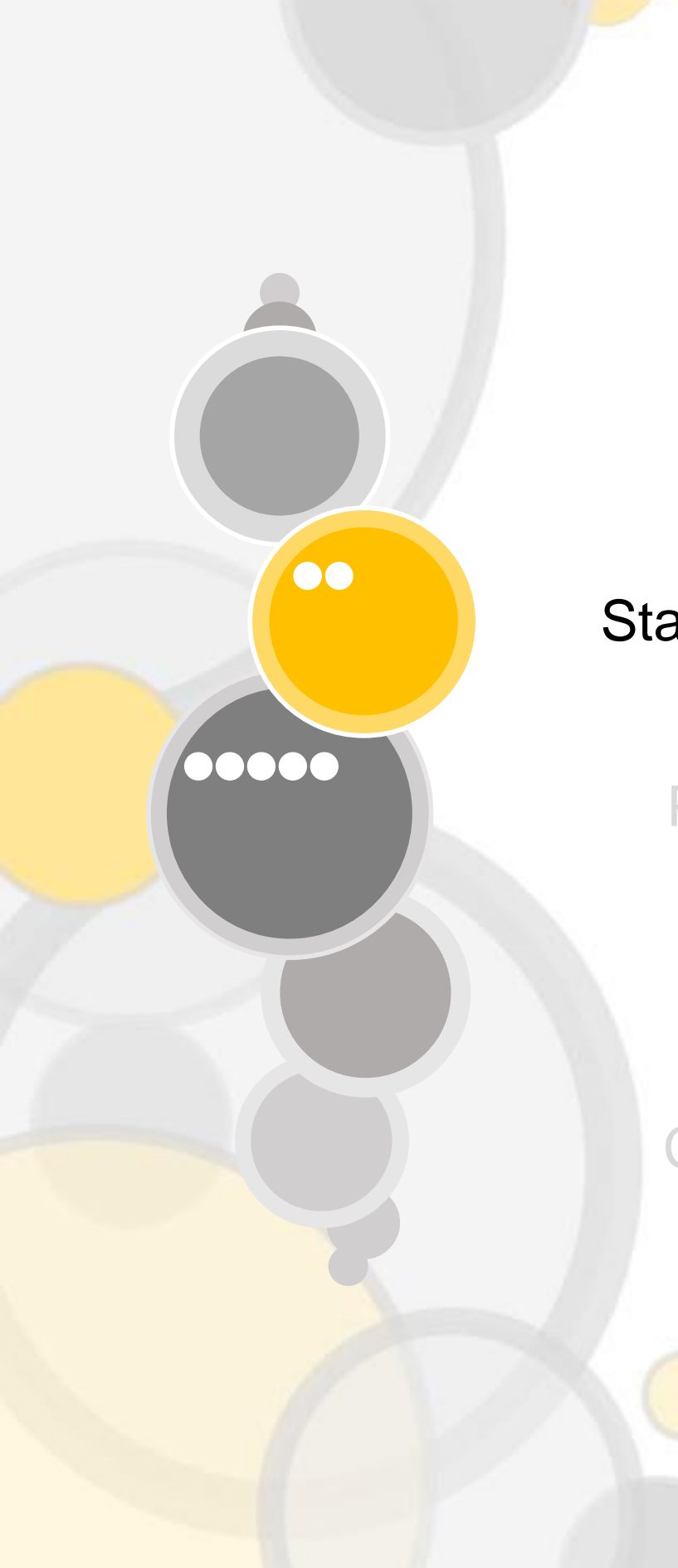
To develop the heat sinks of the cryocooler current leads, an option based on copper pieces covered with a plasma-sprayed alumina (Al_2O_3) coating has been proposed. This layer maintains the electric insulation, but its thermal conductivity needs further improvement. In **publication C**, laser technologies have been applied to densify the plasma-sprayed Al_2O_3 layer by remelting the alumina coating using a pulsed near infrared laser. Laser parameters have been adjusted to minimize crack generation and to improve the microstructure and thermal properties of the system, ensuring at the same time that the ceramic remains attached to the copper.

Laser technologies are also a versatile tool for surface nanostructuring. The final objective of this work has been to explore if superconducting properties can be modified by the interaction of these materials with laser irradiation. A three-month stay at Bundesanstalt für Materialforschung und -prüfung (BAM, Berlin, Germany) opened the possibility of using ultrashort pulsed laser processing. Pulse laser duration in the sub-nanosecond range can easily induce the formation of micro- and nanostructures on the irradiated surface with a well-defined periodicity. Recent advances based on this new phenomenology have opened a new path for surface engineering, creating a vast range of possibilities and applications.

From the superconductivity point of view, in particular type II superconductors, a precise lattice of defects can enhance its magnetic properties, especially in presence of external magnetic fields ranged between lower (H_{C1}) and upper (H_{C2}) critical values. In addition to these studied fields with a relevant bulk component, changes in the surface superconductivity, which persists in a very thin layer for magnetic fields above H_{C2} , have

been examined. The two works, published in **Publications D** and **E**, are the first works where it is demonstrated that these surface laser treatments modify superconducting properties.

These studies have been performed on niobium samples, the superconducting pure metal with the highest critical temperature, T_c (9.28 K) and critical magnetic fields. Different laser sources have been used to generate different nanostructures: An ultraviolet picosecond laser and two near infrared femtosecond lasers. Moreover, the use of different atmospheres during laser treatments has been studied. This surface modification may have great interest in a direct application of this material, as, for instance, in the construction of superconducting radio frequency (SRF) cavities.



Objectives

State of the Art

Publications

Discussion

Conclusions

1. Superconducting Materials and their applications

1.1 Phenomena, History and Materials

More than 100 years ago, in 1911, superconductivity was observed for the first time by Kamerlingh Onnes, Nobel Prize laureate in 1913. He observed that electrical resistance in mercury disappears below 4.2 K. Some years later, in 1933, Walther Meissner and Robert Ochsenfeld discovered the so-called Meissner (Meissner-Ochsenfeld) effect. It consists in the expulsion of the magnetic field, decaying exponentially inside the superconductor over a distance λ , London penetration depth, behaving like a perfect diamagnetic material. The temperature where the transition from superconductor to normal state takes place is defined as critical temperature, T_C . As we will see later, this parameter commonly classifies superconducting materials between low and high critical temperature superconductors, LTS and HTS, respectively.

The response of the material under magnetic field strengths, H , varies from type I to type II superconductor. For the former, an abrupt transition from superconductor to normal state takes place when H reaches a critical value, $H_C(T)$. However, type II superconductors are characterized by an upper critical field $H_{C2}(T)$ and a lower critical field $H_{C1}(T)$. Below H_{C1} , the material is in the Meissner state, above $H_{C2}(T)$ superconductivity in the bulk is lost. Between these two magnetic fields the superconductor is in the so-called mixed state, where the magnetic field penetrates into the material forming a regular lattice of quantized vortices, fluxons. These vortices have a normal core of radius equal to the

coherence length, ξ , surrounded by annular screening supercurrents where the magnetic field decays with λ . Both ξ and λ are characteristic for each material and depend on temperature, being $\lambda/\xi > 1/\sqrt{2}$ for type II superconductors. When the magnetic field is equal to H_{C2} , these vortices overlap and the bulk material turns to normal state. The upper critical field can be different depending on its relative direction respect to superconductor's crystallographic planes, in component parallel to plane ab, $H_{C2}^{\parallel ab}$, or perpendicular to it, $H_{C2}^{\perp ab}$. The ratio between both establishes the anisotropy factor, γ . Above H_{C2} , surface superconductivity phenomena persist in a thin layer until the applied magnetic field reaches a value called H_{C3} . In the case of flat surfaces, it was predicted that the thickness of this layer is similar to the superconducting coherence length and that $H_{C3} \approx 1.69 \times H_{C2}$ when H is applied parallel to superconductor's surface [1]. It is worth noting that all superconductors used for practical applications are type II.

Another important variable to consider is the current density, J , passing through the conductor for a given application. In the case of type II superconductors, in the presence of a magnetic field ($H_{C1} < H < H_{C2}$) this current density produces a force (Lorentz force, F_L) perpendicular to J and H that would tend to move the vortices. Movement of vortices, called flux flow, cause the generation of an electric field, E , and therefore dissipation. Nevertheless, defects with the size close to the coherence length can act, for a given temperature and magnetic field, as vortex pinning sites. Some typical defects able to pin the fluxon's lattice are grain boundaries or interstitial non-superconductive phases. This mechanism generates an average force, called pinning force (F_p), opposite to F_L . Thus, the critical current density, $J_c(T, H)$, can be defined as the limit current density when $F_p = F_L$ and it decreases when increasing magnetic field and temperature. It is needed to mention that in $J < J_c$ regime, the vortices can also move induced by thermal activation, especially in HTS materials. Thermally activated flux-creep processes, which also increase with temperature and magnetic field, will also cause dissipation. Irreversible magnetic field, $H_{irr}(T)$, is defined as the field at which J_c tends to zero, and is always lower than $H_{C2}(T)$. This parameter is thus crucial in superconducting application designs. It is important to notice that in some materials, mainly HTS, there is a large difference between the upper critical magnetic field and the irreversibility field.

After Onnes' work on mercury at the beginning of the twentieth century, superconductivity in many other metals, alloys and compounds have been found, being niobium the pure metal that exhibits the highest critical temperature, 9.3 K. Superconducting properties of several Nb alloys and intermetallic compounds were discovered and have been widely used in different applications. Among these are NbTi

with T_C close to 10 K [2], Nb_3Sn , with T_C of 18.1 K [3] and Nb_3Ge with T_C 22.3 K [4]. The unit cell structure of superconducting materials plays a significant role in their behavior. Pure metal niobium (**Figure 1.1(a)**) and NbTi have a body-centered-cubic structure (the second one, disordered BCC), Nb_3Sn has A15 crystal structure [5] and all of them are considered isotropic.

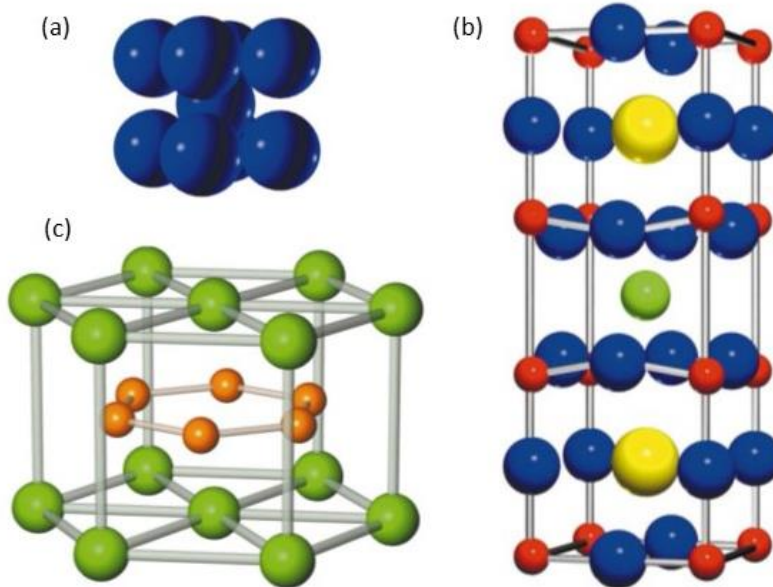


Figure 1.1 Crystal structures of various superconducting materials studied during this thesis adapted from [5]: **(a)** BCC structure of niobium. **(b)** Y-123 perovskite structure (Green – yttrium, yellow – barium, blue – oxygen and red – copper). **(c)** Supercell structure of magnesium diboride where two organised layers of Mg enclose the B one.

75 years after the discovery of superconductivity, in 1986, Bednorz and Müller discovered this property in cuprate-based materials below 35 K (Nobel-prized in 1987) and that was the starting point of the so-called High Temperature Superconductors, HTS. The goal of finding materials with superconducting properties at the highest possible temperature, understanding their behaviour and fundamentals, and improving properties for their applicability, established a new field of research that is open nowadays.

Some of the most widely studied and applied materials are the family of REBCO, meaning RE = Rare Earth elements in the structure of $REBa_2Cu_3O_{7-x}$. Due to its perovskite structure (orthorhombic layered, CuO_2 planes sandwiching RE atom) and its low ξ value, this ceramic has very anisotropic properties, because supercurrents flow easier along the copper oxide planes (ab plane) than in the perpendicular direction (c). Macroscopically, it exhibits weak

link behaviour between grains, so it requires almost perfect crystallinity and very low angle orientation between grains, both in-plane and out-of-plane, to achieve high critical current densities. For instance, $\text{YBa}_2\text{Cu}_3\text{O}_{7-x}$ (Y-123, **Figure 1.1(b)**) belongs to this group of materials. It was the first material discovered with a T_C (92 K) above the boiling point of liquid nitrogen (77 K) [6], showing a $B_{irr} = \mu_0 H_{irr}$ at this temperature between 5 and 7 T. This fact, together with the suitability of the material for many applications and the good knowledge of the manufacturing process, makes REBCO tapes one of the most used superconductors.

Another relevant group of materials are the Bi-based cuprates with a general chemical formula $\text{Bi}_2\text{Sr}_2\text{Ca}_{n-1}\text{Cu}_n\text{O}_{4+2n+x}$ (with $n = 1$ to 3) [7]. The two perovskites of this family with the highest T_C values are the $\text{Bi}_2\text{Sr}_2\text{CaCu}_2\text{O}_{8+x}$ (Bi-2212), with $T_C \approx 85$ K, and the $\text{Bi}_2\text{Sr}_2\text{Ca}_2\text{Cu}_3\text{O}_{10+x}$ (Bi-2223), with $T_C \approx 110$ K. Their crystal structure consists of CuO_2 layers intercalated between Ca, BiO and SrO layers. Owing to this, Bi-2223 and Bi-2212 exhibit even more anisotropy than Y-123 (>100 and around 7, respectively), which causes a large difference between H_{C2} and H_{irr} . This fact makes them not suitable for applications under moderate magnetic fields (> 2 T) unless the operation temperature is lower than 30 K, and consequently, the operation cost is increased. Similar superconductors are the Tl-based like $\text{Tl}_2\text{Ba}_2\text{Ca}_{n-1}\text{Cu}_n\text{O}_{2n+4}$ (with $n = 1$ to 3) or the Hg-based ones, like $\text{HgBa}_2\text{CuO}_4$ (Hg-1201).

Following the timeline observed in **Figure 1.2**, in 2001, superconductivity was found in magnesium diboride, MgB_2 . This material, synthesized for the first time in 1953, has a T_C of 39 K [8] and $B_{C2} = \mu_0 H_{C2}$ of 15 T at 4 K. This discovery evoked great interest both, from a physics point of view, studying the mechanism of superconductivity, and also for its applications. MgB_2 crystallography presents the hexagonal space group P6/mmm composed of alternating B and Mg sheets with boron atoms filling magnesium interstices (**Figure 1.1(c)**). This material is cheap and easy to produce in wires, resulting in a remarkably lower fabrication costs in comparison with cuprates, for example, and making MgB_2 good candidate for many applications, despite its T_C is lower than HTS or its B_{C2} values are slightly smaller in comparison with other superconductors like Nb_3Sn .

An important discovery was made some years later, in 2006: The appearance of superconductivity in the compound LaFePO [9], with a T_C around 4 K, which gave rise to intense research in a new group of superconductors, so called iron-based family (Fe-SC). FeSe is one of the simplest and most studied materials of this family with T_C ranging between 8 K and 38 K depending on the pressure [10][11]. Due to its brittleness, wires

made of these compounds are fabricated using similar techniques than with MgB_2 [12]. Critical temperature record, 109 K, was found in 2014 in single-layer Fe-Se films [13].

More recently, in 2015, superconductivity was reported for the first time in a hydrogen based compound (H_2S) under extremely high pressure (around 150 GPa) with a T_c close to 203 K [14]. Next step was given by *Drozdov et al.* in 2019 reporting superconductivity in LaH at 250 K under 180 GPa [15]. Hydrides and pressure-driven superconductivity have meant an extraordinary boost to this topics popularity, increasing the number of publications in the last decade [16]. On this date, “room-temperature” threshold has been passed and a photochemically transformed carbonaceous sulfur hydride system shows superconducting properties at a maximum temperature of almost 290 K with pressures ranging 140 to 275 GPa [17].

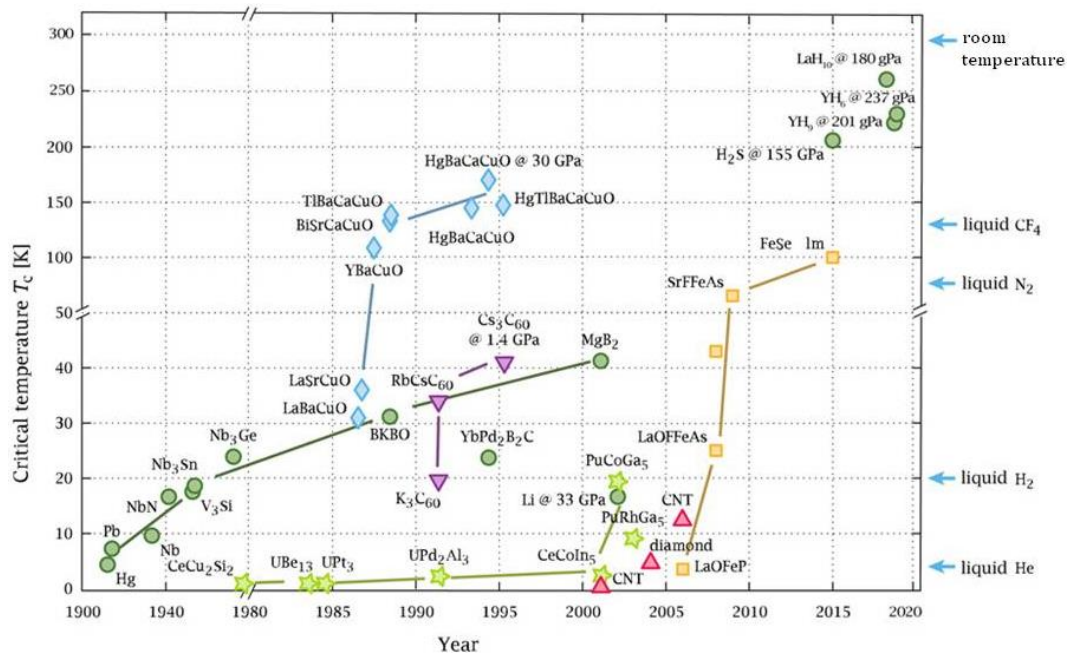


Figure 1.2 Timeline overview of discovery of different superconducting materials plotted against their critical temperature. They are grouped by families depending on the mechanism: Dark green circles – BCS theory. Light green star – Heavy-fermions-based. Blue diamonds – Cuprates/ceramics. Purple inverted triangles – Buckminsterfullerene-based. Red triangles – Carbon-allotropes. Orange squares – Iron-based. Adapted from [18].

It is shown the extraordinary activity, since 1911 until now, aiming at the discovery of new materials that exhibit superconductivity and the continuous improvement of their superconducting performance. One of the latest is graphene. Since its discovery in 2004,

the scientific community has performed many studies on this atomic mono-layer material related with its mechanical, electrical and thermal properties, for example. In 2018, superconductivity was discovered in bilayer graphene twisted a *magic angle* one to another [19].

It is worth clarifying that despite the great number of metals and compounds that have shown superconductivity, just some of them are suitable for practical applications. This is because, besides their superconducting properties, cost, easiness of production, mechanical properties and the possibility of being manufactured in form of wires or tapes (for example) are also important factors for their use in applications. The improvement of superconducting properties in these materials is just the first step in the race of making this technology competitive and useful.

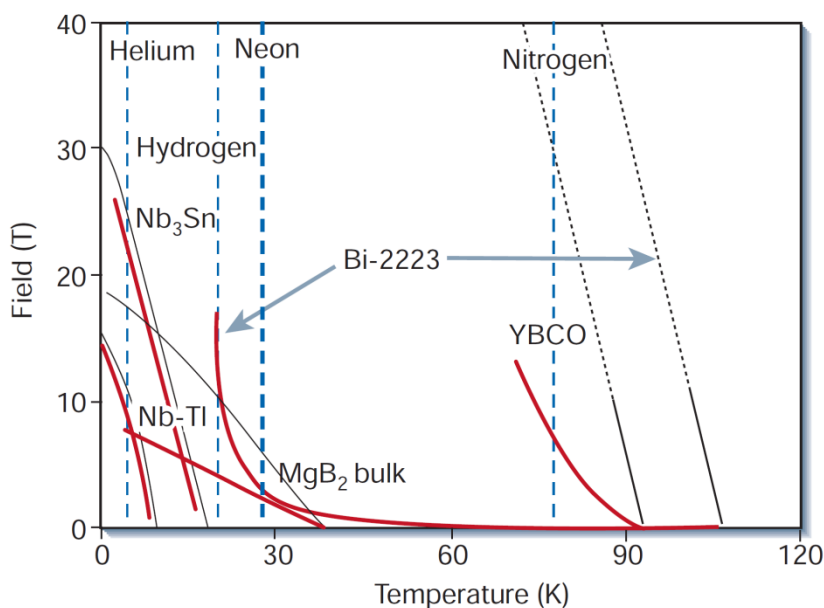


Figure 1.3 Magnetic field - temperature diagram where it is shown B_{c2} (black lines) and B_{irr} (red lines) of several superconducting materials. Above B_{c2} , bulk superconductivity is destroyed and B_{irr} is the limit where bulk critical current density goes to zero. Dashed vertical blue lines represent the boiling point of several cryogenic gases [5].

As it has been mentioned, critical current density depends on temperature and magnetic field. The higher the temperature and the magnetic field, the lower the critical current density is. So, it is very important to know the requirements for the superconducting material within the device in a given practical application. With this information, the choice of the correct material and the design of the whole device to work properly

requires ensuring that the operation conditions of the superconductor are below the constraints, $T < T_c$, $H < H_{irr}$ and $J < J_c$. **Figure 1.3** presents, for diverse materials, the difference between the upper critical magnetic field and the irreversible one, which will determine the applicability of each superconductor.

Besides the superconducting behaviour, other considerations, such as mechanical or thermal stresses, presence of alternating fields and currents, weight, cooling system, vacuum, etc, are relevant and, thus, should also be considered in the design of the superconducting device for each application.

1.2 Applied Superconductivity: From the laboratory to the final application

An important link of the chain that connects the laboratory with the final application of superconducting materials is how they are produced and their easiness to be integrated in the final device. A large number of the applications of superconductors require conductors in the form of wires or tapes with long length to construct cables or coils, which are needed in many devices. In most cases, due to the ceramic nature of many superconductors, and also because of thermal stability and mechanical requirements of the final conductor, different designs of composite conductors (metal/superconductor) are needed. Besides, some applications require other types or forms, such as bulks or thin layer superconducting coatings on substrates.

1.2.1 Wires and tapes fabrication

This section presents a brief summary of the fabrication technologies of most widely used superconducting materials, including some LTS, magnesium diboride wires and HTS conductors.

Starting with some of the most widely used LTS materials, NbTi [20] wires have a multifilamentary architecture (from tens to thousands microfilaments) and they are fabricated by cold work (drawing) of NbTi rods in a copper matrix (shown in **Figure 1.4 (a)**). In the case of Nb₃Sn, due to its high brittleness [3], it cannot be drawn directly from the rods. It is necessary to draw the precursors embedded in a composite matrix and after all the mechanical deformations; a heat treatment is applied to the final device (coil, cable, etc) to form the superconducting Nb₃Sn phase. In this process, a barrier, usually Nb

or Ta, is needed to avoid reaction between different elements during the final synthesis [21] (**Figure 1.4 (b)**).

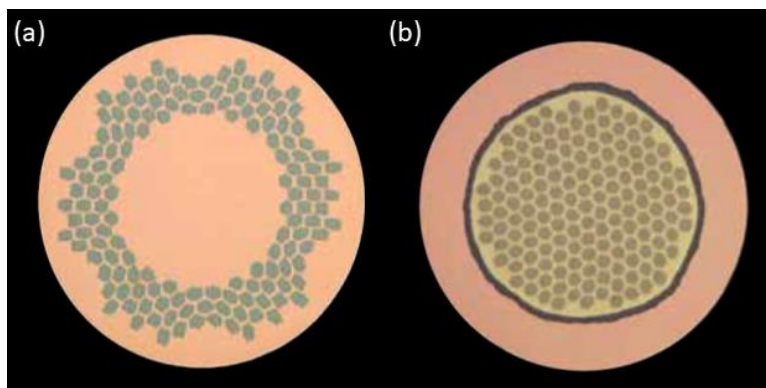


Figure 1.4 Examples of LTS wires: **(a)** Cross-sections of multifilamentary NbTi wire embedded in a Cu matrix. **(b)** Cross-sections of Nb₃Sn wire in a bronze matrix (yellow) surrounded by Cu (orange) fraction 20% to 60% separated by a diffusion barrier, Nb or Ta fraction 6% to 18% [22].

The manufacture of MgB₂ wires has been studied since its discovery, using different methods: The internal diffusion of magnesium (IMD) [23], which consists in the combination of a Mg rod surrounded by boron powder, which after reaction results in hollow tubes of MgB₂ with high density, close to 100%. Another alternative is the Powder-In-Tube (PIT) technique, in-situ [24] or ex-situ [25] methods. In these cases, either the Mg and B precursors or the reacted MgB₂ powders, respectively, are introduced in a metallic tube (sheath). Again, a cold work, such as drawing or swaging, is needed to generate long lengths of wire with the required final shape (circular, flatten, etc). It is common to use copper or similar metals in order to improve the thermal stability, although different alloys have been tested. Due to the high chemical reactivity of Mg, it is important to use a barrier (Nb, Ti, Ta, etc) around the superconducting core to avoid chemical reactions with the stabilizer (usually Cu) during the heat treatment. Both techniques, combined with cold working, allow the production of flexible mono- or multifilament conductors to use in cables and coils. Multifilament wires are more demanded (due to their higher current capability and better thermal and mechanical properties) and can be fabricated in diverse architectures. Filaments are integrated in a metallic matrix with good thermal properties (*e.g.* copper) and they are surrounded by the external sheath, typically a nickel- or copper-based alloy, as well as stainless steel, which provides mechanical strength to the wire. Examples of different configurations are shown in **Figure 1.5**.

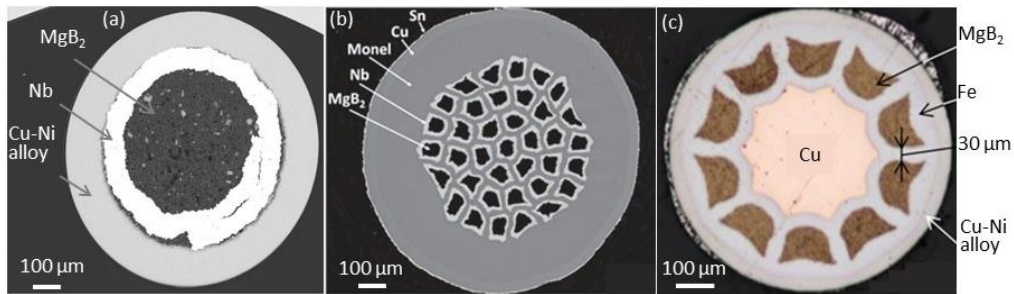


Figure 1.5 Different MgB_2 wire cross sections: (a) SEM image of a monofilament made by HyperTech using in-situ PIT technique. (b) SEM image of a multifilament (37 filaments) made by Columbus (ASG Superconductors) using ex-situ PIT technique [26]. (c) Picture of a multifilament with a copper core, made by Hitachi [27].

The production of wires and tapes with Bi-based superconducting materials has to take into account their anisotropy and brittleness. As it was already mentioned, they are very anisotropic and thus, a good alignment of the ab -planes (uniaxial texture of the grains) is required to ensure high critical current densities of the conductor [28]. The most common manufacturing process for Bi-2223 is the Oxide Powder In Tube (OPIT) [29], very similar to the previously mentioned PIT technique. In this case, oxide precursor powders fill a silver tube (or silver alloy) and drawing and rolling processes induce the alignment of the grains. After the mechanical deformation, a heat treatment is applied to form the superconducting phase inside the filaments. The final conductor also consists of many filaments embedded in a metallic matrix similar to **Figure 1.6**. The conductors manufactured using this technique are called first-generation high temperature superconductors, 1G-HTS. Silver and silver alloys are mandatory because of the chemical compatibility with the precursors and the oxygen permeability during the heat treatment. The high price of silver makes this material relatively expensive.

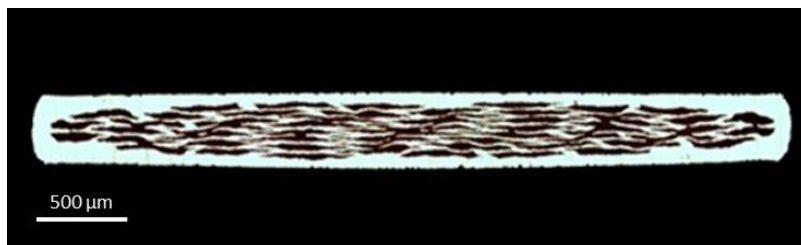


Figure 1.6 Cross-section of a 1G-HTS tape, Ag/Bi-2223 composite [30].

The current-carrying capacity of REBCO strongly depends on the grain to grain contact, so that a small misalignment between crystals reduces J_c exponentially [31]. Because of that,

this superconductor demands more texture control. The required biaxial texture is obtained by epitaxial deposition techniques [32], such as Ion Beam Assisted Deposition (IBAD) [33] or Rolling Assisted Biaxially Textured Substrate (RABiTS) [34]. Other techniques used are Pulsed Laser Deposition (PLD) [35], Metal Organic Deposition (MOD) [35], or Metal Organic Chemical Vapor Deposition (MOCVD) [36]. These so-called coated conductors are the second generation 2G-HTS.

Usually, the 2G-HTS layered tape similar to **Figure 1.7** is composed by: A metallic substrate, in the thickness range between 50 and 150 microns, normally nickel alloys such as Hastelloy; a buffer oxide layer(s) over the substrate (*e.g.* MgO, CeO₂ or Y₂O₃), which avoids the chemical reaction between the thin superconducting layer and the substrate and adapts gradually the lattice parameters to the superconductor; and a REBCO layer deposited over the buffer stack, typically of 1-2 μ m thickness. All this is surrounded by a protective silver layer. Usually, there is a layer of copper around the conductor to improve their thermal and electric stability. Other external sheaths, such as brass or stainless steel instead of copper, can also be used, to improve the mechanical properties of the conductor, or to tune the electrical resistivity at normal state, depending of the foreseen application. These tapes have a typical width between 2 and 12 mm and their thickness varies between 0.05 and 0.3 mm.

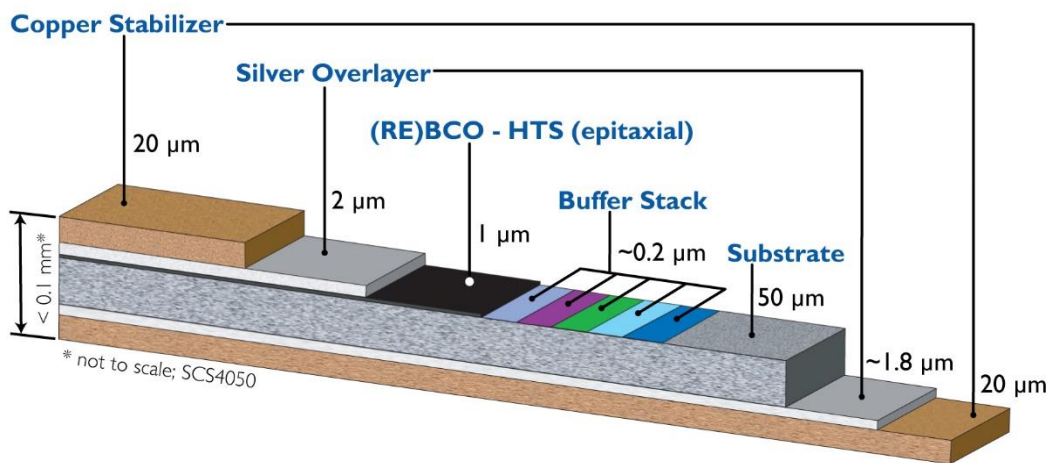


Figure 1.7 Scheme of different layers and composition of a 2G-HTS tape fabricated by SuperPower Inc [37].

An important procedure to enhance the current transport properties of these tapes in presence of magnetic fields is to introduce artificial pinning centres (nanoparticles or other defects in the few-nanometres scale). 2G-HTS tapes behaviour has a strong

dependence with the incidence angle of the magnetic field. The maximum critical current is normally obtained when B is applied parallel to the tape (0°), meaning perpendicular to the superconductor c -axis [38], but it strongly depends on the presence or not of artificial pinning centres, and their type.

1.2.2 Conductors and Coils manufacturing - Technological interest of SC windings

Once the conductors are manufactured in long lengths, they can be used to produce cables and coils for different uses. Before getting into details of these applications, some considerations have to be done. An alternate magnetic field involved in a given application where a type II superconductor is used, or an alternate current passing through it, can induce hysteresis losses and coupling losses (produced by coupling currents flowing through the metallic matrix between different superconducting filaments). There are some strategies to minimize AC losses. In order to reduce the loss component due to hysteresis, fine filaments are required. Besides, the increase of the electrical resistance between the filaments (or strands), and braiding or twisting them is required to uncouple those filaments (or strands) in the presence of AC fields, minimizing this way the losses.

There are different geometries of cables that have been used, depending on the properties of the superconducting material used in their fabrication. For example, it is well-studied and implemented to braid LTS conductors (NbTi and Nb₃Sn) to form Rutherford wires [39][40][41] and recently, so it does MgB₂ (**Figure 1.8**). This helix-shaped cable geometry is composed by several wires packed together, resulting in a conductor with an almost rectangular cross section and fully transposed current paths. Hence, an increase of current capability and a reduction of AC losses are achieved. Sometimes, the strands are braided around a metallic core, reducing the packing factor, changing conductor mechanical properties but improving the overall electric behaviour since the transverse coupling (between two faces of the planar core) is dramatically reduced.

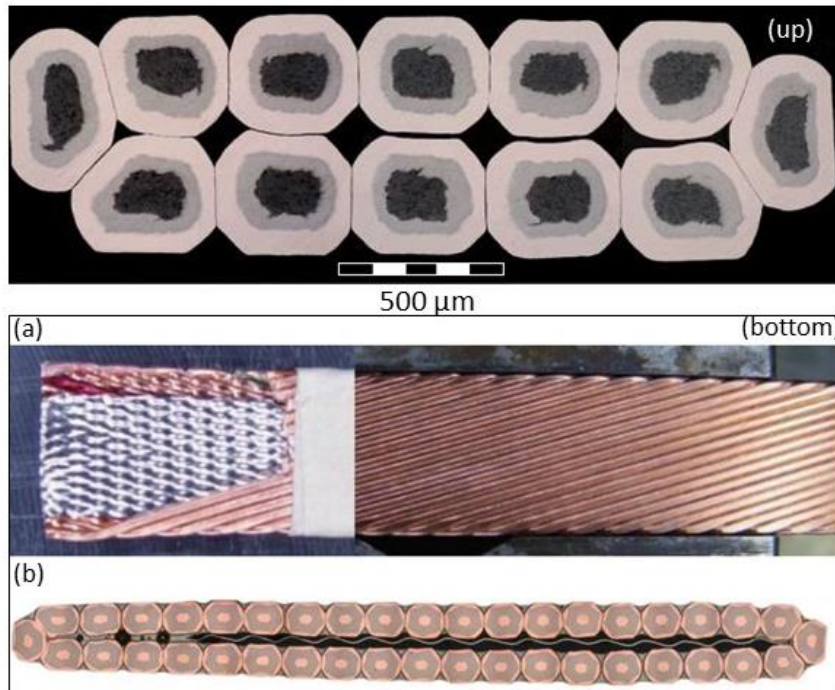


Figure 1.8 Rutherford cables: **(Up)** Cross-section of a 12-strand (each one monofilament) cable of MgB_2 : Braided in IEE, Slovakia and studied during this thesis. **(Bottom)** 40-strand cable of Nb_3Sn with a stainless-steel core: **(a)** Large face view. **(b)** Cross-section view [42].

An important application of Rutherford cables is in coil fabrication for high-energy experiments, for instance the superconducting magnets designed and built for particle accelerators at CERN [40][41][43]. Rutherford cables have also been used to manufacture superconducting coils in motors, where the presence of alternating magnetic fields makes the AC losses reduction relevant [44].

This cable geometry allows good mechanical properties making the conductor suitable for winding it into coils. Thanks to the good packing factor, the close contact between the strands makes really important the study of thermal and electric properties of each strand (metallic sheath's behaviour) and also throughout the whole cable. A good thermal conduction between strands can reduce the risks of hot-spots appearance, making the cable more reliable. However, very low electrical resistance between strands would increase the AC losses. Therefore, an equilibrium between both requirements is usually needed. Rutherford cables based on MgB_2 conductor have been proposed in the last few years, and its thermal stability and quench propagation phenomena have been studied in this thesis work, inducing superconducting-to-normal transitions (irreversible and abrupt)

by both heat pulses and overcurrents. Different MgB_2 cable architectures with diverse strand configurations have been analysed, focusing in a monofilament 12-stranded cable showed in **Figure 1.8 (up)**, with a Cu10Ni alloy sheath. Work related with this analysis can be found in the publication compendium section of this thesis, **publication A**.

Rutherford-geometry has also been implemented with HTS. One example is some tested cables based on Bi-2212 strands [45], with current densities attractive for some applications.

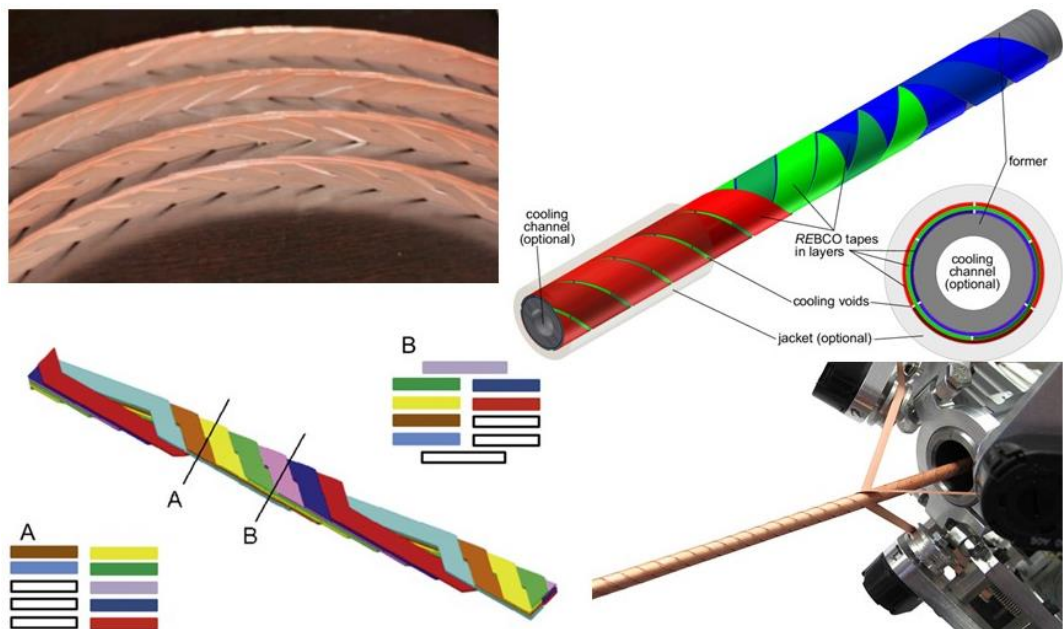


Figure 1.9 Left images present Roebel cables configuration: View of several cables (**top**) and an assembling scheme with two transversal sections A and B (**bottom**) [46]. Right images show CORC® cables: Schematic figure (**top**) [47] and part of the manufacturing process (**bottom**) [48].

In the case of 2G-HTS tapes, Roebel and CORC architectures [49][46] have been chosen in the attempt to achieve cables with high critical currents, improved mechanical properties and reduced AC losses, retaining enough flexibility for the cable design requirements (**Figure 1.9**). In the case of Roebel cable, the idea is similar to Rutherford cables but without bending the superconductor, having a transposition pitch where each, in this case, tape returns to the same relative position in relation to the other tapes that are part of the conductor. Special mention should also be made of the Conductor on Round Core (CORC®) cable architecture, where HTS tapes are wound around a circular-section core, where optionally the cooling channel is fitted. These cables are not only designed for

electric grid applications but also for accelerator magnets and high magnetic field applications, since they can work above 20 T at low temperatures (< 4 K).

Due to the mechanical properties of the 2G tapes, the fabrication process of these cables is in general more complicated than for LTS conductors.

Coils manufacture

As it has been previously mentioned, many of these superconducting wires, tapes and cables are then used to wind them into coils. And, of course, depending on each application, the coils will have different geometries. For example, in the case of motors or generators, the coils use to be racetrack-shaped or saddle-shaped, because the magnetic field is needed to be perpendicular to the long axis of the device (**Figure 1.10**).

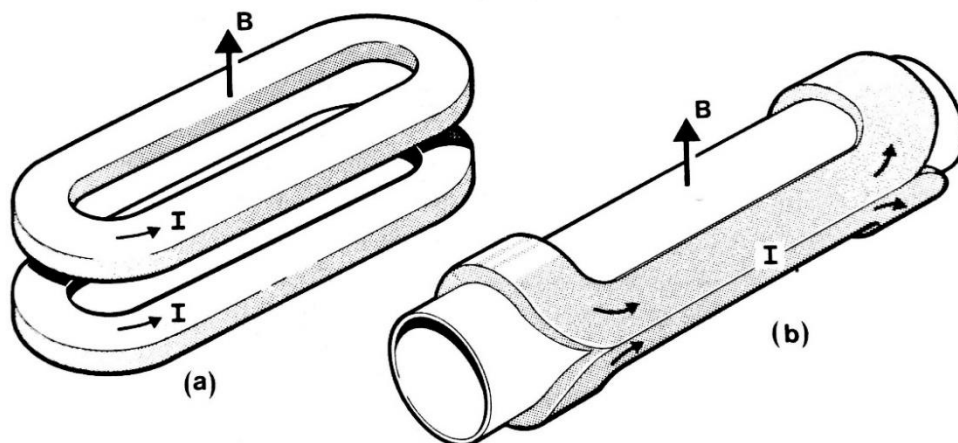


Figure 1.10 Coil architectures representing both current, I , and magnetic field, B , direction. **(a)** Racetrack and **(b)** Saddle configuration [50].

For Nuclear Magnetic Resonance (NMR) or Magnetic Resonance Imaging (MRI) equipments (that will be introduced during application section), is common to use superconducting solenoids in the inner ring, to create a magnetic field parallel to the cylinder's generatrix. On the other hand, high energy applications, such as fusion reactors, need a toroidal architecture to focus the magnetic field lines inside the control chamber (**Figure 1.11**).

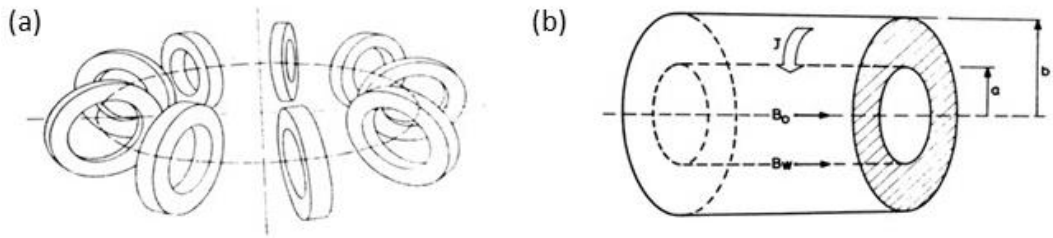


Figure 1.11 Different coil set-up: **(a)** Toroidal set up composed by circular-shaped coils and **(b)** Solenoid shaped winding [50].

In the case of solenoids, two winding processes are more widespread, especially with tapes (or rectangular-cross-section conductors): Pancake (or several pancakes piled up forming a stack) configuration and layer-wound configuration.

In the former scenario, pancake configuration, the conductor is wound from the inside to the outside in one single layer. If required, a double (or triple, etc) pancake coil can be built, with the precaution of connecting each other properly: Innermost turn of one layer with the outermost turn of the next one. Or, if enough superconductor material is available, several pancakes, normally double pancake, could be built continuously (without junction), facilitating thus the current feeding of the coil and avoiding an additional contact resistance between pancakes. In this case, the winding sense has to be changed from one layer to next one. The layer-wound configuration consists in winding from the inside to the outside, all along the “main axis” (generatrix). During this winding process, the mechanical properties of the conductors are relevant, so that the conductor maximum axial tension and its minimum bending radius cannot be exceeded.

In the course of coil operation, it is important to avoid the appearance of a quench as far as it is possible, and to protect the coil adequately if this were the case, to prevent permanent damages. Quench can be produced for several causes, for example due to mechanical or thermal effects. For instance, due to the electromagnetic forces acting during the charge or discharge of the coil, some turns can be bent or move and defects can be induced on the superconducting layer, which may trigger a quench. In particular, for 2G-HTS coils, those tensions can also produce delamination of the tape. Different expansion coefficients of the coil components can also produce enough tensions to damage the coil.

In order to solve these problems, since the early tests, the coils are glued with different resins which give stiffness to the whole device. These resins, mainly epoxies, are

thermostable polymers and, once mixed with a catalyst agent, they cure and became harder. They provide good electrical insulation and mechanical robustness to the coil. Some different resins are tested and reported, even paraffin [51][52] and nowadays there is no a clear choice of what is better to avoid all the possible failure modes (delamination, excess or default of stiffness, etc) for a given application.

A more direct source of quenches is related with the thermal stability. If a hot spot (or area) appears inside the coil, and this heat cannot be easily evacuated, the local operating temperature may eventually surpass the current sharing temperature. That is, the current is shared between the superconductor and the sheath or matrix metal, so that the conductor becomes locally resistive. If this energy is not correctly managed, the temperature of the coil in this region can increase above a safety threshold value. Here, the thermal conductivity of the resins and of the stabilizer layer plays a very important role.

Usually, superconducting coils are constructed by winding wires, tapes or cables, with an insulated material between turns. HTS coils are more prone to hot spots than LTS ones, due to low propagation velocities of quench. If a small zone of the HTS coil transits to normal state, due to the difficulty of evacuating the heat to the surrounding coil area, the temperature locally could increase, eventually damaging the conductor at this point, and so the coil. Due to the difficulty of achieving thermally robust 2G-HTS coils, the construction of coils without turn-to-turn insulation (non-insulated coils, NI coils), were used in **publication B** to improve their thermal stability [53]. This configuration has been studied previously by several groups noticing the coil's robustness and thermal stability but with some drawbacks during charge and discharge regimes [54][55][56]. In these moments, a turn-to-turn electrical current appears. This has important implication in the charge and discharge transitions and should be taken into account.

Summarising, design of coil's protection systems is a fundamental part to improve the associated superconducting technology, taking care of their electrical, thermal and mechanical stability. The electrical functioning of the coil, for instance charge-discharge regimes in addition to current transport affected by the intrinsic magnetic field has also to be considered [54]. Thermal stability is crucial working at cryogenic temperatures, constituting an essential part for the coil's reliability, together with mechanical steadiness, needed to avoid damages to the conductor and the whole device [57].

1.3 Applications

Although superconductivity is almost 110 years old, the technology related with it and its applications are nowadays a boiling field of research and there is a lot of effort and resources (human and material ones) dedicated to improve or to develop new functions of these materials.

Superconductivity is and will be involved in many applications related with medicine, locomotion, physics, energy or electronics. Each one takes advantage of different properties, for example: Some applications need to trap magnetic field and bulks of superconducting materials, mainly BSCCO and REBCO, are used to fabricate extremely compact parts (permanent magnets) for high-field requirements [58][59][60]. On the other hand, electronic applications need nano-wires to fabricate superconducting circuits, based on the Josephson junctions. Many efforts are put together to develop the first quantum computer [61][62] grounded in this effect, although in this group the most widespread application are the Superconducting Quantum Interference Devices (SQUIDs), which are the most sensitive detectors of magnetic flux.

In the following section, some relevant applications of the superconductors, related directly or indirectly with the content of this thesis, are briefly described.

1.3.1 High magnetic field applications

Many applications need to produce very intense magnetic fields. Related with medical diagnosis, Magnetic Resonance Imaging (MRI) equipments are based on the interaction between certain atomic nuclei in the presence of a strong constant external magnetic fields (normally produced by a superconducting coil), when exposed to radiofrequency electromagnetic waves. Gradient coils, which produce a gradient magnetic field that superposed to the main magnetic field, allow spatial encoding of the MR signal inside human bodies (mainly using the resonance signal of hydrogen nuclei). With the same principle, Nuclear Magnetic Resonance (NMR) techniques are used for chemical or biological analysis. Possibly, these are the most commercially successful applications for superconducting magnets, but also important are the magnets for high-energy physics and fusion nuclear energy, where particle accelerators involved in the Large Hadron Collider (LHC) and in the HiLumi (HI-LHC) at CERN and the ITER project [63] are great exponents.

Due to its good behaviour in presence of high magnetic fields, LTS materials like NbTi with $B_{C2}(0\text{ K}) = 14\text{ T}$, and Nb₃Sn with $B_{C2}(0\text{ K}) = 28\text{ T}$, are nowadays the most used superconductors for these applications. MRI coils, typically works in the range of 1.5 – 5 T and NbTi (usually Nb(47% wt)Ti) is a perfect candidate for these working conditions. It also presents the advantage of its manufacturing simplicity as it is relatively easy to draw it into wires. Nb₃Sn is commonly used together with some HTS materials to produce magnets involved in NMR devices, which require stronger magnetic fields. An important drawback of these LTS materials is however that they have to be cooled below 5 K, and the only cryogenic liquid suitable that can be used as a coolant is liquid helium (LHe). Although NbTi and Nb₃Sn are well established materials for these applications, also MgB₂ could play an important role in MRI systems [64][65]. It has higher T_c (39 K) and delivers a good performance in presence of magnetic field values. The introduction of this material reduces cryogenic costs, partly because it makes not necessary the use of LHe, thus being an interesting alternative for their use in remote areas. MgB₂ has also been introduced in projects like HI-LHC [66] thanks to its high current transport and good mechanical properties, keys for the busbars fabrication to feed the superconducting magnets.

1.3.2 Electric power applications

Many superconducting devices, or different parts of the same system, are assembled under the heading of electric power applications. It means that due to the absence of electric resistance, these conductors can carry very high currents without heat generation (Joule effect). With this in mind, power applications can be classified in two groups. In the first group we can consider those already existing that can be improved through the deployment of superconductor technology, by reducing size and weight of the final devices and enhancing its performance, i.e., rotating machines, transformers, cables, etc. A second group, where original systems take advantage of the superconducting properties of the material, are for example Superconducting Fault Current Limiters (SFCL) or Superconducting Magnetic Energy Storage (SMES).

An introduction of the main characteristics and types of these power applications are described as follows. All of them can be found in different stages of the electrical grid: Generation, storage, distribution and consumption. From wind turbines built with superconducting generators, through cables with different architectures or superconducting transformers in the distribution part, to energy storage or motors fabricated with superconducting coils.

Cables

Due to their urban planning, their population and their energy consumption profile, many cities have to be connected through underground power cables (also for safety reasons). Superconducting cables, which are able to transport the same current as a regular power cable in a volume up to five times smaller, could thus answer to the requirements associated with the increasing demand.

Transmission cables based on HTS materials are more efficient than the LTS ones due to their lower refrigeration requirements, although the material costs are significantly higher. Those cable architectures designed to transport alternating current need to take into account the AC losses and to reduce them as much as possible. Additional requirements of these cables are, to optimize the efficiency related with cooling the conductors, to consider the reactive power and to reduce radiated stray electromagnetic fields. Nowadays, the two principal configurations of HTS AC power cables are the warm cable dielectric one and the cold dielectric cable one [67][68].

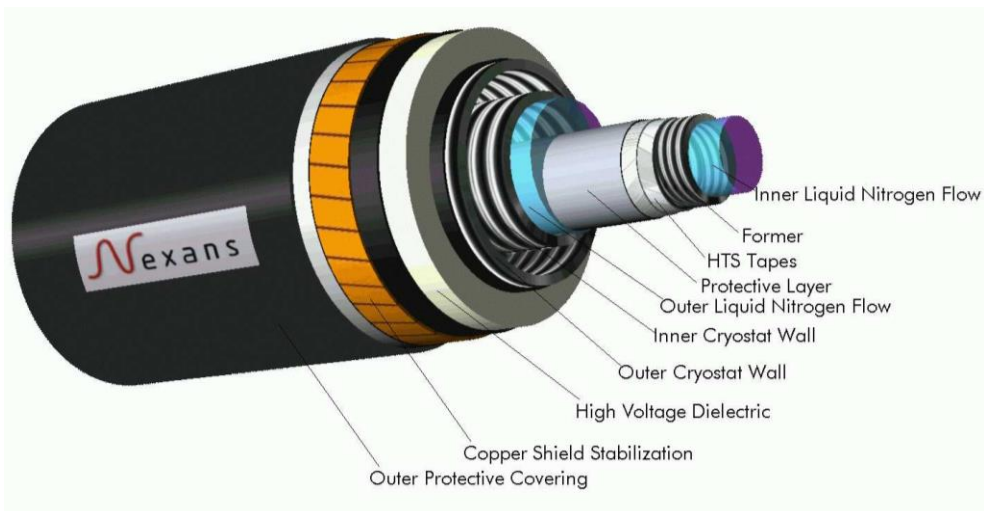


Figure 1.12 Single phase warm dielectric cable [68].

The first configuration (see **Figure 1.12**) is based on a HTS tape winding on a flexible channel where the liquid nitrogen flows. Outer dielectric insulation layer is needed in contact with the room temperature side. The principal advantage of this design is the small amount of HTS material needed for a given power level. On the other hand, it has high inductance and relatively high electrical losses. Cooling stations are needed to be closer to each other in comparison with other configurations.

On the other hand, cold dielectric cable configuration (**Figure 1.13**) has two concentric layers of HTS tapes separated by a cold dielectric. Refrigerant liquid has to be in contact with both layers with two objectives: to cool down the conductors and to isolate them from the outer layer. This solution is more expensive, mainly due to the material costs, but can carry more current and has lower inductance, lower AC losses and lower radiated electromagnetic fields. Both solutions can be implemented in a three-phase line.

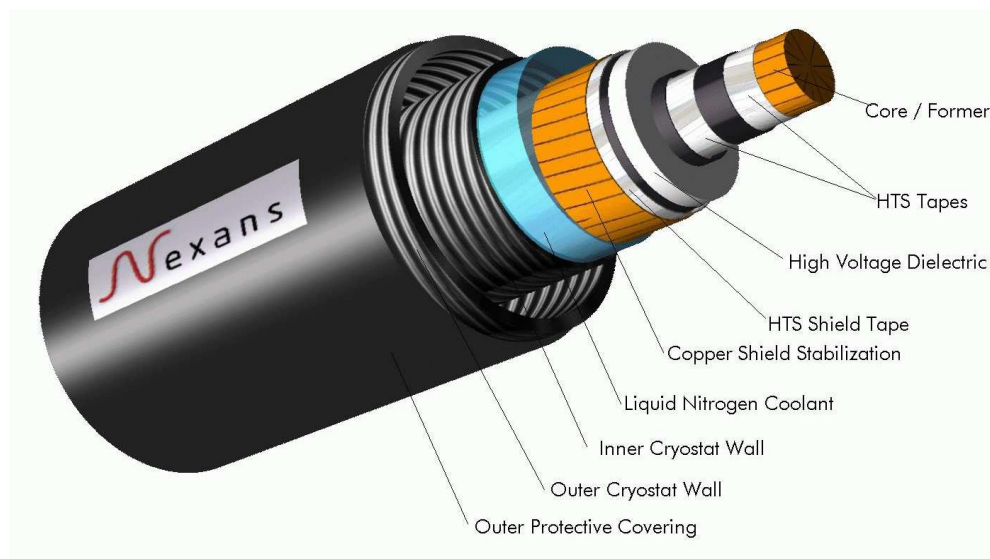


Figure 1.13 Single phase cold dielectric cable [68].

Transformers

In the electric network that connects energy producers and consumers, transformation centres decrease or increase the voltage level to reduce losses during the energy transport. Conventional transformers, with a well-established technology since the end of nineteenth century, are reliable and have an operation regime flexible enough to absorb load changes in different voltage levels. Nevertheless, these systems have many losses, approximately a fifty percent due to the conductors and other fifty percent related with the magnetic hysteresis of the iron cores.

Since superconductors can transport much more current than regular copper conductors, this technology can reduce the size of the transformers' coils, lowering at the same time the losses related with the conductor. But, to do that, it is necessary to have in mind several aspects, as for instance, the implicit constraints of working at cryogenic temperatures or the mechanical properties of the conductors. Two ideas have been

proposed to overcome this situation [69]. The first option would be to design a superconducting transformer following the same architecture of the conventional ones. In this system, liquid nitrogen would replace oil as a coolant (cold core type). The second alternative would be to isolate the core to reduce hysteresis losses and to cool down the coils indirectly (warm core or conduction cooled types) [70].

Superconducting Fault Current Limiters (SFCL)

Superconducting Fault Current Limiters (SFCL) can be used to protect the electrical grid against short-circuits. This type of elements would have small internal impedance during regular operation but would be able to develop high impedance within the very short times when a fault occurs. Superconductors are good candidates to this purpose since they can change from zero impedance to a large one when they transit from the superconducting to the normal state. Different superconducting materials have been tested for this aim, from Nb-Ti to HTS and magnesium diboride conductors [71]. Typically, SFCL are presented in three variants: Resistive, inductive and saturated core type [71][72][73]. According to the necessities of the particular electric grid, there will be a more convenient type (regarding the actuation time, cost, size, etc). For instance, resistive-type fault current limiters can be attractive in DC systems [74], saturated core FCL would be more interesting in high voltage grids whereas in a medium voltage grid inductive ones could be a better choice.

Energy Storage

Superconducting technology can also be found in the energy storage part of the grid. These devices are crucial for the network stability since the system needs to absorb a peak of consumption (demand) for a brief period of time, or to have a backup in case a sudden cut of the energy production. Two technologies presented here are used for different purposes:

Flywheel Electrical Energy Storage (FEES), transforms kinetic into electrical energy. It is used as a short-term spinning reserve in case a frequency regulation or a sudden balance is needed. To reduce the losses related with the rotation, HTS bearings are implemented [75].

The Superconducting Magnetic Energy Storage (SMES) systems are a second alternative. Basically, these systems store electromagnetic energy directly in a superconducting

magnet. This fact makes it a more efficient storage system because of the loss reduction. Other important advantage is the capacity of giving a fast response to energy demands in less than an AC cycle.

The SMES main components are the converter AC/DC, the superconducting magnet and the switch. If this switch is also superconductor, the response of the system will be more efficient. The inverter/rectifier, where the alternating current (AC) is transformed to direct current (DC) and vice versa is the least efficient component, with losses rounding 3%. Despite this, the whole system has a mean efficiency of 95% [5].

The energy stored in a magnet is giving by the following expression:

$$W = \frac{LI^2}{2} = \oint \frac{B^2}{2\mu_0} dV \quad (\text{Eq. 1.1})$$

Where W is the energy, L represents the inductance, I the current, B is the magnetic field and μ_0 is the permeability of free space. Therefore, larger inductance, which increases with number of turns and coil diameter, and higher current, results in more energy stored. In other words, higher magnetic field for a given volume means more energy, as well.

Several SMES configurations have been reported. For example, ones based on LTS conductors (mainly NbTi) that reach energy capacities of hundreds of MJ [75]. Others built with Bi-based HTS [76], usually provide less capacity.

Rotating machines: Locomotion, generators and motors

A different group of applications includes rotating machines; either for producing energy, generators, or to transform this energy into movement, motors. In both cases, superconductors contribute to a significant mass and volume reduction because of the higher current densities going through the coils of both the rotor and the stator. The most extended configuration consists of a superconducting cryogenic rotor where the poles are made by wires or tapes windings, and a copper (room temperature) stator. By doing this, superconducting materials can operate with direct current, reducing losses related with AC operating conditions. Early works in superconducting rotating machines were developed in 1970's decade with LTS materials [77][78]. More recently, high temperature superconductors have been widely tested [79][80].

From the viewpoint of the electric power generation, many efforts have been done in developing, for example, more efficient wind power turbines. Here superconducting

materials will have a relevant role, despite that the material costs (in terms of €/kA·m) are still high. Many efforts have been done, especially in offshore wind turbines of high power (several megawatts), thanks to the weight and volume reduction, the increased efficiency of the system and the avoidance of using extra rare earth elements, needed in actual models based on permanent magnets. To highlight some national and international examples: ICMA and ICMAB Spanish centres of research (both participated by the Spanish national research council – CSIC), together with Gamesa Innovation and Technology company collaborated to design a 2 MW Double-Fed Induction generator (DFIG) oriented to onshore wind turbines [81]. In addition, the EcoSwing European project finished in 2019, reaching the objective of developing the world's first superconducting low-cost and lightweight wind turbine drivetrain on a large-scale commercial near-shore wind turbine [82].

This research field has been boosted in the last few years because of the decision of many governments and institutions of fighting resolutely the climate change. Pollution and the emission of “greenhouse effect” gases have to be reduced and European Union claims for a bigger percentage of renewable energy and more energy efficiency [83], [84].

Finally, due to the long-term strategy executed by the European Commission, the locomotion applications with superconductors involved have also been pushed and many companies have started big R&D projects. Ships, but mainly aircrafts are the centre of all these studies [85][86].

1.3.3 SRF Cavities

A special application of superconducting materials, different to all above mentioned types, has been largely used in high energy facilities such as particle accelerators. The zero-electrical-resistance property of superconductors is crucial to develop high performance radio frequency resonators, commonly named as Superconducting Radio Frequency Cavities (SRF cavities). Their high quality factor, Q , enables to build resonators that store energy with very low losses and a narrow bandwidth. Quality factor refers to the energy lost per cycle; the higher the Q value, the lower the losses of the SRF cavity. An RF cavity is the device through which power is coupled into the particle beam of an accelerator. Electromagnetic fields are excited resonantly by tuning the RF source with the cavity-mode frequency. In operation, the beam of charged particles (e.g., electrons, ions, etc) passing through the cavity is thus accelerated by the resulting electric fields and deflected by the magnetic ones. **Figure 1.14** shows a simplified diagram of SRF cavities.

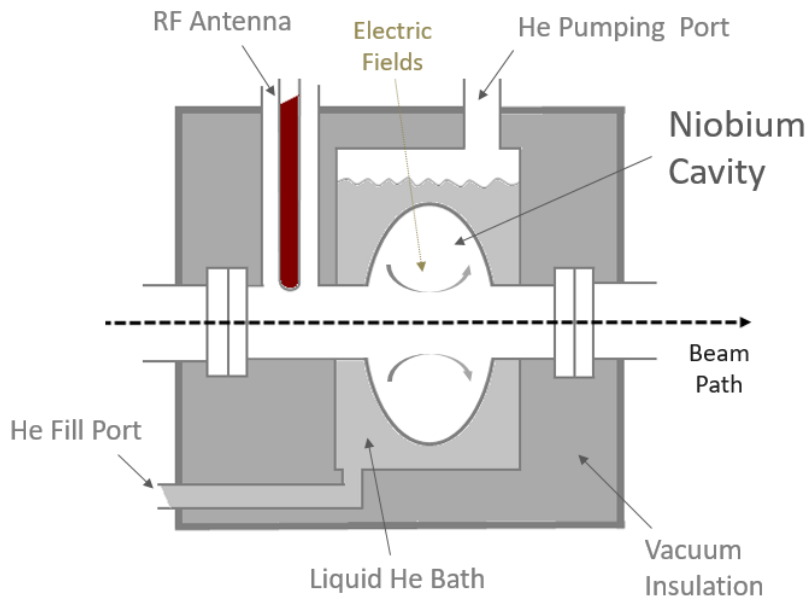


Figure 1.14 Scheme of a niobium SRF cavity with one cell.

Years ago, these cavities were made of copper but nowadays, they turn to be built with superconducting materials in order to improve the Q factor, which is directly linked with the surface resistance. Typically, the resonant frequencies range from 200 MHz to 3 GHz and have wall thickness between 1 and 3 mm of high purity niobium.

Despite some trials with more complex materials, i.e. REBCO [87], the widespread choice for these cavities [88][89] is niobium because it presents type II superconductivity up to 9.2 K and also low microwave surface resistance values. Operating below T_c to ensure a very low resistivity on the surface (R_s), extremely high values of Q can be reached because Q is inversely proportional to R_s . Many studies have been done related with the purity of niobium and its effect on the performance of the SRF cavities [90], and also with the treatments employed to enhance the niobium performance [91].

The presence of defects (*e.g.*, roughness or morphology) may pin the surface current vortices, like grain junctions do with the “bulk” vortices, resulting in an increase by more than two orders of magnitude the surface critical current, i_c . So, controlling surface characteristics of pure niobium is crucial for the correct behaviour of these cavities. Different techniques and their influence on the niobium magnetic properties (and surface superconductivity) have been reported. Thermal etching, electropolishing or buffered chemical polishing are usually done with this purpose [92][93]. Also the combination of some of the preceding treatments together with a previous annealing process in

controlled atmosphere has been shown to produce very low values of the microwave surface resistance [94]. There remains, however, some uncertainty about the reasons of why some of these used treatments lead to success. Some of them induce a reduction (and others a rise) of H_{C3} values, while a certain combination of them eventually produces an enhancement in cavities performance. These mechanisms are nowadays subject of ongoing fundamental SRF research.

These devices are one of the key components for future developments in high energy physics, nuclear physics or light source research. Some applications of these cavities are the XFEL (X-ray Free-Electron Laser) project [95] and the FLASH (Free electron LASer in Hamburg, result of the cancelled TESLA linear accelerator project) [96][97] in the field of lasers and light sources. The same technology will be used, for example at the linear particle accelerator of the International Large Collider (ILC) [98].

1.4 References

- [1] D. Saint-James and P. G. de Gennes, "Onset of superconductivity in decreasing fields," *Phys. Lett.*, vol. 7, 1963.
- [2] T. G. Berlincourt, "Emergence of NbTi as supermagnet material," *Cryogenics (Guildf)*, vol. 27, no. 6, pp. 283–289, 1987.
- [3] B. T. Matthias, T. H. Geballe, S. Geller, and E. Corenzwit, "Superconductivity of Nb₃Sn," *Phys. Rev.*, vol. 95, no. 6, p. 1435, Sep. 1954.
- [4] J. R. Gavaler, "Superconductivity in Nb–Ge films above 22 K," *Appl. Phys. Lett.*, vol. 23, no. 8, pp. 480–482, Oct. 1973.
- [5] D. Larbalestier, A. Gurevich, D. M. Feldmann, and A. Polyanskii, "High-T_C superconducting materials for electric power applications," *Nature*, vol. 414, no. 6861, pp. 368–377, 2001.
- [6] Wu *et al.*, "Superconductivity at 93 K in a new mixed-phase Yb-Ba-Cu-O compound system at ambient pressure.," *Phys. Rev. Lett.*, vol. 58, no. 9, pp. 908–910, Mar. 1987.
- [7] H. Maeda, Y. Tanaka, M. Fukutomi, and T. Asano, "A New High-T_C Oxide Superconductor without a Rare Earth Element," *Jpn. J. Appl. Phys.*, vol. 27, no. Part 2, No. 2, pp. L209–L210, 1988.
- [8] J. Nagamatsu, N. Nakagawa, T. Muranaka, Y. Zenitani, and J. Akimitsu, "Superconductivity at 39 K in magnesium diboride," *Nature*, vol. 410, no. 6824, pp. 63–64, 2001.
- [9] Y. Kamihara *et al.*, "Iron-Based Layered Superconductor: LaOFeP," *J. Am. Chem. Soc.*, vol. 128, no. 31, pp. 10012–10013, Aug. 2006.
- [10] H. Okamoto, "The fese (iron-selenium) system," *J. Phase Equilibria*, vol. 12, no. 3, pp. 383–389, 1991.
- [11] S. Medvedev *et al.*, "Electronic and magnetic phase diagram of β-Fe_{1.01}Se with superconductivity at 36.7 K under pressure," *Nat. Mater.*, vol. 8, no. 8, pp. 630–633, 2009.
- [12] Z. Gao, L. Wang, Y. Qi, D. Wang, X. Zhang, and Y. Ma, "Preparation of LaFeAsO_{0.9}F_{0.1} wires by the powder-in-tube method," *Supercond. Sci. Technol.*, vol. 21, no. 10, p. 105024, 2008.
- [13] J. F. Ge *et al.*, "Superconductivity above 100 K in single-layer FeSe films on doped SrTiO₃," *Nat. Mater.*, vol. 14, no. 3, pp. 285–289, 2015.

-
- [14] A. P. Drozdov, M. I. Eremets, I. A. Troyan, V. Ksenofontov, and S. I. Shylin, "Conventional superconductivity at 203 kelvin at high pressures in the sulfur hydride system," *Nature*, vol. 525, p. 73, Aug. 2015.
- [15] A. P. Drozdov *et al.*, "Superconductivity at 250 K in lanthanum hydride under high pressures," *Nature*, vol. 569, no. 7757, pp. 528–531, 2019.
- [16] J. A. Flores-Livas, L. Boeri, A. Sanna, G. Profeta, R. Arita, and M. Eremets, "A perspective on conventional high-temperature superconductors at high pressure: Methods and materials," *Phys. Rep.*, vol. 856, pp. 1–78, 2020.
- [17] E. Snider *et al.*, "Room-temperature superconductivity in a carbonaceous sulfur hydride," *Nature*, vol. 586, no. 7829, pp. 373–377, 2020.
- [18] P. J. Ray, *Structural Investigation of $La_{(2-x)}Sr_{(x)}CuO_{(4+y)}$: Following a Staging as a Function of Temperature*. Niels Bohr Institute, Copenhagen University, 2015.
- [19] Y. Cao *et al.*, "Correlated insulator behaviour at half-filling in magic-angle graphene superlattices," *Nature*, vol. 556, p. 80, Mar. 2018.
- [20] J. K. Hulm and R. D. Blaugher, "Superconducting Solid Solution Alloys of the Transition Elements," *Phys. Rev.*, vol. 123, no. 5, pp. 1569–1580, Sep. 1961.
- [21] D. Larbalestier, P. Madsen, J. Lee, M. Wilson, and J. Charlesworth, "Multifilamentary niobium tin magnet conductors," *IEEE Trans. Magn.*, vol. 11, no. 2, pp. 247–250, 1975.
- [22] "Bruker." [Online]. Available: <https://www.bruker.com>. [Accessed: 08-Aug-2020].
- [23] J. M. Hur, K. Togano, A. Matsumoto, H. Kumakura, H. Wada, and K. Kimura, "Fabrication of high-performance MgB_2 wires by an internal Mg diffusion process," *Supercond. Sci. Technol.*, vol. 21, no. 3, p. 32001, 2008.
- [24] B. A. Glowacki, M. Majoros, M. Vickers, J. E. Evetts, Y. Shi, and I. McDougall, "Superconductivity of powder-in-tube MgB_2 wires," *Supercond. Sci. Technol.*, vol. 14, no. 4, pp. 193–199, 2001.
- [25] G. Grasso *et al.*, "Large transport critical currents in unsintered MgB_2 superconducting tapes," *Appl. Phys. Lett.*, vol. 79, no. 2, pp. 230–232, Jul. 2001.
- [26] K. Konstantopoulou *et al.*, "Electro-mechanical characterization of MgB_2 wires for the Superconducting Link Project at CERN," *Supercond. Sci. Technol.*, vol. 29, no. 8, p. 84005, 2016.
- [27] "HITACHI - Inspire the Next," 2019. [Online]. Available: <https://www.hitachi.com/rd/news/topics/2019/1016.html>. [Accessed: 08-Dec-2020].
-

- [28] B. Hensel, J.-C. Grivel, A. Jeremie, A. Perin, A. Pollini, and R. Flükiger, "A model for the critical current in $(\text{Bi,Pb})_2\text{Sr}_2\text{Ca}_2\text{Cu}_3\text{O}_x$ silver-sheathed tapes: The role of small-angle c-axis grain boundaries and of the texture," *Phys. C Supercond.*, vol. 205, no. 3, pp. 329–337, 1993.
- [29] T. Hikata, K. Sato, and H. Hitotsuyanagi, "Ag-Sheathed Bi-Pb-Sr-Ca-Cu-O Superconducting Wires with High Critical Current Density," *Jpn. J. Appl. Phys.*, vol. 28, no. Part 2, No. 1, pp. L82–L84, 1989.
- [30] M. I. Adam and P. Mele, "Modulated Rate (Time)–Dependent Strain Hardening of Ag/Bi2223 Composite Wire Flattened in a Low–Strength AgMg Alloy Matrix," *ES Mater. Manuf.*, vol. 1, pp. 27–34, 2018.
- [31] D. Dimos, P. Chaudhari, J. Mannhart, and F. K. Legoues, "Orientation dependence of grain-boundary critical currents in $\text{YBa}_2\text{Cu}_3\text{O}_{7-}$ bicrystals," *Phys. Rev. Lett.*, vol. 61, no. 2, pp. 219–222, Jul. 1988.
- [32] Y. Iijima, N. Tanabe, O. Kohno, and Y. Ikeno, "In-plane aligned $\text{YBa}_2\text{Cu}_3\text{O}_{7-x}$ thin films deposited on polycrystalline metallic substrates," *Appl. Phys. Lett.*, vol. 60, no. 6, pp. 769–771, Feb. 1992.
- [33] Y. Iijima, K. Kakimoto, M. Kimura, K. Takeda, and T. Saitoh, "Reel to reel continuous formation of Y-123 coated conductors by IBAD and PLD method," *IEEE Trans. Appl. Supercond.*, vol. 11, no. 1, pp. 2816–2821, 2001.
- [34] A. Goyal *et al.*, "Recent progress in the fabrication of high- J_c tapes by epitaxial deposition of YBCO on RABiTS," *Phys. C Supercond.*, vol. 357–360, pp. 903–913, 2001.
- [35] D. M. Feldmann, T. G. Holesinger, R. Feenstra, and D. C. Larbalestier, "A Review of the Influence of Grain Boundary Geometry on the Electromagnetic Properties of Polycrystalline $\text{YBa}_2\text{Cu}_3\text{O}_{7-x}$ Films," *J. Am. Ceram. Soc.*, vol. 91, no. 6, pp. 1869–1882, Jun. 2008.
- [36] V. Selvamanickam, Y. Xie, J. Reeves, and Y. Chen, "MOCVD-based YBCO-coated conductors," *MRS Bull.*, vol. 29, no. 8, pp. 579–582, 2004.
- [37] "SuperPower Inc." [Online]. Available: <http://www.superpower-inc.com/content/2g-hts-wire>. [Accessed: 20-Mar-2018].
- [38] G. Ercolano *et al.*, "State-of-the-art flux pinning in $\text{YBa}_2\text{Cu}_3\text{O}_{7-\delta}$ by the creation of highly linear, segmented nanorods of $\text{Ba}_2(\text{Y/Gd})(\text{Nb/Ta})\text{O}_6$ together with nanoparticles of $(\text{Y/Gd})_2\text{O}_3$ and $(\text{Y/Gd})\text{Ba}_2\text{Cu}_4\text{O}_8$," *Supercond. Sci. Technol.*, vol. 24, no. 9, p. 95012, 2011.
- [39] L. Bottura and A. Godeke, "Superconducting Materials and Conductors:

-
- Fabrication and Limiting Parameters,” *Rev. Accel. Sci. Technol.*, vol. 05, pp. 25–50, Jan. 2012.
- [40] A. Devred *et al.*, “High Field Accelerator Magnet R&D in Europe,” *Appl. Supercond. IEEE Trans.*, vol. 14, pp. 339–344, Jul. 2004.
- [41] D. Schoerling and A. V Zlobin, *Nb₃Sn Accelerator Magnets: Designs, Technologies and Performance*. 2019.
- [42] E. Barzi and A. V Zlobin, “Nb₃Sn Wires and Cables for High-Field Accelerator Magnets,” *Nb₃Sn Accel. Magnets*, p. 23, 2019.
- [43] J. Fleiter, B. Bordini, A. Ballarino, L. Oberli, S. Izquierdo, and L. Bottura, “Quench Propagation in Nb₃Sn Rutherford Cables for the Hi-Lumi Quadrupole Magnets,” *IEEE Trans. Appl. Supercond.*, 2015.
- [44] P. Kovac *et al.*, “Rutherford cable made of internal magnesium diffusion MgB₂ wires sheathed with Al-Al₂O₃ particulate metal matrix composite,” *Supercond. Sci. Technol.*, vol. 31, no. 1, 2018.
- [45] R. M. Scanlan *et al.*, “Fabrication and test results for Rutherford-type cables made from BSCCO strands,” *IEEE Trans. Appl. Supercond.*, vol. 9, no. 2, pp. 130–133, 1999.
- [46] W. Goldacker, F. Grilli, E. Pardo, A. Kario, S. Schlachter, and M. Vojenciak, “Roebel cables from REBCO coated conductors: A one-century-old concept for the superconductivity of the future,” *Supercond. Sci. Technol.*, vol. 27, Jun. 2014.
- [47] C. Barth, D. Laan, N. Bagrets, C. Bayer, K.-P. Weiss, and C. Lange, “Temperature- and field-dependent characterization of a conductor on round core cable,” *Supercond. Sci. Technol.*, vol. 28, Apr. 2015.
- [48] “Advanced Conductor - CORC cables.” [Online]. Available: <http://www.advancedconductor.com/corccable>. [Accessed: 20-Nov-2020].
- [49] D. Uglietti, “A review of commercial high temperature superconducting materials for large magnets: From wires and tapes to cables and conductors,” *Supercond. Sci. Technol.*, vol. 32, Apr. 2019.
- [50] M. N. Wilson, “Superconducting magnets,” 1983.
- [51] H.-J. Shin *et al.*, “Effects of impregnating materials on thermal and electrical stabilities of the HTS racetrack pancake coils without turn-to-turn insulation,” *IEEE Trans. Appl. Supercond.*, vol. 23, no. 3, p. 7700404, 2012.
- [52] T. Takematsu *et al.*, “Degradation of the performance of a YBCO-coated conductor double pancake coil due to epoxy impregnation,” *Phys. C Supercond. its Appl.*, vol.
-

- 470, no. 17–18, pp. 674–677, 2010.
- [53] A. Cubero, A. B. Núñez-Chico, R. Navarro, L. A. Angurel, and E. Martínez, “Electromagnetic behaviour and thermal stability of a conduction-cooled, no-insulated 2G-HTS coil at intermediate temperatures,” *Cryogenics (Guildf)*, vol. 108, no. October 2019, p. 103070, 2020.
- [54] S. Hahn, D. K. Park, J. Bascunan, and Y. Iwasa, “HTS Pancake Coils Without Turn-to-Turn Insulation,” *IEEE Trans. Appl. Supercond.*, vol. 21, no. 3, pp. 1592–1595, 2011.
- [55] K. Kim *et al.*, “Operating Characteristics of an Insulationless HTS Magnet Under the Conduction Cooling Condition,” *IEEE Trans. Appl. Supercond.*, vol. 23, no. 3, p. 4601504, 2013.
- [56] S. Yoon *et al.*, “The performance of the conduction cooled 2G HTS magnet wound without turn to turn insulation generating 4.1T in 102mm bore,” *Phys. C Supercond.*, vol. 494, pp. 242–245, 2013.
- [57] A. B. Nuñez-Chico, E. Martínez, L. A. Angurel, and R. Navarro, “Effects of Thermal Cycling and Thermal Stability on 2G HTS Pancake Coils,” *IEEE Trans. Appl. Supercond.*, vol. 25, no. 3, pp. 1–4, 2015.
- [58] J. H. Durrell *et al.*, “Bulk superconductors: a roadmap to applications,” *Supercond. Sci. Technol.*, vol. 31, no. 10, p. 103501, 2018.
- [59] J. R. Hull and M. Murakami, “Applications of bulk high-temperature Superconductors,” *Proc. IEEE*, vol. 92, no. 10, pp. 1705–1718, 2004.
- [60] T. Coombs, “4 - Bulk high temperature superconductor (HTS) materials,” in *Woodhead Publishing Series in Energy*, Z. B. T.-H. T. S. (HTS) for E. A. Melhem, Ed. Woodhead Publishing, 2012, pp. 101–139.
- [61] “intel.com,” 2015. [Online]. Available: <https://newsroom.intel.com/news-releases/intel-invests-us50-million-to-advance-quantum-computing/#gs.cm0jac>. [Accessed: 05-Aug-2020].
- [62] D. Castelvecchi, “Quantum computers ready to leap out of the lab in 2017,” *Nature*, vol. 541, no. 7635, pp. 9–10, Jan. 2017.
- [63] G. Grunblatt, P. Mocaer, C. Verwaerde, and C. Kohler, “A success story: LHC cable production at ALSTOM-MSA,” *Fusion Eng. Des.*, vol. 75–79, pp. 1–5, 2005.
- [64] L. Bertora, “MRI Magnets based on MgB₂,” in *MgB₂ Superconducting Wires*, vol. Volume 2, WORLD SCIENTIFIC, 2015, pp. 485–536.
- [65] W. Yao, J. Bascunan, S. Hahn, and Y. Iwasa, “MgB₂ coils for MRI applications,” *Appl. Supercond. IEEE Trans.*, vol. 20, pp. 756–759, Jul. 2010.

-
- [66] M. Sugano, A. Ballarino, B. Bartova, R. Bjoerstad, C. Scheuerlein, and G. Grasso, "Characterization of mechanical properties of MgB₂ conductor for the superconducting link project at CERN," *IEEE Trans. Appl. Supercond.*, vol. 25, no. 3, pp. 1–4, 2015.
- [67] S. J. Lee, M. Park, I.-K. Yu, Y. Won, Y. Kwak, and C. Lee, "Recent status and progress on HTS cables for AC and DC power transmission in Korea," *IEEE Trans. Appl. Supercond.*, vol. 28, no. 4, pp. 1–5, 2018.
- [68] F. Schmidt and A. Allais, "Superconducting Cables for Power Transmission Applications: A Review," 2005.
- [69] J. Pelegrín, "Study of thermal stability processes in MgB₂ and REBCO wires and tapes," 2013.
- [70] G. Donnier-Valentin, P. Tixador, and E. Vinot, "Considerations about HTS superconducting transformers," *IEEE Trans. Appl. Supercond.*, vol. 11, no. 1, pp. 1498–1501, 2001.
- [71] A. Morandi, "State of the art of superconducting fault current limiters and their application to the electric power system," *Phys. C Supercond. its Appl.*, vol. 484, pp. 242–247, 2013.
- [72] L. Salasoo, A. F. Imece, R. W. Delmerico, and R. D. Wyatt, "Comparison of superconducting fault limiter concepts in electric utility applications," *IEEE Trans. Appl. Supercond.*, vol. 5, no. 2, pp. 1079–1082, 1995.
- [73] M. Noe and M. Steurer, "High-temperature superconductor fault current limiters: concepts, applications, and development status," *Supercond. Sci. Technol.*, vol. 20, no. 3, p. R15, 2007.
- [74] W. R. L. Garcia, P. Tixador, B. Raison, A. Bertinato, B. Luscan, and C. Creusot, "Technical and Economic Analysis of the R-Type SFCL for HVDC Grids Protection," *IEEE Trans. Appl. Supercond.*, vol. 27, no. 7, pp. 1–9, 2017.
- [75] T. M. Mulcahy *et al.*, "Flywheel energy storage advances using HTS bearings," *IEEE Trans. Appl. Supercond.*, vol. 9, no. 2, pp. 297–300, 1999.
- [76] S. S. Kalsi *et al.*, "HTS SMES magnet design and test results," *IEEE Trans. Appl. Supercond.*, vol. 7, no. 2, pp. 971–976, 1997.
- [77] C. Oberly, "Air force applications of lightweight superconducting machinery," *IEEE Trans. Magn.*, vol. 13, no. 1, pp. 260–268, 1977.
- [78] H. Stevens, M. Superczynski, T. Doyle, J. Harrison, and H. Messinger, "Superconducting machinery for naval ship propulsion," *IEEE Trans. Magn.*, vol.
-

- 13, no. 1, pp. 269–274, 1977.
- [79] G. Klaus, M. Wilke, J. Fraunhofer, W. Nick, and H. Neumuller, “Design Challenges and Benefits of HTS Synchronous Machines,” in *2007 IEEE Power Engineering Society General Meeting*, 2007, pp. 1–8.
- [80] W. Nick, J. Grundmann, and J. Fraunhofer, “Test results from Siemens low-speed, high-torque HTS machine and description of further steps towards commercialisation of HTS machines,” *Phys. C Supercond. its Appl.*, vol. 482, pp. 105–110, 2012.
- [81] PROGRAMA RETOS de Colaboración, “Diseño de una nueva generación de generadores y equipos auxiliares para energía eólica basados en superconductores.” .
- [82] “Ecoswing.” [Online]. Available: <https://ecoswing.eu/project>. [Accessed: 08-Jul-2020].
- [83] “EU Climate Strategies & Targets,” 2012. [Online]. Available: https://ec.europa.eu/clima/policies/strategies/2020_en.
- [84] “EU Climate Strategies & Targets,” 2018. [Online]. Available: https://ec.europa.eu/clima/policies/strategies/2050_en#tab-0-1.
- [85] A. Patel, V. Climente-Alarcon, A. Baskys, B. A. Glowacki, and T. Reis, “Design considerations for fully superconducting synchronous motors aimed at future electric aircraft,” in *2018 IEEE International Conference on Electrical Systems for Aircraft, Railway, Ship Propulsion and Road Vehicles & International Transportation Electrification Conference (ESARS-ITEC)*, 2018, pp. 1–6.
- [86] F. Berg, J. Palmer, P. Miller, and G. Dodds, “HTS system and component targets for a distributed aircraft propulsion system,” *IEEE Trans. Appl. Supercond.*, vol. 27, no. 4, pp. 1–7, 2017.
- [87] D. Ahn *et al.*, “Maintaining high Q-factor of superconducting $\text{YBa}_2\text{Cu}_3\text{O}_{7-x}$ microwave cavity in a high magnetic field,” *arXiv Prepr. arXiv1904.05111*, 2019.
- [88] H. Padamsee, “High purity niobium for superconducting accelerator cavities,” *J. Less Common Met.*, vol. 139, no. 1, pp. 167–178, 1988.
- [89] P. Kumar, “High purity niobium for superconducting applications,” *J. Less Common Met.*, vol. 139, no. 1, pp. 149–158, 1988.
- [90] W. Singer, “Metallurgical and technological request for high purity niobium in SRF application,” *AIP Conf. Proc.*, vol. 837, pp. 51–63, 2006.

- [91] Z.-H. Sung, A. Dzyuba, P. J. Lee, D. C. Larbalestier, and L. D. Cooley, "Evidence of incomplete annealing at 800 °C and the effects of 120 °C baking on the crystal orientation and the surface superconducting properties of cold-worked and chemically polished Nb," *Supercond. Sci. Technol.*, vol. 28, no. 7, p. 75003, 2015.
- [92] S. Casalbuoni *et al.*, "Surface superconductivity in niobium for superconducting RF cavities," *Nucl. Instruments Methods Phys. Res. Sect. A Accel. Spectrometers, Detect. Assoc. Equip.*, vol. 538, no. 1–3, pp. 45–64, 2005.
- [93] M. Aburas, A. Pautrat, and N. Bellido, "Change of surface critical current in the surface superconductivity and mixed states of superconducting niobium," *Supercond. Sci. Technol.*, vol. 30, no. 1, p. 15009, 2016.
- [94] A. Grassellino *et al.*, "Nitrogen and argon doping of niobium for superconducting radio frequency cavities: A pathway to highly efficient accelerating structures," *Supercond. Sci. Technol.*, vol. 26, no. 10, 2013.
- [95] "XFEL." [Online]. Available: <https://www.xfel.eu/>.
- [96] "FLASH." [Online]. Available: <https://flash.desy.de/>.
- [97] L. Lilje *et al.*, "Achievement of 35MV/m in the superconducting nine-cell cavities for TESLA," *Nucl. Instruments Methods Phys. Res. Sect. A Accel. Spectrometers, Detect. Assoc. Equip.*, vol. 524, no. 1–3, pp. 1–12, May 2004.
- [98] J. Sekutowicz *et al.*, "Design of a Low Loss SRF Cavity for the ILC," in *Proceedings of the 2005 Particle Accelerator Conference*, 2005, pp. 3342–3344.

2. Surface Processing by Laser Technologies

Laser technology has played an important role in the development of the research works presented in this thesis. In particular, laser melting and laser surface nanostructuring have been used for different applications. In this section, the basics of laser radiation and laser-matter interaction will be described. Moreover, the most relevant laser processing parameters will be defined.

2.1. Laser: Fundamentals

Since the last part of the twentieth century, the humankind is surrounded by laser technology. Not only inside laboratories, but also in everyday products. This can give us an idea of the importance of this invention. The first working laser device was built by T. H. Mainman in 1960 [1], based on the works of C. H. Townes and A. L. Schawlow [2]. Laser is the acronym of **L**ight **A**mplification by **S**timulated **E**mission of **R**adiation and the name itself give us a small description of how it works.

Stimulated emission can be explained following these ideas. Considering individual atoms or molecules, electrons orbiting around the atomic nucleus are placed in discrete levels of energy (**Figure 2.1**). Initially, electron is placed in the energy level where it reaches its equilibrium. This given electron can be excited to higher energy states if it absorbs sufficient energy from photons (light) or phonons (heat), for example, to reach this level. In the case of light, a specific wavelength will be necessary to induce this change, so the electron will jump to the higher level consuming a photon. This electron will not stay in

this level forever, so it will decay again to its ground level, emitting again a photon. When this happens without external influence, it is called spontaneous emission, and the emitted photon has the same wavelength as the absorbed one had, and random phase and direction. But, if the electron is already in the higher level and receives the right energy, for example the mentioned photon, it can drop to its ground level emitting a second photon with the same wavelength, phase and direction. This phenomenon is called stimulated emission.

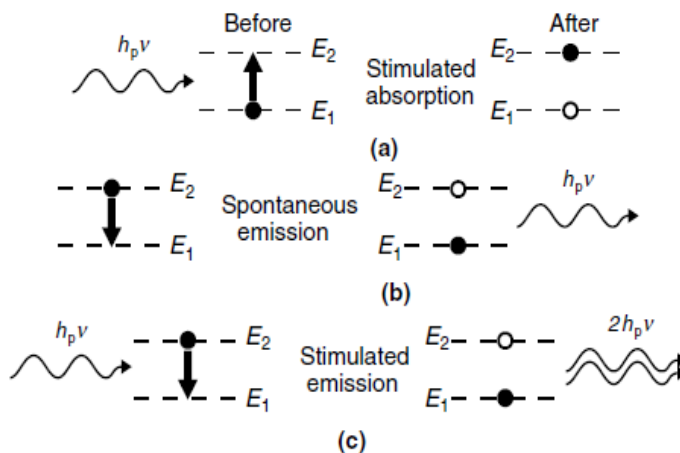


Figure 2.1 Schematic description of (a) absorption, (b) spontaneous emission and (c) stimulated emission phenomena within two discrete energy levels [3].

These physical events take place simultaneously inside the gain medium, where the light is generated, and are caused by the pump source. The third essential part of the laser is the optical cavity that maintains and amplifies the emission. When the number of particles inside the gain medium in the excited state is larger than those in ground state, is called population inversion. It means that the stimulated emission is larger than the rate of absorption of light in the medium, so, finally, the light is amplified. **Figure 2.2** shows the essential parts of a laser.

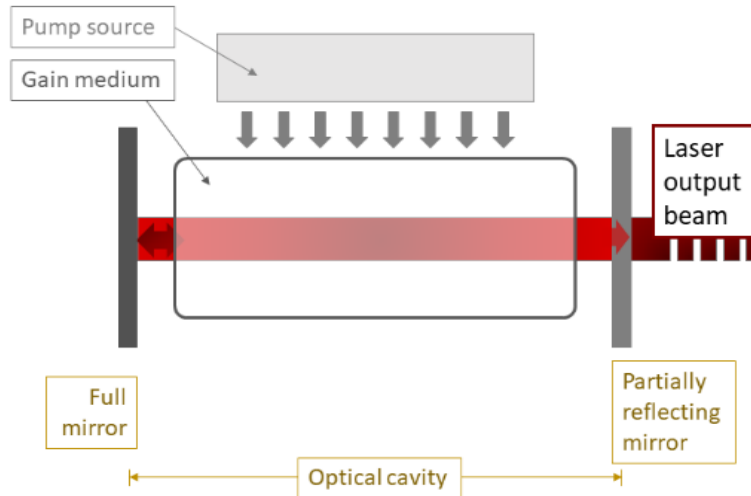


Figure 2.2 Scheme representing laser main components.

What make laser technology so important are the properties of the emitted light. Laser beam is coherent, collimated and monochromatic, as a result of what happen inside the gain medium, ending in an increase of the number of photons, all of them with the same wavelength, direction and phase. The coherence of the electromagnetic wave can be spatial and/or temporal: The spatial coherence can be defined as the distance where the wave keeps its phase correlation. Due to this fact and to the low divergence, the laser beam light is collimated and presents a high directionality. Also, temporal coherence can be defined changing the spatial distance for a temporal range. It is relevant to mention that these two concepts are independent. **Figure 2.3** illustrates different coherent scenarios.

The monochromaticity is also a consequence of the stimulated emission process (temporal coherence). Laser light has a narrow emission spectrum associated with the resonant modes of the laser's cavity. Over time, this wavelength can change due to small fluctuations in cavity dimensions (of the order of 10^{-6} μm for solid state lasers or 10^{-11} μm in the case of high stability gas lasers [3]) in the wavelength scale. These variations define the laser linewidth. In addition to monochromaticity and coherence, directionality is also important in laser systems. In order to minimize divergence, a lens system is generally employed to focus the laser beam.

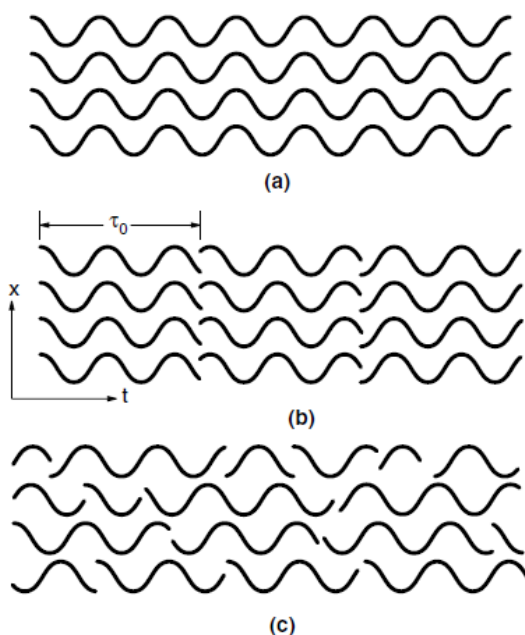


Figure 2.3 Coherence description. **(a)** Perfect coherence. **(b)** Spatially coherent beam with only partial temporal coherence (coherence time τ_0). **(c)** Almost completely incoherent beam [3].

Output light emitted by the different laser sources can be found in the following ranges of the electromagnetic spectrum, ordered by increasing values of wavelength (or the equivalent decreasing photon energy values): Near ultraviolet, **UV**, divided in three parts: UVC (200 - 280 nm, 6.2 - 4.4 eV), UVB (280 - 320 nm, 4.4 – 3.9 eV) and UVA (320 - 380 nm, 3.9 – 3.3 eV). **Visible** ranges from 380 nm (3.3 eV) to 780 nm (1.6 eV) where violet is settled at 400 nm, green at 532 nm and red at 700 nm. Over that, finally appear those that emit in **infrared**, which is also separated in three different ranges: Near infrared, **n-IR** ($780 \text{ nm} > \lambda > 3 \mu\text{m}$, 1.6 - 0.4 eV), mid-infrared, **m-IR** ($3 \mu\text{m} > \lambda > 50 \mu\text{m}$) and far-infrared, **f-IR** ($50 \mu\text{m}$ to 1 mm). In **Figure 2.4** the electromagnetic spectrum is represented far beyond the emitting limits of lasers to put them into context.

In terms of irradiance, power per unit area, laser emission differs substantially from other electromagnetic radiation sources. Pulsed lasers, and especially those with short and ultra-short pulse duration, can reach irradiance values as high as $5 \cdot 10^{12} \text{ W/cm}^2$, many orders of magnitude higher than sunlight. Space agencies NASA and ESA have been measuring total solar irradiance (TSI, at the top of Earth's atmosphere) since 1978 as $1.36 \cdot 10^{-1} \text{ W/cm}^2$ in average [4].

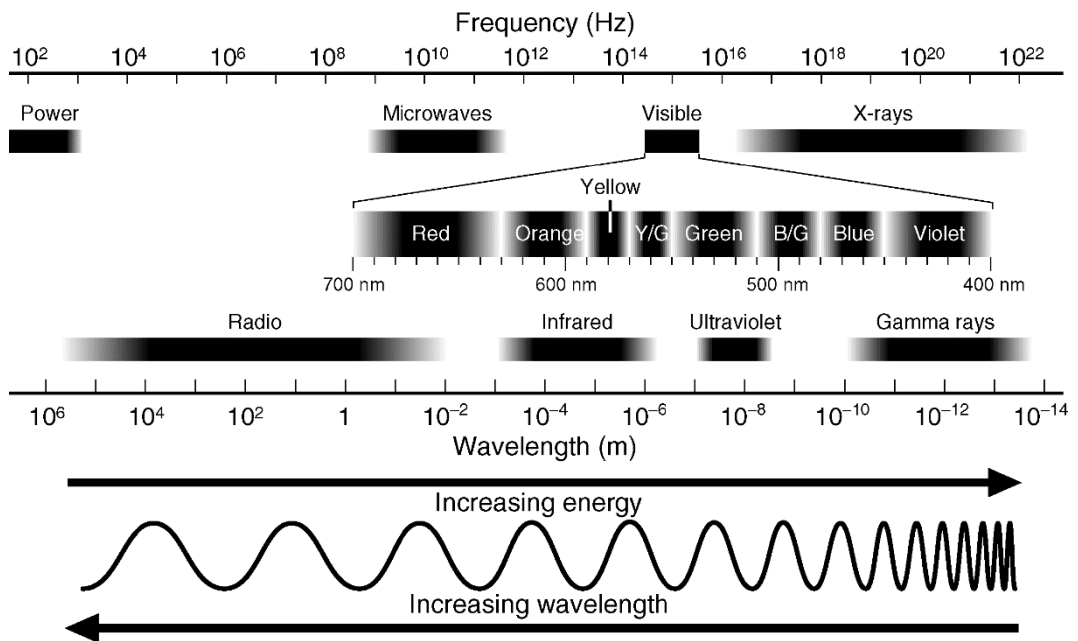


Figure 2.4 Electromagnetic spectrum [3].

2.1.1. Laser classifications

Diverse types of lasers are available, and they can be classified by different specifications. For example, taking into account the operation mode, lasers can be classified in Continuous Wave (CW) and pulsed lasers. CW lasers are used in applications where the output power is needed to be constant. It requires a population inversion of the gain medium in a constant replenishment by a steady pump source, which is not always possible (and practical). Other commonly way to classify lasers, is by the gain medium, because at the same time it characterizes its output wavelength. Output power and pulse duration are also related with the gain medium.

Some well-known **gas lasers** (using gas discharges to amplify light coherently) are HeNe systems, which the best-known operates at 632.8 nm; or CO₂ lasers, a powerful laser operating in m-IR (10.6 μm). **Excimer lasers** are also gas lasers with the special feature that the molecules forming the gain medium only exist with one atom in an excited electronic state. Good examples of this type are those based in noble gas compounds, XeF or XeCl (emitting in 352 and 308 nm, respectively). **Solid-state lasers** form the second big group, where the gain medium is frequently composed by a glass or crystalline material doped with some rare-earth elements. Nd:YAG or Ti:Sapphire are the two main examples within this large list of devices: The former (neodymium doped yttrium aluminum garnet)

emits typically at 1064 nm and can operate in both, continuous CW and pulsed (via Q-switching) modes. Ti:Sapphire lasers are an example of tunable lasers because they can emit between red (650 nm) and infrared (1100 nm), and are frequently used to generate ultrashort pulses. Lasers based on **diodes** (so called **semiconductor lasers**) produce light by the recombination of electrons and holes in a p-n junction. Depending on the semiconductor material, these widespread lasers can emit in the range from IR to UV spectrum. Another *solid* active medium gives name to its own group, the **fibre lasers**, where an optical fibre doped with rare-earth elements works as a gain medium. And finally, there is a third group, the **liquid lasers**, mostly based on **dyes**, where the wide gain spectrum of available dyes (or mixtures of them), allows these lasers to be highly tunable, or to produce very short-duration pulses.

On the other hand, pulsed lasers concentrate the average laser power, P_0 , in short pulses with a constant repetition rate, f_{rep} . Pulse duration, τ_p , has to be much smaller than the inverse of repetition rate. These pulses are characterized by the pulse energy, $E_p = P_0 / f_{rep}$, the average pulse fluence $F_p = E_p / A_0$ and the average pulse irradiance, $I_p = E_p / (A_0 \tau_p)$, when the beam is focused over an area A_0 . Typically, pulsed lasers can be divided in: Long pulse lasers (operating in the range of nanoseconds to microseconds), short pulse lasers (from tens of ps to few ns) and ultra-short pulse lasers (with pulse duration smaller than few ps).

Most pulsed lasers use *Q-switching* or *mode-locking* to obtain the pulses. *Q-switching* systems alter the quality factor of the cavity introducing an attenuator inside the resonator. Hence, the stored energy is released with a high peak power. It leads to much lower pulse repetition rates, much higher pulse energies, and much longer pulse durations than mode-locking systems, which induce a fixed-phase correlation between the longitudinal modes of the resonant cavity. This option is used in lasers that produce extremely short pulses, in the range between pico- and femtoseconds. This fact allows reaching irradiance values above 10^{16} W/cm². A third alternative to operate in pulsed mode is the pulsed pumping, which, as its name suggests, consists of using a pump source also pulsed, like a flash lamps, for example.

Laser technology has evolved to develop ultrafast lasers that are able to emit pulses, whose duration is typically below tens of picoseconds. First advantage of using these lasers comes from the extremely high attainable level of irradiance. They are able to concentrate established amounts of energy within a particularly narrow pulse enabling the emergence of nonlinear events. Another important effect associated with ultrashort

laser pulses and its time scale is that new interaction with matter mechanisms are generated and ablation processes change completely, ending in a so-called “non-thermal” (macroscopic) ablation.

The increasing availability of ps and fs lasers comes from the fact that much more manufacturers are able to assemble very reliable ultrafast equipments and, in some cases, more compact day by day. This, together with the wide range of applications opened, makes this theme a hot-topic of research [5]. The final example of such availability of this type of ultrafast lasers with high repetition rate would be its use in industrial applications, where this technology has an enormous potential [6].

In addition to the above mentioned aspects, there is a special arrangement of matter in some irradiated surfaces, whose study has been pushed up in recent years, thanks to ultrashort pulse lasers: The generation of periodic structures induced by laser that will be detailed in **section 2.3.2**.

2.1.2. Laser safety.

It is important to remark safety issues in the use of lasers. Damage in biological tissues can be caused by lasers in different ways. Thermal damages (burns) occur when temperature rises above the denaturation point of proteins that form the tissue. Photochemical damages (light trigger chemical changes in biological material) can be produced by shorter wavelengths laser sources, in the range from blue to ultraviolet. Radiation is another damage mechanism mainly by photoionization [7]. This last harm has been studied for ultra-short pulse lasers like Ti:Sapphire. Talking about pulsed lasers, it is remarked that the shorter the pulses, the more dangerous they could be. Laser pulses shorter than 1 μs can increase the tissue's temperature very fast and the resulting explosive boiling water will produce a shock wave that is potentially more hazardous than the first impact. Recent experiments on ultra-short pulsed lasers point an extra risk that has to be taken into account: Unwanted hazardous X-ray emissions are generated [8] and, even though the X-ray dose emitted per pulse is low, high repetition rate lasers (several 100 kHz) induce accumulative doses beyond safety limits. Emission levels are especially high when metallic targets are irradiated with those high-intensity lasers (studies performed for 10^{14} W/cm² irradiance peak values). Specific protective protocols have to be taken and shielding materials need to be chosen efficiently (*e.g.*, aluminium requires 30-40 times larger thickness walls than iron or lead to obtain the same protection level) [9].

Even the very low power devices, directly or via an intense reflection in a shiny surface, can produce damages in human eyes. As it has been introduced, different injuries can be caused for different wavelength lasers: Since photochemical cataract (clouding the eye lens) by UV-A laser sources to retinal burn caused by near-infrared light and aqueous flare or corneal burn in the range of 1.4 to 3 μm (IR).

To design the corresponding safety measures, lasers are classified depending on how hazardous are to us. The current system, (view **Table 2.1**) is used since 2002. It is supported by national and European Standards: *UNE-EN 60825-1/A2 CORR:2002*. In the United States, the laser safety is ruled by the *ANSI* (American National Standards Institute) *Z136* series of standards.

CLASS	DESCRIPTION
1	Inherently safe, usually because the light is contained in an enclosure, for example in CD players.
1M	Safe for all conditions of use except when passed through magnifying optics such as microscopes and telescopes.
2	Safe during normal use. The blink reflex of the eye will prevent damage. Usually up to 1 mW power, for example laser pointers.
2M	Safe because of the blink reflex if not viewed through optical instruments. As with class 1M, this applies to laser beams with a large diameter or large divergence, for which the amount of light passing through the pupil cannot exceed the limits for class 2.
3R	Usually up to 5 mW and involve a small risk of eye damage within the time of the blink reflex. Staring into such a beam for several seconds is likely to cause damage to a spot on the retina
3B	Cause immediate eye damage upon exposure
4	It can burn skin, and in some cases, even scattered light can cause eye and/or skin damage. Many industrial and scientific lasers are in this class.

Table 2.1 Classification of lasers according its safety by ANSI Laser Safety Standard and the International Electrotechnical Commission (IEC). Blink reflex is in the order of 0.25 seconds.

2.2. Laser-Matter interaction

One important application of laser technology is material processing. Photon-matter interaction generates a wide phenomenology that can be applied in a broad range of applications.

2.2.1. Photon-matter interaction

With the consistent idea of the laser as a very versatile tool, the interaction between incident laser light and matter can be diverse. Such phenomena are mainly induced by the photon-matter interaction, which is motivated by the promotion of specific electrons from the valence to the conduction band by the precise wavelength range photons. This interaction occurs in an ultra-short period of time and all the subsequent mechanisms happen in different timescales, shown on **Figure 2.5**, where it is illustrated that ionization process happen in the range of femtoseconds. Hot electrons start to transfer energy to the lattice in timescale periods of picoseconds, fact that will trigger other relevant processes.

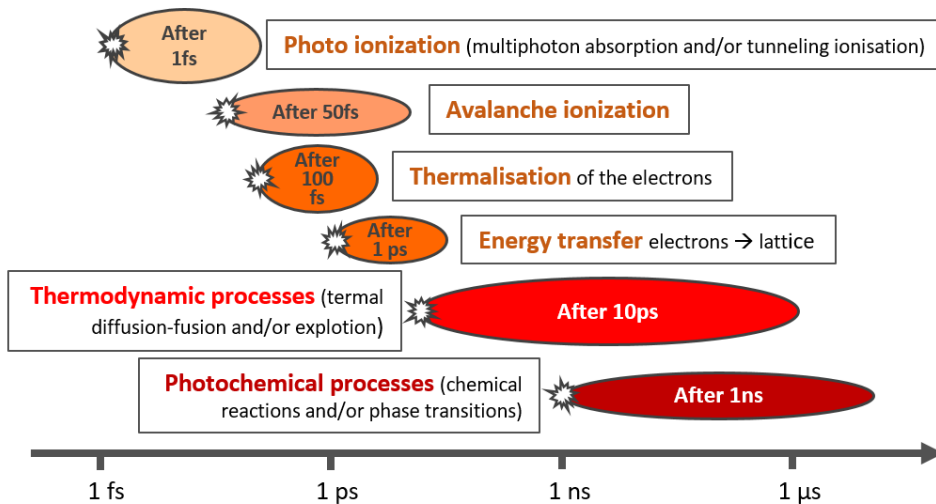


Figure 2.5 Time scale (logarithmic) for different photon-electron induced processes.

As a consequence of the previous diagram, together with the availability of shorter pulse lasers, it is fair to say that new interactions have to be studied when the laser pulse duration is comparable to the time lapse where the energy is transferred by hot electrons to the vast material bulk (lattice). In some cases, multiphoton processes also take place.

The photon absorption implies different electron transitions in the case of metals, semiconductors or insulators. Thus, the final effect will depend not only on the laser characteristics but also on the irradiated material properties, mainly thermal and optical ones [10][11][12].

Overall, laser-matter interaction can be divided into photothermal and photochemical mechanisms. Although, most of the times both interactions come out together with major relevance of one of the terms. The former interaction mechanism is the conventional one, and includes for instance free-electron excitation in metallic materials or lattice vibrations within an insulator [11]. In those cases, the absorbed energy is dissipated as heat, as long as the irradiance is not high enough to go over any damage threshold. The latter group, photochemical mechanisms, is related with changes in chemical bonds caused by the laser energy absorption. These reactions will definitely change the surface behavior of the material.

In the thermal component, absorbed energy is transformed into heat due to several mechanisms [13], which take place in the range of very few picoseconds, as mentioned above. The macroscopic effect is a sudden increase of the surface local temperature (variations that can be from the orders of 10^3 to 10^{10} K/s) where the heat capacity and the global thermal conductivity are key factors to dissipate the heat. This heat accumulation can induce phase changes like fusion, vaporization from the material surface, or even plasma formation if the created vapor plume is enough ionized.

Among non-thermal mechanisms, photochemical processes, which produce the chemical bond formation and rupture, take places in applications such as micro- and nano-machining. Other relevant non-thermal effects include photoelectrical mechanisms, where electrons from the irradiated material surface are emitted as a response to the laser incident irradiation [11][14]. Moreover, photophysical processes should also be considered, which include photoablation, plasma induced ablation and photobreakage [13]. Photoablation is caused by the breakage of the surface molecular bonds, ending in a material disintegration and a local gradient of pressure that induce an ejection of the affected volume. Ablation process induced by plasma differs from the previous case in the small amount of melted material. Here, ionized plasma is commissioned (in charge) to directly sublimate it. Photobreakage mechanisms include phenomena like shock wave generation, jet formation and plasma sparking. All of them induce local mechanical stresses strong enough to break the processed material. In some conditions, the resulting strain of the surface hardens the material (shock hardening, laser blasting) [10][11][14].

It is important to take into account that for ultrashort pulse lasers, pulse duration is in the same time scale of photon-electron interaction (multiphoton absorption, photoionization, electron heating, etc) and the characteristic relaxation times¹ (**Figure 2.5**). Precisely, this time-scale avoids a large part of thermal mechanisms, in comparison with larger pulses. This rapid energy impact on the bulk (“electron lattice”) is transferred to phonon (quantized vibration) subsystem looking for equilibrium until complete thermalization [15]. In the case of laser pulses of picoseconds (or shorter), heat diffusion is frozen during material-laser beam interaction and the shock-like energy deposition leads to ablation. For fs laser pulses, there are two competing mechanisms resulting in material removal and ablation: the Coulomb explosion (“smooth” ablation) and thermal vaporization (strong ablation) [16].

2.2.2. Material optical properties

Laser source emits a collimated coherent monochromatic and well-defined radiation, and when it reaches the material surface, it can be reflected, absorbed or it can pass through the material (transmission). Transmitted component uses to be accompanied with refraction phenomena thanks to the index change between two mediums. Furthermore, diffraction mechanisms are registered when the laser beam face appropriate gratings or scattering effect occurs when light is forced to deviate its previous straight trajectory.

Therefore, all processes introduced during the previous section motivated by the photon-matter interaction, will not arise in every material in the same way because material optical properties also affect the response to laser radiation. In terms of intensity, the incident light (I_0) has to be equal to the sum of transmitted (I_T), absorbed (I_A) and reflected (I_R) components.

The absorbed component of the incident laser beam is the responsible of generating some modifications in the sample surface. In opaque materials, absorption and reflectance are complementary. Reflectance is a component of the response of the electronic structure of the material and has a wavelength dependence (called spectral dependence curve),

¹ τ_{e-e} represents very short electron relaxation time due to degeneration of the excited electron subsystem into equilibrium. τ_{e-p} represents electron phonon relaxation time during which energy is transferred from the electronic to the phononic subsystem. And finally, phonon-phonon relaxation time τ_{p-p} during which the redistribution of the energy is part of which phonon will lead to the equilibrium of the whole bulk material. It can be considered that $\tau_{e-e} \ll \tau_{e-p}$ and $\tau_{p-p} \ll \tau_{e-p}$. In most cases, τ_{p-p} is around 10 τ_{e-e} and τ_{e-p} is from the order of few ps [22][23].

and, it will constrain the amount of energy absorbed for the material. **Figure 2.6 (a)** shows reflectance coefficient for different wavelengths in some metals. It is observed that reflectance values are higher than 0.9 for wavelengths larger than 1 μm, while absorption is much higher in the UV region. By contrast, non-metallic materials are often transparent in the visible range and show a high absorption values in the m-IR range.

Absorption is not only a function of light wavelength but also several processing parameters, as the incident angle or the laser polarization, are also relevant. **Figure 2.6 (b)** also shows that surface temperature modifies absorption, showing a sharp increase when material surface reaches melting temperature. Surface quality is a key factor. Surface roughness, for instance, can induce diffuse reflectivity (instead of specular), which produces surface absorption changes [17]. In case of very rough surfaces, untreated areas can appear. If the surface has pores of a specific size, they can scatter the incident light, increasing, thus, the absorbance.

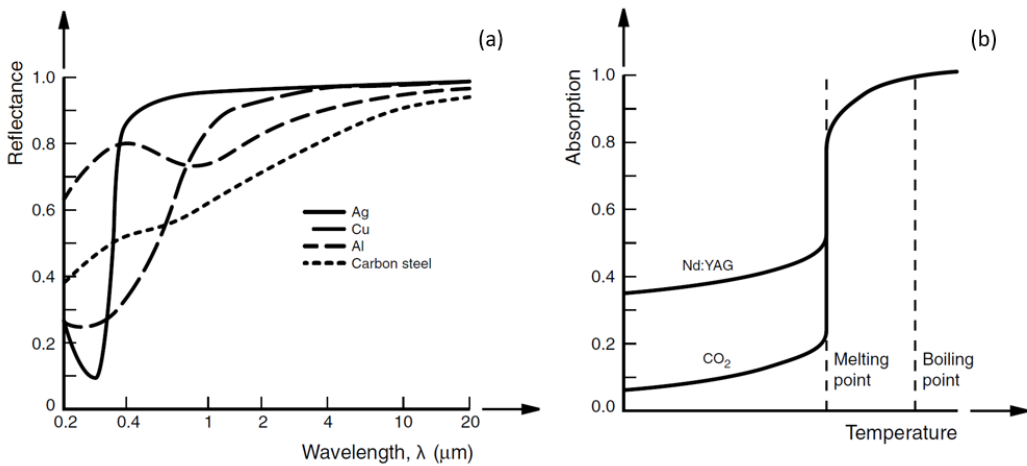


Figure 2.6 (a) Reflectance coefficient for different metals. **(b)** Metals absorption variation with temperature [3].

Once part of the incident light is reflected, absorption happens in a very thin surface layer and later, it will be transferred to the bulk material thanks to conduction mechanisms. The intensity will decay according Beer-Lambert law:

$$I(z) = I_0 e^{-\alpha z} \tag{Eq. 2.1}$$

Where I_0 is the intensity of the incident light, $I(z)$ is the resulting intensity at deep level z , and α is the absorption coefficient (m^{-1}). It is convenient to define the optical penetration depth, $\delta = 1/\alpha$, which is the depth at which the intensity drops to $1/e$ of the initial value

at the interface due to ohmic, dielectric or magnetic losses. $\delta = \frac{\lambda}{4\pi k}$, where k is the imaginary part of the complex-valued refractive index. For instance, in the case of metals irradiated with CO₂ laser ($\lambda = 10.6 \mu\text{m}$), $\delta \approx 10 \text{ nm}$.

Finally, up to this point the processes that have been described correspond to linear absorption where the absorption coefficient is independent of the optical intensity. For non-linear absorption processes, this coefficient is a linear or high-order function of the intensity. For example, two-photon absorption process is ruled by a α linear dependence of the intensity. Multi-photon absorption processes, involved in laser-induced damage by intense laser pulses, have a high-order dependency of intensity. These processes are not exclusive of ultrashort pulse lasers because not-so-short pulses with enough irradiance (and followed with a high repetition rate) can produce similar effects. Basically, electromagnetic waves incident over certain surface induce a non-equilibrium state. Here, Maxwell's equations (classical basis of electromagnetism and laser-matter interaction) have to take into account high-order terms of, for example the polarization field, since EM laser fields are comparable (bigger) to the electric field strength inside the atoms [15].

2.3. Laser induced surface modifications

According to physical mechanisms previously mentioned, laser can induce a variety of changes into different materials. When the irradiance levels are low enough, laser can be considered as a heat source. The thermal component of laser interaction is bigger than the non-thermal one but it does not have enough power to induce a phase change. This situation can occur easily with continuous laser or long pulse duration, but in both cases irradiance should be low.

For larger irradiance values, the thermal effect induces phase changes, like solid-liquid transitions (melting) or, in the case of much higher irradiance values, direct sublimation (vaporization) and plasma formation. This last one leads to distinct phenomena due to the extremely high temperatures of plasma, together with its electric charge, since it is completely ionized (see **Figure 2.7**).

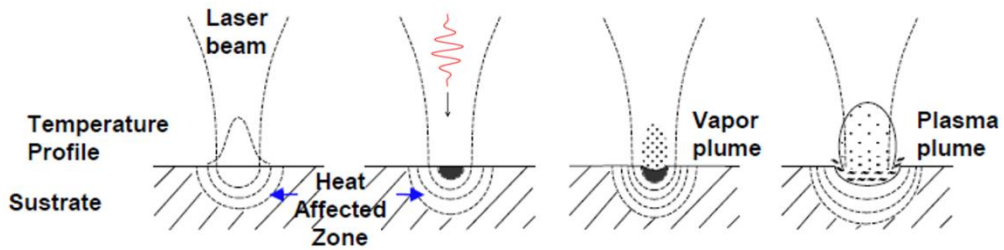


Figure 2.7 Incident laser beam and induced events. From left to right: Heating, melting, evaporation and plasma formation processes.

Chemical changes over material surface can be induced as well by photothermal and/or photochemical interaction with the laser. For example, oxidation or reduction processes are frequent in metallic surfaces depending on the treatment atmosphere. In polymers, for instance, bleaching (loss of colours) and carbonization (degradation of organic forms into carbon forms) processes are also recurrent.

Ablation

Another characteristic thermal features, mostly related with pulsed lasers, although CW lasers could also be involved [18], are those connected with ablation processes. Several mechanisms, already introduced, can induce laser ablation over material surfaces, but generally speaking, it consists of material removal. When pulse irradiance exceeds certain threshold value, material is ablated from the surface. In order to make this happen, various phenomena act together in this particular region limited by the material solid phase (subsurface), its surface and the induced gaseous phase. The more relevant mechanisms involved are heat conduction directed to material inner layers, chemical reactions, gasification, plasma formation, photoacoustic and shock waves formation and melt expulsion and redeposition.

It is important to take into account the number of pulses received for the surface, since it may exhibit incubation phenomena [11][14][16]. This is associated to high repetition rate lasers treating surfaces and occurs when there is not enough time between pulses to reach something similar to thermal steady-state. Hence, energy accumulation over surface takes place and laser-material interaction changes completely. Among other alterations, surface temperature will rise, there will be an increasingly amount of melted material and the consecutive pulses and their accompanying shockwaves will result in an almost-liquid interface. It is important to remind that all mechanisms related with ablation

process happen very fast, even with short laser pulses (pulse duration in the range of nanoseconds). Ultrashort pulses can hardly be involved in incubation processes since the thermal interaction with the surface is really brief. Much larger number of pulses or even higher intensities should irradiate the sample for that to happen.

Nevertheless, ultrafast lasers can induce ablation processes as well, but slightly different than the short-pulse lasers. While ablation induced by short pulses is driven by thermal processes (**Figure 2.8 (a)**), ablation produced by ultrafast lasers changes since the energy cannot be transferred “instantly”. **Figure 2.8 (b)** illustrates, in comparison, bigger pressure effects and roughly no heat conduction towards the bulk material.

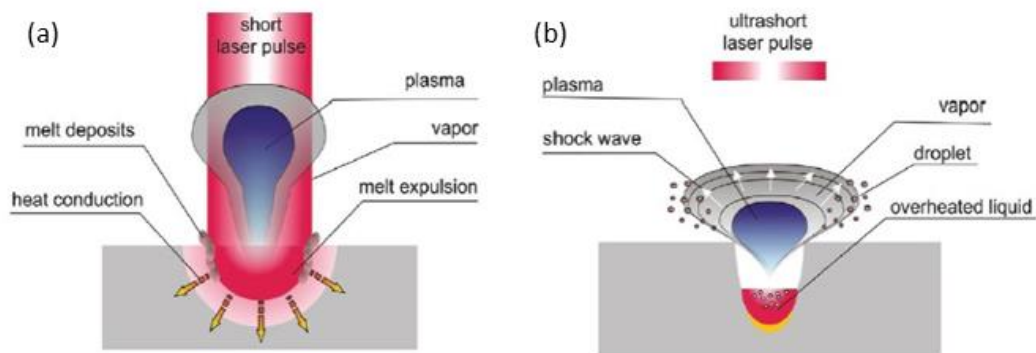


Figure 2.8 Models for different ablation processes for short (a) and ultrashort (b) pulses in metallic surfaces [19].

Short pulse ablation directly depends on the achieved material temperature and is determined by both evaporation and melt expulsion. Pulse duration and its capacity for transfer the given energy will define the dominant mechanism. In the case of ultrashort pulse ablation, the phenomena it is not completely clear but, at least in metals, it is usually explained with the two-temperature model (TTM), electron and grid temperatures. Briefly, TTM consists in the following: Before laser pulse, both temperatures are equal (coupled). Once the pulse reaches the metallic surface, electron temperature becomes much higher than the grid, then energy is transferred to the lattice, rising its temperature and being at this moment much higher than the electron one. Subsequently, the energy of the lattice can diffuse to material’s inner layers and the outer part or the surface can be ablated. All these events, happened within the first picoseconds. **Figure 2.9** shows more in detail the differences between both ablation processes together with mechanisms introduced in **section 2.2**.

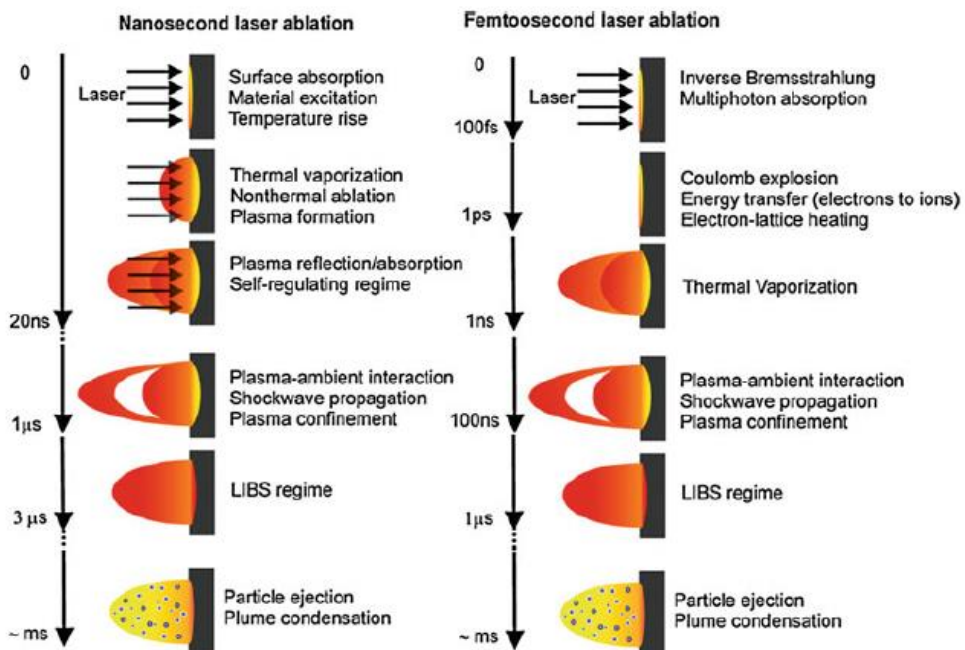


Figure 2.9 Energy absorption approximate time scales for nanosecond and femtosecond laser ablation [16]. Also several processes that occur during and after the laser pulse are indicated. Inverse Bremsstrahlung is connected with the deceleration radiation of particles. LIBS is an acronym for Laser Induce Breakdown Spectroscopy

All these processes open a broad range of applications, where laser technologies have been applied and nowadays are well-implemented in industrial practices (**Figure 2.10**). Using the laser irradiation in controlled machining processes or just as a heat source as an alternative thermal treatment, surface laser processing represents an excellent tool to improve surface properties. The works presented in this PhD are mainly focused in surface melting and surface nanostructuring processes.

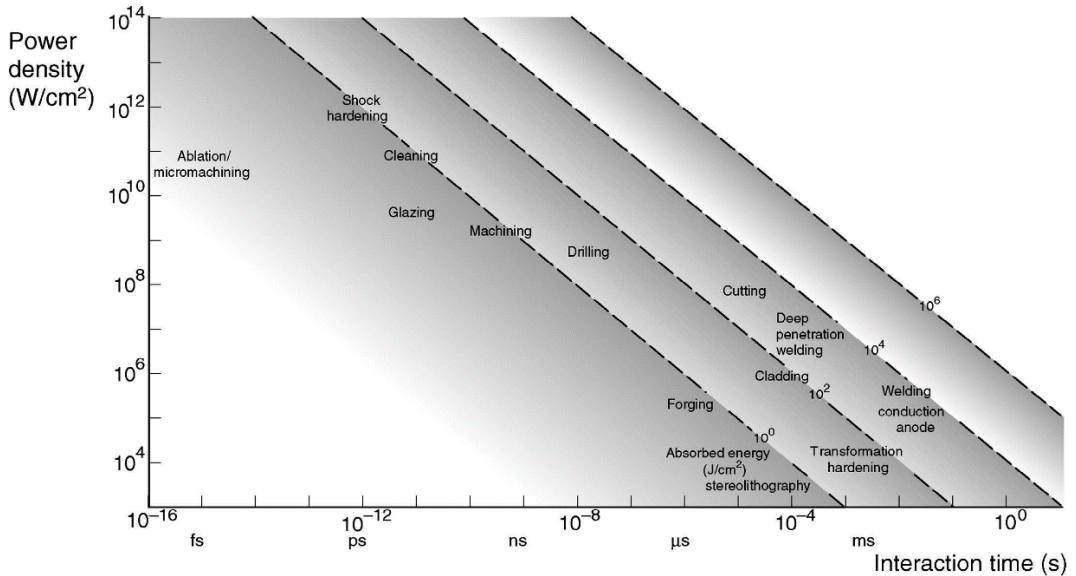


Figure 2.10 Typical power densities and interaction times for various laser processes [3].

2.3.1. Application of melting processes

As it has just been introduced, laser technology is a versatile tool with a relevant role in industrial processes as a heat source and also used in machining processes where ablation mechanisms are involved. It is also possible to engineer surfaces since the needed heat contribution to a given purpose is easily and accurately controllable. These phenomena can be separated in two groups: Those just producing microstructural changes, like hardening, melting or texturing processes; and those that involve also changes in material composition, like metal alloying, cladding, etc.

Some of the main advantages of using laser sources are the controlled power densities supplied to the material surface, the cost-effective enhancement above certain power densities and the attainable process temperature. Thanks to focused laser irradiation, great heating/cooling speeds and large thermal gradients are present in localized areas of the sample. These facts allow reaching enough temperature locally, to overpass the material melting point, even in ceramic materials. That would be impossible (or at least, not sustainable) using other techniques. This combination of melting processes and relatively fast cooling can induce in multi-component samples the appearance of metastable phases of two or more elements with, sometimes, better properties than the regular mix of phases. These microstructures, called eutectic, open the possibility of developing new improvements with better mechanical or chemical (among others)

properties. Obviously, these large thermal gradients also generate thermal stresses in the sample that, in the case of ceramics, is an important issue because they can produce cracks on the sample and deteriorate its properties.

Another application of laser induced controlled melting is the growth of high quality polycrystalline materials and single crystals. A well-studied method to achieve that crystals is Laser Floating Zone (LFZ) technique, also named as Laser-Heated Pedestal Growth (LHPG) [20]. LFZ consists in generate a circular crown-like heat affected zone in cylinder shaped samples thanks to laser irradiation and the appropriate set of mirrors and lenses. Meanwhile, the sample (feed rod and the resulting fibre) is rotating to have a homogeneous melted zone along the cylinder section (see **Figure 2.11**). The first equipment was developed by Haggerty [21], and lead the way to a simple and fast method to growth crystals of large quality and also solving the problem with crucibles. Crucibles were needed in other melting methods to withstand crystal precursors, but in addition to problems with processing certain materials (i.e. refractive ones) they added impurities to the crystal. LFZ do not need crucibles. It is also desirable to work inside a chamber that allows treating samples under high pressures, enabling the growth of volatile and metastable materials.

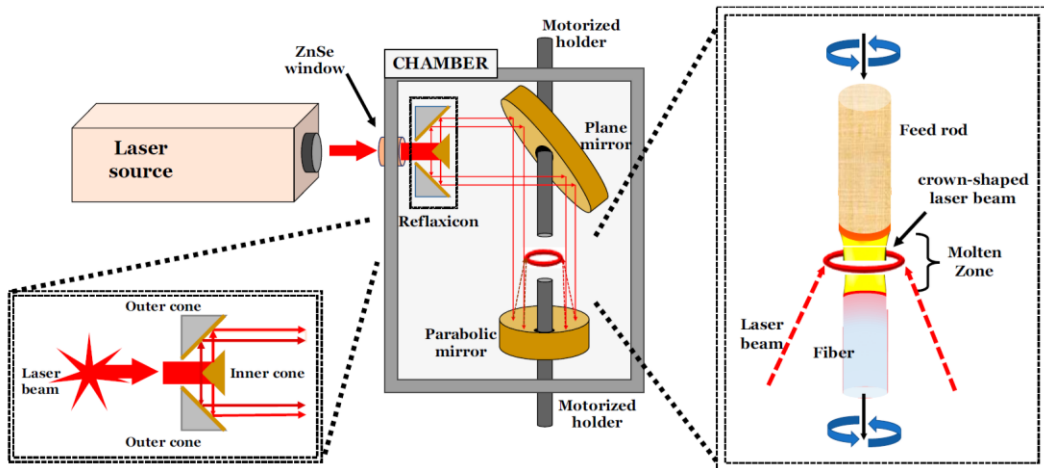


Figure 2.11 Schematic diagram of the typical Laser Floating Zone setup detailing the laser light entrance to the chamber and the molten zone area [20].

LFZ enables the production of high performance materials for several applications: Doped YAG ($Y_3Al_5O_{12}$) for laser medium gains [22], thermoelectrics [23] or superconductors [24] among others.

This technique is very consistent and well-established for many applications. But, on the other hand, there are other purposes that require bigger samples or larger treated surfaces, and LFZ finds difficulties to scale up its results. Because of this, it is also relevant to achieve melting fronts over large horizontal surfaces. This is easily attainable with high power CW or pulsed with high repetition rate lasers attached to galvanometric mirror systems, which allow scanning of large surfaces.

Related with the previous technique, other widespread applications that involve laser melting are those grouped as Additive Manufacturing (AM), particularly Selective Laser Sintering (SLS) together with Selective Laser Melting (SLM). They result as a competitive alternative to the conventional manufacturing process with powder precursors. Traditionally, a powder, binders and stabilizers mixture is formed into the desired shape with a mould before sintering at high temperature, resulting in a dense part. This process involves multiple steps including, for instance, costly moulding process.

On the other hand, AM techniques try to overcome past difficulties. These methods have been used to develop complex designs, especially those fabricated with metals and polymers. Meanwhile, ceramic parts manufactured as the latter, represent a technological challenge. They have an extraordinary potential in a large variety of applications (aerospace industry, biomedical, energy sector, etc) because of the ceramic properties themselves, but are precisely that properties (thermal and mechanical) those who represent harder difficulties for their manufacture.

Ceramic AM can be divided into three groups: Binder-based techniques, extrusion-based techniques and sintering and melting techniques [25]. In the first group, a ceramic-monomer suspension is solidified by photo-polymerization with UV laser. Second group is based on an injection with a ceramic-binder mixture extruded through a nozzle layer by layer. A following thermal treatment is needed in both cases to attain the final dense part. On the other hand, SLS-SLM methods represent a binder-free process where it is possible to synthesize new phases under non equilibrium conditions thanks to high speed laser heating/cooling [26].

SLS is one of the current mainstream AM technologies. It was developed by Beaman and Deckard in 1980's decade [27] and basically consists in a powder bed fusion process, in which fresh powder layers are applied sequentially and each layer is sintered selectively by a laser beam according to a pre-determined path. An appropriate post-processing is required to get the final parts. SLM reproduces the same idea with the difference that the bed powder is melted in only one step using a much higher energy laser source. A scheme

of the production steps **(a)** and the consolidation of the melting process **(b)** is shown in **Figure 2.12**.

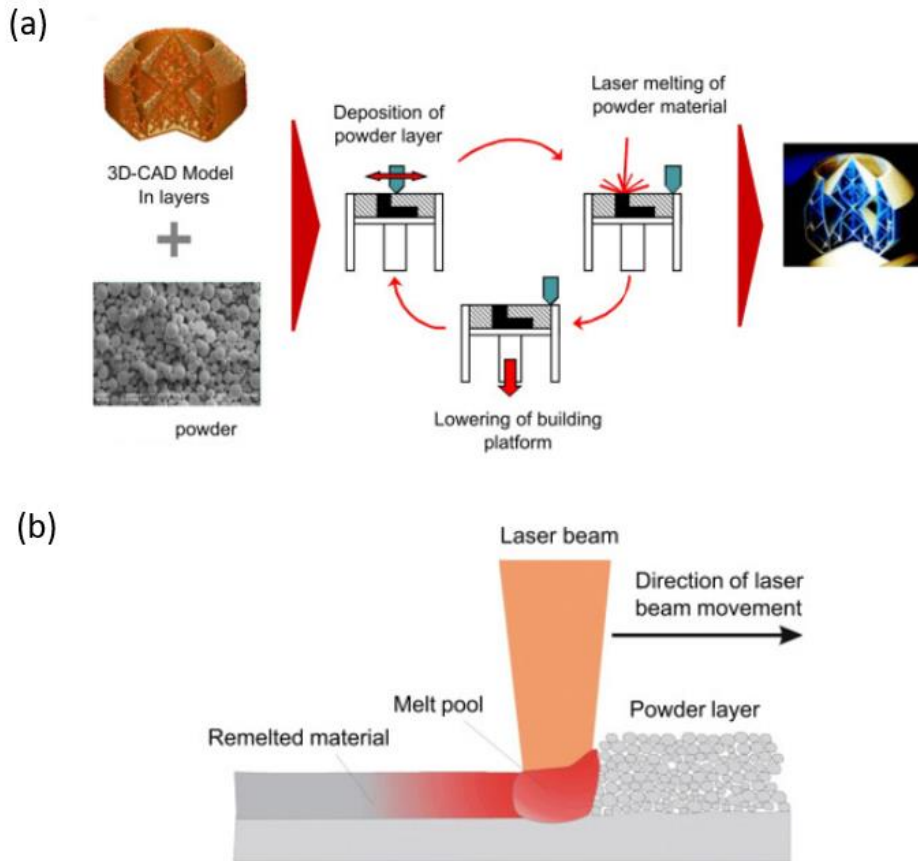


Figure 2.12 (a) Schematic basic steps of the SLM production: Starting with the raw powder and the CAD design, continuing with the laser melting layer by layer, and ending with the final piece. A moving platform is in charge of lower the already manufactured layers and set more powder in the focus of the laser. **(b)** Illustration of the material consolidation process. Adapted from [28].

Sometimes, an additional problem that emerges when laser melting techniques are applied to ceramics is the thermal shock, since those materials have a high melting temperature and low expansion coefficient. Hence, it is frequent the emergence of cracks. To avoid it, samples can be preheated in order to reduce the temperature difference between the molten surface induced by laser and the remaining material. Two alternatives in that sense are to preheat the sample/powder bed with a second laser source (usually a CO₂ laser) [29] (**Figure 2.13 (a)**) or to introduce the powder or the sintered sample in a furnace and irradiate it at the same time (**Figure 2.13 (b)**) [30][31].

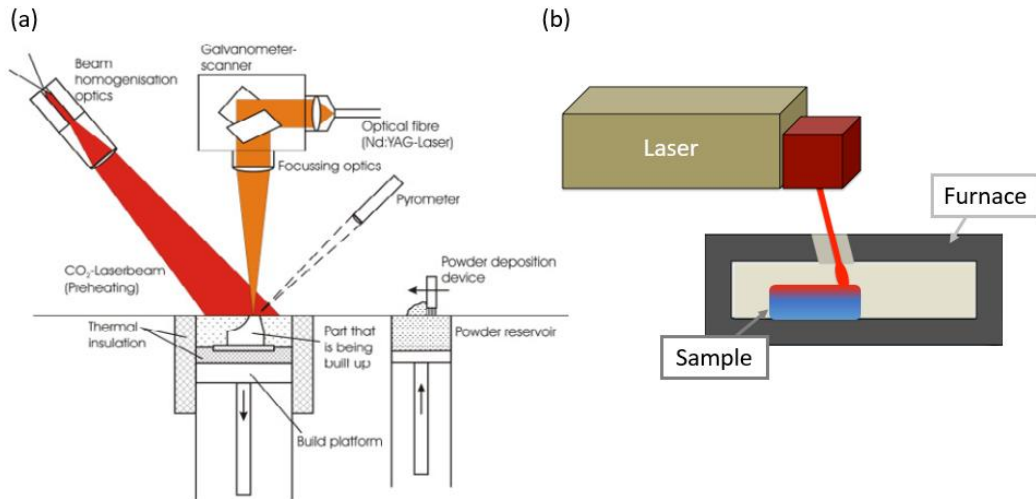


Figure 2.13 Schematic illustration of: **(a)** Ceramic SLM experimental setup [28]. **(b)** Laser processing with the sample placed inside a furnace.

During this thesis, ceramic (Al_2O_3) surface has been remelted by laser irradiation with the additional challenge of being supported by a metallic substrate, where oxidation reactions are important.

2.3.2. Application of nanostructuring surface processes

This universal phenomenon occurs when solid surfaces are exposed to linearly polarized coherent electromagnetic radiation, for instance laser [32]. LIPSS, so-called *ripples*, are formed in a wide range of pulse duration: From continuous wave radiation [33] down to femtosecond pulses [34][35]. These surface structures are gaining prominence within the scientific community. As an example of that, **Figure 2.14** shows the number of publications collected in “ISI Web of Science – Core Collection” database up to de date 03.08.2020. Searched by topic: “*Laser-Induced Periodic Surface Structures*”, 1111 publications are reported with a continuous rising number of references in many different fields of research.

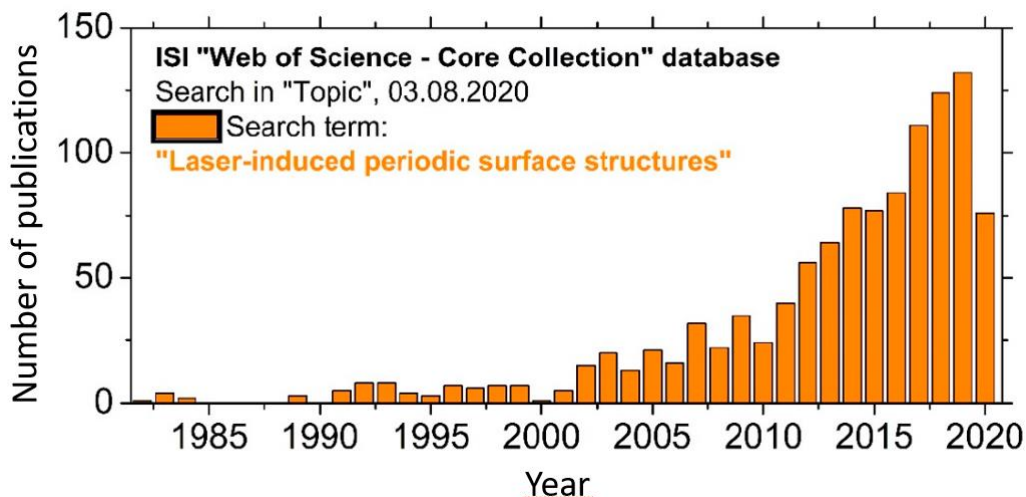


Figure 2.14 Research intensity in the field of “Laser-Induced Periodic Surface Structures” reflected in the number of papers published per year since they were named as LIPSS. Adapted from [36].

The formation of these structures was firstly reported by Birnbaum in 1965 [37] on polished germanium single-crystal surfaces after irradiating them with a ruby laser ($\lambda = 694.3$ nm and pulse duration in the range of milliseconds). Since that moment, many other experimental and theoretical researchers have done an intensive study on this field. Different structures were reported on a wide diversity of materials, and several theories were stated trying to explain how these structures are formed. In 1980's decade, Sipe's group proposed a first-principle theory and coined the actual terminology (*laser-induced periodic surface structures, LIPSS*, see **Figure 2.14**) [38]. After that point, where efficacy factor η was introduced to explain inhomogeneous energy deposition into the irradiated surface, some other approaches were given, including those that involve surface-scattered electromagnetic waves (SEW), especially Surface Plasmon Polariton. Starting 21st century, together with ultrashort pulse laser expansion, different laser-induced arrangements with smaller periodicity were reported and material feedback after laser irradiation represented an attention-grabbing point of view. It becomes relevant, and old theories were complemented with new models (Drude model) [39] and new calculations (finite difference time domain, FDTD) [40], to understand these phenomena [41]. Although there is still controversy about a theory explaining LIPSS formation, two trends are present nowadays: Those theories based on electromagnetic models and those based on matter reorganization models. A complete review of both trends has been collected by *Bonse et al* [42].

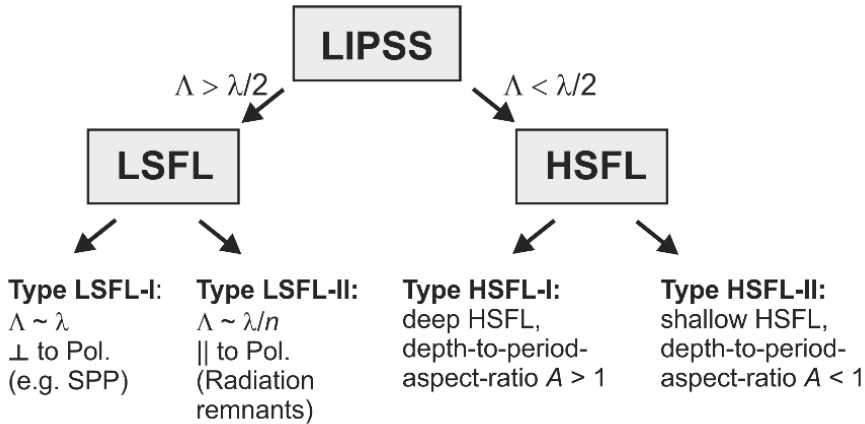


Figure 2.15 Classification scheme of ultrashort pulse laser induced structures [41].

Generated structures have a strong correlation with the incident laser light polarization direction and wavelength and typically range from few hundreds of nanometers to some microns. Reported laser-induced periodic surface structures can be classified respect their spatial periodicity, Λ : Low Spatial Frequency LIPSS (LSFL) exhibit periods in the range between incident irradiation wavelength, λ , and $\lambda/2$. On the other hand, High Spatial Frequency LIPSS (HSFL) have a structure periodicity much smaller than $\lambda/2$. In turn, both formations can be subdivided in type I and II regarding their relative orientation with the incident beam polarization as it is shown in **Figure 2.15**.

In addition to LIPSS, more structures like grooves and spikes have been observed. Both are micrometric structures, and while grooves are typically oriented parallel to polarization direction, spikes are less correlated with beam polarization. Hereunder, **Figure 2.16**, shows several structures formed over niobium surface by UV sub-nanosecond irradiation ($\lambda = 355$ nm, $\tau_p = 300$ ps): **(a)** Ripple arrangements, **(b)** drop-like structures over those ripples, **(c)** groove-like structures and **(d)** spikes in form of protrusions.

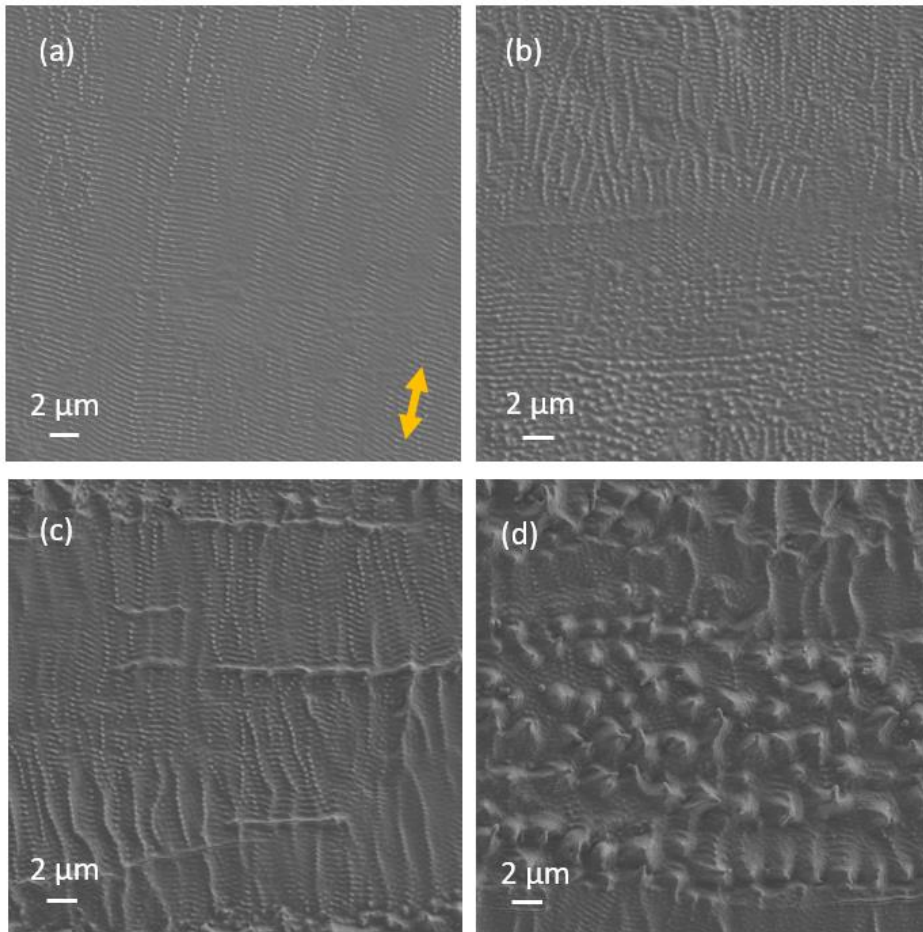


Figure 2.16 SEM images showing structures generated over 6- μm thick Nb sheet. Induced by a UV laser irradiation under N_2 atmosphere and the effective number of pulses, $N_{eff1D} = 34$ and distance between consecutive lines, $d_s = 5 \mu\text{m}$. Coloured arrow indicates laser polarization. Repetition rate of **(a)** and **(b)** was 600 kHz and for **(c)** and **(d)** 300 kHz. The beam scanning velocity, v_L , was changed to maintain constant the effective number of pulses in all cases. Fluence values correspond to: **(a)** 0.26 J/cm^2 . **(b)** 0.33 J/cm^2 . **(c)** 0.66 J/cm^2 . **(d)** 0.74 J/cm^2 .

In many studies, LIPSS have been obtained in single pulses. In **Figure 2.16** it is shown that by controlling the fluence level and the number of pulses it is possible to select the type of micro- and nanostructures. Before going deeper into these parameters, it is needed to clarify that the use of fluence values (expressed in J/cm^2) to characterize the laser treatment is widespread in literature. Nevertheless, since the pulse duration is relevant in the energy deliver process, it is found more accurate to give also the pulse irradiance values, so that different lasers can be compared. From the surface processing side, LIPSS structures can be generated in 1-dimension scanning process, lines, and in 2-dimension

procedures. **Figure 2.17** shows an example of how different surface morphologies can be obtained varying these parameters.

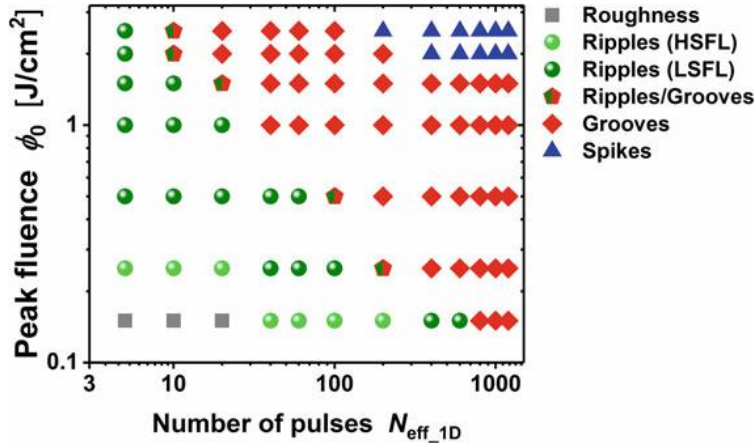


Figure 2.17 Different structures formed along a line processing over 100Cr6 steel with a femtosecond laser. Notice both logarithmic axis and y-axis plots the peak fluence instead of the introduced irradiance procedure (reported pulse duration for the employed laser was 30 fs) [43].

Different kinds of structures are generated as a result of certain irradiance pulse value and a number of pulses. Above some threshold level (intensity and N), structure formation mechanisms can change. Hence, together with Gaussian profiling of the majority of the lasers, it is possible to observe different structures around the same spot (static laser processing, zero-dimensional), like those shown in **Figure 2.18**.

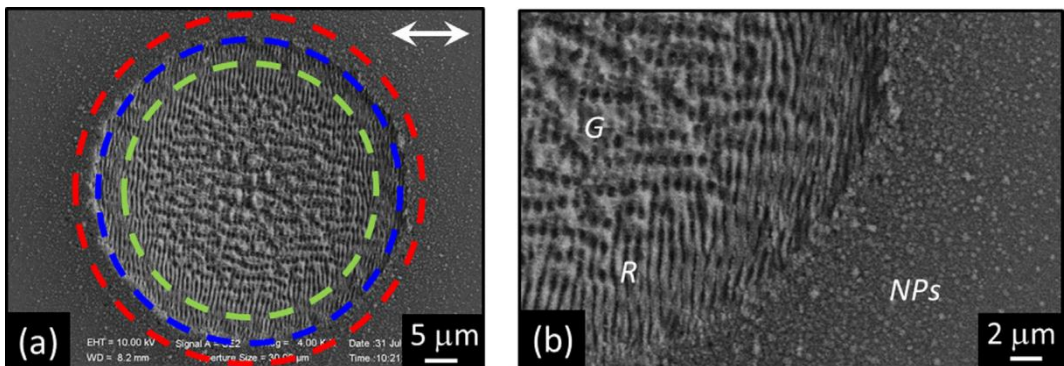


Figure 2.18 SEM images of a silicon surface irradiated 180 fs-laser ($\lambda = 1030$ nm) with $f_{rep} = 50$ kHz, $F_p = 0.5$ J/cm² and $N = 100$ pulses. **(a)** Crater created by the laser pulses. White arrow represents laser polarization direction and dashed colored circles serve for eye-guiding the limited areas with different structures. **(b)** Zoom view of the bottom-right part of the crater where can be found grooves (G) and ripples (R) together with nanoparticles (NPs) spread over crater surroundings [44].

As it has been introduced, LIPSS can be generated in almost every solid material surface [45], being reported over metals [35][46], semiconductors [44][47], dielectrics [39], polymers [48] or composite materials [49].

Many groups have also studied the influence of tuning the delay between consecutive ultrashort pulses (through interferometers, for example) to understand the effect of different pulses with the specific excitation-relaxation times (electron – phonon, etc). Furthermore, other parameters like the angle of incidence, atmosphere or sample temperature can induce changes in the formed structures [45].

These kind of self-ordered structures have become very relevant in the field of surface modification. They can be produced reliably in just one step, without surface contact, avoiding expensive methods (lithography) and in most cases eluding vacuum technologies or the use of extra chemical products. Final nano- and microstructures created (ripples, grooves, spikes, etc) over a wide variety of materials can modify physical and chemical surface properties. This fact opens a considerable amount of new applications and hereunder some are highlighted [45][50].

Due to its spatial periodicity, these structures can diffract the visible part of the spectrum, acting like gratings. This effect produces an iridescence phenomenon (change of the color depending on the illumination angle or the view angle) [46]. The color-change induced by LIPSS can be very attractive to applications like, for example, laser marking, optical data storage, encryption or anti-counterfeiting features, since it is extremely difficult to copy intrinsic irregularities present in these structures. More applications related with photonics are, for instance to induce anti-reflective properties to some glasses, generating randomly distributed nanopillars [51] or an enhancement in luminescence, for instance in light emission diodes based on GaN, producing LIPSS in the p-GaN layer [52].

Moreover, applications related with medicine and biology are also relevant. Some studies reported antibacterial behavior of surface covered with LIPSS reducing the unwanted bacterial film in humid environments [53][54]. Moreover, are notorious the results on cell growth over laser-induced structures in polystyrene surfaces with an enhancement in attachment and proliferation of human cells [55].

Many studies have been done to inspect tribological properties of non-biological surfaces (metallic or ceramic) with laser-induced structures ending in a wear and friction reduction [43].

Another group of applications where these nanostructures play an important role are those related with wetting properties and fluid control [56]. Wettability control can be achieved generating hydrophilic or hydrophobic surfaces on metals, semiconductors or dielectrics. These self-organized structures, induced in most cases by fs-laser irradiation, have also oleophobic and oleophilic properties (LIPSS-covered metals presenting hydrophobic behavior, also show oleophilic properties [57]). More results related with fluidic transport [58] or anti-icing performance [59] are opened thanks to these properties.

Some other innovative and very diverse studies related with LIPSS have been stated: It is reported an increase of the Raman signal in Surface-Enhanced Raman Spectroscopy (SERS, chemical analysis applications) thanks to periodic nanostructures [48]. In addition to an enhancement of THz emitters based on GaAs optoelectronic [60] or an improvement of the fuel atomization in injection nozzles for car engines [61]. An enhancement of the catalytic activity on platinum electrodes [62] or changes in the superconducting properties of niobium have been published as well, **publications D and E** [63][64].

2.4. Gaussian optics and relevant processing parameters

In most laser applications, laser beam scans the material surface in different configurations. In order to understand how energy is distributed on the surface and to define the relevant parameters in laser material processing, an analysis of the energy distribution in the laser beam and in the scanning protocol has to be performed.

2.4.1. Energy distribution within the laser beam

The most extended energy distribution (spatial and temporal) in the output pulsed laser beams corresponds to Gaussian profile, involving the electric and magnetic fields in the transverse plane. In some cases, other different beam profiles with high order modes are used, as for instance the Hermite-Gaussian or Laguerre-Gaussian functions or a flat-topped profile (called tophat beam), usually employed in several industrial applications.

The longitudinal mode of the laser emission has a small influence in the characterization of the beam, by contrast the Transverse Electromagnetic Mode (TEM) has great significance. The TEM depends on the cavity (geometry, alignment, spacing between its internal optics), on the gain medium and on the resonator (if there are apertures on it or not) [65]. Frequently, the laser's cavity is designed to allow only the TEM₀₀ oscillation, that

corresponds to the Gaussian distribution, because it is more suitable to process materials. As it can be observed in **Figure 2.19**, many other modes can be produced modifying the cavity design.

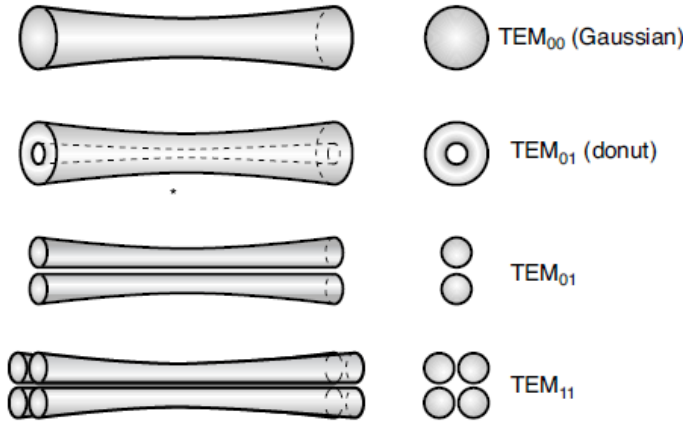


Figure 2.19 Description of various cylindrical transverse mode patterns (TEM_{mn}) [3].

A dimensionless parameter widely used to compare and describe the laser beam is M^2 , the beam quality factor, and represents the variation of a beam from the Gaussian profile. An ideal laser (mode TEM_{00}) with Gaussian profile presents an $M^2 = 1$. Real lasers present a M^2 value bigger than one. For example, solid state lasers present a $M^2 = 1.1 - 1.3$ or lasers based on diodes, $M^2 = 1.1 - 1.7$ [3][66]. The lower M^2 is, the better quality has the laser beam. This factor is useful to compare lasers beyond from their wavelength.

Most TEM_{00} output laser beams have circular cross section with an amplitude envelope in the transverse plane given by Gaussian spatial and temporal profiles. The irradiance distribution is given by the product of two Gaussians:

$$J_p(r, t) = I_{p0} e^{-2(r/r_b)^2} e^{-2((t-t_0)/\tau_p)^2} \quad (\text{Eq. 2.2})$$

Where t is time, τ_p the pulse duration, r is the radial coordinate that gives the distance from the beam axis, and r_b is the beam radius defined with $(1/e^2)$ contour criteria.

E_p can be calculated by the temporal and spatial integration of **Eq. 2.2**, as it is shown in **Eq. 2.3**.

$$E_p = \int_{-\infty}^{\infty} dt \int_0^{\infty} I_p(r, t) 2 \pi r dr = \int_{-\infty}^{\infty} e^{-2t^2/\tau_p^2} dt \int_0^{\infty} I_{p0} e^{-2r^2/r_b^2} 2 \pi r dr$$

$$E_P = \sqrt{\frac{\pi}{8}} \tau_p I_{p0} \pi r_b^2 \quad (\text{Eq. 2.3})$$

In addition, the spatial fluence distribution in a pulse can be calculated as:

$$\begin{aligned} \mathcal{F}_p &= \int_{-\infty}^{\infty} I_p(r, t) dt = I_{p0} e^{-2r^2/r_b^2} \int_{-\infty}^{\infty} e^{-2t^2/\tau_p^2} dt = \frac{\tau_p}{\sqrt{2}} \sqrt{\pi} I_{p0} e^{-2r^2/r_b^2} \\ \mathcal{F}_p &= \frac{\tau_p}{\sqrt{2}} \frac{E_P}{\pi r_b^2 \tau_p} 2\sqrt{2} e^{-2r^2/r_b^2} = 2 \frac{E_P}{\pi r_b^2} e^{-2r^2/r_b^2} = 2F_P e^{-2r^2/r_b^2} \quad (\text{Eq. 2.4}) \end{aligned}$$

Eq. 2.4 shows that $\mathcal{F}_p(r)$ is also a Gaussian distribution with a maximum value at the center of the pulse that is two times the average fluence value ($F_P = E_P/A_0$).

The convergence or divergence associated with an optical system can change the radius of the beam along the propagation direction. This is important because it modifies the fluence and the irradiance values associated with the laser power. The variation $r_b(z)$ can be observed in **Figure 2.20**. Close to the focal point, $r_b(z)$ follows a hyperbolic dependence.

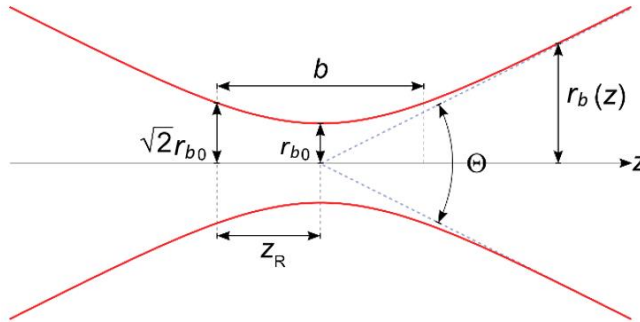


Figure 2.20 Variation of the beam width $r_b(z)$ along the propagation distance z showing divergence waist r_{b0} and Rayleigh length z_R [67].

This hyperbolic dependence allows us to measure the spot size (through the beam waist, w) according the next expressions:

$$r_b(z) = r_{b0} \sqrt{1 + \left(\frac{z}{z_R}\right)^2}, \quad z_R = \frac{\pi n r_{b0}^2}{\lambda} \quad (\text{Eq. 2.5, Eq. 2.6})$$

Where Rayleigh range, z_R is defined as the distance along the propagation axis referenced at the focus where $r_b(z_R)$ is equal to $\sqrt{2} r_{b0}$. This distance between two points separated

$2z_R$ and centred in the focus, is called confocal parameter or depth of focus of the beam. λ is the laser wavelength and n the refraction index of the propagation medium.

With these parameters in mind, divergence (total angular spread) θ is calculated in radians as:

$$\theta = 2 \lim_{z \rightarrow \infty} \left[\arctan \left(\frac{r_b(z)}{z} \right) \right] = 2 \arctan \left(\frac{\lambda}{\pi n r_{b0}} \right) \quad (\text{Eq. 2.7})$$

$$\theta \sim 2 \frac{r_{b0}}{z_R}, \quad \theta \sim 2 \frac{\lambda}{\pi n r_{b0}}$$

As it is shown in **Figure 2.20**, θ can be simplified as a cone formed at $z \gg z_R$ (where the intensity drops to $1/e^2$ and $r_b(z)$ increases linearly with z) whose principal axis would be the propagation axis z , and the radius would be $r_b(z)$. That cone contains 86.5 % of the intensity power of the Gaussian beam. It is important to consider that the beam has a minimum size at the focal point given by:

$$r_{b0} = \frac{\lambda d_f}{\pi n D} M^2 \quad (\text{Eq. 2.8})$$

where D is the output beam radius before the lens, d_f is the focal distance of the lens.

In consequence, the beam width, $r_b(z)$, is the amplitude of the beam radius as a function of z , and r_{b0} ($= r_b(0)$) is the value of the radius in the focus, so called waist radius, and, as it was mentioned before, the intensity evaluated in this point is equal to $1/e^2$. For safer use of lasers, the *American National Standard Z136.1-2007* uses some similar criteria but with a fall of the intensity to $1/e = 0.368$ times, giving a beam width of $r_b / \sqrt{2}$. Full Width at Half Maximum (FWHM) criterion define the beam width as the distance of two diametrically opposite points with intensity half of the maximum value, being $2 r_b$ (the full width of the beam at $1/e^2$) = FWHM / $\sqrt{(2 \ln 2)}$. In **Figure 2.21**, these criteria are shown.

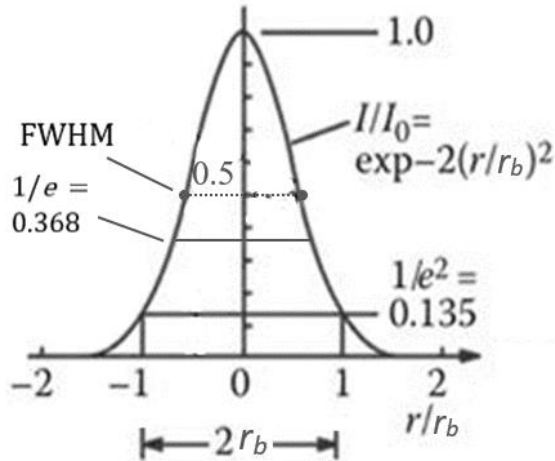


Figure 2.21 Scheme of intensity distribution (Gaussian profile) with different criteria for the beam width marked. Adapted from [68].

Since the beam size is a key factor for a controlled laser treatment, it is important to define it properly. Different alternatives exist to characterize the laser beam experimentally. *ISO 11146-(1,2,3):2005* is the international standard that specifies methods for measuring beam widths (meaning diameters) and divergence angles. Here, $D4\sigma$ (being sigma the standard deviation) method is the standard, more general criterion than $1/e^2$, since it is valid also for multimodal distributions. Nowadays the use of beam profilers based on CCD cameras is widespread, especially for lasers in the visible and n-IR ranges, although there exist detectors for larger wavelengths and also for UV lasers. Other techniques are those profilers based on pinholes, slits or knife-edges that mechanically shutter the laser beam and meanwhile a photodetector can measure the transmitted power.

In the case of Gaussian beams, mainly for those with ellipticity, e_{beam} (ratio between perpendicular minor and major axis of the ellipse) values close to one (circular-shaped), Liu [69] define a simple method to characterize the spot size of a pulsed laser through the evaluation of the mark sizes left by different energy pulses laser blasts.

In some laser treatments e_{beam} is lower than 0.9, usually because of the use of a non-spherical lens. This fact can be beneficial during surface scanning when the spot is more similar to a narrow line than to a circular small point. In that case, the intensity analysis will be parallel to **Eq. 2.2** but being more accurate if it is expressed as a product of three Gaussian distributions: x and y directions, in addition to the temporal one, being a the semi-axis in the x direction b in the y direction.

2.4.2. Processing parameters. Scanning surfaces

Usually laser treatments have to be performed over an area. One option is to couple the laser to a galvanometric mirror system and to scan the sample surface.

There are two different strategies to scan the surface with a laser beam: Laser Beam Scanning (LBS) and Laser Line Scanning (LLS) [70][71]. The first one, the most widely used, consists in scanning the surface with consecutive lines that are separated a distance, d_s , meanwhile the irradiated target remains in a fixed position. The laser beam spot can scan the given surface line by line with the same direction (typewriter-like, unidirectional) or can meander the surface alternating the starting direction and the opposite (meandering, bidirectional). It is important to take into account which strategy is better to scan the surface, having in mind other parameters like scanning speed or repetition rate and the acceleration and deceleration of the galvanometric mirrors: Unidirectional LBS can induce temperature differences between the beginning and the end of each line due to incubation phenomena, resulting in different surface modifications along the line. However, bidirectional LBS strategy, since the beginning of each line is closer to the end of the previous, provokes incubation in both ends of the line.

In the second scanning configuration, Laser Line Scanning (LLS), laser scans continuously a given line with the spot moving in a giving direction (uni- or bidirectional), while sample moves perpendicular to this line. Combining the time needed to scan a line and the sample speed, v_{sample} , it is possible to control the distance, and, in consequence, the distance between two consecutive lines, d_s . An important advantage of LLS is during the processing of big areas (comparable to the size of the laser marking area). To scan large surfaces with the LBS, the laser incident angle has to be modified continuously, which could induce severe changes in the processing. However, laser line scanning maintains a constant angle (between the laser source and the perpendicular to the line) minimizing these problems, making this strategy perfect to scalable industrial processes.

In both configurations, the laser describes initially a line. In this line, the ratio between scanning speed, v_L and f_{rep} gives the distance between the centre of two consecutive pulses, $d_p = v_L/f_{rep}$. This distance controls the energy distribution along the moving direction of the beam due to its Gaussian profile. In **Figure 2.22**, the resulting fluence distributions for different d_p / r_b ratios are shown, being r_b the spot radius. It is observed that for ratios of $d_p / r_b < 0.9$, energy distribution along the scanned line can be considered

uniform with differences between maximum and minimum lower than a 1%. If the criterion is established in 0.8, that difference is lower than 0.2%.

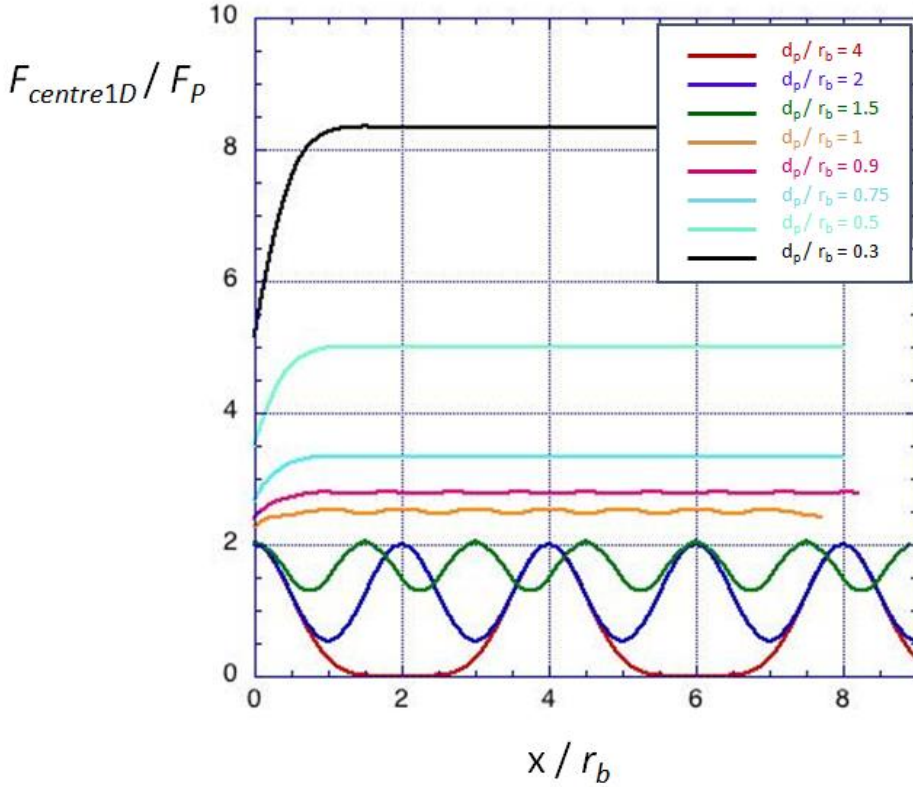


Figure 2.22 Fluence distribution along scanning direction in the centre of the laser processed line for different ratios d_p / r_b .

According to previous equations, accumulated fluence at the centre of the line, for processing parameters that ensure homogenous energy distribution comes from the following expression:

$$F_{centre1D} = 1.588 \frac{\pi r_b}{2 d_p} F_P \quad (\text{Eq. 2.9})$$

Taking into account the overlapping between two consecutive pulses, the effective number of pulses, N_{eff1D} , can be calculated considering that in a given processing time interval, Δt , the laser will emit $N = f_{rep} \Delta t$ pulses and the beam covers a rectangle with an area given by $(2 r_b) (v_L \Delta t)$. The average fluence along the line is:

$$F_{1D} = \frac{N E_P}{2 r_b v_L \Delta t} = \frac{f_{rep} E_P}{2 r_b v_L} = \frac{f_{rep} \pi r_b E_P}{2 v_L \pi r_b^2} = \frac{f_{rep} \pi r_b}{2 v_L} \frac{E_P}{\pi r_b^2} \quad (\text{Eq. 2.10})$$

$$F_{1D} = N_{eff1D} F_P$$

Being N_{eff1D} :

$$N_{eff1D} = \frac{f_{rep} \pi r_b}{2 v_L} = \frac{\pi r_b}{2 d_p}$$

In the perpendicular direction, the fluence also exhibits a Gaussian fluence distribution given by:

$$F(y) = F_{centre1D} \exp \left[-2 \left(\frac{y}{r_b} \right)^2 \right] = 1.588 N_{eff1D} F_P \exp \left[-2 \left(\frac{y}{r_b} \right)^2 \right] \quad (\text{Eq. 2.11})$$

By scanning in the perpendicular direction, also overlapping of Gaussian fluence distributions takes place. Performing a similar analysis in this 2D scanning process, the energy distribution can be considered uniform if $d_s / r_b < 0.9$.

The effective number of pulses in this 2D configuration, N_{eff2D} , can be calculated considering that the number of pulses required to cover a given processed area can be approached by $(N_1 d_p) (N_2 d_s)$ and the total energy deposited by the laser in this area is $N_1 N_2 E_P$.

$$F_{2D} = \frac{N_1 N_2 E_P}{Area} = \frac{N_1 N_2 E_P}{N_1 d_p N_2 d_s} = \frac{\pi r_b^2 E_P}{d_p d_s \pi r_b^2} \quad (\text{Eq. 2.12})$$

$$F_{2D} = N_{eff2D} F_P$$

The effective number of pulses in 2D, N_{eff2D} , can be calculated as:

$$N_{eff2D} = \frac{\pi r_b^2}{d_p d_s}$$

It is important to have in mind that the time between two successive pulses is of the order of microseconds (for f_{rep} of the order of 20-1000 kHz), while the time between two lines is of the order of several milliseconds. Also it is relevant to consider that this time includes the scanning time and also acceleration and deceleration times at the beginning and end of each line.

Another point to consider is that in this analysis we have only considered the energy parameters with the laser emission, but, as it has been described in the previous section,

other parameters as the material surface absorption or the incident angle can modify the effective amount of energy that it is involved in the process.

2.5. References

- [1] T. H. MAIMAN, "Stimulated Optical Radiation in Ruby," *Nature*, vol. 187, no. 4736, pp. 493–494, 1960, doi: 10.1038/187493a0.
- [2] A. L. Schawlow and C. H. Townes, "Infrared and Optical Masers," *Phys. Rev.*, vol. 112, no. 6, pp. 1940–1949, Dec. 1958, doi: 10.1103/PhysRev.112.1940.
- [3] E. Kannatey-Asibu, "J., 2009 Principles of laser materials processing." John Wiley & Sons, Inc.
- [4] R. C. Willson and A. V Mordvinov, "Secular total solar irradiance trend during solar cycles 21–23," *Geophys. Res. Lett.*, vol. 30, no. 5, 2003.
- [5] A. Tuennermann, S. Nolte, and J. Limpert, "Femtosecond vs. Picosecond Laser Material Processing: Challenges in Ultrafast Precision Laser Micromachining of Metals at High Repetition Rates," *Laser Tech. J.*, vol. 1, no. 7, pp. 34–38, 2010, doi: 10.1002/latj.201090006.
- [6] M. Malinauskas *et al.*, "Ultrafast laser processing of materials: From science to industry," *Light Sci. Appl.*, vol. 5, no. 8, pp. 3–5, 2016, doi: 10.1038/lssa.2016.133.
- [7] D. Kuizenga and A. Siegman, "FM and AM mode locking of the homogeneous laser- Part I: Theory," *IEEE J. Quantum Electron.*, vol. 6, no. 11, pp. 694–708, 1970.
- [8] H. Legall, C. Schwanke, S. Pentzien, G. Dittmar, J. Bonse, and J. Krüger, "X-ray emission as a potential hazard during ultrashort pulse laser material processing," *Appl. Phys. A*, vol. 124, no. 6, p. 407, 2018.
- [9] H. Legall, C. Schwanke, J. Bonse, and J. Krüger, "X-ray radiation protection aspects during ultrashort laser processing," *J. Laser Appl.*, vol. 32, no. 2, p. 022004, 2020, doi: 10.2351/1.5134778.
- [10] J. A. Puértolas, R. Ríos, M. Castro, and J. M. Casals, "Tecnología de superficies en materiales," *Ed. Síntesis, Madrid*, pp. 155–173, 2010.
- [11] D. Bäuerle, "Thermal, photophysical, and photochemical processes," in *Laser Processing and Chemistry*, Springer, 2011, pp. 13–38.
- [12] M. S. Brown and C. B. Arnold, "Fundamentals of laser-material interaction and application to multiscale surface modification," in *Laser precision microfabrication*, Springer, 2010, pp. 91–120.
- [13] J. D. Majumdar and I. Manna, "Laser processing of materials," *Sadhana*, vol. 28, no. 3–4, pp. 495–562, 2003.

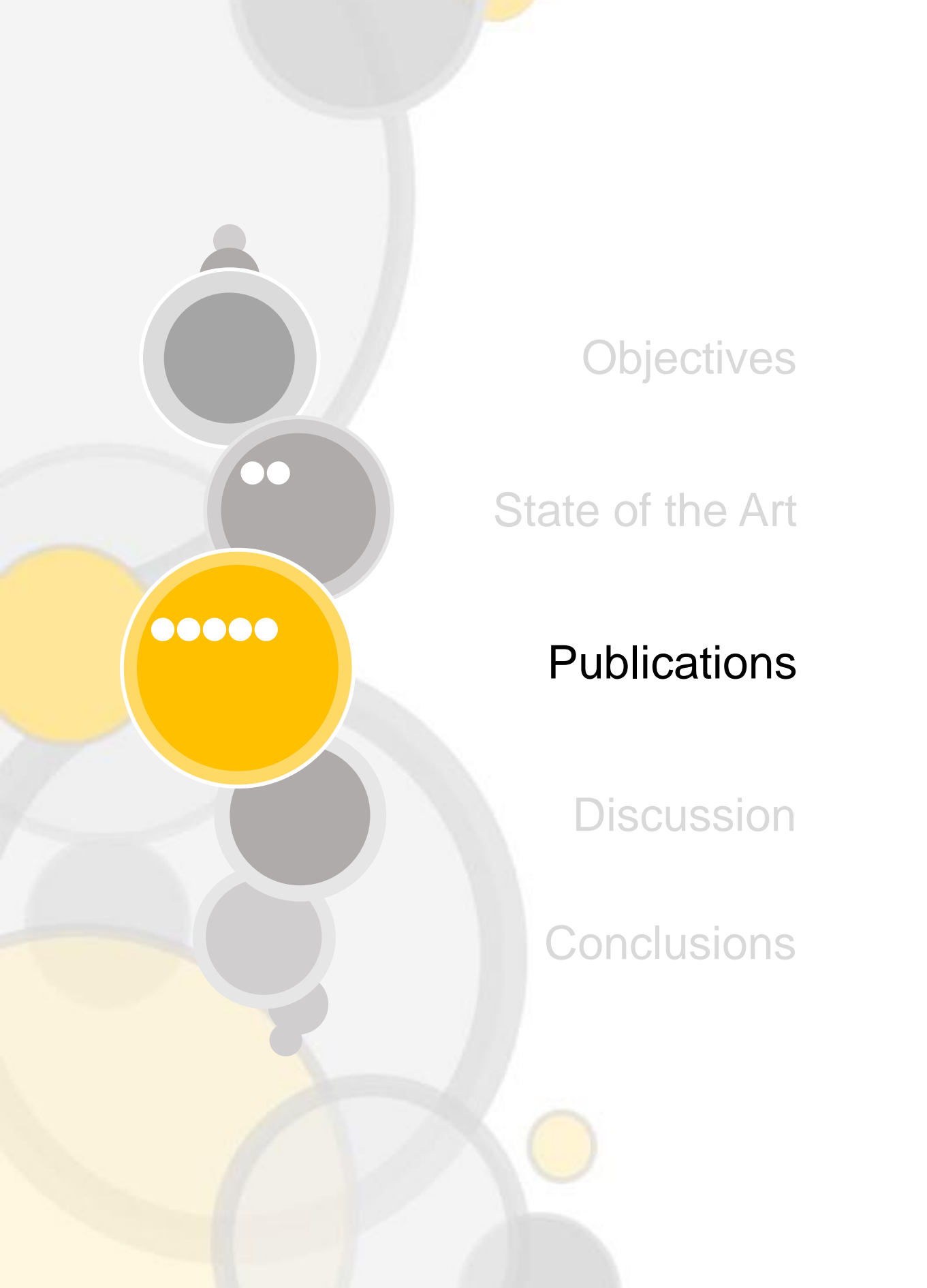
-
- [14] P. Schaaf, *Laser processing of materials: fundamentals, applications and developments*, vol. 139. Springer Science & Business Media, 2010.
- [15] L. Nanai, Z. Benko, R. Letfullin, and T. George, "Laser-Matter Interactions: Nanostructures, Fabrication and Characterization," Jan. 2011, doi: 10.1142/9789814287197_0001.
- [16] S. Musazzi and U. Perini, "Laser-induced breakdown spectroscopy," *Springer Ser. Opt. Sci.*, vol. 182, 2014.
- [17] D. Bergström, "The absorption of laser light by rough metal surfaces." Luleå tekniska universitet, 2008.
- [18] Y. Ding, L. Yang, and M. Hong, "Enhancement of pulsed laser ablation assisted with continuous wave laser irradiation," *Sci. CHINA Physics, Mech. Astron.*, vol. 62, no. 3, p. 34211, 2019.
- [19] K.-H. Leitz, B. Redlingshöfer, Y. Reg, A. Otto, and M. Schmidt, "Metal Ablation with Short and Ultrashort Laser Pulses," *Phys. Procedia*, vol. 12, pp. 230–238, Dec. 2011, doi: 10.1016/j.phpro.2011.03.128.
- [20] S. Materials, B. Applications, and F. Perspectives, "Laser Floating Zone Growth: Overview, Singular Materials, Broad Applications, and Future Perspectives," pp. 1–29, 2021.
- [21] J. S. Haggerty, "Production of fibers by a floating zone fiber drawing technique," 1972.
- [22] M. M. Fejer, J. L. Nightingale, G. A. Magel, and R. L. Byer, "Laser-heated miniature pedestal growth apparatus for single-crystal optical fibers," *Rev. Sci. Instrum.*, vol. 55, no. 11, pp. 1791–1796, 1984.
- [23] B. Özçelik *et al.*, "Low temperature thermoelectric properties of K-substituted $\text{Bi}_2\text{Sr}_2\text{Co}_2\text{O}_y$ ceramics prepared via laser floating zone technique," *J. Eur. Ceram. Soc.*, vol. 39, no. 10, pp. 3082–3087, 2019.
- [24] G. F. de la Fuente, J. Carlos Diez, L. A. Angurel, J. Peña, A. Sotelo, and R. Navarro, "Wavelength dependance in laser floating zone processing. A case study with Bi-Sr-Ca-Cu-O superconductors," *Adv. Mater.*, vol. 7, no. 10, pp. 853–856, 1995.
- [25] W. Yeong, C. Y. Yap, M. Mapar, and C. K. Chua, "State-of-the-art review on selective laser melting of ceramics," *High value Manuf. Adv. Res. virtual rapid Prototyp.*, vol. 1, pp. 65–70, 2013.
- [26] X. Zhang, X. Wu, and J. Shi, "Additive manufacturing of zirconia ceramics: a state-of-the-art review," *J. Mater. Res. Technol.*, vol. 9, no. 4, pp. 9029–9048, 2020, doi:
-

- 10.1016/j.jmrt.2020.05.131.
- [27] J. J. Beaman and C. R. Deckard, "Selective laser sintering with assisted powder handling." Google Patents, Jul. 03, 1990.
- [28] H. Yves-Christian, W. Jan, M. Wilhelm, W. Konrad, and P. Reinhart, "Net shaped high performance oxide ceramic parts by selective laser melting," *Phys. Procedia*, vol. 5, pp. 587–594, 2010.
- [29] J. Wilkes, Y. Hagedorn, W. Meiners, and K. Wissenbach, "Additive manufacturing of ZrO₂-Al₂O₃ ceramic components by selective laser melting," *Rapid Prototyp. J.*, 2013.
- [30] F. Rey-García, F. Gutiérrez-Mora, C. J. Borrel, L. C. Estepa, L. A. Angurel, and G. F. De la Fuente, "Microstructural characterization and tribological behavior of Laser Furnace processed ceramic tiles," *Ceram. Int.*, vol. 44, no. 6, pp. 6997–7005, 2018.
- [31] A. Cubero, J. I. Peña, and M. A. Laguna-Bercero, "Optimization of Ni-YSZ solid oxide fuel cell anodes by surface laser melting," *Appl. Surf. Sci.*, vol. 335, 2015, doi: 10.1016/j.apsusc.2015.01.230.
- [32] H. M. Van Driel, J. E. Sipe, and J. F. Young, "Laser-induced periodic surface structure on solids: a universal phenomenon," *Phys. Rev. Lett.*, vol. 49, no. 26, p. 1955, 1982.
- [33] R. J. Nemanich, D. K. Biegelsen, and W. G. Hawkins, "Aligned, coexisting liquid and solid regions in laser-annealed Si," *Phys. Rev. B*, vol. 27, no. 12, p. 7817, 1983.
- [34] J. Bonse and J. Krüger, "Pulse number dependence of laser-induced periodic surface structures for femtosecond laser irradiation of silicon," *J. Appl. Phys.*, vol. 108, no. 3, p. 34903, 2010.
- [35] Y. H. Liu, S. C. Yeh, and C. W. Cheng, "Two-dimensional periodic nanostructure fabricated on titanium by femtosecond green laser," *Nanomaterials*, vol. 10, no. 9, pp. 1–11, 2020, doi: 10.3390/nano10091820.
- [36] J. Bonse, "Quo vadis LIPSS?—recent and future trends on laser-induced periodic surface structures," *Nanomaterials*, vol. 10, no. 10, pp. 1–19, 2020, doi: 10.3390/nano10101950.
- [37] M. Birnbaum, "Semiconductor surface damage produced by ruby lasers," *J. Appl. Phys.*, vol. 36, no. 11, pp. 3688–3689, 1965.
- [38] J. E. Sipe, J. F. Young, J. S. Preston, and H. M. Van Driel, "Laser-induced periodic surface structure. I. Theory," *Phys. Rev. B*, vol. 27, no. 2, p. 1141, 1983.
- [39] D. Dufft, A. Rosenfeld, S. K. Das, R. Grunwald, and J. Bonse, "Femtosecond laser-induced periodic surface structures revisited: A comparative study on ZnO," *J.*

-
- Appl. Phys.*, vol. 105, no. 3, p. 34908, 2009.
- [40] J. Z. P. Skolski, G. Römer, J. V. Obona, V. Ocelik, and J. T. M. De Hosson, "Laser-induced periodic surface structures: Fingerprints of light localization," *Phys. Rev. B*, vol. 85, no. 7, p. 75320, 2012.
- [41] J. Bonse, S. Höhm, S. V. Kirner, A. Rosenfeld, and J. Krüger, "Laser-induced periodic surface structures – a scientific evergreen," *IEEE J. Sel. Top. Quantum Electron.*, vol. 23, no. 3, p. 9000615, 2017, doi: 10.1109/jstqe.2016.2614183.
- [42] J. Bonse and S. Gräf, "Maxwell Meets Marangoni—A Review of Theories on Laser-Induced Periodic Surface Structures," *Laser Photonics Rev.*, vol. 14, no. 10, pp. 1–25, 2020, doi: 10.1002/lpor.202000215.
- [43] J. Bonse, S. V. Kirner, M. Griepentrog, D. Spaltmann, and J. Krüger, "Femtosecond laser texturing of surfaces for tribological applications," *Materials (Basel)*, vol. 11, no. 5, p. 801, 2018.
- [44] E. Allahyari *et al.*, "Femtosecond laser surface irradiation of silicon in air: Pulse repetition rate influence on crater features and surface texture," *Opt. Laser Technol.*, vol. 126, no. December 2019, p. 106073, 2020, doi: 10.1016/j.optlastec.2020.106073.
- [45] J. Bonse, S. V. Kirner, and J. Krüger, *Laser-Induced Periodic Surface Structures (LIPSS)*. 2021.
- [46] A. Y. Vorobyev and C. Guo, "Direct femtosecond laser surface nano/microstructuring and its applications," *Laser Photon. Rev.*, vol. 7, no. 3, pp. 385–407, 2013.
- [47] A. Borowiec and H. K. Haugen, "Subwavelength ripple formation on the surfaces of compound semiconductors irradiated with femtosecond laser pulses," *Appl. Phys. Lett.*, vol. 82, no. 25, pp. 4462–4464, Jun. 2003, doi: 10.1063/1.1586457.
- [48] E. Rebollar, M. Castillejo, and T. A. Ezquerra, "Laser induced periodic surface structures on polymer films: From fundamentals to applications," *Eur. Polym. J.*, vol. 73, pp. 162–174, 2015, doi: <https://doi.org/10.1016/j.eurpolymj.2015.10.012>.
- [49] V. Oliveira, S. P. Sharma, M. F. S. F. de Moura, R. D. F. Moreira, and R. Vilar, "Surface treatment of CFRP composites using femtosecond laser radiation," *Opt. Lasers Eng.*, vol. 94, pp. 37–43, 2017, doi: <https://doi.org/10.1016/j.optlaseng.2017.02.011>.
- [50] E. Stratakis *et al.*, "Laser engineering of biomimetic surfaces," *Mater. Sci. Eng. R Reports*, vol. 141, no. March, p. 100562, 2020, doi: 10.1016/j.mser.2020.100562.
-

- [51] A. Papadopoulos *et al.*, "Biomimetic omnidirectional antireflective glass via direct ultrafast laser nanostructuring," *Adv. Mater.*, vol. 31, no. 32, p. 1901123, 2019.
- [52] J.-T. Chen, W.-C. Lai, Y.-J. Kao, Y.-Y. Yang, and J.-K. Sheu, "Laser-induced periodic structures for light extraction efficiency enhancement of GaN-based light emitting diodes," *Opt. Express*, vol. 20, no. 5, pp. 5689–5695, 2012.
- [53] A. Cunha *et al.*, "Femtosecond laser surface texturing of titanium as a method to reduce the adhesion of *Staphylococcus aureus* and biofilm formation," *Appl. Surf. Sci.*, vol. 360, pp. 485–493, 2016.
- [54] N. Epperlein *et al.*, "Influence of femtosecond laser produced nanostructures on biofilm growth on steel," *Appl. Surf. Sci.*, vol. 418, pp. 420–424, 2017.
- [55] E. Rebollar *et al.*, "Proliferation of aligned mammalian cells on laser-nanostructured polystyrene," *Biomaterials*, vol. 29, no. 12, pp. 1796–1806, 2008.
- [56] J. Yong, F. Chen, Q. Yang, and X. Hou, "Femtosecond laser controlled wettability of solid surfaces," *Soft Matter*, vol. 11, no. 46, pp. 8897–8906, 2015.
- [57] C. Liang *et al.*, "Preparation of hydrophobic and oleophilic surface of 316 L stainless steel by femtosecond laser irradiation in water," *J. Dispers. Sci. Technol.*, vol. 35, no. 9, pp. 1345–1350, 2014.
- [58] I. Paradisanos, C. Fotakis, S. H. Anastasiadis, and E. Stratakis, "Gradient induced liquid motion on laser structured black Si surfaces," *Appl. Phys. Lett.*, vol. 107, no. 11, p. 111603, Sep. 2015, doi: 10.1063/1.4930959.
- [59] V. Vercillo *et al.*, "Design Rules for Laser-Treated Icephobic Metallic Surfaces for Aeronautic Applications," *Adv. Funct. Mater.*, vol. 30, no. 16, p. 1910268, Apr. 2020, doi: <https://doi.org/10.1002/adfm.201910268>.
- [60] J. Madéo *et al.*, "Ultrafast properties of femtosecond-laser-ablated GaAs and its application to terahertz optoelectronics," *Opt. Lett.*, vol. 40, no. 14, pp. 3388–3391, 2015, doi: 10.1364/OL.40.003388.
- [61] L. Romoli *et al.*, "Ultrashort pulsed laser drilling and surface structuring of microholes in stainless steels," *CIRP Ann.*, vol. 63, no. 1, pp. 229–232, 2014, doi: <https://doi.org/10.1016/j.cirp.2014.03.053>.
- [62] K. Lange, M. Schulz-Ruhtenberg, and J. Caro, "Platinum Electrodes for Oxygen Reduction Catalysis Designed by Ultrashort Pulse Laser Structuring," *ChemElectroChem*, vol. 4, no. 3, pp. 570–576, Mar. 2017, doi: <https://doi.org/10.1002/celec.201600630>.
- [63] A. Cubero *et al.*, "Effects of laser-induced periodic surface structures on the

-
- superconducting properties of Niobium,” *Appl. Surf. Sci.*, vol. 508, p. 145140, Apr. 2020, doi: 10.1016/j.apsusc.2019.145140.
- [64] Á. Cubero *et al.*, “Surface superconductivity changes of niobium sheets by femtosecond laser-induced periodic nanostructures,” *Nanomaterials*, vol. 10, no. 12, pp. 1–16, 2020, doi: 10.3390/nano10122525.
- [65] J. Ion, *Laser processing of engineering materials: principles, procedure and industrial application*. Elsevier, 2005.
- [66] W. M. Steen and J. Mazumder, *Laser material processing*. Springer Science & Business Media, 2010.
- [67] “Gaussian beam.” https://en.wikipedia.org/wiki/Gaussian_beam (accessed Oct. 22, 2020).
- [68] G. F. Marshall and G. E. Stutz, *Handbook of optical and laser scanning*. Taylor & Francis, 2012.
- [69] J. M. Liu, “Simple technique for measurements of pulsed Gaussian-beam spot sizes,” *Opt. Lett.*, vol. 7, no. 5, pp. 196–198, 1982.
- [70] V. Lennikov, B. Özkurt, L. A. Angurel, A. Sotelo, B. Özçelik, and G. F. De La Fuente, “Microstructure and transport properties of Bi-2212 prepared by CO₂ laser line scanning,” *J. Supercond. Nov. Magn.*, vol. 26, no. 4, pp. 947–952, 2013.
- [71] K. Ozturk *et al.*, “IR laser line scanning treatments to improve levitation forces in MgTiO_{0.6}B₂ bulk materials,” *J. Alloys Compd.*, vol. 811, p. 151966, 2019, doi: <https://doi.org/10.1016/j.jallcom.2019.151966>.
- [72] E. G. Gamaly and A. V. Rode, “Physics of ultra-short laser interaction with matter: From phonon excitation to ultimate transformations,” *Prog. Quantum Electron.*, vol. 37, no. 5, pp. 215–323, 2013, doi: 10.1016/j.pquantelec.2013.05.001.



Objectives

State of the Art

Publications

Discussion

Conclusions

Publication A

Title:

Quench dynamics in MgB₂ Rutherford cables

Journal:

Superconductor Science and Technology

A. Cubero, R. Navarro, P. Kováč, L. Kopera, M. A. Rindfleisch and E. Martínez.

Published, Superconductor Science and Technology vol. 31, (**2018**) 045009 (9pp)

DOI: 10.1088/1361-6668/aab0c1

Link to the Version of Record: <https://iopscience.iop.org/article/10.1088/1361-6668/aab0c1>

Impact Factor, Journal Citation Reports (**JCR**): 2.489; Quartile Q2 (Physics, Applied)

SCImago Journal Rank (**SJR**): 0.879; Quartile Q1 (Electrical and Electronic Engineering)

A. Cubero, R. Navarro, P. Kováč, L. Kopera, M. A. Rindfleisch and E. Martínez, *Quench dynamics in MgB₂ Rutherford cables*. Superconductor Science and Technology vol. 31, (2018) 045009 (9pp).

The generation and propagation of quench induced by a local heat disturbance or by overcurrents in MgB₂ Rutherford cables have been studied. 12 strands, each one monocoire MgB₂/Nb/Cu10Ni, compose the analysed cable. The intra- and inter- strand voltages have been examined to measure the superconductor-to-normal transition behaviour. In the case of quenches induced by external local hot-spots, two different time-dynamic regimes have been observed and the propagation velocities have also been analysed. In the case of quench provoked by overcurrents, a distinctive and faster quench dynamics were detected. My contribution has been related with preparation of the cables for quench tests, conducting the experiments, together with the data analysis and the draft version writing.

Postprint of Supercond. Sci. Technol. 31 (2018) 045009

DOI: 10.1088/1361-6668/aab0c1

Quench dynamics in MgB₂ Rutherford cables

A. Cubero¹, R. Navarro¹, P. Kováč², L. Kopera² and M. Rindfleisch³, E. Martínez¹

¹*Instituto de Ciencia de Materiales de Aragón, (CSIC – Universidad de Zaragoza), C/ María de Luna 3, 5018 Zaragoza, Spain*

²*Institute of Electrical Engineering, Slovak Academy of Sciences, Dúbravská cesta 9, 841 04 Bratislava, Slovakia*

³*HyperTech Research, Inc., Columbus, OH 43210, USA*

Keywords: MgB₂, Rutherford cables, quench, thermal stability, superconductor

Abstract:

The generation and propagation of quench induced by a local heat disturbance or by overcurrents in MgB₂ Rutherford cables have been studied experimentally. The analysed cable is composed of 12 strands of monocoire MgB₂/Nb/Cu10Ni wire and has a transposition length of about 27 mm. Measurements of voltages intra- and inter-strands have been performed to analyse the superconducting-to-normal transition behaviour of these cables during quench. In case of external hot spots, two different time-dynamic regimes have been observed, a slow stage for the formation of the minimum propagation zone (MPZ), and a fast dynamics once the quench is triggered and propagates to the rest of the cable. Significant local variations of the quench propagation velocity across the strands around the MPZ have been observed, but with average quench propagation velocities closely correlated with the predictions given by one-dimensional-geometry models. For quench induced by overcurrents (i.e. with applied currents higher than the critical current) the nucleation of many normal zones distributed within the cable, which overlap during quench propagation, gives a distinctive and faster quench dynamics.

1. Introduction

Rutherford-type cables based on low temperature superconductors (LTS) NbTi and Nb₃Sn, have been widely used in the past years to build magnets for High-Energy Physics [1,2]. Compared to monolithic conductors, these cables have high strand packing and fully transposed current paths, which allows a substantial increase of current capability together with a reduction of AC losses. Thus, by using these cables, the magnet inductance, the operating voltage, and the magnetic energy stored in the system can be reduced, which is of great relevance for these large-scale applications.

Initially, one of the main drivers for superconducting Rutherford cables was the development of NbTi dipole and quadrupole magnets for particle accelerators. Later on, the interest in Rutherford cables was extended to other superconducting materials and applications. In this way, cables that allows higher operating magnetic fields and/or temperatures, based on Nb₃Sn [2,3], Bi₂Sr₂CaCu₂O_{8+x} [4,5,6], and more recently MgB₂ [7,8] and coated conductors [9], have already been developed. Certainly, the specific mechanical, chemical and physical characteristics of the superconducting wires or tapes used for cabling create particular challenges and impose different cabling strategies. On the other hand, prototypes of superconducting magnetic energy systems (SMES) [10,11] and very high-field magnets [12], have already been manufactured using Rutherford cables.

Braided or twisted cables are often required in many applications to achieve a reduction of the AC losses when using appropriate transposition length and inter-strand electrical resistance [13-16]. In the presence of alternating fields or during magnet field ramping, coupling currents are induced that loop around a half-pitch of the cable and through the crossover and adjacent strands. Therefore, increasing the contact electrical resistance between strands is beneficial for decreasing AC losses, although on the other hand, as the current transfer among strands reduces, so does the thermal stability of the cable. Therefore, the optimization process of the cables should take into account both mentioned opposing effects, although the optimum balance may differ for each particular application.

The thermal stability of different designs of LTS Rutherford cables has been analysed by several groups [17-22], where the effect on quench characteristics of strand coating, individually insulated strands, contact resistance between strands, as well as the presence of a resistive core inside the cable (between the upper and lower layers of the cable) has been studied.

Since Rutherford cables based on MgB₂ have just been recently proposed [7,8] and are not yet fully developed, it is important to understand their behaviour to further optimize their superconducting properties while providing the required thermal stability for the different applications. The present work aims to analyse the quench dynamics of MgB₂ Rutherford cables, especially focussing on the quench induced by a local heat disturbance. The analysed cable has 12 strands and a transposition length of about 27 mm and was manufactured using monocoil MgB₂/Nb/Cu10Ni round composite wires. During a quench, measurements of the voltages along given strands and between different strands have been performed and analysed to understand the superconducting-to-normal transition characteristics during a quench induced by hot-spots or overcurrents. A further analysis of the experimentally estimated global quench propagation velocities in terms of simple one-dimensional conductor models has been done.

2. Experimental

The characteristics of the Rutherford cable analysed in this study are collected in Table 1. The cables have 12 strands and rectangular cross section of dimensions 2.7 mm wide by ~ 0.7 mm thick. The transposition length, also referred to as the transposition pitch, is ~ 27 mm. The cable was made from monocoil wires with undoped Mg and B precursors and Cu10Ni alloy as outer sheath. The used wires were cold drawn down to 0.39 mm and have Nb barrier between the superconducting core and the sheath. After the final cable manufacturing, *in situ* reaction of the Mg + B precursor powders to form the superconducting MgB_2 phase was done at 650 °C for 30 minutes in Ar atmosphere. The wires were manufactured by HyperTech Research and the cabling was performed in the Institute of Electrical Engineering of Bratislava. The cabling procedure and the superconducting properties of Rutherford cable and wire are described in detail in [8].

Table 1. Characteristics of analysed MgB_2 Rutherford cable (samples RC-1 and RC-2) and of one isolated strand extracted from the cable. I_c is the critical current at self-field and R the resistance per unit length.

Sample ID	Transversal dimensions	I_c (A)			R (m Ω /cm)		Description
		$T= 35$ K	33 K	32 K	$T= 40$ K	293 K	
RC-1	0.7 mm x 2.7 mm	69	---	170	0.16	----	CABLE with 12 strands and transposition length
RC-2	0.7 mm x 2.7 mm	110	220	---			$L_p \sim 27$ mm
strand	~ 0.12 mm ²	8.5	19	21	1.9	16	Monocoil MgB_2 /Nb/Cu10Ni

Both analysed samples, RC-1 and RC-2, of length 11 cm, come from the same cable and therefore have similar manufacturing procedure, except that RC-1 was heat treated at 650 °C with a bend diameter of 80 mm and subsequently straightened, while RC-2 was directly heated in straight form. Before the final reaction heat treatment, a strand was extracted from another piece of the same cable and subsequently heated at the same conditions (650 °C for 30 minutes). The measured critical currents of a 5-cm-long segment of this single strand, $I_{c,strand}$, are also collected in Table 1. Thus, the critical currents of cable RC-2 are about 12 times $I_{c,strand}$, as expected for a cable with rather homogenous strands. On the contrary, the smaller I_c values of cable RC-1 suggest a certain deterioration of this cable, probably due to the straightening process after heat treatment.

All measurements were performed with the samples in vacuum and cooled by conduction from both ends (current-feeding contacts), which were thermally anchored to the 2nd stage of the used cryocooler. A thermometer was glued to the cable to control the initial temperature of the sample, T_0 , before quench measurements. This operating temperature was controlled with a Lakeshore temperature controller.

For quench measurements under local heat disturbances, the energy was deposited to the cable, carrying a current, $I < I_c(T_0)$, by passing a rectangular current pulse of variable duration in a heater. This input energy is increased in small steps by increasing either the current or the duration of the pulse, t_p , estimating this way the minimum energy able to trigger the quench of the cable (minimum quench energy, MQE). Usually, to simulate local heat disturbances in cables, either carbon-paste heaters attached to a single strand [17-18] or heaters that spanned over the width of the cable [20] have been previously used. Here, a strain gage of

r

resistance 120Ω and dimensions $3 \text{ mm} \times 2 \text{ mm}$ on a $20\text{-}\mu\text{m}$ -thick kapton foil is used as heater. It was glued to the surface of the cable, at mid distance between current contacts, and overlaps 5 strands.

Several voltage taps were used to analyse the development and propagation of the quench. Unlike most monolithic conductors, where the full cross-section at a given position x_0 ($0 < x_0 < L$, where L is the length) can be considered equipotential in a good approximation [23], for MgB_2 Rutherford cables this assumption is not always valid and the measured voltages may depend on the relative position of voltage taps between the strands, as it will be discussed later. Thus, the quench analysis may become very complicated by using in these multistrand cables, the same voltage taps' disposition as in monolithic conductors [23,24]. On the other hand, global voltage taps, which are in electrical contact with all the strands at a given cross-section, were disregarded, except for measuring the total voltage of the cable, because they would provide additional electrical and thermal paths and therefore, they would change the real conditions of the cable.

Although different arrangements of voltage taps were tried in preliminary tests, due to the above-mentioned reasons, the tap configuration shown in Figure 1 has been chosen, following a procedure similar to that proposed by Willering *et al* [21] [22]. In this configuration all the voltages given in the figure are measured between two taps soldered in a given strand (the distance between each pair of taps following the strand is $d \sim 1.2\text{-}1.3 \text{ cm}$). This way, V_0 and $V_{0,b}$ correspond to the voltages measured in the heater area in segments of two strands that are symmetrically crossed. The former is at the top side of the cable, in direct contact with the heater, and the latter at the bottom. Since taps b, g, d and i are soldered in the same strand, voltages V_1 and V_1' are measured in symmetric segments of the same strand sensed by $V_{0,b}$, at the right- and the left-hand side of the heater, respectively. At a distance of $L_p/2 + \Delta x_{1,2}$ ($\Delta x_{1,2} \sim 1 \text{ cm}$), 10 strands away from the central strand section sensed by V_0 , voltages V_2 and V_2' are measured in two different strands, which are farther away and also in symmetric positions around the heater. Note that these two strands are not in direct contact with the heater, neither sensed by any other tap. Finally, the total voltage of the cable, V_{cable} , is measured between two global taps, C' and C , which are close to the current contacts. These taps, separated by a distance of 8 cm , connect electrically all the strands at cross sections C and C' by means of Sn-Pb-Ag solder. In the experiments, all voltages are always measured using the same polarity, left-right, in such a way that in the normal state all measured voltages are positive.

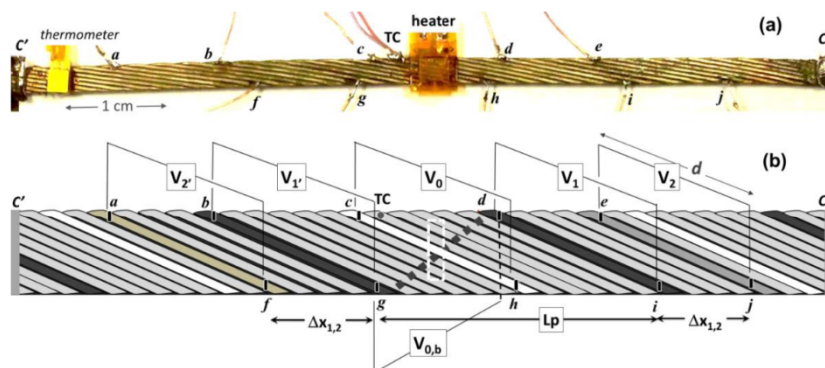


Figure 1. (a) Photograph of Rutherford cable RC-2 showing the heater, 10 voltage taps (a to j) and a thermocouple (TC). (b) Scheme of the same cable (drawn wider than real for clarity purposes) showing some highlighted strands, heater position, voltage taps and some measured voltages: V_0 (between taps c and h), $V_{0,b}$ (g - d), V_1 (d - i), V_2 (e - j), etc. The total length of the measured cable is 11 cm and the distance between global voltage taps C' and C is 8 cm , $\Delta x_{1,2} \sim 1 \text{ cm}$ and $d \sim 1.2\text{-}1.3 \text{ cm}$.

A thermocouple was also attached to measure the temperature near the hot-spot. The voltages between different taps and the temperature measured by the thermocouple were recorded using a Data Acquisition (DAQ) device. The experiment is controlled through LabVIEW graphical interface. In order to protect the cables during a quench the power supply is switched-off via GPIB when the total voltage measured in the cable reaches a value of 80-100 mV.

3. Results and discussion

Two similar samples RC-1 and RC-2, with different critical currents (see Table 1), were measured at different temperatures and currents. Nevertheless, since RC-1 suffered some deterioration, in this paper the detailed analysis of the voltage development during quench has been focussed on cable RC-2, as it is more relevant. However some results of cable RC-1 have also been reported and analysed.

3.1 Development of quench induced by local heat disturbances

Figure 2(a) shows the time evolution of the voltages measured in cable RC-2 after a heat pulse of energy 27 mJ and duration 40 ms, which induces a quench. Recovery is observed after applying slightly lower energy, 25 mJ, in a pulse of the same duration. The inset of the figure shows the comparison of voltage and temperature time evolution near the hot spot, in the events of quench and recovery. In case of quench, the heat pulse produces a metastable state, with voltage value $V_0(t)$ almost constant $\sim 30 \mu\text{V}$ for about 2 s, which eventually results in a fast increase of the voltage. During this metastable state, the temperature measured by the thermocouple TC is about 36.5 K, just 1.5 K above the initial temperature $T_0 = 35 \text{ K}$ and below the critical temperature, $T_c \sim 38 \text{ K}$. Within the strand, current sharing between the superconducting core and the metal sheath (current sharing regime) would be present at this stage.

Among all the measured voltages, only those at the heater area (V_0 and $V_{0,b}$) shows signal above noise level before the quench triggers. Nevertheless, while $V_0(t)$ increases fast up to $30 \mu\text{V}$ and remains almost constant, $V_{0,b}(t)$ increases more slowly but continuously. Eventually, at $t \sim 2.5 \text{ s}$, both voltages equal and increase sharply at the same rate. This can be observed in Figure 2(b), where the same voltages are plotted in an expanded time scale for better observation of the quench propagation dynamics. The time interval from the initial hot-spot to quench triggering is considerably longer than for monolithic conductors [23], which may be favoured by current redistribution among strands.

Attention should be paid to the coincidence of both voltages V_0 and $V_{0,b}$ with the total voltage $V_{\text{cable}}(t)$ from the time of quench triggering (at $t \sim 2.5 \text{ s}$) until the onset of $V_1(t)$ at $t \sim 2.69 \text{ s}$, which would be expected for parallel resistances with negligible current transfer between them. This behaviour differs in some aspects from the results obtained in NbTi Rutherford cables immersed in liquid helium at 4.3 K [22], although it is important to note that the differences between both experiments are not limited to the type of analysed samples and cooling conditions, but also to the way the heat is deposited. Willering *et al* [22] used a graphite paste heater positioned in a small section of a strand to induce the quench. They observed that the current of the normal conducting strand section created by the hot-spot is transferred to its neighbouring strands. Besides, voltages of several mV were measured in strands segments around the heater before measuring voltage by the global taps of the cable.

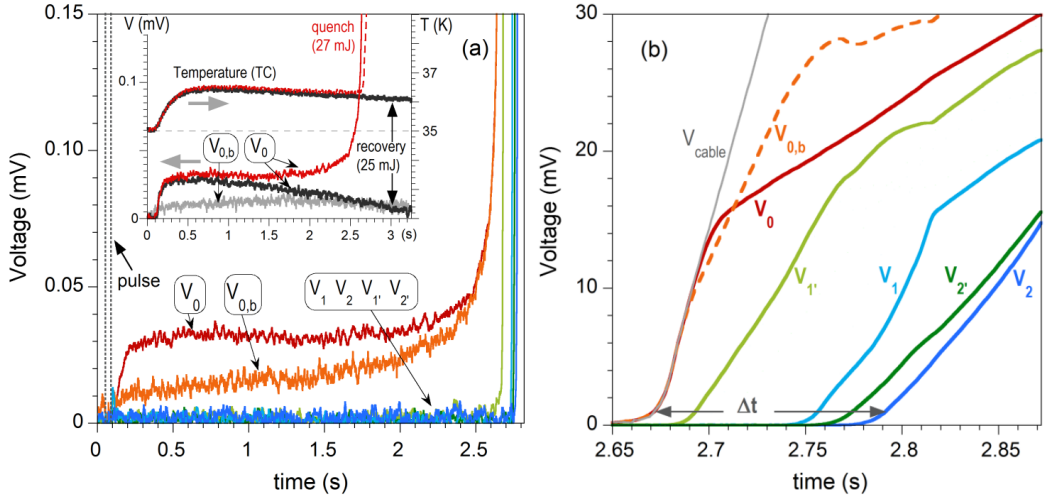


Figure 2. Time evolution of the different voltages, named as in Figure 1(b), measured in cable RC-2 during quench at $T_0 = 35$ K and $I = 82$ A. (a) Detail of the initial stages of quench development. *Inset:* Comparison of the time evolution of voltages and temperature near the heater for quench and recovery cases (temperature was measured by thermocouple TC). $V_{0,b}(t)$ in case of recovery, is also shown for comparison. (b) Voltages measured during quench propagation. Δt is the time delay between $V_0(t)$ and $V_2(t)$ at voltage values of 1 mV. Note that the time- and voltage- scales are different in (a) and (b).

At later stages, there are some observations that suggest complex current transfer between strands. For example, voltage $V_{0,b}(t)$ presents some fluctuations (it decreases at $t \sim 2.76$ s before increasing again some ms later), which are not due to current variations in the cable. Besides, there are some differences in shape among the different $V_i(t)$ curves during quench propagation, unlike the behaviour observed in single conductors, where all $V_i(t)$ curves measured along the conductor during a quench are very similar, just displaced in time [23].

The above experimental results point-out two different time scales in quench dynamics. At the beginning, the formation of a minimum propagating zone (MPZ) is slow and dominated by the conductive heat flow from the strands in the upper part of the cable close to the heater, to those at the bottom in contact with them. The formation of a MPZ, which includes several strands, triggers the quench that propagates to the rest of the cable on a shorter time scale. It is also remarkable that although the quench propagation is not symmetric around the heater, as there is a delay of ~ 63 ms between the onset of voltages $V_1(t)$ and $V_{1'}(t)$, this delay decreases considerably, down to 15 ms, between the filament segments more distant from the heater, which are sensed by voltages $V_2(t)$ and $V_{2'}(t)$. This suggests that the presence of inhomogeneities in the local critical current of the strands, and/or in the thermal contact resistance among them, is evidenced mainly in the area close to the quench origin.

Further analysis of the first stages of quench evolution can be done by studying the voltages measured between taps of different strands as seen in Figure 3(a). The onset of voltages $V_{1'A}(t)$ and $V_{1A}(t)$, which correspond to taps pairs (b,c) and (h,i) , respectively, and have point of symmetry in the centre of the heater, occurs at the same time ($t \sim 2.7$ s) and coincides with a change of the slope $V_0(t)$ at ~ 15 mV. This value corresponds to the voltage of an insulated strand of length equal to segment between taps c and h ($d = 1.2$

cm) when carrying a current $I/12$ at 40 K (normal state) and thus indicates that the quench arrives to taps c and h when the strand segment (c,h) is fully in the normal state.

On the other hand, voltages $V_{1'B}(t)$ and $V_{1B}(t)$, which correspond to tap pairs (f,g) and (d,e) and also have point of symmetry in the centre of the heater, exactly coincide with $V_1(t)$ and $V_{1'}(t)$, respectively, during the first stages. Therefore, the quench in the strand segment sensed by V_1 (between taps d and i) propagates from the upper to the lower edge but not from the cable centre towards the edges. Similarly, in the strand segment sensed by $V_{1'}$ (taps b,g), quench propagates from the lower to the upper edge. Therefore, the quench propagation along each strand, following the “twisted” geometry of the cable, would be predominant near the hot-spot.

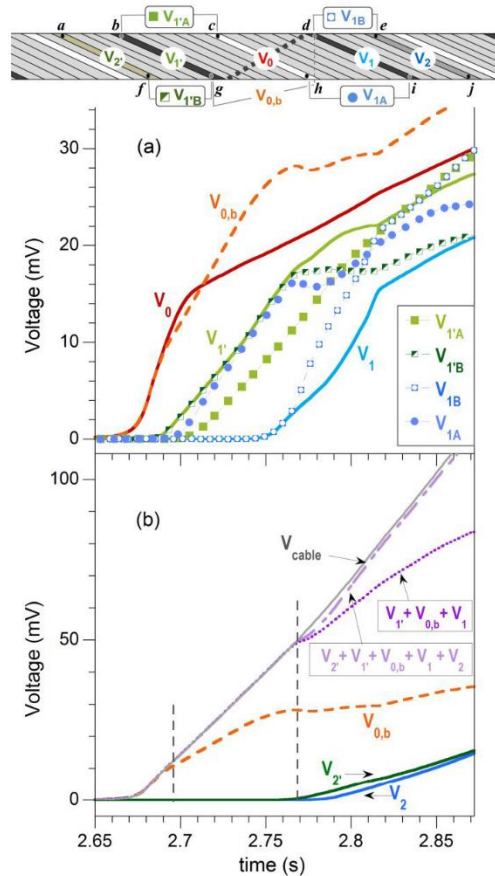


Figure 3. Time evolution of different voltages measured in cable RC-2 during the same quench as in Figure 2. (a) Voltages measured across strands (symbols defined in the inset), and along given strands (lines without symbols). (b) Comparison between the total voltage (V_{cable}) and the sum of different voltages measured in several strand segments.

For a better understanding of the quench behaviour, it is also interesting to compare the total voltage of the cable, $V_{cable}(t)$, with the sum of the voltages measured in several strand segments, as it is shown in Figure 3(b). It must be remarked that since not all these intra-strand voltages have common references, their sum could differ from $V_{cable}(t)$. As it is shown in the figure, the whole $V_{cable}(t)$ curve is almost coincident with the

sum of voltages V_2 , V_1 , $V_{0,b}$, V_1 and V_2 ; and three time intervals are clearly distinguished. First, for $t < 2.7$ s, the total voltage overlaps with $V_{0,b}$ (and V_0), so that the normal zone in this time interval would be restricted to the cable region limited by taps c , d , g and h , in the centre of the cable. Furthermore, V_{cable} coincides with the sum of voltages V_1 , $V_{0,b}$ and V_1 until $t \sim 2.77$ s, moment when voltages V_2 and V_2 start given signal. These results suggest that a normal zone is first created in the centre of the cable around the heater, and subsequently, the normal-superconducting front propagates towards the ends of the cable. In general terms, this is similar to the behaviour of monolithic conductors, although the cabling structure introduces complexity in quench propagation.

3.2 Quench propagation velocities

The quench propagation velocities can be estimated experimentally from the time delay between measured voltages in different strand segments (see Figure 1) and the distance between corresponding voltage taps. Global quench propagation velocities were obtained as $v_p = \Delta x / \Delta t$, where Δt is the time delay between voltages $V_0(t)$ and $V_2(t)$ at a given voltage value, $V_{\Delta t}$, and Δx is the distance between corresponding taps, $\Delta x = \Delta x_{1,2} + L_p/2$ (Figure 1(b)). As it is seen in Figure 2(b), $V_0(t)$ and $V_2(t)$ curves are not parallel during the superconducting-to-normal transition of the sensed strand segments. The time delay Δt would therefore depend on the used $V_{\Delta t}$ value, and consequently also v_p . To analyse this effect, the values of v_p have been estimated using two different voltage levels: $V_{\Delta t} = 1$ mV, which is equivalent to an electric field of ~ 0.8 mV/cm and is near the onset of the transition; and $V_{\Delta t} = V_{\text{normal}}/2$, where V_{normal} corresponds to the voltage in the normal state of the sensed strand segment, i.e. $V_{\Delta t} \sim 15/2$ mV = 7.5 mV for a quench performed at operating current $I = 82$ A.

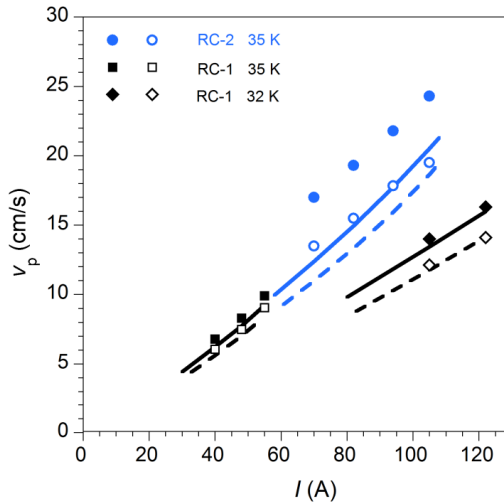


Figure 4. Quench propagation velocity in Rutherford cables RC-1 and RC-2 for different operating currents, I , and temperatures ($T_0 = 32$ K and 35 K). Symbols correspond to experimental values. Two set of data are given for each condition, corresponding to the values obtained using $V_{\Delta t} = 1$ mV (solid symbols) or $V_{\Delta t} = V_{\text{normal}}/2$ (open symbols), as explained in the text. Continuous lines are predictions by eq. (1), Wilson's model; and discontinuous lines by Dresner's formula, eq. (2).

Figure 4 displays v_p values obtained experimentally for cables RC-1 and RC-2 as a function of the operating current at different temperatures. The differences between v_p values estimated using both mentioned $V_{\Delta t}$ levels, range between 10 to 25 %.

During quench measurements of cable RC-1, it was observed that the zone of the cable at the right-hand side of the heater, around strand segment $d-i$, had lower critical current than the rest of the cable. Therefore, in this case, the time delay between voltages $V_0(t)$ and $V_2(t)$ were chosen to estimate v_p . For cable RC-2 it would be possible to use either $V_2(t)$ or $V_2'(t)$ to estimate global values of quench propagation velocities, and the differences between both values are also about 10-25% depending on the current. Although these are global values, the quench propagation velocity may have significant local variations, as evidenced by the time delay between voltages V_1 and V_1' seen in Figure 2(b). It must be remarked that this behaviour is not unique to these MgB₂ cables, since differences in the local propagation velocity across the strands have also been reported for Nb-Ti Rutherford cables [21].

Analytical predictions for quench propagation in superconductors have been given by several authors. Wilson's model [25] assumes one-dimension geometry of the conductor, which is represented during a quench by a normal conducting region adjacent to a superconducting region, with the transition between both at the temperature T_s . The temperature profile along the conductor is supposed to propagate at constant velocity, v_p , which in adiabatic conditions is given by:

$$v_p = \frac{I}{A} \frac{1}{c_v} \left(\frac{\rho_n k}{T_s - T_0} \right)^{1/2} \quad (1)$$

where A is the area of the cross section (m²), k the thermal conductivity (W/m K), c_v the heat capacity per unit volume (J/m³ K), and ρ_n the resistivity of the composite in the normal state (Ω m). T_0 is the initial temperature and $T_s = (T_c + T_g)/2$, is the mid-value between the critical temperature, T_c , and the temperature T_g , which is defined as the temperature at which the critical current equals the transport current, $I = I_c(T_g)$. Note that since T_g depends on the applied current, so does T_s . In Wilson's model, c_v and ρ_n are assumed constant (or averaged).

Similar equation is given by Dresner in [26], but in this case the strong temperature dependence of the specific heat is taken into consideration:

$$v_p = \frac{I}{A} \left(\frac{\rho_n k}{\Delta u_s c_v} \right)^{1/2} \quad (2)$$

where $\Delta u_s = u(T_s) - u(T_0)$ is the internal energy variation in the conductor, and k , ρ_n and c_v are values at the transition temperature.

In the cables analysed in this study, the predictions given by Wilson and Dresner show rather good agreement with the experimental values. It is worth noting that despite of the simplifying assumptions of these models, they give valuable estimations of propagation velocities, at least as first approximations, not only for wires and tapes [23] but also for cables [27]. For example, recent studies by Manfreda *et al* [27] in quench propagation along Nb₃Sn Rutherford cables concluded that predictions by Wilson's and Dresner's analytical

models give close approximations, although they tend to overestimate the experimental values, mainly at lower temperatures (1.9 K), whereas at 4.2 K they give more accurate predictions, especially when using Dresner's equation.

There are some aspects to consider in the analysis of the experimental estimations of v_p . Ideally, it is preferable to estimate quench propagation velocities farther away from the heater, which is even more relevant in Rutherford cables, as during the first stages of quench development different velocities can be obtained from different individual strands [21][27]. Nevertheless, in real experiments if longer distances from the heater are sensed to estimate v_p , the temperature of the hot-spot may also increase considerably depending on the sheath properties, and may cause the irreversible damage of the cable. In our experiments, maximum temperatures in the range between 50 K and 65 K, depending on the operating current, have been measured by the thermocouple (TC) during quench, without any apparent degradation of the cable. Nevertheless, the high electrical resistance of Cu10Ni alloy and the quasi-adiabatic conditions (sample in vacuum) result in an insufficient thermal stability of these cables, which are prone to deteriorate if transition to the normal state occurs during high current operation. Therefore the introduction of higher conductive sheaths would be beneficial in terms of thermal stability and robustness during operation. For example, RC-2 was damaged irreversibly during critical current measurement at 33 K (this test was performed after having measured all quench measurements at 35 K).

3.3 Quench induced by overcurrents

As previously mentioned, the observed inhomogeneities in quench propagation could be caused by small inhomogeneities in the cabling structure and/or in the local I_c 's of strands. In order to analyse this effect, we have measured quench induced by overcurrents in sample RC-2. In this experiment there is not any external heat source, and the cable eventually quenches when a current higher than I_c is applied. In contrast to the quench activated by local heat sources at $I < I_c$, for overcurrents the transition to the normal state would initiate in unknown regions and it will propagate from there to the rest of the cable. Ideally, the quench would occur in all strands almost simultaneously if the current is distributed uniformly in all them and if there is homogeneity in temperature, cable structure and local critical currents. On the contrary, a lack of homogeneity or the existence of a temperature gradient in the sample would cause the quench to initiate at the weakest points of the cable.

The time evolution of the voltages measured in the different parts of the cable RC-2 is plotted in Figure 5(a). In this experiment, the temperature of the cable was set to 35 K and, once stabilized, the current was increased up to $130 \text{ A} > I_c(35 \text{ K}) = 110 \text{ A}$ at the maximum rate allowed by the power supply. At $t = 0.4 \text{ s}$ the set current was reached and kept constant. The apparition of a voltage of $\sim 50 \mu\text{V}$, which becomes unstable due to self-heating, eventually produces a quench. The whole cable does not quench at the same time, instead the quench was first detected in the central part of the cable by the coincident onset and values of $V_0(t)$, $V_{0,b}(t)$ and $V_{\text{cable}}(t)$ curves. Shortly thereafter ($\sim 5 \text{ ms}$), the simultaneous onset of $V_2(t)$ and $V_1(t)$ marks the transition to normal state of these strand segments at the left-hand side of the cable. This is followed by the onset of $V_2(t)$ and finally by $V_1(t)$.

Remarkably, some voltages measured between two different strands, could be negative, as seen in Figure 5(a), behaviour also observed for cable RC-1. This is caused by the unequal quenching of the strands or strand segments, which causes local differences in $E(J)$ between them (being E the local electric field and J the

current density). In these cases, it is possible to measure transient negative voltages that will turn positive due to redistribution and transfer of current between strands and by the eventual transition to the normal state of the full sensed region.

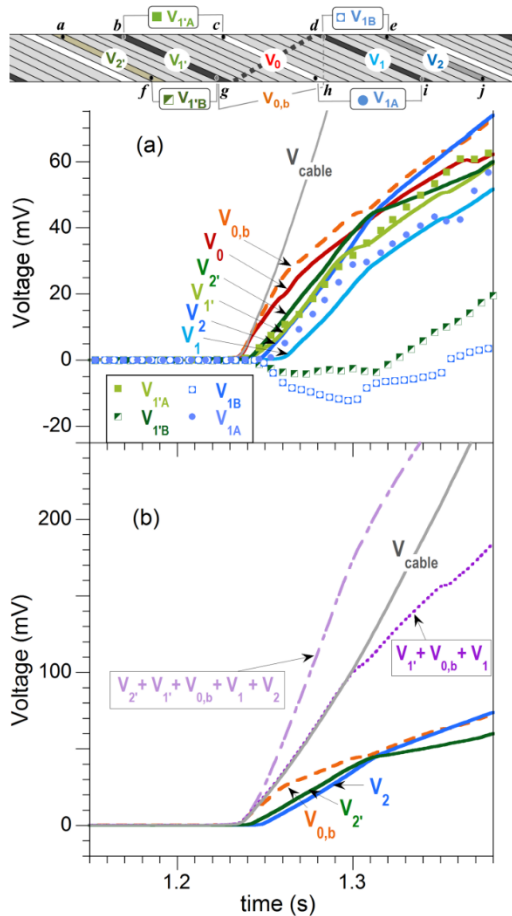


Figure 5. Time evolution of voltages measured in cable RC-2 at $T_0 = 35$ K and overcurrent $I = 130$ A $> I_c = 110$ A. (a) Voltages measured across strands (symbols defined in the inset), and along given strands (lines without symbols). (b) Comparison between the total voltage measured in the cable (V_{cable}) with the sum of different voltages measured in several strand segments.

Figure 5(b) shows the overall voltage in the cable, $V_{cable}(t)$, together with the sum of the voltages measured in several strand segments. Unlike the case of quench induced by a hot spot, shown in Figure 3(b), the overall voltage of the cable is not equal to the sum of these voltages in the full time interval. This is in agreement with the measurement of negative values for inter-strands voltages, thus indicating that the quench does not propagate from the centre towards the ends, but instead it is produced by the nucleation of many normal zones distributed within the cable, i.e. different strand segments would quench almost simultaneously in different parts of the cable.

4. Conclusions

The analysis of the quench behaviour of MgB₂ Rutherford cables has been presented. By careful measurement of the voltages measured along given strands and between strands, it is possible to analyse the quench dynamics in these cables under local hot-spots and due to overcurrents.

In the case of quench induced by a local heat disturbance, we have observed two different time scales in the quench development. First, a slow dynamics for the formation of a minimum propagating zone (MPZ), dominated by heat flow from the strand segments in contact with the heater to those at the bottom of the cable in contact with them. During this stage the heated strand segments are in the current-sharing regime, with the current shared between the superconducting core and the metal sheath. This time interval is considerably longer than for single conductors, which may be favoured by current redistribution among strands. Once a MPZ is developed, which is formed by segments of several strands, the quench propagates towards the ends of the cable in a shorter time scale.

The average quench propagation velocities estimated experimentally show a close correlation with the predictions given by one-dimensional-geometry models proposed by Wilson [25] and Dresner [26]. Nevertheless, there are important local variations of the quench propagation velocity across the strands near the hot-spot, also observed in LTS Rutherford cables. The presence of some inhomogeneities in the cable structure or local differences in $E(J)$ among strands could cause these variations, which have also been observed in the case of quench produced by overcurrents.

For quench induced by overcurrents, we observed almost simultaneous nucleation of many normal strand segments surrounded by superconducting ones in different parts of the cable. These normal regions grow and collapse, resulting eventually in the transition of the entire cable.

The high electrical resistance of Cu10Ni alloy and the quasi-adiabatic conditions result in an insufficient thermal stability of these cables, which are prone to deteriorate if transition to the normal state occurs during high current operation. The introduction of a higher conductive sheath in the strands would be beneficial to make these cables more robust during operation.

Acknowledgments

This work was supported by project ENE-2014-52105-R (from Spanish Ministerio de Economía, Industria y Competitividad and European FEDER Program) and by the Slovak Scientific Agency under the APVV-14-0522.

References

- [1] Bottura L and Godeke A 2012 Superconducting Materials and Conductors: Fabrication and Limiting Parameters *Reviews of Accelerator Science and Technology* **5** 25-50.
- [2] Barzi E, Andreev N, Boffo C, Borissov E, Elementi L, Del Frate L, Yamada R and Zlobin AV 2004 Development and study of Rutherford-type cables for high-field accelerator magnets at Femilab *Supercond. Sci. Technol.* **17** S213-S216

- [3] Fleiter J, Ballarino A, Bonasia A, Bordini B and Richter D 2017 Optimization of Nb₃Sn Rutherford Cables Geometry for the High-Luminosity LHC *IEEE Trans. Appl. Supercond.* **27** 4004305 (5pp)
- [4] Collings EW, Sumption MD, Scanlan RM, Dietderich, DR, Motowidlo LR, Sokolowski RS, Aoki Y and Hasegawa T, 1999 Bi:2212/Ag-based Rutherford cables: Production, processing and properties *Supercond. Sci. Technol.* **12** 87-96
- [5] Ha D-W, Kim S-C et al 2008 Study on Bi-2212 Rutherford Cabling Process for SMES *IEEE Trans. Appl. Supercond.* **18** 1192-1195
- [6] Hasegawa, T, Ohtani N, Koizumi T, Aoki Y, Nagaya S, Hirano N, Motowidlo L, Sokolowski RS., Scanlan RM, Dietderich DR and Hanai S 2001 Improvement of Superconducting Properties of Bi-2212 Round Wire and Primary Test Results of Large Capacity Rutherford Cable *IEEE Trans. Appl. Supercond.* **11**, 3034-3037
- [7] Kopera L, Kováč P, Hušek I and Melišek T, 2013 Rutherford cable made of single-core MgB₂ wires *Supercond. Sci. Technol.* **26** 125007 (6pp)
- [8] Kopera L, Kováč P, Kulich M, Melišek T, Rindfleisch M, Yue J and Hušek I 2017 Critical currents of Rutherford MgB₂ cables compacted by two-axial rolling *Supercond. Sci. Technol.* **30** 015002 (6pp)
- [9] Kario A, Vojenciak M, Grilli F, Kling A, Ringsdorf B, Walschburger U, Schlachter SI and Goldacker W 2013 Investigation of a Rutherford cable using coated conductor Roebel cables as strands *Supercond. Sci. Technol.* **26** 085019 (6pp)
- [10] Kim HJ, Seong KC, Cho JW, Bae JH, Sim KD, Kim S, Lee EY, Ryu K, and Kim SH 2006 3 MJ/750 kVA SMES System for Improving Power Quality *IEEE Trans. Appl. Supercond.* **16** 574-577
- [11] Ohsemochi K, Koyanagi K, Kurusu T et al 2006 Test Results of an Experimental Coil with Bi2212 Rutherford Cable for High Energy-density HTS-SMES *J. Phys.: Conf. Ser.* **43** 825
- [12] Awaji S, Watanabe K, Oguro H, Miyazaki H, Hanai S, Tosaka T and Ioka S 2017 First performance test of a 25 T cryogen-free superconducting magnet *Supercond. Sci. Technol.* **30** 065001 (8pp)
- [13] Campbell AM 1982 A general treatment of losses in multifilamentary superconductors *Cryogenics* **22** 3–16
- [14] Martínez E, Yang Y, Beduz C and Huang Y 2000 Experimental study of loss mechanisms of AgAu/PbBi-2223 tapes with twisted filaments under perpendicular AC magnetic fields at power frequencies *Physica C* **331** 216–226
- [15] Wilson MN 2008 NbTi superconductors with low ac loss: A review *Cryogenics* **48** 381-395
- [16] Terzieva S, Vojenciak M, Pardo E, Grilli F, Drechsler A, Kling A, Kudymow A, Gömöry F and Goldacker W 2009 Transport and magnetization ac losses of ROEBEL assembled coated conductor cables: measurements and calculations *Supercond. Sci. Technol.* **23** 014023 (8pp)
- [17] Ghosh AK, Sampson WB and Wilson MN 1996 Minimum quench energies of Rutherford cables and single wire *IEEE Trans. Appl. Supercond.* **7** 954-957
- [18] Willering GP, Werweij AP, Kaugets J and ten Kate HJJ 2008 Stability of Nb-Ti Rutherford cables exhibiting different contact resistances *IEEE Trans. Appl. Supercond.* **18** 1263-1266
- [19] Collings EW, Sumption MD, Susner MA, Dietderich DR, Krooshoop E and Nijhuis A 2012 Interstrand contact resistance and magnetization of Nb₃Sn Rutherford cables with cores of different materials and widths *IEEE Trans. Appl. Supercond.* **22** 6000904 (4pp)
- [20] Fleiter J, Bordini B, Ballarino A, Oberli L, Izqueirido S and Bottura L 2015 Quench propagation in Nb₃Sn Rutherford cables for the Hi-Lumi quadrupole magnets *IEEE Trans. Appl. Supercond.* **25** 4802504 (4pp)

- [21] Willering GP, 2009 "Stability of Superconducting Rutherford Cables for Accelerator Magnets" Ph.D. thesis, University of Twente, The Netherlands
- [22] Willering GP, Verweij AP, Ten Kate HHJ 2008 Current redistribution around the superconducting-to-normal transition in superconducting Nb-Ti Rutherford cables *J. Phys.: Conf. Ser.* **97** 012119
- [23] Martínez E, Lera F, Martínez-López M, Yang Y, Schlachter SI, Lezza P and Kováč P 2006 Quench development and propagation in metal/MgB₂ conductors *Supercond. Sci. Technol.* **19** 143-150
- [24] Ye L, Cruciani D, Xu M, Mine S, Amm K and Schwartz J 2015 Magnetic field dependent stability and quench behavior and degradation limits in conduction-cooled MgB₂ wires and coils *Supercond. Sci. Technol.* **28** 035015 (16pp)
- [25] Wilson MN, "Superconducting Magnets" 1983 (Oxford: Clarendon press)
- [26] Dresner L "Stability of superconductors (Selected topics in superconductivity)" 1995 Plenum Press, New York
- [27] Manfreda G, Bellina F, Bajas H and Perez JC 2016 Analysis of the quench propagation along Nb₃Sn Rutherford cables with the THELMA code. Part II: Model predictions and comparison with experimental results *Cryogenics* **80** 364–373

Publication B

Title:

Electromagnetic behaviour and thermal stability of a conduction-cooled, no-insulated 2G-HTS coil at intermediate temperatures

Journal:

Cryogenics

A. Cubero, A.B. Nuñez-Chico, R. Navarro, L.A. Angurel and E. Martínez

Published, Cryogenics 108 (2020) 103070 (9pp)

DOI: 10.1016/j.cryogenics.2020.103070

Impact factor (**JCR**, 2019): 1.818; Quartile Q3 (Physics, Applied)

SCImago Journal Rank (**SJR**, 2019): 0.606; Quartile Q2 (Materials Science)

A. Cubero, A.B. Núñez-Chico, R. Navarro, L.A. Angurel and E. Martínez, *Electromagnetic behaviour and thermal stability of a conduction-cooled, no-insulated 2G-HTS coil at intermediate temperatures*. *Cryogenics* 108 (2020) 103070 (9pp).

A double pancake coil has been wound with 2G-HTS tape without turn-to-turn insulation. Glued to a copper plate, the coil has been thermally anchored to the cryocooler cold finger and cooled by conduction. Its electromagnetic behaviour and thermal properties have been analysed during several thermal cycles, being fed with high currents at different temperatures in the range between 5 K and 77 K, with special focus for temperatures above 30 K. Charge and discharge characteristics, loss contributions during current ramps and critical current measurements and numerical estimations have been analysed. Moreover, the thermal contact conductance between the different parts of the coil have been measured and discussed. My contribution to this work has been related to the coil fabrication, the experimental procedures and formal analysis, together with the writing cooperation.

Electromagnetic behaviour and thermal stability of a conduction-cooled, no-insulated 2G-HTS coil at intermediate temperatures

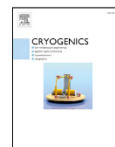
Cryogenics 108 (2020) 103070



Contents lists available at ScienceDirect

Cryogenics

journal homepage: www.elsevier.com/locate/cryogenics



Research paper

Electromagnetic behaviour and thermal stability of a conduction-cooled, no-insulated 2G-HTS coil at intermediate temperatures



A. Cubero, A.B. Núñez-Chico, R. Navarro, L.A. Angurel, E. Martínez*

Instituto de Ciencia de Materiales de Aragón (CSIC – Universidad de Zaragoza), C/ María de Luna 3, 50018 Zaragoza, Spain

ARTICLE INFO

Keywords:

Superconductor
HTS no-insulation coils
Conduction-cooling
Thermal stability
Thermal contact conductance
Coil losses

ABSTRACT

The electromagnetic and thermal properties of a double pancake coil made of second generation high temperature superconductor, 2G-HTS, have been studied. The coil was wound with no-insulation between turns (NI coil) and was later impregnated with epoxy resin and glued to a copper support plate. The coil was thermally anchored to the cryocooler cold finger and cooled by conduction. After several thermal cycles no degradation of its superconducting properties was observed.

The coil was operated under high vacuum and high currents (up to 400 A in steady conditions) at different temperatures in the range between 5 K and 77 K, with special focus on the analysis above 30 K. The charge and discharge characteristics, and the experimentally measured and numerically estimated critical currents, have been studied. The different loss contributions during current ramp and the thermal contact conductance between different parts of the double pancake coil have been measured. The implications of these two factors on the thermal stability and the behaviour of the whole cryogenic system are discussed.

1. Introduction

Superconducting coils based on high temperature superconductors (HTS) are of great interest for their possible use in electric power applications, such as superconducting generators, motors, magnetic energy storage systems, etc. [1–4]. Also they may offer important advantages compared to low-temperature superconducting (LTS) coils. Some examples of traditional and well-established LTS applications are resonance magnetic imaging, nuclear magnetic resonance and high-energy particle accelerators. HTS would allow higher operating temperatures or magnetic fields, eliminating the requirement of liquid helium in certain commercial applications [5–7].

Superconducting magnets may suffer from quench during operation, that is, the irreversible superconducting-to-normal transition of the coil, which could cause a permanent damage if it is not appropriately handled. No-insulated (NI) coils, without turn-to-turn insulation, have been the subject of intense research in the last few years [8–15], especially those based on second generation high temperature superconductors, 2G-HTS. NI coils reach greater compactness than the standard ones, and are more robust against thermal instabilities [16]. Thus, they would enable safer operation at large currents, preventing possible coil degradation in case of quench. On the contrary, they present a delay between the field and the current ramp that can be a drawback for certain applications.

Since HTS and MgB₂ coils are usually designed to operate at temperatures above 20 K, they can be cooled by direct thermal contact with the cryocooler cold head [10,13,14,17–20]. Thus, no liquid helium would be needed, unlike traditional low temperature superconducting magnets, although cryogen-free LTS working at 4–10 K [21,22] as well as hybrid magnets [23–24] have also been built and tested. Achieving high thermal conductance values between the cryocooler and the whole system, including current leads and current contacts, is crucial. Otherwise, thermal runaway can occur if the system is not sufficiently thermalized. Since this is more critical for high operating currents, the range of 100–200 A has been usually chosen for conduction-cooled HTS magnets [10,13,14,17–19]. Nevertheless, due to the high price of the HTS conductors, increasing the operating current even at the expense of certain reduction in the operating temperature, would reduce the cost, as less length of conductor would be necessary.

The aim of the present work is to analyse the superconducting behaviour of a 2G-HTS NI double pancake coil and its thermal stability under conduction-cooling conditions. The coil has been energized with high currents, up to around 450 A, and operated at variable temperatures, focusing on intermediate temperatures between 30 K and 60 K. The critical current values have been estimated numerically and compared with the experimental values. The characteristic parameters of the coil as a function of the temperature, such time constants during

* Corresponding author.

E-mail address: elenamar@unizar.es (E. Martínez).

<https://doi.org/10.1016/j.cryogenics.2020.103070>

Received 28 October 2019; Received in revised form 6 March 2020; Accepted 16 March 2020

Available online 23 March 2020

0011-2275/© 2020 The Author(s). Published by Elsevier Ltd. This is an open access article under the CC BY-NC-ND license (<http://creativecommons.org/licenses/by-nc-nd/4.0/>).

Table 1
Characteristics of the 2G-HTS tapes and double-pancake coil.

Conductor used	2G-HTS, SuperPower Inc SCS4050-AP Ref. M4-180-4 0508
Width (w)/Thickness/Total length	4 mm/163 μm /14 m
Coil geometry	Round, double pancake
Impregnation	Stycast 1266 (after dry winding)
Insulation between turns	Bare
Diameter inner/outer (D_{in}/D_{out})	67 mm/77 mm
Distance between pancake coils	1 mm
Number of turns	30×2
Magnetic field per ampere at centre	0.985 mT/A (Experimental) 1.035 mT/A (Simulation)
Max. field per ampere in the winding	3.5 mT/A (Simulation)
Inductance, L	0.386 mH (Experimental) 0.406 mH (Simulation)

charge and discharge tests, as well as the characteristic resistance of the coil, have been analysed. The effect of thermal cycling in the superconducting and thermal properties of the coil has also been analysed.

2. Experimental

2.1. Characteristics of the double pancake 2G-HTS coil

A double pancake (DP) coil, without electrical contact resistance between both pancake coils, was manufactured using 2G-HTS conductors provided by SuperPower Inc. The main characteristics of the used tape and fabricated coil are collected in Table 1. The conductor has a critical current $I_c = 124$ A at 77 K and self-field. It has a width of 4 mm and a total thickness of 163 μm (including the 50- μm Hastelloy substrate and 110- μm total thickness of copper stabilizer). Each pancake coil has 30 turns and the distance between the upper and lower coil is 1 mm. The coil was dry-wound around a 304L stainless steel cylinder of 67 mm diameter and 0.3 mm thickness, which acts as mechanical support. No-insulation between turns was used. During winding, several thin copper sheets were soldered to the HTS conductor to easily solder voltage taps and thermocouples after coil fabrication. Subsequently, it was impregnated with Stycast-1266 epoxy resin, which has low viscosity. Stycast-2850 FT, which has higher thermal conductivity and viscosity, was used to glue the DP coil to a 2-mm thick copper plate and to fill the gap between both pancake coils. The copper support plate was mechanically anchored to the second stage of the cryocooler ensuring a good thermal contact between them.

The coil was instrumented using several voltage taps and two thermocouples, as shown schematically in Fig. 1. The measured voltages are

named as follow. V_{COIL} is the total voltage of the DP coil; V_{Low} and V_{Up} the voltages of the lower and upper pancake coils, respectively. The voltage of the innermost turn (#1) of the upper pancake coil, $V_{\text{U-1}}$, was also measured to rule-out any possible damage during fabrication.

A Hall probe is installed at the centre of the DP coil to measure the axial magnetic field, B_{centre} . Two thermocouples, TC-up and TC-low, were placed in the outermost turns of the upper and lower pancake coils, respectively. Moreover, to measure the thermal contact conductance between both pancakes and between the lower coil and the copper support plate, a manganin heating wire with resistance of 5 Ω was glued to the top surface of the coil using GE varnish, as shown in Fig. 1(b).

2.2. Experimental set-up

An experimental set-up was developed to test superconducting devices cooled by conduction at variable operating temperatures and currents up to 500 A. The analysed devices are in high vacuum and thermally anchored to the second stage of a cryocooler (SRDK-415D, Sumitomo). The system enables variable operating temperatures, T , from 5 K to 77 K, controlled by means of an additional heater and a Lakeshore temperature controller.

The voltages between different taps of the coil and current leads, the Hall probe and thermocouple signals were recorded using a data acquisition device, which is controlled by a LabView program. Two Agilent DC power supplies were used for these experiments, one provides maximum currents and voltages of 100 A and 20 V, and the other of 875 A and 5 V.

2.3. Current leads

Current leads, which connect room temperature (RT) to the coil, were designed to work in vacuum at operating currents up to 400 A (in steady conditions) and at 500 A (for pulses of several seconds). In order to minimize the heat input into the superconducting device, each current lead has three sections whose ends are connected by bolted joints that are thermally anchored to three heat sinks per lead, HS0, HS1 and HS2, as it is shown in Fig. 2(a). Electrical insulation is achieved by coating the Cu with an alumina layer. HS0 is thermally anchored to the 2nd stage of the cryocooler (cold finger) and HS1 to the 1st stage. The coldest section of the current lead (between HS1 and HS0 sinks) is a commercial HTS current lead from HTS-110, made from 1st generation HTS wires with an alloyed matrix used to minimise the thermal conductivity. The other sections were fabricated with copper. A small liquid nitrogen (LN) vessel was built inside the cryostat to add some extra

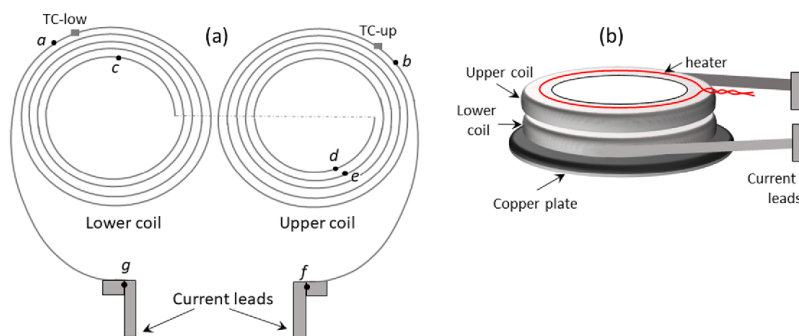


Fig. 1. (a) Scheme of the voltage tap positions and thermocouples within the double pancake coil (only few turns are drawn for clarity purposes). Both points connected by the discontinuous line in this drawing correspond to the same point in the real DP coil. The voltage of the total coil, V_{COIL} , was measured with taps a and b; voltages of the upper (V_{Up}) and lower (V_{Low}) pancake coils with taps d-b and a-c, respectively. $V_{\text{U-1}}$ (d-e) is the voltage of turn #1 (the innermost turn) of the upper coil. (b) Schematic 3D view of the DP coil with the heater glued at the top surface of the coil.

Electromagnetic behaviour and thermal stability of a conduction-cooled, no-insulated 2G-HTS coil at intermediate temperatures

A. Cubero, et al.

Cryogenics 108 (2020) 103070

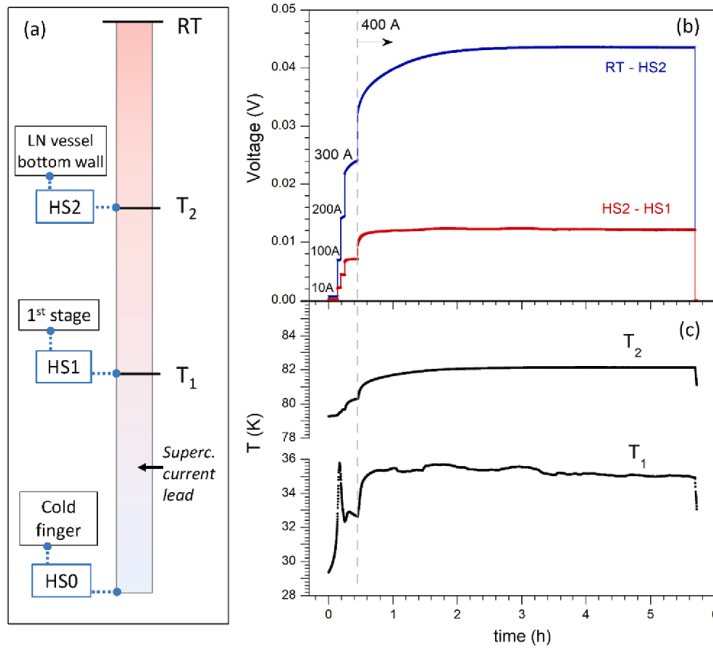


Fig. 2. (a) Scheme of the thermal links of each current lead with the heat sinks HS2, HS1 and HS0. (b) Time evolution of the voltages measured in the current lead copper sections between room temperature (RT) and HS2, and between HS2 and HS1 for DC applied currents up to 400 A. (c) Temperatures $T_2(t)$ and $T_1(t)$ measured at the positions of the current lead in thermal contact to HS2 and HS1 sinks, respectively.

refrigeration power, since the cooling power of the used cryocooler is not sufficient to achieve temperatures below 70–77 K in the 1st stage, for currents of 500 A. Note that the theoretical minimum heat input value of a metal current lead between 300 K and 77 K in vacuum conditions is ≈ 0.04 W/A (per lead) [25]. The sink HS2 is in thermal contact with the LN vessel, bolted to the outer surface of the bottom of the vessel, i.e. it is neither immersed in the liquid nor cooled by interchange gas.

Considering Ekin predictions [25] and using finite element software COMSOL, the current leads were optimised for steady operating currents of 400 A. The warmer section of each current lead consists of a copper cylinder (25 cm length, 1 cm diameter) soldered to a copper braided wire (13 cm length, 25 mm² cross sectional area), which ends in HS2. The part between HS2 and HS1 is a Cu braided wire of 30 cm length and 25 mm² section. At 400 A, the estimated heat inleak values into the heat sinks HS2 and HS1 are 14.7 W and 5 W, respectively, per lead. Moreover, the numerically calculated heat loads in each lead due to ohmic losses are 15 W (in the lead section between RT and HS2), and 3.5 W (between HS2 and HS1 heat sinks).

Different experiments were performed to test the current leads before measuring the superconducting coil. Fig. 2 shows the time evolution of voltages in the current lead copper sections and temperatures $T_1(t)$, and $T_2(t)$, measured in the lead at the thermal joints to HS1 and HS2, respectively, for different values of the applied current ranging from 10 A to 400 A. It is observed that the system achieves steady conditions, although the equilibrium in the section between HS2 and HS1 is reached considerably faster than in the warmer section (between RT and HS2). The larger temperature differences between this lead section ends, together with the greater copper mass and the higher heat capacity of the warmer section, explain this behaviour. Therefore, this would be the most critical part of the current lead. The smooth evolution of $T_2(t)$ for all applied currents contrasts with the oscillations of $T_1(t)$, which might be due to refrigeration fluctuations of the cryocooler

compressor. These fluctuations were not observed in the second stage and do not affect the thermal stability of system. The current is kept constant by the power supply.

At equilibrium conditions, the measured heat loads due to ohmic losses at 400 A were 17.5 W per lead (in the section between RT and HS2) and 4.8 W (between HS1 and HS2). These values are of the order but systematically higher than the numerical predictions, probably due to underestimations of the electrical contact resistances between the different sections of the lead. The values of the thermal contact conductance of the electrically insulated joints at the heat sinks, h_j , have been estimated as:

$$h_j = \frac{1}{A_c} \frac{\dot{Q}}{\Delta T}, \quad (1)$$

where \dot{Q} is the numerically calculated total heat inleak into the heat sink, ΔT is the measured temperature difference across the thermal joint in steady state conditions, and A_c is the contact area of the joint. We have obtained values of $h_j \approx 850$ and 1800 W m⁻² K⁻¹ for HS1 ($A_c = 20$ cm²) and HS2 ($A_c = 17$ cm²), respectively.

3. Results and discussion

3.1. Charge and discharge tests

Charge and discharge tests of the coil have been performed at operating temperatures from 5 K to 77 K and currents well below I_c . A typical test at two different current ramp rates (10.3 A/s and 3.4 A/s) is displayed in Fig. 3. Once reached the set current of 98 A, it was kept constant during several seconds and, subsequently, switched-off (sudden discharge).

The electrical behaviour of the NI coil has been modelled [9] by a simple equivalent circuit consisting of two impedances in parallel, and thus the applied current, $I(t)$, divides in two paths: One carries the

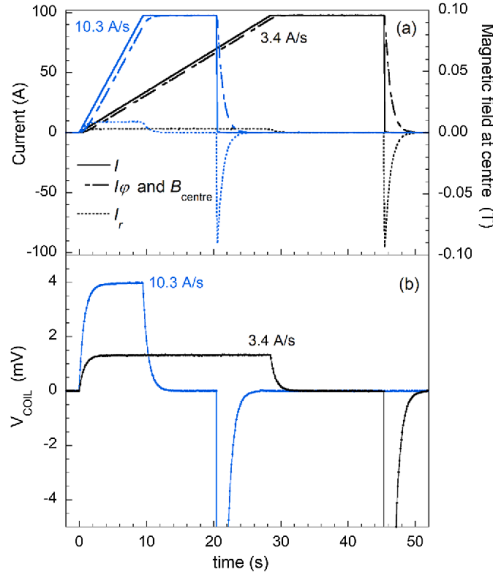


Fig. 3. Charge and discharge tests of the NI coil at 30 K, up to 98 A, for two different charging rates (10.3 and 3.4 A/s): (a) Applied current, $I(t)$, axial magnetic field at the coil centre, $B_{\text{centre}}(t)$, and estimated $I_{\phi}(t)$ and $I_r(t)$ curves. (b) Coil voltage $V_{\text{COIL}}(t)$ measured during the experiment. Note that the scale has been cut-off for better observation of the voltage during charge.

current along the spiral conductor path, $I_{\phi}(t)$, and its impedance is given by the coil self-inductance, L , in series with a current-variable resistance, $R_{\phi}(I_{\phi})$. The other is the equivalent resistance, R_r , which would be mainly determined by the turn-to-turn electrical contacts and carries the current in the radial direction of the coil, $I_r(t)$. The Kirchhoff and charge conservation laws relate the parameters of the equivalent circuit to $I(t)$ and the coil voltage, $V_{\text{COIL}}(t)$, by Eqs. (2)–(3). Due to the axial symmetry of the coil, $I_r(t)$ does not contribute to the magnetic field, and, in consequence, the magnetic field is proportional to I_{ϕ} , Eq. (4). The constant k is fixed by the geometry of the coil and does not change with temperature.

$$V_{\text{COIL}}(t) = R_r I_r(t) = L \frac{dI_{\phi}(t)}{dt} + R_{\phi}(I_{\phi}) I_{\phi}(t) \quad (2)$$

$$I(t) = I_r(t) + I_{\phi}(t) \quad (3)$$

$$I_{\phi}(t) = \frac{B_{\text{centre}}(t)}{k} \quad (4)$$

The current dependence of $R_{\phi}(I_{\phi})$ is caused by current sharing between the thin superconductor layer and the metallic components of the 2G-HTS tape conductor. It takes into account the non-linear I - V behaviour of the superconductor and the ohmic resistance of the metallic components [8,9].

According with these equations, k was firstly determined experimentally from the magnetic field at the coil centre, B_{centre} , measured at constant current and steady conditions ($I_{\phi} = I$), obtaining $k = 0.985(5)$ mT/A for the analysed DP coil. $I_{\phi}(t)$ was derived from Eq. (4); and $I_r(t)$ using Eq. (3). Finally, from $I_{\phi}(t)$ and $I_r(t)$, the values of L and R_r can be estimated from the experimental $V_{\text{COIL}}(t)$ values using Eq. (2).

The $B_{\text{centre}}(t)$, $I(t)$ and $V_{\text{COIL}}(t)$ curves directly measured, and $I_{\phi}(t)$ and $I_r(t)$ currents derived from the above equivalent circuit equations, are displayed in Fig. 3. The higher the current ramp rates, the larger the

maximum values of $I_r(t)$, in consonance with longer time delays between $I(t)$ and $B_{\text{centre}}(t)$. For these conditions, the maximum I_r values were 9 A and 3 A for 10.3 A/s and 3.4 A/s, respectively. Moreover, values of $L = 0.386$ mH and $R_r = 0.44$ m Ω were estimated at 30 K. During the linear ramp, after a transient, $V_{\text{COIL}}(t)$ becomes constant, with values increasing proportionally with the applied current ramp rate. When the set current is reached, after a similar transient time, $B_{\text{centre}}(t)$ becomes constant and $V_{\text{COIL}}(t)$ zero, indicating that all the current flows through superconducting paths, with the entire coil below I_c .

The sudden switch-off of the applied current, which has a characteristic time constant of about 10 ms, produces an exponential decay of $B_{\text{centre}}(t)$ with much larger time constants, $\tau \approx 860$ ms at 30 K. It also produces sharp negative peaks of the coil voltage ($V_{\text{COIL}} \approx -60$ mV in this case) and turn-to-turn flowing current inverse to I_{ϕ} ($I_r = -I_{\phi} = -98$ A), followed by an exponential relaxation (Fig. 3). In these conditions, the sudden coil discharge produced a temperature rise of ≈ 0.5 K (measured by the thermocouple TC-up).

For further analysis of the adequacy of the used equivalent circuit, it is interesting to evaluate the electric energy loss, $Q_{\text{loss}}(t)$, given by:

$$Q_{\text{loss}}(t) = Q_{\text{in}}(t) - Q_{\text{m}}(t) \quad (5)$$

where $Q_{\text{in}}(t)$ is the energy supplied to the coil from the beginning of the current ramp ($t = 0$) to the time t ; and $Q_{\text{m}}(t)$ is the magnetic energy stored in the coil at time t :

$$Q_{\text{in}}(t) = \int_0^t V_{\text{COIL}}(t) I(t) dt \quad (6)$$

$$Q_{\text{m}}(t) = \frac{1}{2} L I_{\phi}^2(t) \quad (7)$$

Moreover, the energy dissipated by the currents flowing in the radial direction during the ramp is estimated by:

$$Q_r(t) = \int_0^t \dot{Q}_r(t) dt = \int_0^t R_r I_r^2(t) dt \quad (8)$$

Fig. 4 shows $Q_{\text{loss}}(t)$, $Q_{\text{in}}(t)$, $Q_{\text{m}}(t)$ and $Q_r(t)$, calculated using Eqs. (5)–(8) from the measurements at 30 K, ramp rate of 10.3 A/s up to 98 A, already displayed in Fig. 3. It is worth mentioning the good correspondence between $Q_{\text{loss}}(t)$ and $Q_r(t)$. This behaviour, which was also observed for ramp rate of 3.4 A/s, indicates that the main energy loss contribution during charging is due to the turn-to-turn current, whereas the magnetization loss [26] is negligible for these conditions. The electric energy loss during the whole ramp up to 98 A decreases from 0.3 J (for 10.3 A/s) to 0.11 J (for 3.4 A/s). The power losses due to turn-

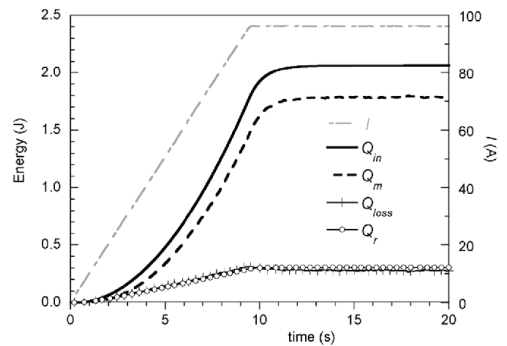


Fig. 4. Total energy supplied to the coil at 30 K, $Q_{\text{in}}(t)$, energy loss, $Q_{\text{loss}}(t)$, magnetic energy stored in the coil, $Q_{\text{m}}(t)$, and energy dissipated by the currents flowing in the radial direction, $Q_r(t)$, when the current is linearly ramped up to 98 A at 10.3 A/s, calculated using Eqs. (5)–(8) from the experimental results in Fig. 3.

Electromagnetic behaviour and thermal stability of a conduction-cooled, no-insulated 2G-HTS coil at intermediate temperatures

A. Cúbero, et al.

Cryogenics 108 (2020) 103070

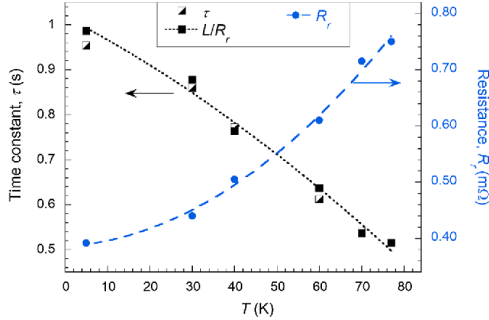


Fig. 5. Temperature dependence of the exponential decay time constant, τ , of the magnetic field, B , in case of sudden discharges of the coil; equivalent radial resistance, R_r , estimated experimentally during coil charging; and corresponding L/R_r values for $I < I_c$. Dashed and dotted lines are 2nd order polynomial fits to guide the eye.

to-turn current, \dot{Q}_t , reach maximum values of 36 mW (for 10.3 A/s) and 4 mW (for 3.4 A/s) during the same ramp. The balance between the electric power loss and the conduction cooling power results in a small temperature increment of 0.1 K (measured by TC-up) at the end of the current ramp up to 98 A for the rate of 10.3 A/s, but no temperature increase was measured for 3.4 A/s. This is the reason why the latter was chosen to estimate experimentally the critical current of the coil, as it will be seen in Section 3.3.

The time constant $\tau(T)$ obtained from the magnetic field decay for sudden discharges of the coil at different temperatures is plotted in Fig. 5, together with the equivalent resistance $R_r(T)$ and the $L/R_r(T)$ ratio estimated from Eqs. (2)–(4). Since the experimentally obtained L values are almost constant between 5 K and 77 K ($L = 0.386$ mH, $\pm 2\%$), the temperature variation of the characteristic time constant $\tau(T)$ is only due to $R_r(T)$. Note that $R_r(T)$ almost doubles from 5 K to 77 K, in good agreement with the reported temperature dependence of electric contact resistance between two single 2G-HTS tapes [27].

From the deduced equivalent resistance in the radial direction R_r , it is possible to estimate the turn-to-turn electrical contact resistance, R_t , assuming that this is homogeneous for all turns, so that:

$$R_r = 2 \sum_{t=1}^N \frac{R_t}{2\pi r_t w} \quad (9)$$

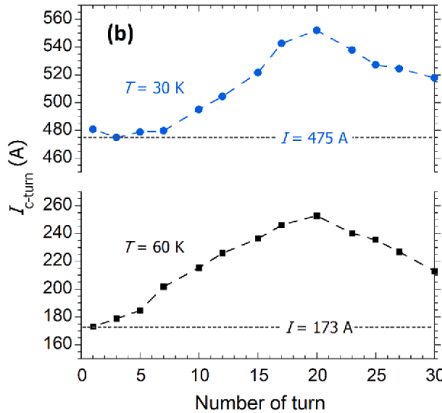
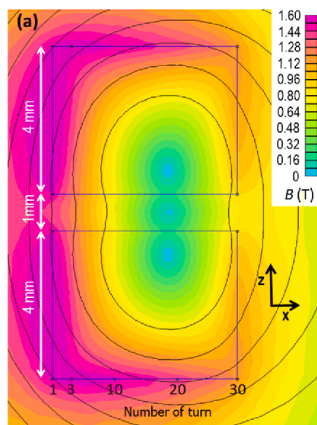


Fig. 6. (a) Magnetic field distribution and flux line plot of the DP coil for $I = 475$ A, calculated using FEMM software considering uniform current densities. Turns “1” and “30” correspond to the innermost and the outermost turns, respectively. (b) Critical currents of several turns, $I_{c\text{-turn}}$, calculated at 30 K and 60 K for applied currents of 475 A and 173 A, respectively.

where N is the number of turns of each pancake, r_i is the radius of i -turn and w is the tape width. At 77 K, the obtained $R_r = 0.74 \pm 0.01$ m Ω , would then correspond to $R_t \approx 110$ $\mu\Omega$ cm 2 .

The values of R_r for NI coils would depend on many factors, such as the tape surface condition (oxidation and roughness), the use of metal cladding between turns, the resin impregnation or the winding tension [9,11,13,26,27]. At 77 K, reported R_r values typically range between 10 and 100 $\mu\Omega$ cm 2 . The estimated value obtained in this work is thus in this range, but in the upper bound, probably due to the use of Stycast after winding, although this does not alter significantly the behaviour observed for non-impregnated coils.

3.2. Numerical estimation of the coil critical currents at different temperatures

For design purposes, as well as to prevent damaging the coil during testing, it is very useful to have an estimation of the expected critical currents of the coil at different temperatures. The load-line method has been commonly used in LTS coils to calculate their critical current [28]. This method compares the calculated maximum magnetic field in the winding at different operating currents, with the $I_c B$ isotherms measured in a single conductor. By plotting these values together, the crossing points would give the coil’s critical current value at each temperature. In case of HTS, this procedure is not as straightforward as in LTS. This is because critical current of HTS does not only depend on the magnitude of the magnetic field, B , but also on the orientation of this field with respect to the tape surface, θ . Moreover, $I_c(\theta)$ depends on temperature and field [29].

Different methods have been proposed to estimate the critical current of HTS coils [29–31]. In this work, we used a method similar to the so-called “modified load-line method” in [31], which takes into account the anisotropy of the superconductor. As for the conventional load-line method, the first step is to calculate the magnetic field inside the winding for a given applied current, I , assuming that the current distributes uniformly in the winding. Fig. 6(a) shows the magnetic flux lines and the field amplitude inside the winding calculated for $I = 475$ A. As it is observed in the figure, for a particular turn (fixed x value), the amplitude and orientation of the magnetic field vary significantly along the z direction, i.e. along the width of the tape. The field gradient across the tape thickness, d , was not considered here because, due to the geometry of these conductors ($d \ll w$), it would be much less relevant. For each turn, $B(z)$ and $\theta(z)$ curves can be obtained from Fig. 6(a) for a given operating current. With these data and by using the dependence on (B, θ, T) of the critical current per unit width, I_c/w , previously

measured in a similar short sample (SuperPower Inc, SCS4050-AP, M4-134-3) [32], the local $I_c(w)(z)$ values can be calculated for each turn. The integration of these values along the width of the tape would give an estimation of the critical current of each turn, $I_{c\text{-turn}}$. Note that this assumption is an approximation to the critical state model behaviour. This process is repeated for different current values. Analogously to the standard load-line method, the minimum of all $I_{c\text{-turn}}$ values, coincident with the applied current, would give the critical current of the coil.

Fig. 6(b) shows the calculated critical currents of several turns at temperatures of 30 K and 60 K and applied currents $I = I_c = 475$ A and 173 A, respectively. It must be remarked that in both cases the innermost turns limit the critical current of the coil. This is because this region has the lower local critical currents, whereas the coil zone around turn number 20 has the highest critical current, which coincides with the lowest magnetic field region. Similar behaviour has been observed experimentally in single pancake coils fabricated with similar coated conductors [33]. As it can be seen in the figure, the distribution of local critical currents inside the winding depends on the temperature, because so does $I_c(B, \theta)$. It is worth mentioning that although for self-field conditions, as considered here, the innermost turns become typically critical before the rest of the coil, this is not always the case for 2G-HTS coils due to the relevance of the specific $I_c(B, \theta)$ behaviour of the used tape [31]. The validity of the assumptions used in the modeling will be discussed further below.

3.3. Experimental critical currents of the DP coil at different temperatures

To estimate experimentally the critical current of the coil, the current was ramped up at rates of 3.0 or 3.3 A/s up to a set value, held constant for several seconds and subsequently set to zero. The voltages in different regions of the coil were measured during these experiments, which were performed at different temperatures from 70 K down to 30 K. At each temperature, several current ramps were applied. The maximum current of the ramp was increased progressively in different runs. If the ramp current exceeds the local critical current in any part of the winding, a significant increase in the coil voltage will be measured. In this case, a resistive component of the coil voltage will be seen when the current is held constant after the ramp, unlike the purely inductive behaviour observed in Fig. 3(b) when the applied current is well below I_c .

As an example of this behaviour, Fig. 7 displays the obtained results when ramping the current up to 159 and 447 A, at 60 K and 30 K, respectively. The figure shows the applied current; the magnetic field at coil centre; the voltages $V_{\text{Up}}(t)$, $V_{\text{Low}}(t)$ and $V_{\text{U-1}}(t)$; and temperature $T_{\text{Up}}(t)$, measured by the thermocouple placed in the upper coil.

As it is seen in Fig. 7(b) and (f), when ramping-up the current, the voltages measured in the upper and lower coils have initially an inductive component (with almost constant values of about 0.6 mV). But once reached a certain current value during the ramp, voltage $V_{\text{Up}}(t)$ increases significantly, indicating that the applied current has exceeded the local critical current in this part of the coil. These resistive signals can be easily visualised when the current is held constant after the ramp. In the conditions of Fig. 7, resistive signals were observed in fact in both pancakes, but with V_{Up} always considerably higher than V_{Low} , which indicates that the upper coil has lower critical current than the lower one. For example, at 60 K and 159 A, $V_{\text{Up}} \approx 280$ μV and $V_{\text{Low}} \approx 25$ μV were measured (Fig. 7(b)). Besides, the voltage of the innermost turn of the upper coil, $V_{\text{U-1}}(t)$, also shows a transition to the resistive regime during the ramp, with $V_{\text{U-1}} \approx 31$ μV after the ramp (Fig. 7(c)), which is significantly smaller than V_{Up} . This indicates that several turns are above their local I_c values, especially at low temperatures, which is in agreement with numerical estimations of Fig. 6(b), showing several turns with similar $I_{c\text{-turn}}$ in the inner part of the coil. Note that at 60 K, there was a small irregularity in the current ramp linearity at $t \approx 54.4$ s, which produced an additional inductive contribution in the voltages, without further consequences.

Fig. 7(d) and (h) shows the time evolution of the temperature $T_{\text{Up}}(t)$

during the experiments at 60 K and 30 K, respectively. In the first case, the temperature remains constant during most of the current ramp, but begins to increase in the later stages of the ramp and continues rising when the current is kept constant. The appearance of resistive losses when current exceeds the local critical current caused a coil temperature increment $\Delta T_{\text{Up}} \approx 0.3$ K during the entire experiment. Note that the increase of $T_{\text{Up}}(t)$ finishes at the beginning of coil discharge, with a delay of about 4–6 s, which is also observed in the experiment at 30 K.

At 30 K, there is no appreciable temperature increase in the initial stages of the ramp ($t < 55$ s, $I < 150$ A), but later the temperature starts rising and reaches $\Delta T_{\text{Up}} \approx 0.3$ K at $t \approx 135$ s ($I \approx 420$ A). Finally, T_{Up} increases sharply, and so does V_{Up} . In order to further analyse the behaviour of the coil at 30 K, Fig. 8 shows the time dependence of the total energy provided to the coil during the ramp, $Q_{\text{in}}(t)$, together with other relevant energy curves, $Q_{\text{loss}}(t)$, $Q_{\text{in}}(t)$ and $Q_{\text{t}}(t)$, calculated using Eqs. (5)–(8). In this case, it is clearly seen that $Q_{\text{loss}}(t)$ is higher than the turn-to-turn loss contribution, $Q_{\text{t}}(t)$. For example, at the end of the current ramp $Q_{\text{loss}} = 2.75$ J while $Q_{\text{t}} = 0.46$ J. As it is shown in the inset of Fig. 8, this is because the loss power produced in the superconducting tapes, \dot{Q}_{sc} , becomes relevant for these conditions, where:

$$\dot{Q}_{\text{sc}}(t) = \left(V_{\text{COIL}}(t) - L \frac{dI_{\text{p}}(t)}{dt} \right) I_{\text{p}}(t) = R_{\text{p}}(I_{\text{p}}) I_{\text{p}}^2(t) \quad (10)$$

For the slow current ramp used here, this loss power component becomes increasingly relevant upon increasing the current. For $I < I_c$, this term gives the losses produced in the superconductor, which is subjected to variable current and variable magnetic field during the ramp. When the current is close or exceeds the critical current, the resistive contribution of the metallic elements of the tapes is added [26]. On the contrary, \dot{Q}_{t} remains almost constant ≈ 4 mW during the ramp. This would explain the coil heating observed in Fig. 7(h), in contrast with the case analysed in 3.1, when at the same temperature and ramp rate, but with applied currents well below the critical current of the coil, the temperature of the coil remained constant.

As expected, at 30 K the heating of the coil is more important than at 60 K. This is caused by several factors. In one hand, at 30 K the applied currents are much higher than at 60 K (with similar coil voltages). On the other hand, upon decreasing the temperature, the heat capacity decreases and the absolute thermal resistance increases, as it will be further analysed in the next section. Nevertheless, it must be remarked that resistive coil voltages above 250 μV and high applied currents were held for several seconds without triggering a quench.

Critical currents of superconductors are usually defined using the 1 $\mu\text{V}/\text{cm}$ criterion. However, due to the uneven magnetic field distribution inside the coil, it should be preferable to use more restrictive criteria to define I_c [30,31], otherwise some regions may be well below their local I_c while others can withstand high voltages, which can cause local hot spots and, eventually, produce irreversible damage to the coil.

Fig. 9 compares the coil critical current values obtained experimentally using the 0.1 $\mu\text{V}/\text{cm}$ criterion and the $I_c(T)$ values estimated with the modified load-line method explained in Section 3.2. It is worth noting the good correspondence between experimental and estimated values, with almost identical temperature dependence but with experimental values about 10% lower than numerical estimations. Some of the assumptions considered in the model could explain the observed differences: i) The current was assumed uniformly distributed in the winding, but in reality the differences of $I_c/w(z)$ would produce a re-distribution of the current across the tape's width, which would then affect the magnetic field distribution in the winding [31]. ii) The $I_c(B, \theta)/w$ dependence was assumed to be independent of w . iii) In the numerical calculation, the lift factors, $I_c(T, B, \theta)/I_c(77 \text{ K, self-field})$, have been obtained from experimental results measured in a different short sample [32]. That tape corresponds to the same type (SCS4050-AP) and was produced in the same reactor (M4), as the conductor used in this work. Nevertheless, several groups have reported differences among

Electromagnetic behaviour and thermal stability of a conduction-cooled, no-insulated 2G-HTS coil at intermediate temperatures

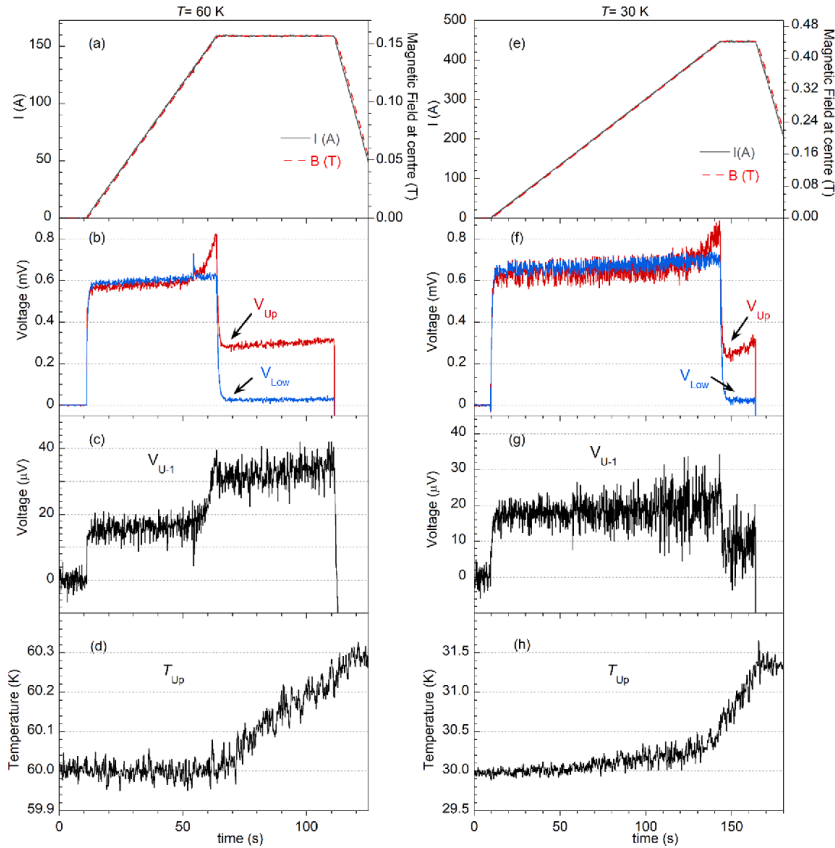


Fig. 7. Applied current, $I(t)$, magnetic field at the coil centre, $B_{centre}(t)$; voltages measured in both pancake coils ($V_{Up}(t)$ and $V_{Low}(t)$) and in the innermost turn of the upper pancake coil (V_{U-1}); and temperature T_{Up} , measured by the thermocouple TC-up (placed in the upper coil). Figs. (a)–(d) correspond to measurements at $T = 60\text{ K}$ and current ramp rate of 3 A/s up to 159 A ; (e)–(h) at $T = 30\text{ K}$ and current ramp rate of 3.3 A/s up to 447 A .

identical nominal commercial tapes [34–36], which could be attributed to pinning centre density variations [36]. Therefore, the used $I_c(B, \theta)/\omega$ dependence can only be considered as typical but not universal.

3.4. Effect of thermal cycling and thermal properties

2G-HTS coils may suffer certain degradation of their superconducting properties if delamination of the tapes during thermal cycling occurs [37]. To analyse this effect, the coil voltage during current ramping above I_c was measured after subjecting the coil to a number of thermal cycles (N_{cycles}) between 300 K and cryogenic temperatures.

Fig. 10 shows the upper coil voltage $V_{Up}(t)$ at 60 K for identical linear current ramps up to 159 A at 3 A/s , after 3, 4 and 5 thermal cycles. The resistive voltage at 159 A increased from $280\text{ }\mu\text{V}$ to $390\text{ }\mu\text{V}$ from the third to the fourth cycle, which in principle may indicate certain deterioration of the coil. Nevertheless, when heating up the system after this measurement, it was observed that the epoxy that joined the coil to the copper support plate was partially separated from the copper plate. Therefore, the coil and copper plate were reglued. When the system was subsequently cooled ($N_{cycles} = 5$), the measured resistive voltage V_{Up} decreased down to about $210\text{ }\mu\text{V}$ at the same conditions (see Fig. 10).

Therefore, this indicates that the differences in the measured resistive voltage upon thermal cycling were not due to the coil degradation but to the inadequate epoxy adhesion to copper.

To analyse the properties of the thermal contact between the different parts of the DP coil, a constant power $\dot{Q}_{heater} = 0.1\text{ W}$ was applied to the heater glued to the uppermost surface of the coil (see in Fig. 1(b)). As seen in Fig. 11, this produces an increase of the temperatures in the upper, $T_{Up}(t)$, and lower, $T_{Low}(t)$, pancake coils. The temperature in the copper support was maintained constant by a temperature controller (see 2.2), so that all the system eventually reaches a steady state.

Thus, the absolute thermal resistance between the lower coil and the copper plate can be estimated as $R_{th(Low-Cu)} = \Delta T_{Low-Cu} / \dot{Q}_{heater}$, with $\Delta T_{Low-Cu} = T_{Low} - T_{Cu}$ at the steady state. Similarly, the absolute thermal resistance between the upper and lower coils $R_{th(Up-Low)} = \Delta T_{Up-Low} / \dot{Q}_{heater}$ with $\Delta T_{Up-Low} = T_{Up} - T_{Low}$. The obtained values $R_{th(Low-Cu)} = 7.6\text{ K/W}$ and $R_{th(Up-Low)} = 4.3\text{ K/W}$ at 60 K ; increase to 12.6 and 5.9 K/W , respectively, at 30 K .

The corresponding thermal contact conductance values of the joint between the lower coil and the copper plate, h_c can be estimated using Eq. (1). In this case $\dot{Q} = \dot{Q}_{heater} = 0.1\text{ W}$, $\Delta T = \Delta T_{Low-Cu}$ and $A_c =$

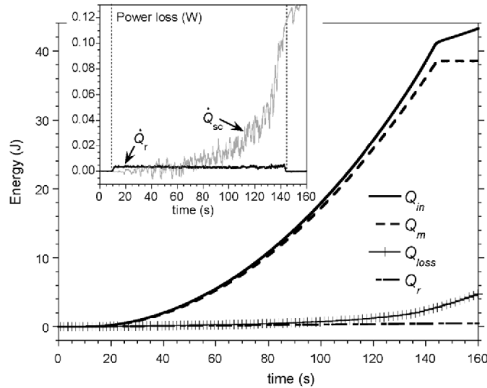


Fig. 8. Total energy supplied to the coil, $Q_{in}(t)$, energy loss, $Q_{loss}(t)$, magnetic energy stored in the coil, $Q_m(t)$, and energy dissipated by the currents flowing in the radial direction, $Q_r(t)$, calculated from experiments at 30 K, current ramp up to 447 A at 3.3 A/s. The inset shows the power loss contributions \dot{Q}_r and \dot{Q}_{sc} for the same experiment. The vertical dotted lines in the inset marks the beginning and the end of the current ramp.

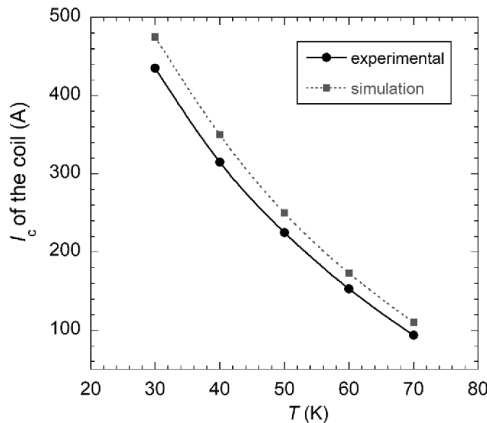


Fig. 9. Critical current of the DP coil obtained experimentally (using a 0.1 $\mu\text{V}/\text{cm}$ criterion) compared with the estimated values using the modified load-line method explained in 3.2.

$\pi(D_{out}^2 - D_{in}^2)/4 = 11.3 \text{ cm}^2$, and thus, we obtain values of $h_j = 116.3$ and $70.2 \text{ W m}^{-2} \text{ K}^{-1}$ at 60 K and 30 K, respectively. There are many factors that influence h_j , such as copper surface preparation, thickness and type of epoxy, area of the joint, etc. [38]. Nevertheless, considering the value of $h_j = 500 \text{ W m}^{-2} \text{ K}^{-1}$ at 10 K reported for Cu/epoxy/Cu joints by other authors [38,39] (for $A_c = 1 \text{ cm}^2$, epoxy SC5 and epoxy thickness of 80 μm), and the values obtained here for the electrically insulated thermal joints at the current lead heat sinks in Section 2.3, there is considerable scope for enhancing this thermal joint.

4. Conclusions

The thermal stability, thermal cycling and electromagnetic behaviour of a non-insulated (NI) conduction-cooled double pancake (DP) 2G-HTS coil have been studied between 5 K and 77 K, focusing on the

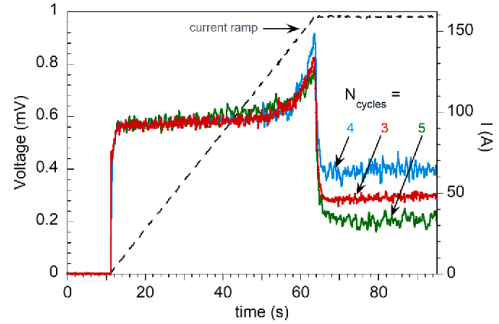


Fig. 10. $V_{up}(t)$ measured at 60 K for three different thermal cycles, $N_{cycles} = 3, 4$ and 5 when ramping the current from 0 up to 159 A at 3 A/s and then kept constant. Note that measurement shown in Fig. 7(b) corresponds to $N_{cycles} = 3$.

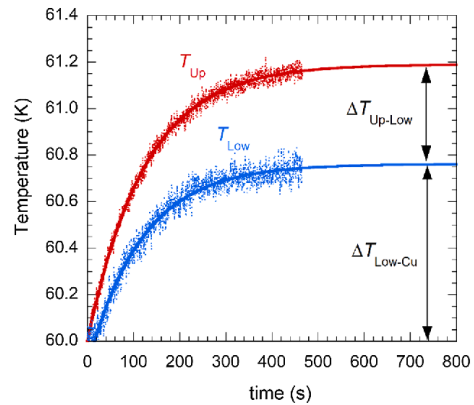


Fig. 11. Evolution of temperatures $T_{up}(t)$ and $T_{low}(t)$ when applying constant heating power $\dot{Q}_{heater} = 0.1 \text{ W}$ to the uppermost surface of the coil, and with the copper plate maintained at 60 K. Points correspond to experimental values and the continuous lines to exponential fits that give $\Delta T_{Low-Cu} = 0.76 \text{ K}$ and $\Delta T_{Up-Low} = 0.43 \text{ K}$ at the steady state.

analysis above 30 K. The DP coil was operated at high currents, both above and below the coil critical current, and in high vacuum conditions. The coil was epoxy impregnated after winding and subsequently glued with an epoxy resin to a copper support plate, which was anchored the second stage of a cryocooler.

The thermal stability of the whole cryogenic system was analysed, with especial attention to the behaviour of current leads, which were designed with two intermediate heat sinks. The electrically insulated thermal joints of the heat sinks, which have high thermal contact conductance ($h_j \approx 1800$ and $850 \text{ W m}^{-2} \text{ K}^{-1}$ at $\approx 80 \text{ K}$ and $\approx 35 \text{ K}$, respectively) provides the necessary thermal stability to the system.

Charging and discharging tests of the coil have been performed and analysed using a simple equivalent circuit to estimate the contributions of turn-to-turn and magnetization losses during the ramp, for different ramp rates, obtaining good correspondence with the observed coil heating. The derived turn-to-turn contact resistance $R_c \approx 110 \mu\Omega \text{ cm}^2$ at 77 K and about half at 5 K, are of the order but in the upper bound of results reported by other groups in similar non-insulated 2G-HTS coils without epoxy resin impregnation.

A good correspondence between the experimental coil critical

Electromagnetic behaviour and thermal stability of a conduction-cooled, no-insulated 2G-HTS coil at intermediate temperatures

A. Cubero, et al.

Cryogenics 108 (2020) 103070

currents and the estimated values, using a modified load-line method to account for the tape anisotropy, were found between 30 K and 70 K with almost identical temperature dependence, but experimental values $\approx 10\%$ lower.

At 30 K, with applied overcurrents (currents above I_c) of 447 A that gave coil resistive voltages above 250 μV , it was possible to hold the system for several seconds without triggering a quench. Moreover, the coil was subjected to several thermal cycles from 300 K to the cryogenic operating temperatures without observing degradation of its superconducting properties, indicating the electro-thermal robustness of the NI manufacture.

Several experiments were performed to analyse the thermal contact between the different parts of the DP coil (i.e., copper support plate, and lower and upper coils). It was found that the joint between the coil and the support plate constitutes the weak-point of the coil system. This was due to an inadequate adhesion between copper and epoxy, and needs further work.

CRediT authorship contribution statement

A. Cubero: Investigation, Resources, Formal analysis, Writing - original draft. **A.B. Núñez-Chico:** Investigation, Formal analysis, Writing - review & editing. **R. Navarro:** Conceptualization, Methodology, Writing - review & editing. **L.A. Angurel:** Methodology, Resources, Writing - review & editing, Project administration. **E. Martínez:** Conceptualization, Formal analysis, Investigation, Resources, Writing - original draft, Project administration.

Declaration of Competing Interest

The authors declare that they have no known competing financial interests or personal relationships that could have appeared to influence the work reported in this paper.

Acknowledgements

This work was supported by projects ENE2017-83669-C4-1-R (MINECO/AEI/FEDER, EU) and ENE-2014-52105-R (MINECO/FEDER, EU) and by the Gobierno de Aragón “Construyendo Europa desde Aragón” (research group T54.17R). The authors acknowledge the use of Servicio General de Apoyo a la Investigación-SAI, University of Zaragoza.

References

- [1] Barnes PN, Sumption MD, Rhoads GL. Review of high power density superconducting generators: Present state and prospects for incorporating YBCO windings. *Cryogenics* 2005;30:670.
- [2] Abrahamsen AB, Mijatovic N, Seiler E, et al. Superconducting wind turbine generators. *Supercond Sci Technol* 2010;23(3):034019.
- [3] Chen XY, Jin JX, Xin Y, Shu B, Tang CL, Zhu YP, Sun RM. Integrated SMES Technology for Modern Power System and Future Smart Grid. *IEEE Trans Appl Supercond* 2014;24(5):3801605.
- [4] Haran KS, Kalsi S, Tabea Amdt T, et al. High power density superconducting rotating machines development status and technology roadmap. *Supercond Sci Technol* 2017;30:123002.
- [5] Parizh M, Lvovsky Y, Sumption M. Conductors for commercial MRI magnets beyond NbTi: requirements and challenges. *Supercond Sci Technol* 2017;30:014007.
- [6] Zhang K, Hgley H, Liyang Y, et al. Tripled critical current in racetrack coils made of Bi-2212 Rutherford cables with overpressure processing and leakage control. *Supercond Sci Technol* 2018;31:105009.
- [7] Rossi L, Badel A, Kajias H, et al. The EuCARD2 Future Magnets Program for Particle Accelerator High-Field Dipoles: Review of Results and Next Steps. *IEEE Trans Appl Supercond* 2018;28(3):8239658.
- [8] Hahn S, Park DK, Bascañán J, Iwasa Y. HTS Pancake Coils Without Turn-to-Turn Insulation. *IEEE Trans Appl Supercond* 2011;21(3):1592-5.
- [9] Wang X, Hahn S, Kim Y, Bascañán J, Vecchio J, Lee H, Iwasa Y. Turn-to-turn contact characteristics for an equivalent circuit model of no-insulation ReBCO pancake coil. *Supercond Sci Technol* 2013;26:035012.
- [10] Kim K, Jung S-J, Sung H-J, Kim G-H, Kim S, Lee S, et al. Operating characteristics of an insulationless HTS magnet under the conduction cooling condition. *IEEE Trans Appl Supercond* 2013;23(3):460150.
- [11] Lee TS, Hwang YJ, Lee J, Lee WS, Kim J, Song SH, et al. The effects of co-wound Kapton, stainless steel and copper, in comparison with no insulation, on the time constant and stability of GdBCO pancake coils. *Supercond Sci Technol* 2014;27:065018.
- [12] Wang Y, Song H, Xu D, Li ZY, Jin Z, Hong Z. An equivalent circuit grid model for no-insulation HTS pancake coils MgB₂ coil segment for MRI applications. *Supercond Sci Technol* 2015;28:045017.
- [13] Jang JY, et al. Design, construction and 13 K conduction-cooled operation of a 3 T 100 mm stainless steel cladding all-ReBCO magnet. *Supercond Sci Technol* 2017;30:105012.
- [14] Yoon S, Cheon K, Lee H, Moon S-H, Kim S-Y, Kim Y, et al. The performance of the conduction cooled 2G HTS magnet wound without turn to turn insulation generating 4.1 T in 102 mm bore. *Physica C* 2013;494:242-5.
- [15] Choi YH, Song JB, Yang DG, Kim YG, Hahn S, Lee HG. A novel no-insulation winding technique for high temperature superconducting racetrack coil for rotating applications: a progress report in Korea university. *Rev Sci Instrum* 2016;87:104704.
- [16] Kim SB, Saitou A, Joo JH, Kadota T. The normal-zone propagation properties of the non-insulated HTS coil in cryocooled operation. *Physica C* 2011;471:1428-31.
- [17] Zhang D, et al. Instrumentation, cooling and initial testing of a large, conduction-cooled, react-and-wind MgB₂ coil segment for MRI applications. *Supercond Sci Technol* 2018;31:085013.
- [18] Kim HS, Kovacs C, Rindfleisch M, Yue J, Doll D, Tomsic M, et al. Demonstration of a conduction cooled react and wind MgB₂ coil Segment for MRI. *IEEE Trans Appl Supercond* 2016;26(4):4400305.
- [19] Ren L, Xu Y, Chen L, Wang Z, Qi D, Wang Z, et al. Study on the thermal characteristic of a 150 kJ/100 kW conduction-cooled HTS magnet. *IEEE Trans Appl Supercond* 2018;28(6):5701408.
- [20] Song X, Mijatovic N, Kellers J, Bührer C, Rebsdorf AV, Hansen J, et al. A full-size high-temperature superconducting coil employed in a wind turbine generator setup. *IEEE Trans Appl Supercond* 2017;27(4):5201105.
- [21] Dai Y, Yan L, Zhao B, Song S, Lei Y, Wang Q. Tests on a 6 T Conduction-Cooled Superconducting Magnet. *IEEE Trans Appl Supercond* 2006;16(2):961.
- [22] Laskaris ET, Ackermann R, Doni B, Gross D, Herd K, Minas C. A Cryogen-Free Open Superconducting Magnet For Interventional MRI Applications. *IEEE Trans Appl Supercond* 1995;5(2):163.
- [23] Watanabe K, Nishijima G, Awaji S, Takahashi K, Koyama K, Kobayashi N, et al. Performance of a Cryogen-Free 30 T-Class Hybrid Magnet. *IEEE Trans Appl Supercond* 2006;16(2):934.
- [24] Awaji S, Watanabe K, Oguro H, Miyazaki H, Hanai S, Tosaka T, et al. First performance test of a 25 T cryogen-free superconducting magnet. *Supercond Sci Technol* 2017;30:065001.
- [25] Ekin J. Experimental techniques for low-temperature measurements. Oxford, UK: Oxford Univ. Press; 2006.
- [26] Wang Y, Song H, Yuan W, Jin Z, Hong Z. Ramping turn-to-turn loss and magnetization loss of no-insulation (RE)Ba₂Cu₃O₇ high temperature superconductor pancake coil. *J Appl Phys* 2017;121:113903.
- [27] Lu J, Goddard R, Han K and Hahn S Contact resistance between two REBCO tapes under load and load cycles. *Supercond Sci Technol* 2017;30:045005.
- [28] Wilson MN. Superconducting Magnets. Oxford, U.K.: Oxford Univ. Press; 1987.
- [29] Wimbush SC, Strickland NM. The Magnetic-Field Dependence of Critical Current: What We Really Need to Know. *IEEE Trans Appl Supercond* 2017; 27(4): 8000505.
- [30] Zhang M, Kim J-H, Pamidi S, Chudy M, Yuan W, Coombs TA. Study of second generation, high-temperature superconducting coils: Determination of critical current. *J Appl Phys* 2012;111:083902.
- [31] Liu ZY, Ou J, Grilli F, Schreiner F, Zernheo VMR, Min Zhang M, et al. Comparison of 2D simulation models to estimate the critical current of a coated superconducting coil. *Supercond Sci Technol* 2019;32:014001.
- [32] Wimbush SC, Strickland NM. Critical current characterisation of SuperPower M4 Advanced Pinning 2G HTS superconducting wire; 2017. <https://doi.org/10.6084/m9.figshare.3759318.v2>.
- [33] Núñez-Chico AB, Martínez E, Angurel LA, Navarro R. Enhanced quench propagation in 2G-HTS coils co-wound with stainless steel or anodised aluminium tapes. *Supercond Sci Technol* 2016;29:085012.
- [34] Jirsá M, Rameš M, Ďuraň I, Melišek T, Kováč P, Vieraň R. L. Electric currents in REBaCuO superconducting tapes. *Supercond Sci Technol* 2017;30:045010.
- [35] Tsuchiya K, Kikuchi A, Terashima A, Norimoto K, Uchida M, Tawada M, et al. Critical current measurement of commercial REBCO conductors at 4.2 K. *Cryogenics* 2017;85:1-7.
- [36] Rossi L, Hu X, Kametani F, Abrahimov D, Polyanski A, Jaroszynski J, et al. Electric currents in REBaCuO superconducting tapes. *Supercond Sci Technol* 2016;29:054006.
- [37] Takematsu T, Hu R, Takao T, Yanagisawa Y, Nakagome H, Uglietti D, et al. Degradation of the performance of a YBCO-coated conductor double pancake coil due to epoxy impregnation. *Physica C* 2010;470:674-7.
- [38] Gmelin E, Asen-Palmer M, Reuther M, Villar R. Thermal boundary resistance of mechanical contacts between solids at sub-ambient temperatures. *J Phys D Appl Phys* 1999;32:R19-43.
- [39] Matsumoto DS, Reynolds Jr CL, Anderson AC. Thermal boundary resistance at metal-epoxy interfaces. *Phys Rev B* 1977;16:3303-7.

Publication C

Title:

Large enhancement of thermal conductance at ambient and cryogenic temperatures by laser remelting of plasma-sprayed Al₂O₃ coatings on Cu

Journal:

Journal of the European Ceramic Society

A. Cubero, E. Martínez, G.F. de la Fuente, I. García-Cano, S. Dosta, L.A. Angurel

[Preprint] Submitted, Journal of the European Ceramic Society (2021)

Impact factor (**JCR**, 2019): 4.495; Quartile Q1 (Materials Science, Ceramics)

SCImago Journal Rank (**SJR**, 2019): 1.164; Quartile Q1 (Ceramics and Composites)

A. Cubero, E. Martínez, G.F. de la Fuente, I. García-Cano, S. Dosta, L.A. Angurel, *Large enhancement of thermal conductance at ambient and cryogenic temperatures by laser remelting of plasma-sprayed Al₂O₃ coatings on Cu.* [Submitted] Journal of the European Ceramic Society.

Alumina coatings of around 150-micron thickness were plasma-sprayed over copper substrates. The objective of this work is to analyse and to improve the thermal contact conductance of this composite material, designed to electrically insulate the heat-sink junctions of the current leads inside a cryocooler. Nanosecond pulsed laser irradiation has been used to remelt and to densify the ceramic layer. Laser processing parameters have been adjusted to reduce holes and crack formation in Al₂O₃ surface and to ensure that no detachment takes place. Thermal contact conductance at cryogenic temperatures has been measured. My contribution to this work has involved laser processing together with thermal and surface characterization of the samples.

Large enhancement of thermal conductance at ambient and cryogenic temperatures by laser remelting of plasma-sprayed Al₂O₃ coatings on Cu

Álvaro Cubero¹, Elena Martínez^{1*}, Germán F. de la Fuente¹, Irene García Cano², Sergi Dosta², Luis A. Angurel¹

¹ Instituto de Nanociencia y Materiales de Aragón (INMA), CSIC-Universidad de Zaragoza, Zaragoza 50009, Spain

² Centre de Projecció Tèrmica (CPT), Dept. Ciència de Materials i Química Física, Universitat de Barcelona, Barcelona, Spain

* Corresponding author

Abstract:

Joints of high thermal contact conductance and electrical insulation have been obtained by coating copper supports with thin alumina (Al₂O₃) layers (of 140-150 μm thickness). This has been achieved by a combination of plasma spraying process and the subsequent coating remelting by a near-Infrared (n-IR) laser. With a proper optimization of the laser processing conditions, it is possible to transform the metastable γ-Al₂O₃ phase of the as-sprayed coatings to stable α-Al₂O₃, and to achieve denser alumina coatings. This results in a large enhancement of the thermal conductance of the joints, that enables their application as heat sinks at cryogenic and ambient temperatures. The used process here is scalable for the formation of alumina coatings on large metallic pieces of complex geometries.

Keywords: Laser melting, Plasma-sprayed Al₂O₃ coatings, Thermal contact resistance, Heat sink, Electrical insulation, Cryogenic temperatures

1. Introduction

Many power applications require the use of heat sinks to adequately transfer the heat generated in the system to the cold focus, thus avoiding excessive temperature rise and the eventual damage of the device. The development of technological applications based on MgB₂ and high temperature superconductors using cryocoolers allows operating temperatures between 20 K and 77 K (boiling temperature of liquid nitrogen at atmospheric pressure). In these superconducting devices, such as magnets and the current leads feeding them, heat intercept connections working from room temperature down to the operating cryogenic temperatures are particularly crucial for those systems cooled by conduction and working under high vacuum [1-3].

For demountable joints, heat transfer across the solid-solid interface is the main component of the overall thermal resistance. Thus, the needed optimization of bolted joints implies the achievement of low thermal boundary resistances. This is strongly determined by the thermal and physical properties of the contact material surfaces, such as geometry, roughness and topography, as well as the type of materials in the interface (metal-metal, metal-ceramic, etc), their bulk thermal conductivity, κ , and the interposition of intermediate layers (usually, Apiezon-N grease or indium foil for cryogenic applications) [1,4,5]. The thermal contact resistances of mechanical contacts between two solids of different materials have been studied at temperatures close and above room temperature and also below 4.2 K [1,4,5,6], but there are few results at intermediate temperatures, between 20 K and 300 K [7].

The metallic materials in the heat sink should be electrically insulated from those carrying current. Alumina single crystal, sapphire, has been widely used with this aim in cryogenic applications due to its high thermal conductivity at low temperatures (2900 Wm⁻¹K⁻¹ at 10 K) [1]. However, the use of single crystals is limited to small elements, with typical contact areas of around 1 cm². When larger contact areas are needed, low temperature epoxy resins and fiberglass-epoxy composites have been used [8-10], but their thermal conductivities are usually much lower, typically < 1 Wm⁻¹K⁻¹ below 77 K [1]. By contrast, some sintered ceramics such as Al₂O₃, AlN and BN [11], exhibit high thermal conductivity at ambient and cryogenic temperatures, with increasing values for denser ceramics with low impurity concentration [1,12]. However, their main drawback arises from the difficulty of machining and obtaining complex-shaped parts [13]. Besides, the differences in thermal contraction of the different materials that form the heat sink cause thermal stress during cooling down to cryogenic temperatures. This can result in a drastic decrease of the thermal conductance of the joint and also produce large cracks in the ceramic material [14]. The use of large size bulk ceramics is thus normally disregarded for this cryogenic application.

Thermal sprayed coatings on metals, which are widely used as a barrier to protect the metal component from abrasive or corrosive environments or high heat conditions, can also provide additional functionalities [15,16]. The use of plasma-sprayed alumina coatings on a metallic substrate to achieve the dual function of providing electrical insulation together with a good thermal conductance was first proposed by Mackay and Muller [17] for heat sinks in electronic packaging at ambient temperatures. This technology may solve the above-mentioned problems of bulk ceramics, as it can be used to fabricate parts with no limitations in size and with very diverse shapes. The copper or aluminum substrates can be easily machined to the desired geometry for the

application, including the holes for bolt joints, before plasma spraying of the ceramic coated layer. One main drawback of as-sprayed coatings is their high porosity, which would result in lower thermal conductivity as compared to corresponding high dense and pure ceramics. Moreover, the presence of the metastable phases gives rise to some undesired effects, as it can produce a deterioration of the dielectrical properties of alumina [18].

Laser remelting of the plasma-sprayed Al₂O₃ coatings can overcome this problem, by achieving a denser and more homogenous layer. CO₂-laser melting of ceramic coatings (such as alumina or alumina-based eutectics) on pure metals or alloys has been reported by several groups [19-28], mainly with the aim of enhancing their mechanical properties. CO₂ lasers are frequently used due to the much higher absorption values measured at $\lambda = 10.6 \mu\text{m}$ in comparison with those obtained at $\lambda \approx 1 \mu\text{m}$ [29,30]. The advantage of using mid-IR CO₂ lasers is obvious, as 10.6 μm radiation absorption is nearly at the 90% level in Al₂O₃, while it is only about 3% under 1 μm irradiation at an irradiance level of 10^4 W cm^{-2} [29]. Although other ceramic materials, like those based on ZrO₂, enable increased absorption at ca. 1 μm laser wavelengths, apparently because of the presence of defects associated to oxygen vacancies [30], Al₂O₃ behaves quite differently. Its absorption at $\lambda \approx 1 \mu\text{m}$ may be more significant when in powder form, because of the presence of pores [31] and difficult to control in a sustained manner when highly densified [31,32]. The use of pulsed ns lasers enables improved melt stability control [31] and has thus paved the way towards increased use of near-infrared (n-IR) lasers [30,33,34]. Some cracks in the ceramic layer can be produced during this process due to thermal shock caused by the rapid heating and cooling processes intrinsic to laser heating [34,35,36]. One alternative to reduce thermal stresses is to induce a preheating step using two lasers, for instance, a larger spot CO₂ laser for heating the sample and a smaller spot n-IR laser within the preheated large spot to melt the ceramic surface [37]. A more industrially scalable alternative is to perform the laser treatment when the sample is moving at constant speed inside a furnace at high temperature [38]. Laser processing conditions should be then carefully analyzed to overcome this unwanted effect, with the aim of minimizing the number, size and impact of microcracks in the final sample properties.

This work aimed at enhancing thermal contact resistance of plasma-sprayed Al₂O₃ coatings on copper for their use in cryogenic and ambient temperature applications, by subsequently remelting of the ceramic layer using n-IR laser irradiation at room temperature. Laser processing parameters have been found to affect strongly the microscopic properties of the final coating. Optimized processing conditions are a key issue to minimize the presence of cracks and obtain a final dense ceramic layer. The thermal contact resistance of representative samples processed under optimized conditions is reported and compared with the behavior of non-irradiated samples.

2. Experimental and Methods

2.1 Plasma spraying of Al₂O₃ coatings on copper

Alumina coating was produced by atmospheric plasma spraying (APS). APS coatings were sprayed on copper substrates using a using the F4 gun attached to a A3000S system (automated and

robotised) from Sulzer Metco, with argon and hydrogen the process gases. The applied parameters of 600A intensity, 35/12 Ar/H₂ l/min gas flow and 120mm distance were based on previous knowledge as shown in references [39-41].

The surface of the copper substrate was subjected to a grit blasting process before coating. Commercial Al₂O₃ powders of 10 to 20 μm particle size, provided by H.C. Starck were used. The alumina coating thickness was set around 150 μm and its surface had typical roughness Ra values of 5 - 7 μm (measured in representative areas of 600 μm x 400 μm). Copper of 99.9 % purity, residual-resistance ratio, RRR = 80, and dimensions 5mm thickness and area 1 cm x 2 cm was used as substrate.

2.2 Laser processing

Al₂O₃ coatings were irradiated with a n-IR Ytterbium pulsed fiber laser (Perfect Laser, model PEDB-400B), with central wavelength $\lambda = 1060-1070$ nm, $1/e^2$ beam diameter $2r_b = 65$ μm, using a pulse repetition frequency, $f_{rep} = 900$ kHz, and pulse durations $\tau_p = 200$ ns. Given a nominal average laser power, P_L , each laser pulse is characterized by its energy, E_p ($E_p = P_L / f_{rep}$), its fluence, F_p ($F_p = E_p / (\pi r_b^2)$) and its irradiance, I_p ($I_p = F_p / \tau_p$). Laser processing was carried out using the meandering laser beam scanning (MLBS) method, where the laser beam follows a meander-shaped path in order to completely irradiate the whole substrate sample surface (see Figure 1). Each scanned line starts and ends outside the sample. The combination of pulse fluence, laser beam scanning velocity (v_L) and hatch distance between adjacent lines (d_s), determines the total accumulated fluence, which takes into account the overlapping between consecutive pulses in a line and between adjacent lines:

$$F_{2D} = \frac{\pi r_b^2}{d_p d_s} F_p \quad (1)$$

Here, $d_p = v_L / f_{rep}$ is the distance between the centers of two consecutive laser pulses in a line. The ratios d_p / r_b and d_s / r_b control the overlapping in both directions. Table 1 collects some representative laser processing conditions analyzed in this work.

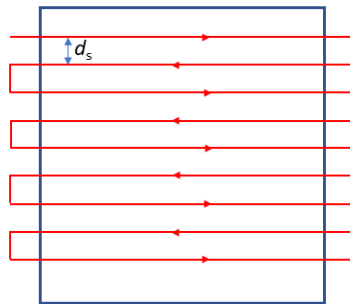


Figure 1: Scheme of the trajectory of the center of the laser beam in a meandering laser beam scanning (MLBS) configuration.

Large enhancement of thermal conductance at ambient and cryogenic temperatures by laser remelting of plasma-sprayed Al_2O_3 coatings on Cu

Table 1. Some representative laser processing parameters used to irradiate the alumina coating.

Name	P_L (W)	v_L (mm/s)	d_s (μm)	d_p (μm)	F_p (J/cm^2)	I_p (MW/cm^2)	F_{2D} (kJ/cm^2)
LP1	27.3	80	15	0.09	0.91	4.57	2.3
LP2	27.3	80	20	0.09	0.91	4.57	1.7
LP3	27.3	80	25	0.09	0.91	4.57	1.4
LP4	27.3	80	30	0.09	0.91	4.57	1.1
LP5	27.3	100	20	0.11	0.91	4.57	1.4
LP6	27.3	50	20	0.055	0.91	4.57	2.7
LP7	31.5	80	20	0.09	1.06	5.27	2.0
LP8	35.0	80	20	0.09	1.17	5.86	2.2

2.3 Microscopy characterization

The microstructure of plasma sprayed coatings, before and after laser processing, was studied by field-emission scanning electron microscopy (FE-SEM), (MERLIN, Carl Zeiss). In general, an accelerating voltage of 3 - 5 kV was used for surface images and 15 kV for cross-sectional views. Different detectors were used: secondary electrons (SE), angle-selective backscattered electrons (AsB) and InLens. The latter is a high-efficiency annular SE detector used to map the surface structure. The roughness of the coatings was measured by confocal microscopy (sensofar PI μ -200). The phase composition was analysed by X-ray diffraction (XRD) patterns collected at room temperature on a RIGAKU D-max /2500 X-ray diffractometer using Cu K α radiation. The "JCPDS-International Centre for Diffraction Data- 2000" database was used for phase determination. Rietveld analysis of XRD patterns, using the PDXL 2 commercial software from RIGAKU, was performed to calculate the weight ratio content of the different phases present in the as-sprayed coating.

2.4 Method for characterization of the joint thermal resistance

To determine experimentally the thermal resistance of these joints at cryogenic temperatures, steady-state measurements [42] were performed with the set-up schematically shown in figure 2. The analyzed samples were placed between two larger copper plates, which constitute the heat source and heat sink, and are joined between them by two screws. Apiezon-N grease was applied over all contact surfaces (ceramic and copper).

The heat sink copper plate is mechanically and thermally attached to the cold finger of a cryocooler. It is equipped with a thermometer (T_{cold}) and a heater (HT) that allows controlling the operating temperature of the joint by using a Lakeshore temperature controller. The second copper plate also holds a thermometer (T_{hot}) and another heater HS (heat source), which provides a prefixed constant power, P_0 that can be varied. Heat transfer across the joint takes place mainly by conduction. The convective component is residual as the sample is inside a cryostat in high vacuum ($\approx 10^{-5}$ hPa), and the radiation contribution has also been neglected because of the presence of a thermal radiation shield around the joint. The validity of this hypothesis will be discussed in section 3.3.

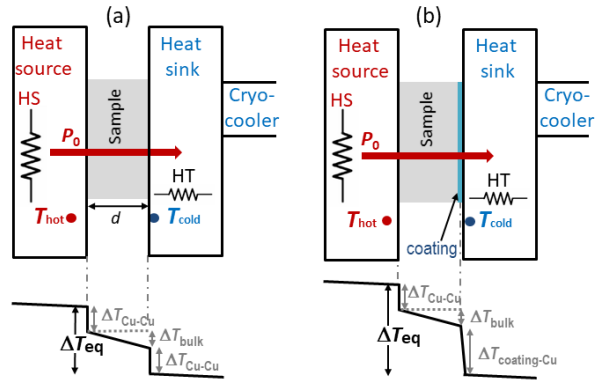


Figure 2: Schematic of the set-up for the measurement of thermal contact resistances at cryogenic temperatures of (a) copper sample (reference) (b) copper coated with alumina. The schematics of thermal profiles in each case are given. P_0 is the constant heat flow rate across the joint. The cryocooler, heater HT and a temperature controller allows controlling the temperature T_{cold} .

For each measurement run, once the whole joint is at the set temperature, a constant heat power P_0 is applied by the HS, which produces a constant heat flow rate across the joint ($\dot{Q} = P_0$). Eventually, after a time that depends on the enthalpy and the thermal resistance of the joint at this temperature, the system reaches thermal equilibrium, and a constant temperature difference between T_{hot} and T_{cold} is established, ΔT_{eq} , which is proportional to the overall thermal resistance of the joint at this temperature:

$$R_H(T) \sim \frac{\Delta T_{eq}}{P_0} \quad [\text{K/W}] \quad (2)$$

The measured R_H (or ΔT_{eq}) value across the joint at each temperature is the sum of different contributions. In the case of the non-coated copper sample (see figure 1a) it is given by the sum of the thermal resistance of the bulk copper and the contact resistance at the two Cu-Cu surfaces, i.e.:

$$R_H(T) = R_{H,bulk}(T) + 2R_{H,Cu-Cu}(T) \sim \left(\frac{1}{P_0}\right) (\Delta T_{bulk} + 2\Delta T_{Cu-Cu}) \quad (3)$$

ΔT_{Cu-Cu} is the temperature difference between both copper surfaces in contact. Note that there are two nominally identical Cu-Cu interfaces, thus, we assume that similar temperature gradients are generated in both interfaces. ΔT_{bulk} is the temperature drop across the bulk sample (copper in this case), given by the thermal conductivity of the used copper sample, $\kappa_{Cu}(T)$, which is known, its thickness, $d = 5 \cdot 10^{-3}$ m, and the contact area $A = 2 \cdot 10^{-4}$ m²:

$$\Delta T_{bulk} \sim P_0 R_{H,bulk} \quad \text{with} \quad R_{H,bulk}(T) \sim \frac{1}{\kappa_{Cu}(T)} \frac{d}{A} \quad (4)$$

Using eqs (2)-(4), it is thus possible to estimate the thermal contact resistance between the copper surfaces as:

$$R_{H,Cu-Cu}(T) \sim \frac{\Delta T_{Cu-Cu}}{P_o} \sim \frac{1}{2} (R_H(T) - R_{H,bulk}(T)) \quad (5)$$

In the case of the copper sample with alumina coating in one of their faces (see figure 2b), the total resistance across the joint R_H is given by:

$$\begin{aligned} R_H(T) &= R_{H,Cu-Cu}(T) + R_{H,bulk}(T) + R_{H,alumina-Cu}(T) \\ &\sim \left(\frac{1}{P_o}\right) (\Delta T_{Cu-Cu} + \Delta T_{bulk} + \Delta T_{alumina-Cu}) \end{aligned} \quad (6)$$

Therefore, eq. (6) allows us to estimate the contribution of the contact resistance between the alumina coating and the copper, $R_{H,alumina-Cu}$, from the experimentally measured R_H , the contact resistance $R_{H,Cu-Cu}$, which was previously derived from the measurement of the non-coated sample, and $R_{H,bulk}$, given by eq. (4). The equivalent thermal contact conductance (TCC) or h_j , which is normalized to the contact area of the joint, is given by:

$$h_{j,alumina-Cu}(T) \sim \frac{1}{A} \frac{1}{R_{H,alumina-Cu}(T)} = \frac{1}{A} \frac{P_o}{\Delta T_{alumina-Cu}} \quad [\text{W m}^{-2} \text{K}^{-1}] \quad (7)$$

It must be noted here that this term has the contribution of the contact joint between the surfaces of the alumina and copper, as well as those corresponding to the coating itself and at the interface between the coating and the substrate, since this experimental configuration does not allow to derive separately these contributions.

Before cooling down, the thermal resistance of the joints was also measured at room temperature, 290 K, with the sample in vacuum.

3. Results and Discussion

3.1 Microstructure of the laser remelted coatings

Figure 3 shows SEM micrographs of the surface (Figure 3a) and cross-sections (Figure 3b and 3c) of the alumina plasma sprayed coating on copper. The typical features of plasma-sprayed coatings are observed, which are inherent to this technique, where a large number of melted and partially-melted particles is deposited, giving rise to the observed microstructure and surface roughness [18]. The transversal cross-sections of polished samples show the boundary between the alumina coating and the copper substrate (light color in the figure 3b). As it is observed in this figure, the alumina layer follows the surface topography of the copper substrate and is highly porous (black areas in the figure). A detail of the coating can be seen in Figure 3c, showing the lamella stacking structure of the as-sprayed coating, and pores that range typically from 1 μm to 10 μm .

In order to find the optimum MLBS parameters, preliminary studies were carried out by irradiating the surface at different scanning velocities and laser power values, finding a range between 50 and 100 mm/s at P_t higher than 25 W, where this is generally achieved. Thus, a more detailed analysis of laser processing parameter influence was performed by changing systematically one parameter

at the time. For this purpose, areas of about 10 mm x 2 mm of an alumina coated copper sample were laser treated under different conditions.

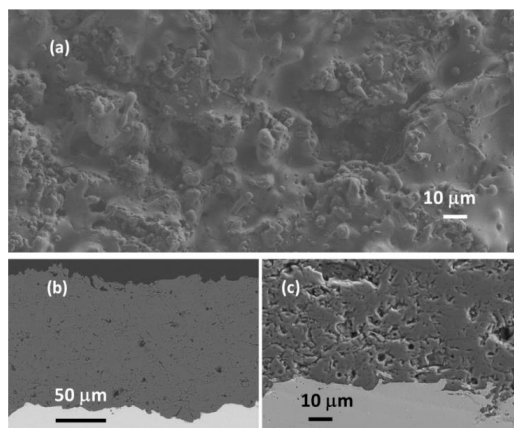


Figure 3: SEM images of alumina coated samples (as-sprayed), showing (a) the surface topography (SE); (b) and (c) are images of transversal cross-sections of polished samples with different magnifications and detectors: (b) AsB and (c) SE.

The hatch distance was varied from 5 to 30 μm while fixing $P_L = 27.3 \text{ W}$ and $v_L = 80 \text{ mm/s}$. Figure 4 shows the SEM images of four representative sample surfaces, which correspond to d_s of 15, 20, 25 and 30 μm . It was found that the d_s value strongly affects the surface homogeneity of the processed samples. For $d_s = 15 \mu\text{m}$ (Figure 2a), an uneven and irregular surface topography is obtained, with the presence of marked peaks and valleys. These irregularities are even more pronounced when decreasing the hatch distance below 15 μm (not shown). The best results are obtained for $d_s = 20 \mu\text{m}$ (Figures 4b and 4e), which corresponds to $d_s/r_b = 0.615$. Figure 4e shows a detail of this surface, where elongated grains of alumina aligned parallel to the laser beam scan direction are observed, along with some cracks in the perpendicular direction. A reduced number of micropores are also observed throughout the sample, usually located along the transversal cracks. Surface topography obtained for $d_s = 25 \mu\text{m}$ (Figure 4c) is similar, although with more cracks and pores. By increasing the hatch distance further to 30 μm (figures 4d and 4f), the melted surface becomes less uniform, with an increasing size and number of pores and cracks. This result indicates that a certain overlap between adjacent scanned lines is required, with an optimum condition for $d_s/r_b \sim 0.6 - 0.7$. Note that in those cases the surface becomes smoother than for as-sprayed samples. The R_a measured in representative areas of 600 $\mu\text{m} \times 400 \mu\text{m}$ is about 4 μm .

Next, on the basis of the best optimum laser processing conditions obtained in Figure 4b, the effect of varying the scan velocity and the laser power was analyzed. For this purpose, samples were processed with fixed $d_s = 20 \mu\text{m}$ and $P_L = 27.3 \text{ W}$, varying the laser beam scan velocity between 50 mm/s and 100 mm/s. Figures 5a and 5b show the surface topography of the samples processed with $v_L = 100 \text{ mm/s}$ and 50 mm/s, respectively. It is observed that the former condition results in very irregular melting, identified by the presence of numerous bumps and holes. It must be remarked here that, even with increasing P_L values, satisfactory results were not achieved using this v_L . On the contrary, by decreasing v_L , the surface appears more homogeneous, although some

cracks in the direction perpendicular to the beam scan are still observed (see figure 5e). The samples processed with $v_t = 80$ mm/s and increasing power values are shown in Figures 5c and 5d, respectively. Very homogeneous surfaces were obtained in both cases, with the direction of laser scans clearly visible. Alumina crystals are larger than with the previous processing parameters, as observed in Figure 5e, and cracks in the perpendicular to the beam scan direction extend longer than in the previously analyzed cases, as larger grains would facilitate the crack propagation in this direction.

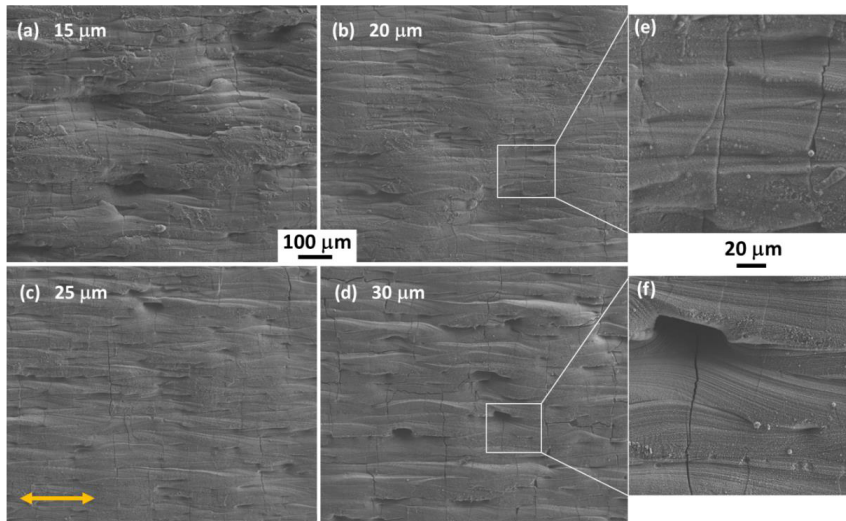


Figure 4: SEM images (SE) of alumina surfaces processed with the same $P_l = 27.3$ W and $v_t = 80$ mm/s values, and with different hatch values from 15 μm to 30 μm as indicated: (a) LP1, (b) LP2, (c) LP3, (d) LP4. The same magnification was used in the four cases. (e) and (f) show the areas highlighted by a white rectangle in the corresponding (b) and (d) images, respectively, with higher magnification. A voltage of 3 kV was used in all cases. The arrow in (c) marks the laser beam scan direction, which is the same in all cases.

The observed transverse cracks, i.e., perpendicular to the laser scanning direction, have similar characteristics as those reported by Zheng et al. [34] for Al₂O₃ ceramics obtained by selective laser melting (SLM). These have been attributed to the extremely high temperature gradient and to the internal stress caused by the thermal shock effect of laser reheating. Longitudinal cracks, which have also been observed in alumina SLM specimens, also appear in our study for conditions where unmelted zones coexist with partially melted ones (see for example Figures 4a, 4d and 5a), but are scarce in samples with homogeneous melted surfaces (LP2, LP6, LP7 and LP8, for example). When laser melting is very inhomogeneous (as the case shown in Figure 5a), besides the two types of cracks, holes are abundant.

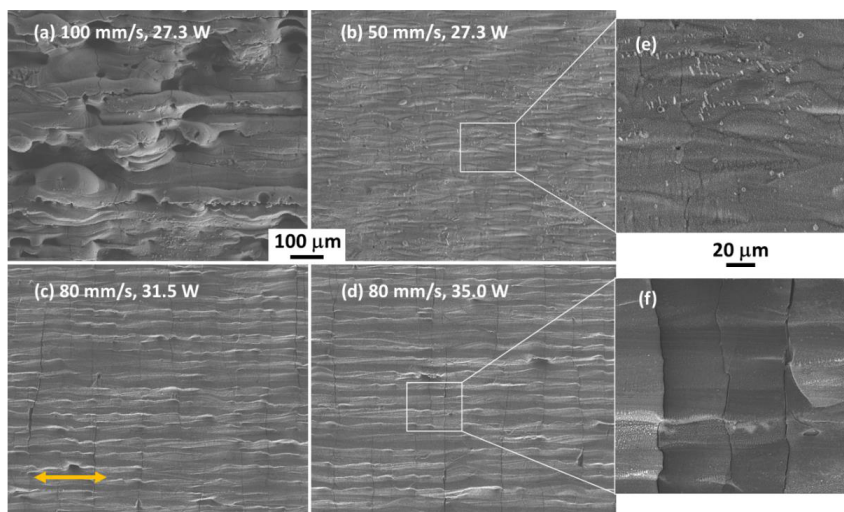


Figure 5: SEM images (SE) of surfaces processed with fixed hatch value $d_s = 20 \mu\text{m}$; obtained with fixed $P_l = 27.3 \text{ W}$ and varying the scanning velocity: (a) LP5, (b) LP6. With fixed v_l and varying P_l : (c) LP7, (d) LP8. The same magnification was used in the four images. (e) and (f) show the areas highlighted by a white rectangle in the corresponding (b) and (d) images, respectively, with higher magnification (in-lens detector). A voltage of 5 kV was used in all images. The arrow in (c) marks the laser beam scan direction, which is the same in all images.

The transversal cross-sections of some of the above samples are shown in Figure 6. In general, all laser processing conditions that give inhomogeneous surface topographies also result in irregular cross-sectional views. For example, laser conditions LP1 shown in Figure 6a (corresponding surface in Figure 4a) shows a columnar-type microstructure, with cracks in the direction perpendicular to the coating-metal boundary that extend along the entire thickness of the coating. Additionally, cracks in the direction parallel to the surface are also observed near the surface. The corresponding cross-sections of the optimum surface microstructure, LP2 and LP6, previously shown in Figures 4b and 5b, are shown in Figure 6b and 6c, respectively. Both are characterized by a layer of dense recrystallized alumina in the upper part of the coating, near the surface, with a more porous layer near the copper. Some holes at the alumina/copper boundary, of about 20 - 30 nm size, are observed. Some particles of copper and copper oxide are present in the latter layer, especially in case of LP6. Finally, Figure 6d shows an example of a fully remelted coating, characterized by the presence of a very dense and homogeneous alumina layer, although this is completely separated from the copper substrate. It is expected that heating of the metallic substrate during laser processing could help to avoid this unwanted effect. For this reason, samples LP2 and LP6 were selected to analyse their thermal behaviour, and to compare with as-sprayed samples.

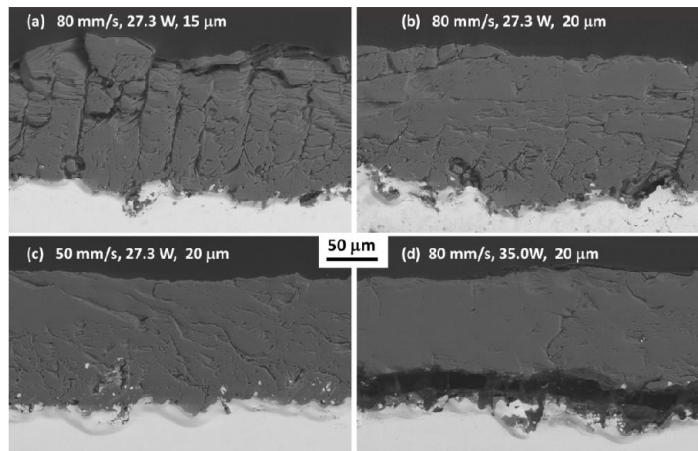


Figure 6: SEM images (backscattered electrons) of transversal cross-sections of polished samples treated with different laser processing parameters: (a) LP1; (b) LP2; (c) LP6; (d) LP8. The laser beam scan direction is in the direction perpendicular to the plane of the images.

3.2 Phase composition

Figure 7 shows the X-ray diffraction patterns of two alumina coated samples, in the cases of as-sprayed (a) and after subsequent laser remelting using optimized conditions (LP2) (b). In the former, the main phase corresponds to the metastable $\gamma\text{-Al}_2\text{O}_3$ phase, with the presence of some $\alpha\text{-Al}_2\text{O}_3$ (corundum), $\beta\text{-Al}_2\text{O}_3$ and copper (substrate). The weight ratio content of crystalline $\alpha\text{-Al}_2\text{O}_3$ and $\gamma\text{-Al}_2\text{O}_3$ phases in the as-sprayed coating was estimated to be 5.8(3) % and 91.3(19) %, respectively. The formation of metastable phases in plasma-sprayed alumina coatings has already been reported [18,43-45] and explained in terms of classical nucleation theory and the thermal history of the particles during solidification [43,46]. After laser remelting under optimum conditions, only the phase corresponding to corundum is essentially present, with a marginal content of the γ -alumina phase (see Figure 7b).

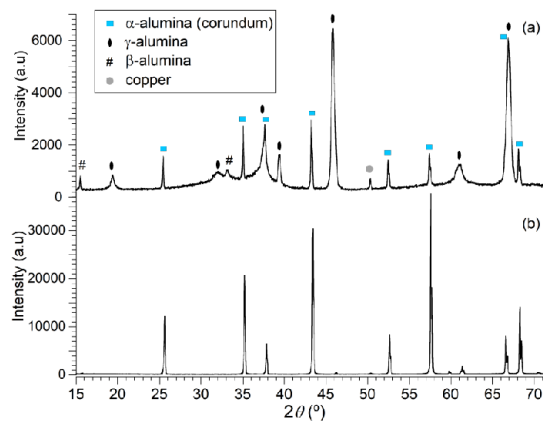


Figure 7: XRD of alumina coated samples (a) as-sprayed sample (a) after laser remelting with condition LP2.

3.3 Thermal conductance characterization

Thermal contact conductance as a function of the temperature was characterized in four representative samples, detailed as follows. A non-coated Cu sample was measured as a reference, as explained in 2.4 (Figure 2a). Three alumina-coated Cu samples were also measured: one of them corresponding to the as-sprayed plasma coating, and the other two were subsequently processed with laser parameter conditions LP2 and LP6. Hereafter, these samples will be referred to as non-coated, as-sprayed, LP2 and LP6, respectively. Each sample was measured twice in order to estimate the error and to check the reproducibility of the measurements. For that purpose, each sample was cooled down and measured at different temperatures. Afterwards, it was warmed up at room temperature, un-installed and installed again, and cooled down for another complete test run. In all cases the differences between two different runs were within 5-8 %.

Figure 8 shows the time evolution of the difference between the hot and cold temperatures across the joint, $T_{hot}(t) - T_{cold}(t)$, at a temperature of 50 K, for three different samples: non-coated copper, as-sprayed and laser processed (LP2). In all cases, after setting the constant heat flow, the system reached eventually a steady state and a constant ΔT_{eq} was established for each P_0 , which allows the estimation of R_H of the whole joint using eq. (2). A significant enhancement of the thermal joint is observed for the laser-processed alumina-coated sample, as compared to the as-sprayed coated sample, with a significant reduction of ΔT_{eq} from 3.01 K to 1.03 K, respectively, for $P_0 = 2$ W. The value obtained under similar conditions for the non-coated copper sample was 0.38 K. To calculate the R_H value of the joint at each temperature, different values of P_0 were applied. The results corresponding to sample LP2, for the two different measurements runs and at different temperatures, are plotted in Figure 9. A good linear fit of the data is obtained, suggesting that the radiation heat income does not vary significantly during each measurement [7], thus supporting the above-mentioned hypothesis.

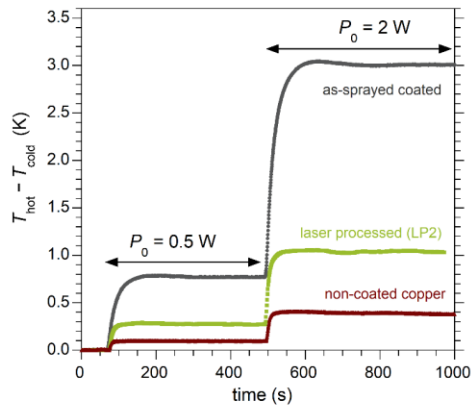


Figure 8: Temporal evolution of difference between $\Delta T(t) = T_{hot}(t) - T_{cold}(t)$ temperatures across the joint (see Figure 2) for constant heat flow $P_0 = 0.5$ W and 2 W at set temperature 50 K. The results correspond to the non-coated Cu, as-sprayed alumina, and laser processed sample with conditions LP2, as indicated.

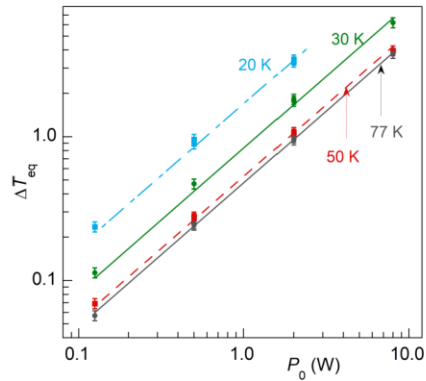


Figure 9: Measured ΔT_{eq} values (symbols) for sample LP2 as a function of the applied P_0 and at different temperatures. Lines are best fits to eq (2).

The temperature dependence of thus derived R_H values is plotted in figure 10 for the four analyzed samples. Note that thermal resistance of the bulk copper ($R_{H,bulk}$), which was calculated by eq. (4) and is also plotted for comparison purposes, does not contribute significantly to the total R_H , as expected. The improved thermal behavior observed for the coated samples with subsequent laser remelting was observed for all measured conditions, from cryogenic to ambient temperatures. The difference becomes particularly marked in the range between 40 K and 77 K, where the R_H values of the laser treated samples are about three times lower than those corresponding to the as-sprayed sample. The larger improvement in this temperature range is due to the temperature dependence of thermal conductivity of $\alpha\text{-Al}_2\text{O}_3$, which presents a maximum at this temperature range [1]. An increase of the thermal conductivity of the components of the thermal joint, also results in an improvement of the thermal contact conductance [7].

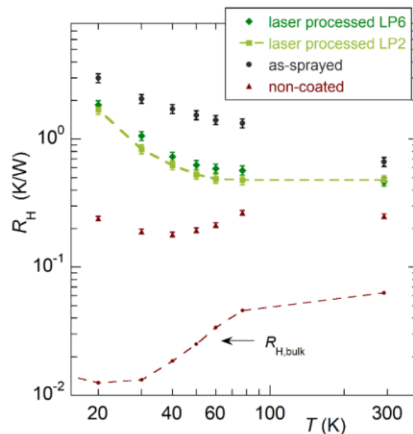


Figure 10: Temperature dependence of the thermal resistance of the whole joint, R_H , estimated from eq. (2) for the four measured samples (contact area $A = 2 \text{ cm}^2$). The contribution of $R_{H,bulk}$ (eq. 4) is also plotted for comparison.

Figure 11 displays the values of the thermal contact conductance $h_j(T)$ between copper and alumina. These were calculated from $R_{jt}(T)$ curves using the procedure described in section 2.4, and include the contribution of the thermal resistance of the alumina coating layer, as it was already mentioned. Values of about 0.95×10^4 and $1.55 \times 10^4 \text{ Wm}^{-2}\text{K}^{-1}$ are obtained for the laser processed sample LP2 at temperatures of 40 K and 77 K, respectively. This is an important enhancement when comparing with as-sprayed coatings or other technologies. For example, Datskov et al. [2] reported heat transfer coefficient of about $3600 \text{ Wm}^{-2}\text{K}^{-1}$ at 77 K for a heat sink, which consisted in two copper plates with three layers of fiberglass tape between them and were used in conduction-cooled current leads working at a maximum current of 250 A. In a previous work [3], our group reported values of about $1800 \text{ Wm}^{-2}\text{K}^{-1}$ at 80 K for a heat sink made with plasma-sprayed alumina coating on aluminum, for a similar application. The latter value was estimated from the numerically calculated total heat inleak into the heat sink and the measured ΔT across the whole joint. The obtained results in the present work by laser-processing of the plasma-sprayed coating imply thus a remarkable upgrade, which would allow higher current application (in case of current-leads) and an important improvement of the thermal stability of the system in all cases.

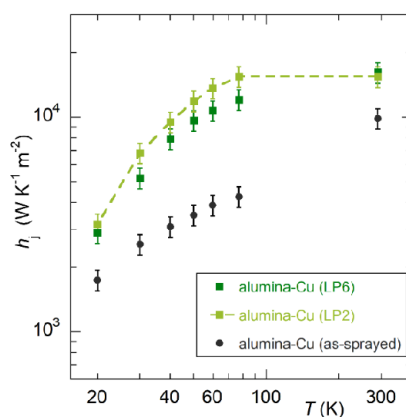


Figure 11: Temperature dependence of the thermal contact conductance between copper and alumina, for the as-sprayed alumina coatings and laser processed coatings with laser processing conditions LP2 and LP6.

It should also be highlighted that the h_j values for both analyzed laser-processed samples (LP2 and LP6), which were selected on the basis of their better microstructural characteristics, do not differ significantly between them. Particularly, LP2 sample shows slightly higher h_j values than LP6, but with differences just above the estimated errors. The fact that both samples exhibit similar thermal behavior indicates that the range of laser parameters resulting in an enhancement of thermal behavior is not narrow. This provides important advantages from a practical point of view. Moreover, this may also indicate that the small differences between both samples would be likely due to the exact number of defects in the final samples. This suggests that a way to achieve further enhancement of these joints could involve heating the substrate (or the whole sample) during laser processing to minimize thermal shock between the molten pool and the recrystallized grains. By doing so, it is expected that the number of cracks and other defects could be further minimized. The purpose would be to achieve denser coating layers (as seen in Figure 6d), without a degradation of the bonding between the metal and ceramic components. This procedure, however, could have

the risk of introducing metallic copper into the alumina layer, which could result in the loss (or deterioration) of its dielectric properties and should be avoided. This would thus require a complete and careful study to probe its viability for this application.

4. Conclusions

Laser remelting of plasma-sprayed alumina coatings on copper have been performed aiming at achieving electrical insulation together with a good thermal conductance. Laser processing was done by the meandering laser beam scanning method, using a n-IR Ytterbium pulsed fiber laser, with central wavelength $\lambda = 1060\text{-}1070$ nm, $1/e^2$ beam diameter $2r_b = 65$ μm , pulse repetition frequency of 900 kHz, and pulse duration of 200 ns. The effect of the main laser processing parameters, including pulse fluence (F_p), laser beam scanning velocity (v_l) and hatch distance between adjacent lines (d_s) has been reported. The optimum microstructures were obtained for $F_p \sim 0.9$ J/cm², $d_s \sim 20$ μm (corresponding to $d_s/r_b \sim 0.6$) and v_l between 50 and 80 mm/s.

Thermal contact conductance as a function of temperature was characterized for two laser-processed samples, which were selected on the basis of their better microstructural characteristics. These were characterized by a layer of dense recrystallized alumina in the upper part of the coating, near the surface, with a more porous layer near the copper interface. An important improvement of the thermal behavior was observed for these laser treated samples under all conditions, from cryogenic to ambient temperatures, as compared to the as-sprayed samples. The observed differences became particularly marked in the range between 40 K and 77 K, where the thermal resistance R_H values of the laser treated samples were about three times lower than those corresponding to the plasma-sprayed samples. Values of the thermal contact conductance, h_j , as high as 0.95×10^4 and 1.55×10^4 Wm⁻²K⁻¹ at temperatures of 40 K and 77 K, respectively, were obtained for the optimized laser processed sample. These values include the contribution at the alumina/copper interface and across the alumina coating layer itself. Further improvement of thermal contact conductance is expected to be possible by simultaneous heating of the substrate or the whole sample during the laser remelting process. This could further minimize the inherent defects in the alumina coating appearing by thermal shock during the rapid melting and cooling associated to laser remelting.

Acknowledgments

This work was funded by project ENE2017-83669-C4-1-R (MCIU/AEI/FEDER, EU), by the Gobierno de Aragón "Construyendo Europa desde Aragón" (research group T54_20R) and Generalitat de Catalunya for the project SGR2017_01777. The authors acknowledge the use of Servicio General de Apoyo a la Investigación-SAI at the University of Zaragoza.

References

- [1] J W Ekin, *Experimental techniques for low-temperature measurements*, Oxford University Press (2006).
- [2] V. Datskov, A. Bleile, E. Fischer, and G. Hess, *Conduction-Cooled HTS Current Leads for the SIS100 Corrector Magnets*, *IEEE T. on Appl. Supercond.* 28 (2018) 4801803.
- [3] A. Cubero, A.B. Núñez-Chico, R. Navarro, L.A. Angurel, E. Martínez, *Electromagnetic behaviour and thermal stability of a conduction-cooled, no-insulated 2G-HTS coil at intermediate temperatures*, *Cryogenics* 108 (2020) 103070.
- [4] A.L. Woodcraft, *Comment on 'thermal boundary resistance of mechanical contacts between solids at sub-ambient temperatures*, *J. Phys. D: Appl. Phys.* 34 (2001) 2932-2934.
- [5] E.T. Swartz and R.O. Pohl, *Thermal boundary resistance*, *Rev. Mod. Phys.* 61 (1989) 605-668.
- [6] L.J. Salerno, P. Kittle, and A.L. Spivak, *Thermal Conductance of Pressed Metallic Contacts Augmented with Indium Foil or Apiezon-NTM Grease at Liquid Helium Temperatures*, *NASA Technical Memorandum* 108779, July 1993.
- [7] E. Gmelin, M. Asen-Palmer, M. Reuther, and R. Villar, *Thermal boundary resistance of mechanical contacts between solids at sub-ambient temperatures*, *J. Phys. D: Appl. Phys.* 32 (1999) R19-R43.
- [8] R.C. Niemann, J.D. Gonczy, P.E. Phelan and T.H. Nicol, *Design and performance of low-thermal resistance, high-electrical-isolation heat intercept connections*, *Cryogenics* 35 (1995) 829-832.
- [9] J Pelegrín, G. Romano, E. Martínez, L. A. Angurel, R. Navarro, C. Ferdeghini, S. Brisigotti, G. Grasso and D. Nardelli, *Experimental and numerical analysis of quench propagation on MgB₂ tapes and pancake coils*, *Supercond. Sci. Technol.* 26 (2013) 045002.
- [10] S.-H. Jeong, J.-B. Song, K.L. Kim, Y.H. Choi, H. Lee, *Enhanced thermal properties of epoxy composite containing cubic and hexagonal boron nitride fillers for superconducting magnet applications*, *Compos. B Eng.* 107 (2016) 22-28.
- [11] G.A. Slack, *Nonmetallic Crystals with High Thermal Conductivity*, *J. Phys. Chem. Solids* 34 (1973) 321–335.
- [12] N.J. Simon, *Cryogenic Properties of Inorganic Insulation Materials for ITER Magnets*, *NISTIR 94-5030*, National Institute of Standards and Technology, Boulder, CO (1994).
- [13] M. Qina, H. Lua, H. Wua, Q. Hea, C. Liua, X. Mua, Y. Wanga, B. Jiaa, X. Qu, *A Powder injection molding of complex-shaped aluminium nitride ceramic with high thermal conductivity*, *J. Eur. Ceram. Soc.* 39 (2019) 952-956.
- [14] K. Takahata, H. Tamura, T. Mito, S. Imagawa, and A. Sagara, *A cooling concept for indirectly cooled superconducting magnet for the fusion reactor FFHR*, *Plasma Fusion Res.* 10 (2015) 3405011.
- [15] S. Sampath, *Thermal spray applications in electronics and sensors: Past, present, and future*, *J. Therm. Spray Technol.* 19 (2010) 921-949.
- [16] D. Tejero-Martin, M. Rezvani Rad, A. McDonald, T. Hussain, *Beyond Traditional Coatings: A Review on Thermal-Sprayed Functional and Smart Coatings* *J. Therm. Spray Technol.* 28 (2019) 598–644.
- [17] T.L. Mackay and A.N. Muller, *Plasma-Sprayed Dielectric Coatings for Heat Sinks in Electronic Packaging*, *Am. Ceram. Soc. Bull.*, 46 (1967), 833.

- [18] F.-L. Toma, L.-M. Berger, S. Scheitz, S. Langner, C. Rödel, A. Potthoff, V. Sauchuk, and M. Kusnezoff, Comparison of the microstructural characteristics and electrical properties of thermally sprayed Al₂O₃ coatings from aqueous suspensions and feedstock powders, *J. Therm. Spray Technol.*, 21 (2012) 480-488
- [19] N.R. Quick "Laser processed coatings on electronic circuit substrates" US patent 5,391,841 (1995)
- [20] R. Sivakumar & B. L. Mordike, Laser melting of plasma sprayed ceramic coatings, *Surf. Eng.* 4 (1988) 127-140.
- [21] Y. Yuanzheng, Z. Youlan, L. Zhengyi, Ch. Yuzhi, Laser remelting of plasma sprayed Al₂O₃ ceramic coatings and subsequent wear resistance, *Mater. Sci. Eng. A* 291 (2000) 168–172.
- [22] C. Batista, A. Portinha, R.M. Ribeiro, V. Teixeira, M.F. Costa, C.R. Oliveira, Morphological and microstructural characterization of laser-glazed plasma-sprayed thermal barrier coatings, *Surf. Coatings Technol.* 200 (2006) 2929-2937.
- [23] Y. Wang, C.G. Li, W. Tian, Y. Yang, Laser surface remelting of plasma sprayed nanostructured Al₂O₃–13wt%TiO₂ coatings on titanium alloy, *Appl. Surf. Sci.* 255 (2009) 8603–8610.
- [24] Y. Wang, C. Li, L. Guo, W. Tian, Laser remelting of plasma sprayed nanostructured Al₂O₃–TiO₂ coatings at different laser power, *Surf. Coatings Technol.* 204 (2010) 3559-3566.
- [25] J. Yu, Y. Wang, F. Zhou, L. Wang, Z. Pan, Laser remelting of plasma-sprayed nanostructured Al₂O₃–20 wt.% ZrO₂ coatings onto 316L stainless steel, *Appl. Surf. Sci.* 431 (2018) 112-121.
- [26] R. Krishnan, S. Dash, R. K. Sole, A. K. Tyagi, B. Raj, Fabrication and characterisation of laser surface modified plasma sprayed alumina coatings, *Surf. Eng.* 18 (2002) 208-212.
- [27] R. Krishnan, S. Dash, R. Kesavamoorthy, C. Babu Rao, A. K. Tyagi, B. Raj, Laser surface modification and characterization of air plasma sprayed alumina coatings, *Surf. Coatings Technol.* 200 (2006) 2791-2799.
- [28] F.E. de Freitas, F.P. Briguente, A.G.D. Reis, G. de Vasconcelos, D.A.P. Reis, Investigation on the microstructure and creep behavior of laser remelted thermal barrier coating, *Surf. Coatings Technol.* 369 (2019) 257-264.
- [29] N.K. Tolochko, T. Laoui, Y.V. Khlopkov, S.E. Mozzharov, V.I. Titov, M. B. Ignatiev, Absorbance of powder materials suitable for laser sintering, *Rapid Prototyping J.* 6 (2000) 155-160.
- [30] R.S. Pavlov, J. Guimbao, F. Ramos, Low-power laser-induced absorption in YSZ ceramics through formation of F-centers, *Opt. Laser. Technol.* 121 (2000) 105759
- [31] B. Qian, Z. Shen, Laser sintering of ceramics, *J. Asian Ceram. Soc.* 1 (2013) 315–321.
- [32] A.N. Samant, N. B. Dahotre, Laser machining of structural ceramics – A review, *J. Eur. Ceram. Soc.* 29 (2009) 969-993.
- [33] Z. Fan, M. Lu, H. Huang, Selective laser melting of alumina: A single track study, *Ceram. Intern.* 44 (2018) 9484-9493.
- [34] Y. Zheng, K. Zhang, T.T. Liu, W.H. Liao, C.D. Zhang, H. Shao, Cracks of alumina ceramics by selective laser melting, *Ceram. Int.* 45 (2019) 175-184.
- [35] S. Das, A.K. Nath, P.P. Bandyopadhyay, Online monitoring of laser remelting of plasma sprayed coatings to study the effect of cooling rate on residual stress and mechanical properties, *Ceram. Int.* 44 (2018) 7524-7534.
- [36] B.S. Yilbas, S.S. Akhtar, C. Karatas, Laser Cutting of alumina tiles: Heating and stress analysis, *J. Manuf. Process.* 15 (2013) 14-24.

- [37] Y.-C. Hagedorn, J. Wilkes, W. Wilhelm, K. Wissenbach, R. Poprawe, Net shaped high performance oxide ceramic parts by selective laser melting, *Phys. Procedia* 5 (2010) 587-594.
- [38] F. Rey-García, F. Gutiérrez-Mora, C.J. Borrell, L.C. Estepa, L.A. Angurel, G.F. de la Fuente, Microstructural characterization and tribological behavior of Laser Furnace processed ceramic tiles, *Ceram. Int.* 44 (2018) 6997-7005.
- [39] I.G. Cano, D. Dosta, J.R. Miguel, J.M. Guilemany, Production and characterization of metastable $\text{Al}_2\text{O}_3\text{-TiO}_2$ ceramic materials, *J. Mater. Sci.* 42 (2007) 9331-9335.
- [40] S. Dosta, M. Torrell, I.G. Cano, J.M. Guilemany, Functional colored ceramic coatings obtained by thermal spray for decorative applications, *J. Eur. Ceram. Soc.* 32 (2012) 3685-3692.
- [41] D. Rodriguez, I.G. Cano, J. Fernandez, J.C. Fariñas, R. Moreno, Rheological behaviour of submicron mullite carbon nanofiber suspensions for Atmospheric Plasma Spraying coatings, *J. Eur. Ceram. Soc.* 34 (2014) 475-483.
- [42] Y. Xian, P. Zhang, S. Zhai, P. Yuan, D. Yang, Experimental characterization methods for thermal contact resistance: A review, *Appl. Therm. Eng.* 130 (2018) 1530-1548
- [43] R. McPherson, Formation of metastable phases in flame- and plasma-prepared alumina, *J. Mater. Sci.* 8 (1973) 851-858.
- [44] J. Suffner, M. Latteman, H. Hahn, L. Giebeler, C. Hess, I. G. Cano, S. Dosta, J. M. Guilemany, C. Musa, A.M. Locci, R. Licheri, R. Orrú, G. Cao, Microstructure Evolution During Spark Plasma Sintering of Metastable $(\text{ZrO}_2\text{-}3 \text{ mol}\% \text{ Y}_2\text{O}_3)\text{-}20 \text{ wt}\% \text{ Al}_2\text{O}_3$ Composite Powders, *J. Am. Ceram. Soc.* 93 (2010) 2864-2870.
- [45] J. Suffner, H. Sieger, H. Hahn, S. Dosta, I.G. Cano, J.M. Guilemany, P. Klimczyk, L. Jaworska, Microstructure and mechanical properties of near-eutectic $\text{ZrO}_2\text{-}60\text{wt}\% \text{ Al}_2\text{O}_3$ produced by quenched plasma spraying, *Mater. Sci. Eng. A* 506 (2009) 180-186.
- [46] M. Plummer, The formation of metastable aluminas at high temperatures, *J. Appl. Chem.* 8 (1958) 35-44.

Publication D

Title:

Effects of laser-induced periodic surface structures on the superconducting properties of Niobium

Journal:

Applied Surface Science

A. Cubero, E. Martínez, L.A. Angurel, G.F. de la Fuente, R. Navarro, H. Legall, J. Krüger
and J. Bonse

Published, Applied Surface Science 508 (2020) 145140 (7pp)

DOI: [10.1016/j.apsusc.2019.145140](https://doi.org/10.1016/j.apsusc.2019.145140)

Impact factor (**JCR**, 2019): 6.182; Quartile Q1 (Materials Science, Coatings and Films)

SCImago Journal Rank (**SJR**, 2019): 1.23; Quartile Q1 (Surfaces, Coatings and Films)

A. Cubero, E. Martínez, L.A. Angurel, G.F. de la Fuente, R. Navarro, H. Legall, J. Krüger and J. Bonse, *Effects of laser-induced periodic surface structures on the superconducting properties of Niobium*. Applied Surface Science 508 (2020) 145140 (7pp)

Ultrashort pulsed lasers can easily induce the generation of (quasi-) periodic nanostructures (LIPSS, ripples) on the surface of different materials. In this work, pico- and femtosecond laser has been used to irradiate niobium sheets surfaces. The objective has been the characterization of the generated nanostructures and the study of their possible influence on the superconducting properties of niobium. This is the first work where the influence of surface nanostructure in superconducting properties has been observed. My contribution has been related with the laser processing of the samples and its characterization and with the original draft writing.



ELSEVIER

Contents lists available at ScienceDirect

Applied Surface Science

journal homepage: www.elsevier.com/locate/apsusc



Full Length Article

Effects of laser-induced periodic surface structures on the superconducting properties of Niobium

A. Cubero^a, E. Martínez^a, L.A. Angurel^{a,*}, G.F. de la Fuente^a, R. Navarro^a, H. Legall^b, J. Krüger^b, J. Bonse^b

^a ICMA (CSIC-University of Zaragoza), c/María de Luna 3, 50018 Zaragoza, Spain

^b Bundesanstalt für Materialforschung und -prüfung (BAM), Unter den Eichen 87, 12205 Berlin, Germany



ARTICLE INFO

Keywords

LIPSS
Femtosecond n-IR laser
Sub-nanosecond UV laser
Niobium
Superconductivity

ABSTRACT

It is well known that the use of ultrashort (fs) pulsed lasers can induce the generation of (quasi-) periodic nanostructures (LIPSS, ripples) on the surface of many materials. Such nanostructures have also been observed in sample's surfaces irradiated with UV lasers with a pulse duration of 300 ps. In this work, we compare the characteristics of these nanostructures on 1-mm and on 25- μm thick niobium sheets induced by 30 fs n-IR and 300 ps UV pulsed lasers. In addition to conventional continuous or burst mode processing configurations, two-dimensional laser beam and line scanning modes have been investigated in this work. The latter allows the processing of large areas with a more uniform distribution of nanostructures at the surface. The influence of the generated nanostructures on the superconducting properties of niobium has also been explored. For this aim, magnetic hysteresis loops have been measured at different cryogenic temperatures to analyse how these laser treatments affect the flux pinning behaviour and, in consequence, the superconductor's critical current values. It was observed that laser treatments are able to modify the superconducting properties of niobium samples.

1. Introduction

The generation of laser-induced periodic surface structures (LIPSS) is observed in many materials when their surface is irradiated using a linearly polarized laser [1,2]. In the last years the number of theoretical and experimental works increases continuously. Further on, it has been observed that these nanostructures feature new surface properties that are very useful in a wide range of applications, such as control of the colour [3], iridescence [3,4], wettability [5] or antibacterial properties [6], for example. Among the different laser processing parameters, the local fluence has been proven to influence strongly the morphology of the generated LIPSS, whose periodicity and orientation is also determined by the laser wavelength and the polarization. Besides, it has been observed that the laser incidence angle, the crystal orientation of the grains of the irradiated material, the presence of local defects, as well as the surface roughness can also modify the characteristics of these nanostructures [7–9].

Niobium is the pure metal presenting type II superconductivity with the highest critical temperature $T_c = 9.28$ K and critical magnetic fields [10]. It also may reach low microwave surface resistance, and therefore it is used to improve the efficiency of superconducting radio frequency

(SRF) cavities in particle accelerators [11]. The quality of Nb SRF resonators is strongly affected by the surface properties [12–14]. In addition to morphology issues, surface studies reveal the presence of oxides, hydrides and groups of hydrocarbons in the surface of high-purity niobium materials [15]. Commonly, chemical polishing or electrolytic polishing are used to reduce roughness and to remove surface contamination in order to improve the performance of Nb SRF cavities. Furthermore, niobium alloys have been used in the last decades in the fabrication of superconducting coils. In type II superconducting materials, magnetic fields above a certain threshold field value, named *lower critical field* (H_{c1}), penetrate the material forming a lattice of quantized line vortices. Upon increasing the magnetic field, the number of vortices increases and the distance between them reduces. Finally, at an *upper critical field* H_{c2} , the vortex lattice collapses and the bulk superconducting state disappears. At intermediate magnetic fields, when a current is applied to the superconductor, a Lorentz force acts on the vortices, which may cause them to move generating a dissipative voltage. To avoid this, a network of defects has to be generated in the superconductor to locally pin the vortex lattice.

The potential use of ultrashort laser pulse sources for high-speed manufacturing of periodic nanostructures (LIPSS) as pure surface

* Corresponding author.

E-mail address: angurel@unizar.es (L.A. Angurel).

<https://doi.org/10.1016/j.apsusc.2019.145140>

Received 18 September 2019; Received in revised form 7 December 2019; Accepted 19 December 2019

Available online 20 December 2019

0169-4332/ © 2019 The Author(s). Published by Elsevier B.V. This is an open access article under the CC BY-NC-ND license (<http://creativecommons.org/licenses/by-nc-nd/4.0/>).

defects and how they can modify the surface characteristics, and in consequence, the superconducting properties, is the main aim of this research. With this aim in mind, an analysis of the different surface morphologies that can be generated by fs n-IR and ps UV lasers on the Nb surfaces, both in beam and line scan mode [16,17] is presented in this paper. Representative samples were chosen in order to check whether the superconducting properties of the laser treated samples had been modified in comparison with the original ones.

2. Experimental

Laser irradiation experiments have been performed on 1-mm thick Nb sheets (99.9% purity, Goodfellow) and on 25- μm thick Nb foils (99.8% purity, Alfa Aesar) with a surface micro-roughness of 0.25 μm . A picosecond UV laser (Rofin-Sinar - wavelength $\lambda = 355 \text{ nm}$, pulse duration $\tau_p = 300 \text{ ps}$, $1/e^2$ beam diameter $D_b = 34 \mu\text{m}$, and pulse repetition frequencies $f = 250\text{--}800 \text{ kHz}$) and a femtosecond n-IR Ti:Sapphire laser (Femtolasers Compact Pro - wavelength $\lambda = 790 \text{ nm}$, pulse duration $\tau_p = 30 \text{ fs}$, $1/e^2$ beam diameter $D_b = 130 \mu\text{m}$, and pulse repetition frequency $f = 1 \text{ kHz}$) were used to scan the surface of the samples.

In the ps UV laser facility, the beam is moved using an optical beam steering system at a given speed, using two different scanning protocols: i) *Beam scanning mode*. The sample has a fixed position and the laser scans across the surface, controlling the overlapping between successive laser scans. ii) *Line scanning mode*. The laser spot moves in a given direction writing a line of length l_s for a given number of times, while the sample is moving in the perpendicular direction. In this mode, the distance between two laser-line scans is controlled by adjusting the laser scanning speed, the length of the line and the sample traverse speed.

In the fs n-IR laser facility, the laser beam focus position is fixed and the sample describes a meandering movement in two perpendicular directions. In one direction the sample velocity is set constant in order to control the spatial overlapping between successive laser dots, while in the other orthogonal direction, the distance between successive lines is also controlled.

Using the ps UV laser, the sample can be placed inside a processing chamber and the laser goes in through an optical window allowing the control of the gas atmosphere during the laser treatment. In 1 mm thick samples the irradiation was performed in N_2 atmosphere, while the 25 μm thick samples were processed in ambient air in order to have similar processing conditions with both laser systems.

The generated surface nanostructures are imposed by the individual characteristics of each laser beam, but also by cumulative effects due to the overlapping of successive laser spots along a line and the lateral distance between successive lines [18,19]. In order to characterize the laser treatments, several parameters have been defined:

Pulse fluence: Energy per unit area of a given pulse, $F_p = \langle P \rangle f / A_b$, where P is the average laser power, f is the pulse repetition frequency and A_b the cross-section of the laser beam at the sample.

Pulse irradiance: Power per unit area of a given pulse, $I_p = F_p / \tau_p$, where τ_p is the pulse duration.

Effective number of pulses in a line: The effective number of pulses received by any point of the surface scanned in an isolated line is given by $N_L = D_b / d_b = D_b f / v_s$, where d_b is the displacement of two successive dot centres and, v_s the laser beam scanning velocity. N_L is a measure of the number of pulses that overlap and has manufacture relevance because it controls the homogeneity of the total fluence along the line.

Average cumulative energy per unit area in a line, F_L : Total energy per unit area when laser beam scans in one direction taking into account the average fluence of the individual pulse and the pulse to pulse overlap in this direction, $F_L = N_L F_p$.

Effective number of line scans. The effective number of scans that affect any point of the final scanned surface is given by $N_S = D_b / d_s$,

where d_s corresponds to the distances of the centres of two successive scanning lines. If the laser line scan mode is used, v_s defines the sample velocity and t_s the time that the laser needs to completely scan a line, $N_S = D_b / d_s = D_b / (v_s t_s)$. N_S controls the total fluence homogeneity in the direction perpendicular to the scanned lines.

The surface morphology of the irradiated samples was analysed by scanning electron microscopy (SEM) in a field-emission scanning electron microscope (FE-SEM, Carl Zeiss MERLIN) using secondary electrons (SE) and in-lens secondary electron detectors. Nanostructure periodicity has been determined by measuring in several regions of the images the distance to cover several consecutive periods. Chemical surface characterization was performed by energy dispersive X-ray analysis (EDX, INCA350 Oxford Instruments) employing electron acceleration voltages of 5 kV. Atomic force microscopy (AFM) measurements were performed with a scanning probe microscope (SPM) Ntegra Aura system of NT-MDT. The analysis of the AFM measurements was carried out using Gwyddion software (version 2.53). Finally, the superconducting properties of selected samples were analysed using a SQUID-based Quantum Design MPMS-5T system performing DC magnetic $M(H)$ measurements at constant temperature in zero magnetic field cooling conditions. For the latter purpose, the representative samples studied were cut in rectangular shape with dimensions ranging between 3 and 4 mm.

3. Initial experiments in 1-mm thick Nb samples

Initial experiments were performed on 1-mm thick samples. Before laser treatments, sample surfaces were polished with sand paper and Al_2O_3 -based polishing suspensions. Samples C1 and C2 were processed with the 300 ps UV laser inside the chamber in a N_2 atmosphere (1.4 atm) with the particular parameters recorded in Table 1. The samples showed here have been processed using the laser *line scanning mode* [16,17] with a sample traverse velocity of $v_s = 0.04 \text{ mm/s}$ that would be equivalent to a *beam scanning mode* with $d_s = 5 \mu\text{m}$. The pulse irradiance I_p was set to similar vales in both samples, but the higher N_L gives laser conditions slightly more intense for sample C2.

Fig. 1 shows the typical nanostructures obtained in these samples after the applied laser surface treatment. Sample C1 (Fig. 1a) exhibits rippled nanostructures with spatial periodicity $\Lambda_{\text{LIPSS}} = 276 \pm 13 \text{ nm}$, between the neighbouring nanostructures observed in the SEM micrograph. This value is very close to the laser wavelength, and the orientation of these structures is almost perpendicular to the laser polarization direction. It should be pointed out that the structure of the ripples is not smooth, but accompanied by some drop-like protrusions that appear in the SEM micrographs as small circles. Their appearance is consistent with the melting of a thin layer of the sample during the laser scanning and the alignment of small volumes (micro-drops) of molten material with the ripples. Sample C2 (Fig. 1b), processed with slightly more intense conditions, also presents well-defined nano-protrusions along the ripples, with $\Lambda_{\text{LIPSS}} = 294 \pm 8 \text{ nm}$, similar to sample C1. It should be remarked that those of nearest ripples interact, inducing a certain degree of order in the direction perpendicular to the ripples.

EDX measurements indicate that, during the laser treatment with the ps UV laser in a N_2 atmosphere, the amount of oxygen in the surface of the sample is slightly reduced. Before laser treatment, the ratio O/Nb in atomic percentage is 0.41 ± 0.05 , a value that reduces down to

Table 1
Laser processing parameters used on 1-mm thick Nb samples irradiated with the ps UV laser in N_2 atmosphere.

Sample	P (W)	f (kHz)	v_s (mm/s)	d_s (μm)	I_p (GW/cm^2)	N_L	N_S
C1	0.85	700	300	5	0.45	79	7
C2	1	800	300	5	0.46	91	7

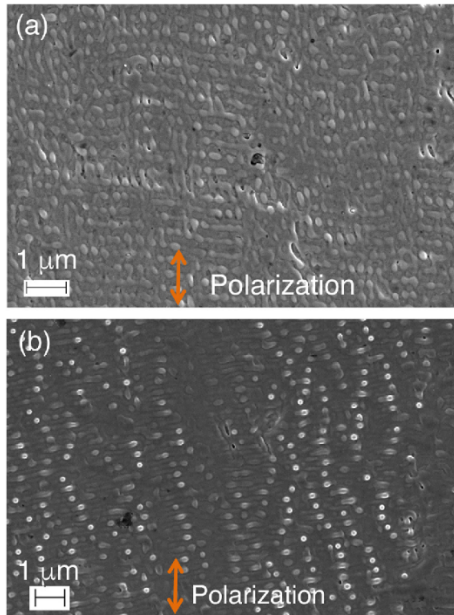


Fig. 1. Nanostructures obtained in 1-mm thick Nb samples C1 (a) and C2 (b) processed in N_2 atmosphere. The arrows indicate the laser polarization direction.

0.34 ± 0.01 after laser interaction.

Self-organized multiscale surface structures similar to those presented in Fig. 1 have been observed in thin films of metals [20] and oxides [21] deposited on glass and on metallic sheets. These were observed upon irradiation by superposition, on the same spot, of series of tens to hundreds of UV laser shots with fs and ps pulse duration. In some cases, these structures were also observed in larger areas obtained by laser beam scanning [21]. This self-organization may be affected by the minimization of the free-surface energy, needs the presence of a fluid phase (molten material) and evolves with the number of shots. In our case, this fluid phase is easily obtained due to the higher pulse duration, the high absorption coefficient and the low penetration depth that characterize the interaction with the UV radiation [22]. When the temperature changes substantially along the target surface, the gradients of the surface tension, $\nabla\gamma$, result in thermocapillary forces, which can move the fluid from the hot regions to the cold ones. This phenomenon is known as the Marangoni effect or capillary motion [23]. These gradients produce the flow of molten liquids away from areas with higher laser intensity. The self-organized structures evolve with the overlap of subsequent pulses.

The effect of the generated periodic surface nanostructures on the superconducting properties of Nb can be analysed from the magnetic hysteresis curves, $M(H)$. Fig. 2a compares the measured curves at $T = 8$ K for a sample whose top and bottom surfaces were irradiated with laser conditions C1, and for a polished non-treated reference (original) sample. In the first quadrant of Fig. 2a, the $M(H)$ dependence in the original sample is linear in a broad range of magnetic field values, whereas in the laser treated C1 sample, a small kink at about 0.05 T is observed. It is important to recall here that the width of the magnetic hysteresis loops, $\Delta M(H)$, which is defined as the difference between the descending- and the ascending-branch magnetization, is proportional to the critical current density, $J_c(H)$ [24,25]. J_c is

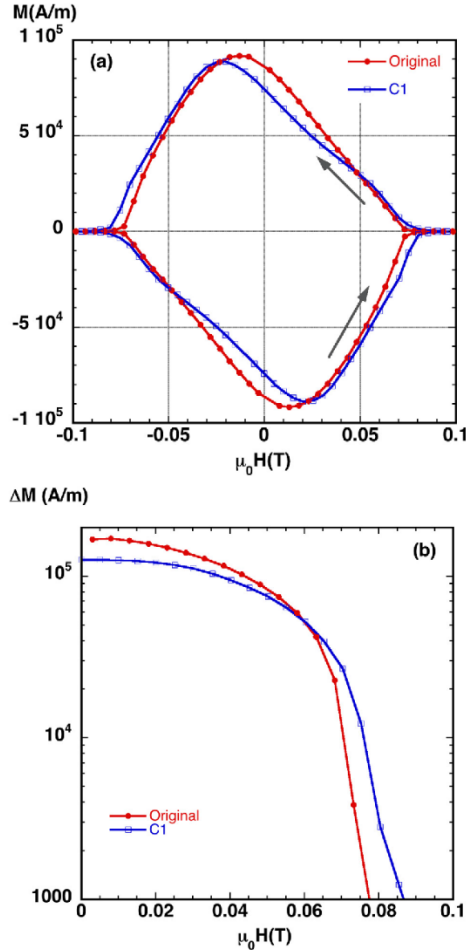


Fig. 2. (a) Magnetic hysteresis loops measured at 8 K in an original reference sample and in sample C1 of 1-mm thickness. The magnetic field, H , was applied perpendicular to the surfaces. Arrows indicate field sweep directions. (b) Magnetic field dependence of the width of hysteresis loops, $\Delta M(H)$, of the same samples, calculated as explained in text.

determined by the ability of the material to trap vortices (flux vortex pinning) and therefore it is strongly dependent on the material defects structure that are able to pin the vortices, such as nano-sized impurities, dislocations or grain boundaries. Fig. 2b compares the $\Delta M(H)$ curves for both samples. It is clearly observed that the ps-laser treatment has produced some changes in the superconducting properties of the processed sample compared to the reference one, with a small reduction of the ΔM values at low fields, and an increase at magnetic fields above 0.6 T. Obviously, the ps-laser treatment only affects a very thin surface layer, whereas ΔM values are also associated to bulk pinning effects. For this reason, we decided to continue this work in 25 μm thick samples, in order to improve the ratio between surface and bulk effects.

Table 2
Laser processing parameters used in 25 μm thick Nb samples irradiated with the fs n-IR and with the ps UV lasers (PS and PS, respectively).

Sample	P (W)	f (kHz)	v_t (mm/s)	d_t (μm)	F_p (J/ cm^2)	I_p (GW/ cm^2)	N_t	N_s
FS1	0.012	1	6	20	0.09	3014	20	7
FS2	0.015	1	6	20	0.11	3767	20	7
FS3	0.020	1	6	20	0.15	5023	20	7
PS1	0.5	600	600	5	0.1	0.32	34	7
PS2	1.1	300	300	7	0.4	1.35	34	5
PS3	1.1	300	300	3	0.4	1.35	34	11

4. Comparison of nanostructures in 25 μm thick foils using fs n-IR and ps UV lasers

A systematic search of different nanostructures generated on the Nb surface by irradiation with these two laser systems has been done. Due to the large difference in the pulse duration in both lasers, the pulse

irradiance is three orders of magnitude higher for the fs n-IR laser and only comparisons of samples with similar fluence values are possible. In addition, due to the difference in pulse duration, thermal processes are more relevant when the ps UV laser is used. The laser parameters used in the processing of the samples analysed in this contribution are compiled in Table 2.

4.1. Nanostructures generated with the fs n-IR and ps UV laser

The top-view SEM micrographs collected in Fig. 3 compare the surface microstructures of the samples chosen in Table 2. Furthermore, details of some of these nanostructures are presented in Fig. 4. In the case of the samples processed with the fs n-IR laser, surface modification starts when a pulse fluence of 0.09 J/cm² is reached (Fig. 3a). The initial features generated on the irradiated samples are small surface structures, parallel to the laser polarization direction with a periodicity close to 40 nm (Fig. 4a). This structure can be considered as a type of high spatial frequency LIPSS (HSFL). When the pulse fluence increases up to 0.11 J/cm², the typical low spatial frequency LIPSS (LSFL) that

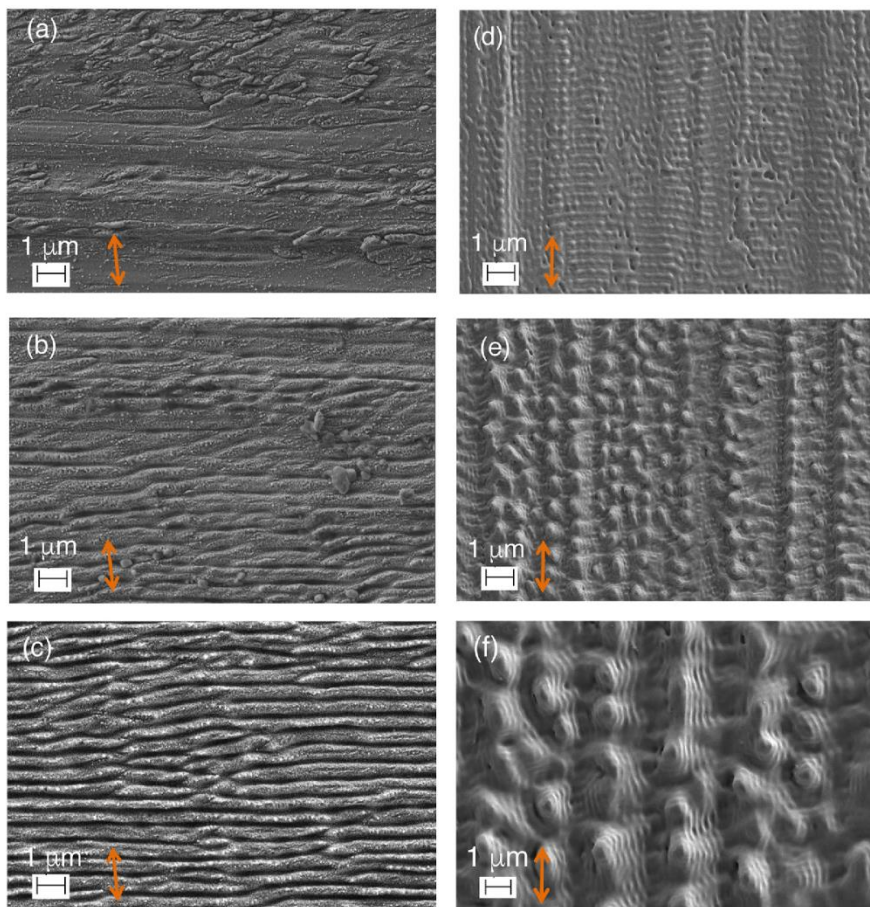


Fig. 3. SEM images showing the nanostructures obtained in 25- μm thick Nb foils processed with the fs n-IR laser: samples PS1 (a), PS2 (b) and PS3 (c) and with the ps UV laser: samples PS1 (d), PS2 (e) and PS3 (f). The arrows indicate the laser polarization direction.

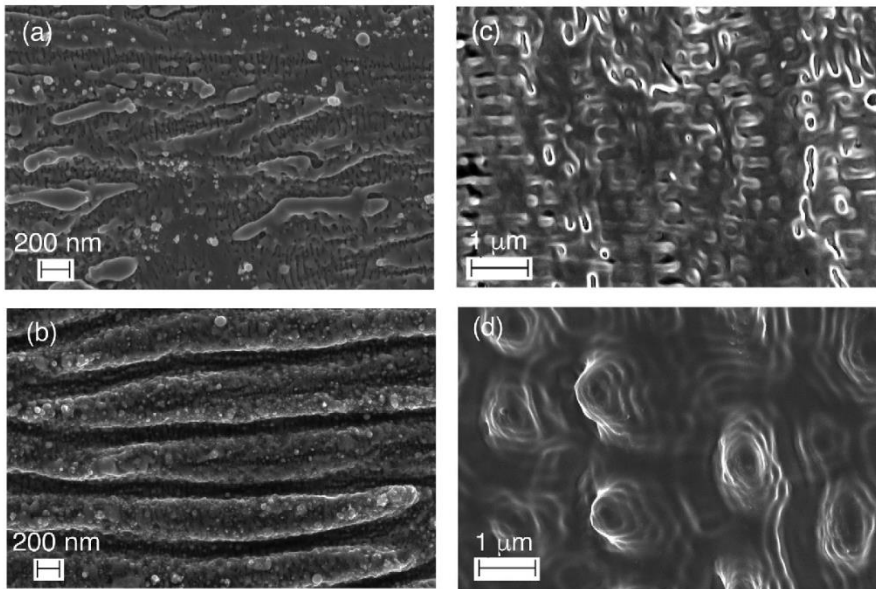


Fig. 4. SEM micrographs showing details of the nanostructures generated in some of the samples: PS1 (a), FS3 (b), PS1 (c) and PS3 (d) shown in Fig. 3.

are observed in many metals [2,26] and in Nb [27], in particular when irradiated with fs laser pulses, have been generated (Fig. 3b). The HSFL nanostructures observed in sample FS1 are detected between two of these LSFL structures. Increasing the irradiance, these LSFL are more pronounced at the surface (Figs. 3c and 4b). The images clearly show that melting effects are negligible with this laser. With the low pulse repetition frequency (1 kHz), the time between two consecutive laser pulses is 1 ms, much larger than the typical relaxation times (10–30 ps). In consequence, once a given fluence threshold is surpassed, an individual pulse modifies the surface, as well as the material absorption for the following pulse.

The UV laser is characterized by a pulse duration of 300 ps. In consequence, thermal processes are relevant. In addition, this laser system operates at high pulse repetition frequencies and, in consequence, the time between two consecutive pulses is in the range of 1–4 μs. Furthermore, the time between two scanning lines is in the order of 1–10 ms. For the nanostructure generation process the cumulative effect of the different pulses during a given line scan is the main parameter that defines the final surface structure. The generated nanostructure modifies the laser absorption during the next laser scan cycle, slowly changing the aspect of the final surface nanostructure. It has been established that the minimum value of F_L to generate nanostructures here is $2.26 \pm 0.07 \text{ J/cm}^2$.

Fig. 3(d–f) shows the surfaces of the three samples collected in Table 2. Sample PS1 (Figs. 3d and 4c), which has been processed with a value of $F_L = 3.31 \text{ J/cm}^2$, close to the LIPSS threshold, exhibits a ripple nanostructure. In case of samples PS2 (Fig. 3e) and PS3 (Figs. 3f and 4d), the pulse repetition frequency has been reduced to 300 kHz. Using similar laser power levels, the pulse fluence and, in consequence, the pulse irradiance values are increased and F_L reaches values of 13.73 J/cm^2 . These conditions generate new structures, denominated here as microprotrusions, with distances between two maxima in the order of 1–2 μm. In the case of sample PS2 ($N_S = 5$), the laser irradiation conditions produce a structure that is intermediate between the ripples and the microprotrusions that are predominant in sample PS3

($N_S = 11$). Fig. 4d also shows that inside these protrusions there is a nanostructure with a periodicity very close to the UV laser wavelength.

The characteristics of the different surface nanostructures generated by fs n-IR and ps UV laser irradiation have been further analysed by AFM measurements in samples FS3 and PS1. The results shown in Fig. 5 correspond to AFM topographies and their corresponding line profiles obtained for samples FS3 (upper figures) and PS1 (lower figures). It can be seen that the structures of the FS3 sample have a periodicity of $515 \pm 70 \text{ nm}$, approximately 65% of the laser wavelength, and a depth of $150 \pm 25 \text{ nm}$ (distance between peak to valley). Sample PS1 exhibits a periodicity of $337 \pm 25 \text{ nm}$, very close to the used UV laser wavelength (355 nm), and the ripples have considerably lower depth values ($18 \pm 5 \text{ nm}$) than for sample FS3. It is worth noting that the structure of line profiles is quite different in both cases, since for sample PS1, valleys and peaks are very similar following a sinusoidal-type curve, whereas sample FS3 shows rather flat peaks with sharper valleys. The different characteristics of the generated periodic structures, with elongated grooves for fs n-IR laser irradiated samples that contrasts with the two-dimensional periodicity for the sample irradiated with ps UV laser, can be clearly observed in the insets of Fig. 5a and c. These show 2D-Fourier transforms of the AFM surface area images of samples FS3 and PS1, respectively.

4.2. Comparison of the superconducting behaviour of samples processed with the two lasers

Fig. 6 represents the $\Delta M(H)$ curves as a function of the applied magnetic field for the 25 μm-thick irradiated FS3 and PS1 samples, together with the results obtained for an original reference, nontreated sample, for comparison. These values were obtained as explained in Section 3 from $M(H)$ hysteresis loops measured at 7 K, applying the magnetic field perpendicular to the irradiated surfaces. Note that both the top and bottom surfaces of the samples were irradiated with the laser. It can be seen that the laser irradiation produces changes in the superconducting properties of the samples. An increase of ΔM values is

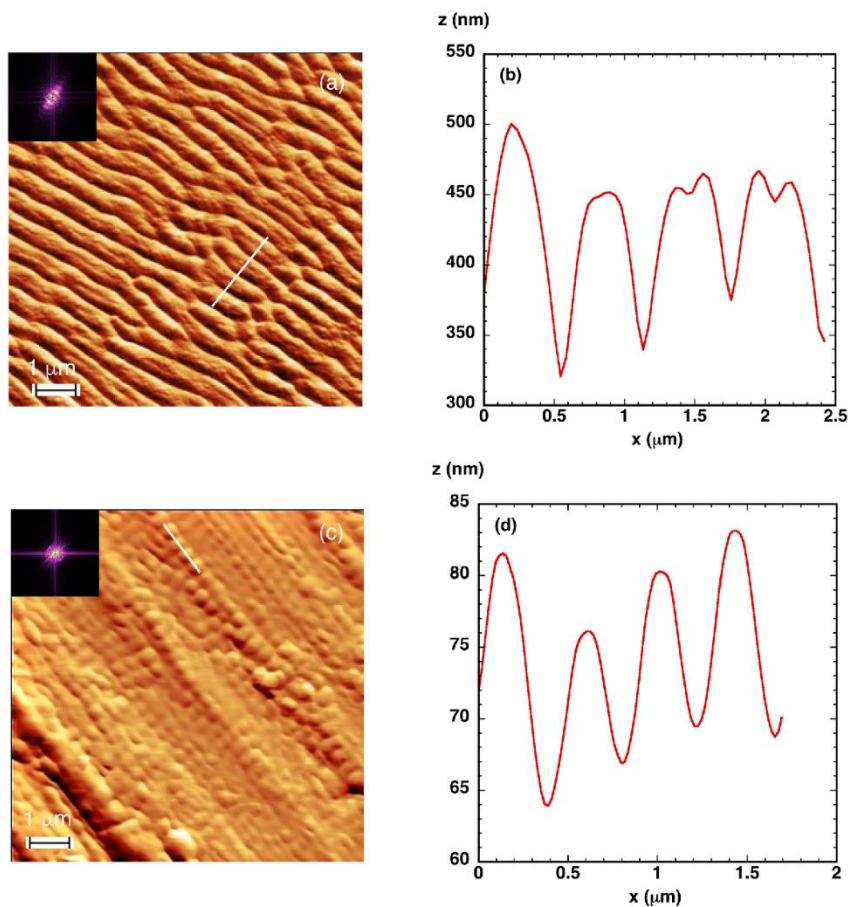


Fig. 5. AFM topography (a, c) and line profile (b, d) of samples PS3 (a, b) and PS1 (c, d). Insets in (a) and (c) are the 2D-Fourier transforms of the corresponding AFM images and the lines mark the regions where the profiles have been measured.

thus observed in sample FS3 for $\mu_0 H < 0.1$ T, whereas a decrease is observed for sample PS1. These results show that laser processing is able to modify the superconducting properties of Nb films either by introducing new defects that are able to create additional vortex pinning centres, or by producing a decrease in the number of vortex pinning centres (cleaner surface). The strong change in the irradiance of both used lasers, which are three orders of magnitude higher for FS than for PS samples, produces surface structures one order of magnitude deeper in the former case. Since a larger depth of material near the surface is affected, more effective pinning is expected for FS samples, in agreement with the results shown in Fig. 6. The observed differences in ΔM imply that surface flux pinning plays an important role in Nb [12]. This behaviour thus suggests that the laser surface treatments herewith presented open new possibilities to control the pinning properties of Nb thin samples in large areas, offering the potential for scale-up to continuous manufacture processes.

5. Conclusions

Differences in pulse width and in pulse repetition frequency values between the fs n-IR and the ps UV lasers employed in this study induce sample irradiation conditions where laser pulse irradiance values differ by more than three orders of magnitude. The latter induce very different nanostructures in Nb foil surfaces. When the fs n-IR laser is used, the nanostructures observed evolve from a HSFL to a LSFL type. In the case of the ps UV laser, the induced surface features initially appear with a ripple nanostructure where some nanoprotusions start to form and evolve, as the laser intensity is increased, into micro-protrusions. The use of a laser line scanning configuration allows obtaining uniform nanostructures in large areas.

The study of magnetic properties proves that the laser irradiated samples exhibit slightly higher critical current density values in a particular range of magnetic fields, in comparison with reference non-treated samples. This is observed even in the case of 1 mm thick samples, thus opening the possibility to develop a simple, dry and scalable method for improving superconductors at the manufacture level.

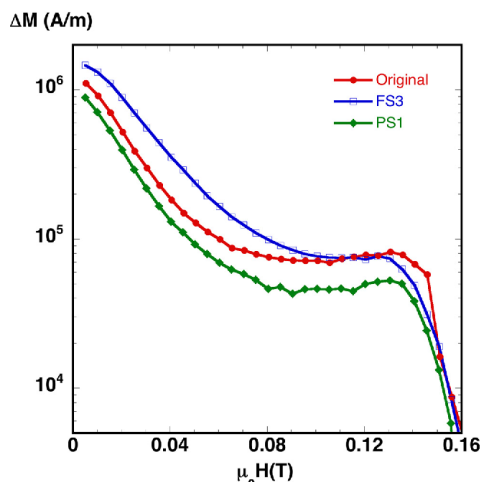


Fig. 6. Magnetic field dependence of the width of the magnetization hysteresis loops, $\Delta M(H)$, measured at 7 K for 25 μm -thick Nb samples: FS3 (processed with the fs n-IR), PS1 (processed ps UV laser) and original (non-treated). The laser conditions are collected in Table 2.

CRediT authorship contribution statement

A. Cubero: Investigation, Formal analysis, Writing - original draft. **E. Martínez:** Methodology, Investigation, Supervision, Writing - review & editing, Project administration. **L.A. Angurel:** Conceptualization, Methodology, Resources, Investigation, Writing - review & editing, Project administration. **G.F. de la Fuente:** Conceptualization, Methodology, Resources, Writing - review & editing. **R. Navarro:** Conceptualization, Writing - review & editing. **H. Legall:** Resources, Writing - review & editing. **J. Krüger:** Resources, Writing - review & editing, Project administration. **J. Bonse:** Investigation, Software, Resources, Methodology, Writing - review & editing, Project administration.

Declaration of Competing Interest

The authors declare that they have no known competing financial interests or personal relationships that could have appeared to influence the work reported in this paper.

Acknowledgements

The authors gratefully acknowledge the financial support from MINECO-AEI-FEDER (project ENE2017-83669-C4-1) and from Gobierno de Aragón “Construyendo Europa desde Aragón” (research group T54_17R). Authors also would like to acknowledge the use of Servicio General de Apoyo a la Investigación-SAI, Universidad de Zaragoza.

References

[1] H.M. van Driel, J.E. Sipe, J.F. Young, Laser-induced periodic surface structure on

solids: a universal phenomenon, *Phys. Rev. Lett.* 49 (1982) 1955–1958.

[2] J. Bonse, S. Höhm, S.V. Kirner, A. Rosenfeld, J. Krüger, Laser-induced periodic surface structures – a scientific evergreen, *IEEE J. Sel. Top. Quant. Electron.* 23 (2017) 9000615.

[3] Y.M. Andreeva, V.C. Luong, D.S. Lutoshina, O.S. Medvedev, V.Yu. Mikhailovskii, M.K. Moskvina, G.V. Odintsova, V.V. Romanov, N.N. Shchedrina, V.P. Velko, Laser coloration of metals in visual art and design, *Opt. Mater. Exp.* 9 (2019) 1310–1319.

[4] E.I. Ageev, V.P. Velko, E.A. Vlasova, Y.Y. Karlagina, A. Krivosonov, M.K. Moskvina, G.V. Odintsova, V.E. Pshenichnov, V.V. Romanov, R.M. Yatsuk, Controlled nanostructures formation on stainless steel by short laser pulses for products protection against falsification, *Opt. Exp.* 26 (2018) 2117–2122.

[5] J.M. Romano, A. García-Girón, P. Penchev, S. Dimov, Triangular laser-induced submicron textures for functionalising stainless steel surfaces, *Appl. Surf. Sci.* 440 (2018) 162–169.

[6] A.H.A. Lutey, L. Gemini, L. Romoli, G. Lazzini, F. Fusco, M. Faucon, R. Kling, Towards laser-textured antibacterial surfaces, *Sci. Rep.* 8 (2018) 10112.

[7] L. Jiang, W. Han, X. Li, Q. Wang, F. Meng, Y. Li, Crystal orientation dependence of femtosecond laser-induced periodic surface structure on (100) silicon, *Opt. Lett.* 39 (2014) 3114–3117.

[8] X. Sedao, C. Maurice, F. Garrelle, J.P. Colombier, S. Reynaud, R. Query, F. Pigeon, Influence of crystal orientation on the formation of femtosecond laser-induced periodic surface structures and lattice defects accumulation, *Appl. Phys. Lett.* 104 (2014) 171605.

[9] C. Li, G.H. Cheng, J.P. Colombier, N. Faure, S. Reynaud, H. Zhang, D. Jamon, R. Stoian, Impact of evolving surface nanoscale topologies in femtosecond laser structuring of Ni-based superalloy CMSX-4, *J. Opt.* 18 (2016) 015402.

[10] J. Eisenstein, Superconducting elements, *Rev. Mod. Phys.* 26 (1954) 277–291.

[11] P. Kumar, High purity niobium for superconducting applications, *Jour. Less Com. Met.* 139 (1988) 149–158.

[12] S. Casalbuoni, E.A. Knabbe, J. Kötzler, L. Lilje, L. von Sawilski, P. Schmäser, B. Steffen, Surface superconductivity in niobium for superconducting RF cavities, *Nucl. Instrum. Meth. Phys. Res. A* 538 (2005) 45–64.

[13] Z.-H. Sung, A. Dzyuba, P.J. Lee, D.C. Larbalestier, L.D. Cooley, Evidence of incomplete annealing at 800 °C and the effects of 120 °C baking on the crystal orientation and the surface superconducting properties of cold-worked and chemically polished Nb, *Supercond. Sci. Technol.* 28 (2015) 075003.

[14] H. Padamsee, 50 years of success for SRF accelerators—a review, *Supercond. Sci. Technol.* 30 (2017) 053003.

[15] N. Singh, M.N. Deo, M. Nand, S.N. Jha, S.B. Roy, Raman and photoelectron spectroscopic investigation of high-purity niobium materials: oxides, hydrides, and hydrocarbons, *J. Appl. Phys.* 120 (2016) 114902.

[16] V.V. Lennikov, B. Özkurt, L.A. Angurel, A. Sotelo, B. Özçelik, G.F. de la Fuente, Microstructure and transport properties of Bi-2212 prepared by CO₂ laser line scanning, *J. Supercond. Novel Magn.* 26 (2013) 947–952.

[17] K. Öztürk, C. Aksoy, L.A. Angurel, B. Savaskan, E. Martínez, A. Badía-Majós, G.F. de la Fuente, B. Güner, C.E.J. Dancer, S. Celik, IR laser line scanning treatments to improve levitation forces in MgTi_{0.96}B₂ bulk materials, *J. Alloys Comps.* 811 (2019) 151966.

[18] M. García-Lechuga, D. Puerto, Y. Fuentes-Edfuf, J. Solís, J. Siegel, Ultrafast moving-spot microscopy: birth and growth of laser-induced periodic surface structures, *ACS Photo.* 3 (2016) 1961–1967.

[19] Y. Fuentes-Edfuf, J.A. Sánchez-Gil, C. Florian, V. Giannini, J. Solís, J. Siegel, Surface plasmon polaritons on rough metal surfaces: role in the formation of laser-induced periodic surface structures, *ACS Omega* 4 (2019) 6939–6946.

[20] T.T.D. Huynh, N. Semmar, Dependence of ablation threshold and LIPSS formation on copper thin films by accumulative UV picosecond laser shots, *Appl. Phys. A* 116 (2014) 1429–1435.

[21] A. Talbi, C. Tefiffo Tameko, A. Stolz, E. Millon, C. Boulmer-Leborgne, N. Semmar, Nanostructuring of titanium oxide thin film by UV femtosecond laser beam: From one spot to large surfaces, *Appl. Surf. Sci.* 418 (2017) 425–429.

[22] C. Acosta-Zepeda, P. Saavedra, J. Bonse, E. Haro-Poniatowski, Modelling of silicon topographies induced by single nanosecond laser pulse induced melt-flows, *J. Appl. Phys.* 125 (2019) 175101.

[23] M. Gedvilas, G. Raciukaitis, V. Kucikas, K. Regulekis, Driving forces for self-organization in thin metal films during their partial ablation with a cylindrical focused laser beam, *AIP Conf. Proc.* 1464 (2012) 229–243.

[24] C.P. Bean, Magnetization of high-field superconductors, *Rev. Mod. Phys.* 36 (1964) 31–39.

[25] E.H. Brandt, Electric field superconductors with rectangular cross section, *Phys. Rev. B* 52 (1995) 15442–15457.

[26] U. Hermens, S.V. Kirner, C. Emonts, P. Comanns, E. Skoulas, A. Mimidis, H. Mescheder, K. Winands, J. Krüger, E. Stratakis, J. Bonse, Mimicking lizard-like surface structures upon ultrashort laser pulse irradiation of inorganic materials, *Appl. Surf. Sci.* 418 (2017) 499–507.

[27] C. Kunz, J.F. Bartolomé, E. Gnecco, F.A. Müller, S. Graf, Selective generation of laser-induced periodic surface structures on Al₂O₃-ZrO₂-Nb composites, *Appl. Surf. Sci.* 434 (2018) 582–587.

Publication E

Title:

Surface Superconductivity Changes of Niobium Sheets by Femtosecond Laser-Induced Periodic Nanostructures

Journal:

Nanomaterials

A. Cubero, E. Martínez, L.A. Angurel, G.F. de la Fuente, R. Navarro, H. Legall, J. Krüger
and J. Bonse

Published, Nanomaterials 10 (**2020**) 2525

DOI: 10.3390/nano10122525

Impact factor (**JCR**, 2019): 4.324; Quartile Q2 (Materials Science, Multidisciplinary)

SCImago Journal Rank (**SJR**, 2019): 0.858; Quartile Q1 (Materials Science)

A. Cubero, E. Martínez, L.A. Angurel, G.F. de la Fuente, R. Navarro, H. Legall, J. Krüger and J. Bonse, *Surface Superconductivity Changes of Niobium Sheets by Femtosecond Laser-Induced Periodic Nanostructures*. *Nanomaterials* 10 (2020) 2525.

Surface superconducting properties of niobium samples after different laser processes have been studied. Based on previous works, femtosecond lasers have been used to induce well-organized nanostructures over niobium surfaces. The possible influence of the present atmosphere during the laser treatment has also been analysed. In addition to magnetic measurements, chemical and morphological surface characterization has been done. My contribution has been related with laser processing of the samples and posterior analysis and also with the original draft writing.



Article

Surface Superconductivity Changes of Niobium Sheets by Femtosecond Laser-Induced Periodic Nanostructures

Álvaro Cubero ¹, Elena Martínez ^{1,*}, Luis A. Angurel ¹, Germán F. de la Fuente ¹,
Rafael Navarro ¹, Herbert Legall ², Jörg Krüger ² and Jörn Bonse ²

¹ Instituto de Nanociencia y Materiales de Aragón (INMA), CSIC-Universidad de Zaragoza, 50009 Zaragoza, Spain; acubero@unizar.es (A.C.); angurel@unizar.es (L.A.A.); german.delafuente.leis@csic.es (G.F.d.l.F.)

² Bundesanstalt für Materialforschung und -prüfung (BAM), Unter den Eichen 87, 12205 Berlin, Germany; herbert.legall@bam.de (H.L.); joerg.krueger@bam.de (J.K.); joern.bonse@bam.de (J.B.)

* Correspondence: elenamar@unizar.es

Received: 23 November 2020; Accepted: 14 December 2020; Published: 16 December 2020



Abstract: Irradiation with ultra-short (femtosecond) laser beams enables the generation of sub-wavelength laser-induced periodic surface structures (LIPSS) over large areas with controlled spatial periodicity, orientation, and depths affecting only a material layer on the sub-micrometer scale. This study reports on how fs-laser irradiation of commercially available Nb foil samples affects their superconducting behavior. DC magnetization and AC susceptibility measurements at cryogenic temperatures and with magnetic fields of different amplitude and orientation are thus analyzed and reported. This study pays special attention to the surface superconducting layer that persists above the upper critical magnetic field strength H_{c2} , and disappears at a higher nucleation field strength H_{c3} . Characteristic changes were distinguished between the surface properties of the laser-irradiated samples, as compared to the corresponding reference samples (non-irradiated). Clear correlations have been observed between the surface nanostructures and the nucleation field H_{c3} , which depends on the relative orientation of the magnetic field and the surface patterns developed by the laser irradiation.

Keywords: niobium; surface superconductivity; laser-induced periodic surface structures (LIPSS); femtosecond n-IR laser

1. Introduction

It is well established for type II superconductors that both a lack of material's extended lattice periodicity (grain boundaries, stacking faults, etc.) and local crystallographic defects (vacancies, substitutions) interact with magnetic vortices and act as effective pinning centers of the magnetic flux lines. The vortex pinning forces generated by these structural imperfections cause flux density gradients that contribute to the irreversible behavior of the magnetization [1] and to low frequency AC losses. Vortex pinning is a phenomenon of great relevance for practical conductors since it allows the superconductor to carry resistance-less current.

Type II superconductors with negligible bulk pinning may also present hysteresis effects, due to Bean–Livingston surface barriers [2] or due to geometrical edge barriers (specimen-shape dependent) [3]. Both types have been observed in low- and high-temperature superconductors (LTS and HTS, respectively) [2–8]. The former type of barriers is generally observed in clean single crystals, whereas the latter is more pronounced for thin films of constant thickness in perpendicular magnetic fields. In both cases, the magnetic irreversibility is caused by the asymmetry between the magnetic flux entry

and exit. In type II superconductors, vortex cores overlap at the upper critical field strength, H_{c2} , and superconductivity becomes extinguished from the bulk. However, it is worth noting that a surface superconducting layer can persist above H_{c2} , up to the surface critical field strength, H_{c3} . For flat surfaces, Saint James and De Gennes [9] predicted a superconducting layer of a thickness approximately equal to the superconducting coherence length, up to a field $H_{c3} \approx 1.69 \times H_{c2}$ when the field is applied parallel to the superconductor's surface. These surface current vortices can be pinned, resulting in a surface critical current (i_c), which depends on the surface characteristics, such as roughness and morphology. These can be changed, for example, by different polishing procedures [10–12], or by low-energy Ar^+ ion irradiation of the surface [13].

Within the class of type II LTS, pure niobium has been widely studied in the literature by its intrinsic properties and by its application in superconducting radio frequency (SRF) cavities, where surface control has the greatest relevance. In SRF applications, very clean surfaces are required to achieve a high quality factor, Q_0 , which is inversely proportional to the surface resistance [11]. Surface treatment procedures including thermal etching, electropolishing and buffered chemical polishing are usually used to achieve the former requirement [10,12]. Grassallino et al. [14] also found that the annealing in a partial pressure of nitrogen or argon gas, followed by the electropolishing of the niobium cavity, yields very low values of the microwave surface resistance and, therefore, more efficient accelerating structures.

Nowadays, focused laser pulsed sources allow surface control on the near micrometer and submicrometer scales, enabling surface specialized functionalities in a wide variety of materials and with increasing processing speeds. Different processing techniques, such as laser direct writing, laser interference patterning or laser-induced self-organization, enable the control and modification of the laser-processed surface morphologies [15–21]. Particularly here, a laser-induced self-ordering process [22] has been chosen that enables the generation of laser-induced periodic surface structures (LIPSS) in a robust single-step approach. In general, such surface structures may exhibit the shape of grating-like ripples, grooves, spikes, pillars, cones, etc., featuring spatial periods ranging from a few tens of micrometers to a few tens of nanometers far beyond the wavelength diffraction limit [17,18,21,22]. Furthermore, femtosecond (fs) laser pulses facilitate the attainment of LIPSS with minimum thermal heating effects on the irradiated target.

Ultra-short laser processing, thus, opens the possibility of changing the surface morphology through periodic surface structures on large areas and in continuous fabrication processes featuring currently maximal areal processing rates at the m^2/min level for both the laser interference patterning and the self-organization approaches [23]. Moreover, the spatial period of the LIPSS can be controlled via the laser irradiation wavelength, the laser pulse fluence or by the effective number of incident pulses [21]. Particularly, close to the ablation threshold of fs-laser irradiated metals, a significant variation of the ripple period can be realized [24–26]. Hence, the localized generation and control of surface defects, such as ripples, is a promising approach to affect the surface superconducting properties.

In this work, two different near-infrared (n-IR) fs-lasers, which differ in wavelength and pulse duration, have been used for laser structuring of Nb foil samples. Ultra-short laser irradiation produces distinctive quasi-periodic nanostructures that vary with the laser pulse fluence or with the effective number of incident pulses. Here, these values have been chosen to produce elongated quasi-parallel morphologies of ripples that are not isotropic. The microstructural changes following irradiation have been analyzed and compared with non-irradiated samples. The effects of applying different atmospheres (argon, nitrogen and air) during the laser treatment process have also been analyzed. In a previous work, it was reported that the laser-generated structures on Nb foils produce some irreversible changes in the magnetic behavior of this superconductor [18]. Nevertheless, discriminating between bulk and surface effects frequently presents important challenges. The aim of the present work is to study the effect of femtosecond n-IR laser structuring of Nb foil samples on their surface superconductivity characteristics. These properties were characterized using DC magnetization and AC susceptibility measurements with the magnetic field applied parallel to the Nb foil surface in order

to maximize H_{c3} values and to minimize the geometric specimen-shape factor. The effect of the LIPSS anisotropy on the surface superconductivity behavior has been studied and is reported here.

2. Materials and Methods

Commercial Nb foil samples (rolled, 25 μm thickness, 99.8% purity and typical roughness of 0.30–0.35 μm) (Sigma-Aldrich, Darmstadt, Germany) have been irradiated with two different n-IR femtosecond lasers located in different laboratories, i.e., at the Institute of Nanoscience and Materials of Aragón (INMA) in Zaragoza (Spain), and at the German Federal Institute for Materials Research and Testing (BAM) in Berlin: (i) L1 at INMA: n-IR Yb:YAG laser (Light Conversion, Vilnius, Lithuania), (Carbide CB3-40W), center wavelength $\lambda = 1030$ nm, pulse duration $\tau_p = 280$ fs. The focusing of the laser beam was realized by means of a cylindrical lens system (focal length of 150 mm) leading to an elliptical beam with $1/e^2$ diameters of $2a_b = 1500$ μm and $2b_b = 26$ μm . (ii) L2 at BAM: n-IR Ti:Sapphire laser (Femtolasers, Vienna, Austria) (Compact Pro), center wavelength $\lambda = 790$ nm, pulse duration $\tau_p = 30$ fs. For properly handling such extremely short femtosecond laser pulses, the focusing of the laser beam was realized by a spherical dielectric mirror (Layertec GmbH, Mellingen, Germany) (focal length of 500 mm) resulting in a circular beam of $1/e^2$ diameter $D_b = 2 r_b = 130$ μm . For both laser systems, the experiments were performed with a pulse repetition frequency $f_{\text{rep}} = 1$ kHz and the focused $1/e^2$ beam diameters were determined in the sample processing plane using the D^2 -method proposed by Liu [27,28]. At the given conditions, the areal processing rates were approximately 1.0 mm^2/s for L1 and 0.12 mm^2/s for L2 here. For irradiation with L1, the sample was placed inside a chamber that allows laser processing in different gaseous atmospheres, such as air, Ar or N_2 ; and the line-wise laser scanning was performed in the direction perpendicular to the major axis of the elliptical beam. In all experiments, the laser scanning direction coincides with that of the linear laser beam polarization.

Table 1 collects the laser processing conditions of the irradiated Nb samples. With laser L1, two samples were processed with the same conditions but changing the atmosphere (Ar and N_2). In both cases, the laser polarization was parallel to the rolling direction. The two samples that were processed with laser L2 were treated in air. The difference between samples “FS_air1” and “FS_air2” is that they were irradiated with orthogonal orientation with respect to the Nb foil rolling orientation. Sample FS_air2 sample was oriented in order to have laser beam polarization perpendicular to the rolling direction. A reference non-irradiated sample, named “REF”, was also studied for comparison.

Table 1. Laser processing parameters used in 25 μm thick Nb foil samples irradiated with fs-lasers.

Sample	Laser	Atm.	P (W)	f_{rep} (kHz)	v_L (mm/s)	d_s (μm)	F_p (J/cm^2)	I_p (GW/cm^2)	F_{2D} (J/cm^2)
FS_Ar	L1	Ar	0.18	1	1	1000	0.61	2671	17.1
FS_N	L1	N_2	0.18	1	1	1000	0.61	2671	17.1
FS_air1	L2	Air	0.02	1	6	20	0.15	5023	16.6
FS_air2	L2	Air	0.02	1	6	20	0.15	5023	16.6

The main parameters of laser processing were described in detail in [18] but are summarized here as follows. P is the nominal average laser power and f_{rep} the pulse repetition frequency. Each laser pulse is characterized by the peak fluence (F_p) and the peak irradiance (I_p). For a given value of f_{rep} , the laser beam scanning velocity (v_L) controls the distance between two laser pulses in a line, $d_p = v_L/f_{\text{rep}}$. Taking into account the Gaussian beam profile in the processing plane, a uniform fluence distribution is obtained in the full 2D scanned area if line-to-line overlap is above a critical threshold value (d_s/r_b for L2 or d_s/a_b for L1 is below 0.9, where d_s is the distance between adjacent lines). This is

fulfilled for the treatments performed with laser L2, where d_s is 20 μm while the characteristic beam radius is $r_b = 65 \mu\text{m}$. In this situation, the total accumulated fluence can be calculated as

$$F_{2D} = \frac{\pi r_b^2}{d_p d_s} F_P \quad (1)$$

Laser parameters were selected in order to have similar F_{2D} values with both lasers. A constant value of $F_{2D} = 16.6 \text{ J/cm}^2$ was obtained for samples treated with laser L2. In the case of laser L1, the distance between two lines ($d_s = 1 \text{ mm}$) is larger than the characteristic line size ($a_b = 0.75 \text{ mm}$) leading to a non-uniform fluence distribution on the surface, with an average value of 17.1 J/cm^2 .

The optical penetration depth $1/\alpha = \lambda/(4\pi k)$, with α being the linear absorption coefficient and k the imaginary part of the complex valued refractive index, accounts to $\sim 16 \text{ nm}$ at both laser irradiation wavelengths.

The surface microstructural characterization was performed in a MERLIN field-emission scanning electron microscope (FE-SEM) (Carl Zeiss, Jena, Germany) equipped with an energy dispersive X-ray spectroscopy (EDX) system (Oxford Instruments, Abingdon, UK) operated at 5 kV. Surface topographic cross-sections were analyzed by Scanning Transmission Electron Microscopy (STEM) using a Tecnai F30 microscope (FEI Company, Hillsboro, OR, USA), also equipped with a high-angle annular dark field (HAADF) detector. Sample preparation was performed with a Focused Ion Beam (FIB) in a Dual Beam Helios 650 (FEI Company, Hillsboro, OR, USA) apparatus, using 30 kV Ga^+ ions for the initial steps and 5 kV for final thinning. Prior to the preparation of a FIB lamella, a protective Pt cap layer was deposited at the region of interest. X-ray photoelectron spectroscopy (XPS) was applied to characterize the changes in the chemical state of the surface using an AXIS Supra spectrometer (Kratos, Manchester, UK). The photoemission was excited with monochromatic Al K_{α} X-ray radiation at 1486 eV over a spot size of $700 \times 300 \mu\text{m}^2$, resulting in an XPS information depth between 5 and 10 nm. The carbon C1s peak at 284.8 eV served as the reference signal for energy calibration.

Measurements of DC magnetization (M) and complex AC susceptibility, χ_{ac} (with in-phase, χ' , and out-of-phase, χ'' , components) were carried out in a SQUID-based MPMS-5T system (Quantum Design, San Diego, CA, USA). The Reciprocating Sample Option (RSO) of the system was used for DC measurements. For χ_{ac} measurements, the AC drive magnetic field (sine wave of amplitude $\mu_0 h_0$ and frequency f) is superimposed on the constant DC magnetic field, $\mu_0 H$. In this work, AC and DC components of the applied magnetic field have the same direction. Values of $f = 10 \text{ Hz}$ and $\mu_0 h_0 = 10$ and $100 \mu\text{T}$ have been used. The magnetic field was applied parallel to x - and y - axes of the foil's surface plane (see Figure 1), in order to analyze if laser polarization and rolling orientations have any effect on their magnetic and superconducting behavior. For magnetic measurements, the size of the measured sample area is in the range of (3–4) mm \times (3–4) mm and both surfaces of the samples were irradiated. The critical temperature (T_c) was determined as the onset of diamagnetism from $\chi'(T)$, being T the temperature, obtaining T_c values ranging between 9.30 and 9.35 K in all samples. The heat capacity was measured in a PPMS-9T (Quantum Design, San Diego, CA, USA) apparatus.

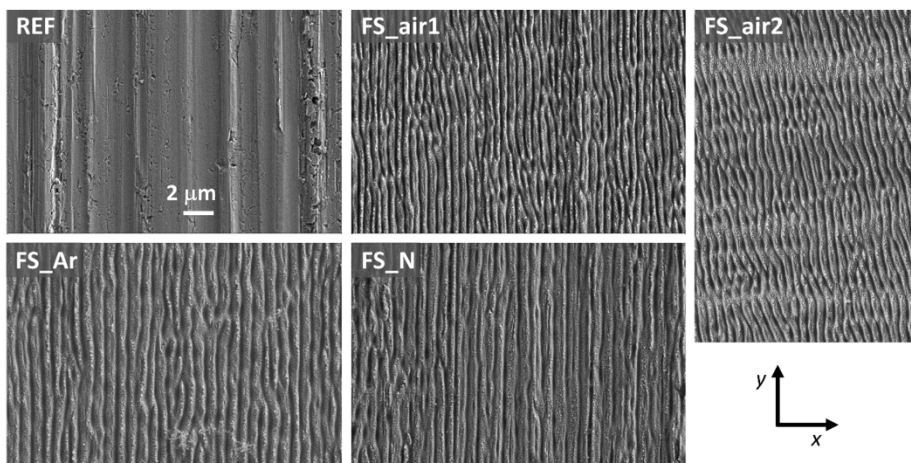


Figure 1. FE-SEM micrographs (secondary electrons) of the surfaces of all analyzed representative samples (same magnification for all images). The rolling direction is parallel to the y -axis in all samples, except for FS_air2, where it is parallel to x . The linear laser beam polarization is parallel to x in all cases.

3. Results and Discussion

3.1. Microstructural Characterization

Figure 1 shows SEM micrographs from the surface of each of the five analyzed samples. The reference sample clearly shows the microstructural characteristics arising from rolling, with defects parallel to the rolling direction (y -axis in the figure). These are also visible, although with less clarity, after laser irradiation. This rolling direction coincides with the y -axis in all the samples, except in the case of sample FS_air2, which was rotated by 90° . Surface irradiation of the samples with both fs-lasers produces, in all cases, elongated quasi-periodic surface structures aligned perpendicular to the laser polarization (direction x in the figure). This type of near-wavelength sized ripples is known as low spatial frequency LIPSS (LSFL) [17,22]. These structures are caused by the excitation of surface plasmon polaritons (SPPs) at the rough metallic surface and their interference with the incident laser radiation. The intra-pulse interference modulates the spatial pattern of optical energy absorbed by the electronic system of the solid and leads—after electron-phonon energy relaxation—to spatially modulated ablation [22]. This formation mechanism is supported by the values of the dielectric permittivity of the material Nb at the laser irradiation wavelengths that account to $\epsilon = -10.1 + i \times 15.6$ at 790 nm and $\epsilon = -24.4 + i \times 16.8$ at 1030 nm, respectively [29]. Hence, at both irradiation wavelengths, the condition $\Re(\epsilon) < -1$ is fulfilled here—a prerequisite for the excitation of SPPs [30,31]. The relevance of specific hydrodynamically driven supra-wavelength sized ripples that were observed upon irradiation of thin metal films on dielectric substrates with high aspect ratio elliptical ns-laser beams parallel to the direction of scanning [32] can be ruled out here, since, in our case, the ripples (LSFL) are formed perpendicular to the direction of beam scanning—always perpendicular to the laser beam polarization and they exhibit near wavelength sized periods (see Figure 1).

The EDX analyses of the sample surfaces revealed an increase in the % of O elemental composition in the samples processed in air (6.2 wt%, 27.7 at%) compared to the reference sample (4.1 wt%, 19.9 at%), and a reduction for samples processed in N_2 or Ar (3.4 wt%, 17.0 at%). The standard deviations of the wt% values range between 0.2 and 0.4. A small amount of nitrogen (0.6 wt%, 3.0 at%, 0.1 wt% sigma) was detected in sample FS_N. Note that the absolute percentage values must be taken with care here due to the large EDX information depth and due to surface corrugations being present in the laser processed areas.

Quasi-periodic submicrometer-structures induced by both lasers can be better analyzed using higher magnification, as it is demonstrated in Figure 2 for samples FS_Ar and FS_air2. The upper row images in the figure correspond to cross-sectional views obtained by STEM for a lamella extracted from the samples (cut parallel to x -axis). The lower row images correspond to surface views by FE-SEM using an in-lens secondary detector. LSFL were formed in both samples and have similar modulation depths (peak-to-valley distances of about 200 nm). These structures are more homogeneous for sample FS_air2, as it is clearly seen in the cross-sectional view. The spatial period of the LSFL is 775 nm for samples irradiated with laser L1 and 570 nm for those irradiated with laser L2. These are mean values that have been calculated by analyzing statistically representative areas observed on samples by FE-SEM, and have standard deviations of 68 and 35 nm, respectively. The differences in the observed periods are assigned to the different laser wavelengths emitted by L1 and L2. It must be pointed out that the geometrical characteristics of the LSFL are in good agreement with the atomic force microscopy measurements published for fs-laser irradiated niobium in [18,33]. High spatial frequency LIPSS (HSFL) with periods of 50 to 80 nm, which form between LSFL structures, being perpendicular to them, are also observed in both samples (see Figure 2c,d), in line with the observations reported in [34].

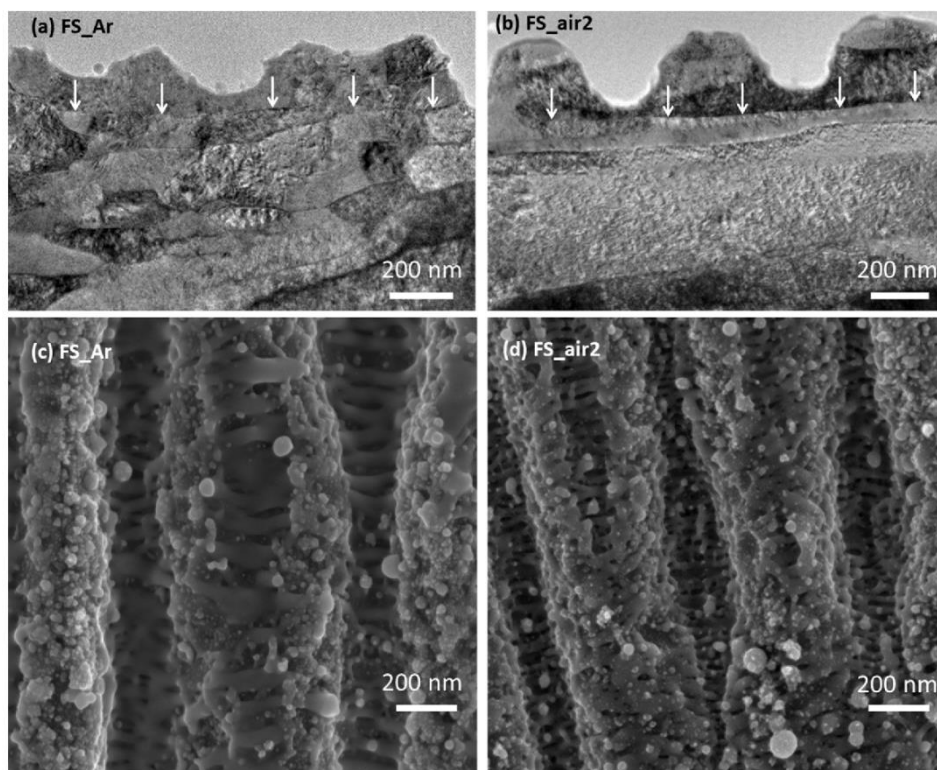


Figure 2. (a,b) STEM micrographs of the cross-sectional images near the surface. (c,d) FE-SEM top-view images (in-lens detector) of the surface of the same samples. (Left column) FS_Ar, (Right column) FS_air2. The white arrows in (a,b) point at the boundary between laser-affected and non-affected regions.

It is important to note here that, due to the rolling process involved in the manufacturing of the Nb foils, the grains are elongated in the bulk of the material, with the longest grain axis oriented parallel to the rolling direction. This is also parallel to the ripple orientation in sample FS_Ar, but perpendicular in sample FS_air2. This is the reason for the different grain shapes observed in Figure 2a,b, with a clear

texture of grains oriented perpendicular to the nanostructure observed in sample FS_air2. Interestingly, a boundary can be observed in both samples that is separating the laser-affected region from the non-affected bulk material underneath (marked by white arrows in Figure 2a,b. Supposedly, the Nb surface was melted up to this depth during the fs-laser scan processing, resulting in a re-solidified layer of 40 to 300 nm here (depending on the position across the LIPSS). This thickness is larger than the optical penetration depth of the laser radiation in Nb, which can be explained by the multi-pulse laser treatment upon scan-processing.

Figure 3 shows HAADF-STEM images of the cross-section of samples FS_N and FS_air2. Corresponding STEM-EDX analyses confirm the presence of O and Nb elements in the darker areas observed near the sample surface (data not shown here). These zones are more abundant in the sample processed in air (Figure 3b) than in the samples processed in nitrogen (Figure 3a) or argon (not shown here). The oxide layer can be associated with the dark interfacial zones and exhibits a thickness of a few nanometers for the sample FS_N (≈ 5 nm in the zone shown in the inset of Figure 3a). For sample FS_air2, however, this layer exhibits an increased thickness (reaching values up to 20 nm) and is much less uniform. Note that the thickness of the oxide layer formed upon fs-laser processing in nitrogen here is very similar to that found for the natural Nb passivation layers that are characterized by a thickness of about 6–8 nm and Nb₂O₅ as the outermost layer [33].

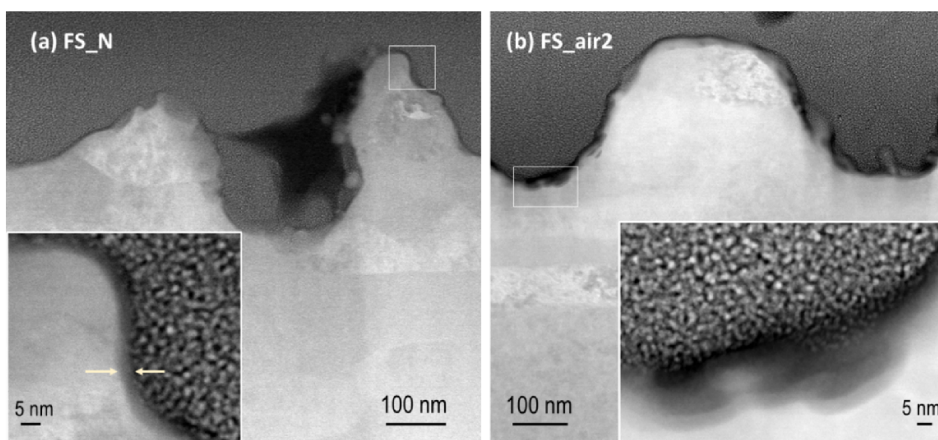


Figure 3. HAADF-STEM images of a cross-section of sample (a) FS_N and (b) FS_air2, near the surface. The insets show the areas highlighted by a white rectangle in the corresponding main images, with higher magnification.

The high resolution XPS spectra of niobium Nb 3d, plotted in Figure 4, show very similar behavior for all samples, with the presence of the Nb 3d doublet at binding energies (BEs) of 209.80 and 207.05 eV, corresponding to Nb₂O₅, as the main chemical compound at the surface [35–37]. The peaks corresponding to metallic Nb, Nb⁰, are also observed in all samples except in the one processed in air, FS_air2. The latter indicates a thickness of the laser-induced oxide layer exceeding the XPS information depth here—fully in line with Figure 3b and with previous observations made for fs-irradiation of Ti in the air environment [38]. The sample irradiated in nitrogen atmosphere exhibits a very weak signal in the N 1s spectrum with a BE of approximately 400.0 eV (see Figure 5), thus discarding the presence of niobium nitrides, NbN_x, which are expected to appear at lower binding energies (396.5 eV [39], 397.5 eV [40]). This is very similar to the results reported for nitrogen doped niobium [37], where the peak at 399.84 eV in the N 1s spectrum was attributed to the formation of CH₃CN.

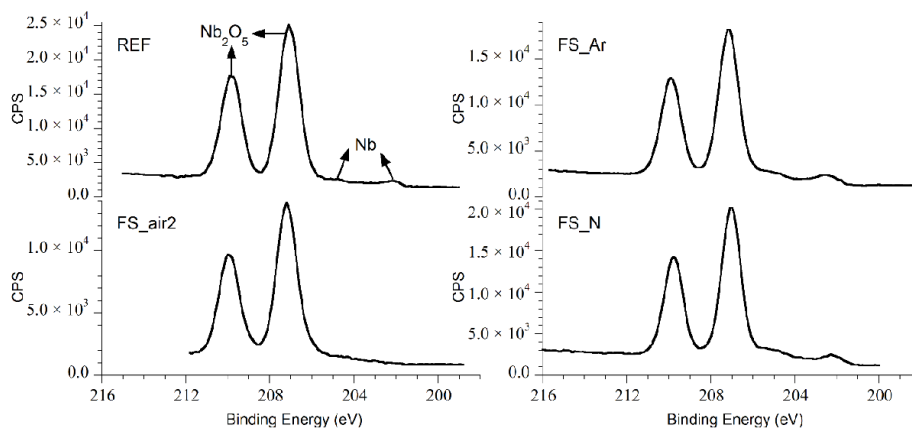


Figure 4. High resolution Nb 3d XPS spectra for the analyzed samples discussed in the text. CPS: counts per second.

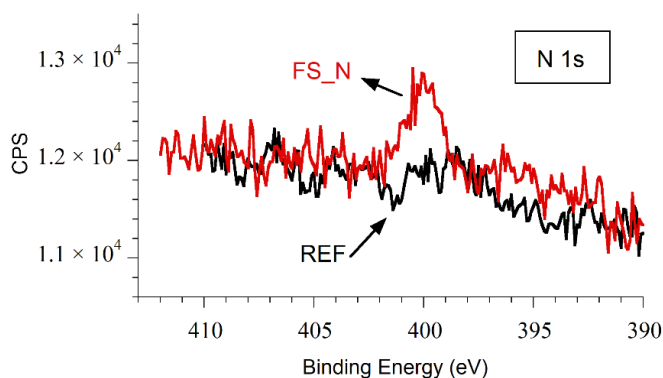


Figure 5. High resolution XPS spectra of the N 1s line of samples REF (non-irradiated, black line) and FS_N (laser irradiated in nitrogen atmosphere, red line). CPS: counts per second.

3.2. Irreversible Magnetization and Upper Critical Field, H_{c2}

Figure 6a shows the width of the magnetic hysteresis loop, ΔM , as a function of the magnetic field for the reference non-irradiated sample (REF) and the irradiated sample (FS_N), at the temperature $T = 5$ K, and with the magnetic field applied parallel to the x - and y -axes. ΔM was obtained for each H value as $\Delta M = M_{\downarrow} - M_{\uparrow}$, where M_{\uparrow} and M_{\downarrow} are the corresponding values measured for increasing and decreasing fields, respectively.

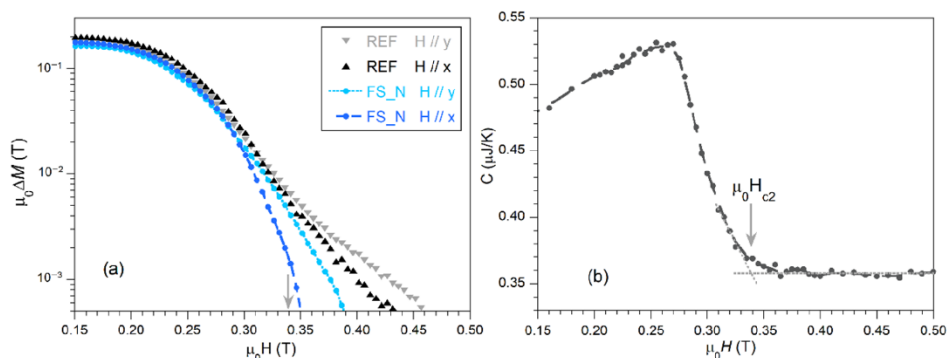


Figure 6. (a) Field dependence of the magnetic hysteresis loop width, $\mu_0 \Delta M(H)$ at $T = 5$ K of the REF and FS_N samples with the external DC field applied in the x - and y -directions, both parallel to the surface as indicated in Figure 1; (b) heat capacity of the non-irradiated reference (REF) sample recorded at 5 K. The derived upper critical field $\mu_0 H_{c2}$ is marked by an arrow. Both arrows point to the same magnetic field, for better comparison.

In these measurements, the sharp increase of the magnetic irreversibility, which is related to ΔM , is frequently associated to the onset of bulk superconductivity and, therefore, to the upper critical field $\mu_0 H_{c2}$ [10]. Nevertheless, this value is not always easy to derive from magnetization curves, due to the appearance of a tail at high magnetic fields in some conditions, as in this case [41]. With this aim, heat capacity, which is essentially a bulk property, could better allow the determination of $\mu_0 H_{c2}$, as marked by the arrow in Figure 6b [12,13]. It must be noted that the $C(H)$ curve for the FS_N sample (not shown here for clarity reasons) is very similar to that of the reference sample, indicative of similar bulk properties (and $\mu_0 H_{c2}$) between both samples.

The results in Figure 6a thus clearly show irreversible magnetization values above $\mu_0 H_{c2}$, with differences between samples and orientations. The existence of non-zero ΔM values above $\mu_0 H_{c2}$ is indicative of the presence of surface critical currents, i_c . As it is observed, fs-laser irradiation produces a significant decrease of ΔM above H_{c2} , particularly when the magnetic field is applied in the direction perpendicular to the nanostructures (x -direction, as indicated in Figure 1). This effect is observed for all analyzed irradiated samples, independently of the processing atmosphere. It must be noted that the reference sample also exhibits some anisotropy in ΔM , with higher values above H_{c2} for the field applied parallel to the rolling direction (y -axis). This is indicative of an influence of the anisotropy of the microscopic grain structure induced by rolling, as visualized in Figures 2a,b and 3, in agreement with previous studies [41].

Changes in the ΔM (or i_c) at fields above H_{c2} for different surface treatments have been reported by several groups. For example, Scola et al. [13] observed an increase of i_c values after irradiating the Nb surface with low-energy Ar^+ ions; Aburas et al. [12] observed changes by polishing the surface using different processes (sandpaper, diamond, colloidal silica and chemical polishing), with lower i_c values for smoother surfaces; Casalbuoni et al. [10] also reported differences in i_c values of Nb cylinders subjected to buffered chemical polishing or to electropolishing; and van Gorp [41] observed higher i_c values for cold rolled Nb foils compared to electrolytic Nb foils.

The behavior observed here would thus suggest that surface critical currents present a marked anisotropy, with higher values for magnetic fields applied along the ripples in the irradiated samples. Further analysis of the surface superconducting characteristics and the effects of the different laser irradiation conditions can be better performed from $\chi_{ac}(H)$ measurements because of their higher sensitivity, as discussed in the following section.

3.3. Surface Superconductivity Characterization

H_{c3} values can be estimated from $\chi_{ac}(H)$ following a procedure similar to that described in [10,11,42]. The complex $\chi_{ac}(H)$ curve was measured in descending DC magnetic fields applied parallel to the Nb sheet surface, starting from normal-state conditions and then approaching the superconducting transition by decreasing the DC magnetic field. Low frequency ($f = 10$ Hz) and low amplitude ($\mu_0 h_0 = 10$ μ T) of the AC alternating magnetic field were used for the present measurements, similarly to those reported in references [10,11], for ease of comparison. Figure 7 shows $\chi'(H)$ and $\chi''(H)$ curves measured at 5 K with decreasing fields from 1.5 T down to 0 T for different samples and for two orientations of the external magnetic field. Note that the value of the initial DC magnetic field ($\mu_0 H = 1.5$ T) was chosen considerably larger than $\mu_0 H_{c2}$ to ensure that the entire sample, including its surface, was in the normal state at the beginning of each measurement run [11]. All values in the graphs have been scaled by χ'_{-1} , which is the value of χ' measured at zero field, and it is close to the expected value for perfect diamagnetism for each sample, i.e., $\chi'_{-1}(\text{emu}) \approx V(\text{cm}^3)/(4\pi)$, where V is the volume of the sample. H_{c3} at each temperature can be defined as the first deviation point from the values at normal state of χ'' or as the onset of χ' (above noise level). In the figure, arrows indicate the position of the H_{c3} values of two of the samples (REF and FS_N), for clarity purposes.

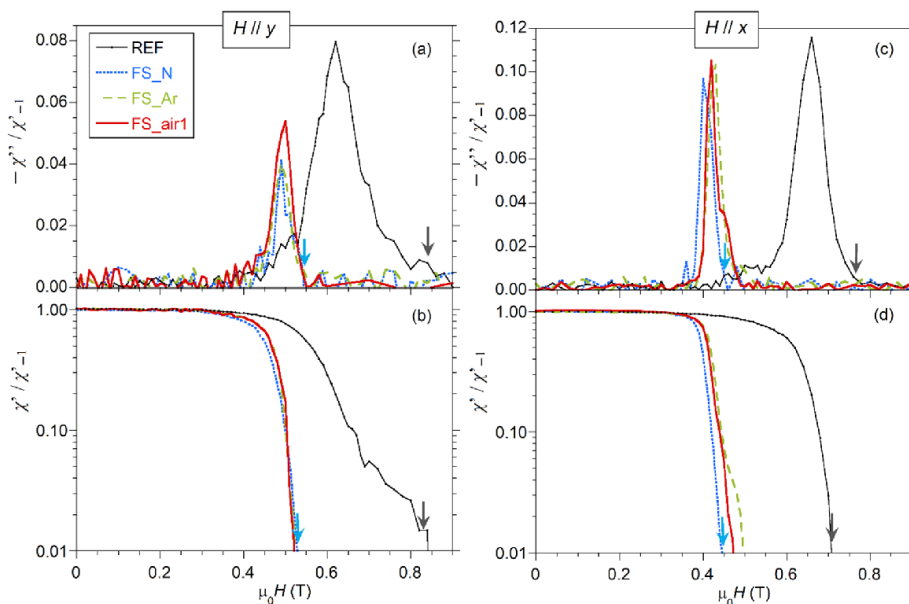


Figure 7. Components of the χ_{ac} : χ'' (a,c) and χ' (b,d), scaled by χ'_{-1} , as a function of the DC magnetic field, $\mu_0 H$, applied parallel to the y -axis (a,b) or the x -axis (c,d), at $T = 5$ K, $f = 10$ Hz and $\mu_0 h_0 = 10$ μ T measured in descending fields from the initial field 1.5 T. The arrows mark $\mu_0 H_{c3}$ values for samples REF (black arrow) and FS_N (blue arrow), derived as explained in the text.

From Figure 7, it is worth pointing out that fs-laser processing produces a pronounced shift of the transition towards smaller magnetic fields together with much narrower transitional widths, as compared to the reference sample. Two non-irradiated samples were measured, showing very similar curves (see Figure S1 presented in Supplementary Material), thus confirming this laser-modified behavior. The onset of the normal-to-superconducting transition of fs-laser processed samples occurs at higher fields when H is applied parallel to the nanostructures produced by the laser (y -axis) than when it is applied perpendicular to them (x -axis). The effect of the used atmosphere during laser processing is not significantly relevant, although some differences are observed, especially for fields

applied along the x -axis (Figure 7c,d). The non-irradiated sample REF also shows some anisotropy, assigned to the elongated defects/grains produced by the rolling during its manufacture. Note that the maximum of $\chi''(H)$ curves is lower (thus indicating lower AC losses, which represent the energy dissipation during a cycle), for the fs-laser processed samples, especially for those irradiated in Ar and N_2 atmosphere and for magnetic fields applied parallel to the induced nanostructures (y -axis). This could suggest lower surface resistance in these samples and conditions [43].

$\chi''(H)$ curves also allow the estimation of H_{c2} , which is defined as the point where $\chi''(H)$ decreases to zero after the transition when ramping down the field [10,11]. As seen in Figure 7a, the increase of $\chi''(H)$ around H_{c2} is smooth at these conditions, so that we can only have an estimate of this value in the range between 0.35 T and 0.40 T in all samples, as the low-intensity signal makes the noise relevant, thus preventing more precise estimation of H_{c2} here. Nevertheless, it is possible to derive H_{c2} values using higher amplitude of the AC field, since the directly measured signal by the magnetometer is proportional to $h_0 \cdot \chi_{ac}(H, f, h_0)$, so that the signal-to-noise ratio increases with h_0 . Figure 8 compares the same samples and conditions as in Figure 7a but for $\mu_0 h_0 = 100 \mu\text{T}$. H_{c2} values defined this way would be about 0.34 T for all the samples (dotted arrow in the figure). This is in good agreement with the result obtained previously from the heat capacity measurement shown in Figure 6b. It must be pointed out that, as expected, H_{c2} does not depend on the field orientation, since similar H_{c2} values are derived when the field is oriented parallel to the x -axis (see Figure S2 in the Supplementary Material).

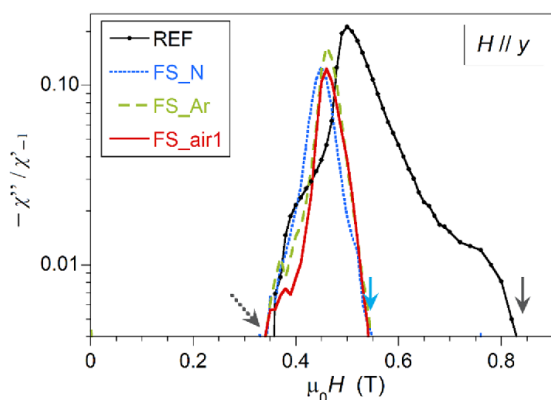


Figure 8. $\chi''(H)$ for the same samples and under the same conditions as in Figure 7a, but in this case $\mu_0 h_0 = 100 \mu\text{T}$. χ'' is plotted in a log scale. The dotted arrow indicates the estimated $\mu_0 H_{c2}$ value for these samples. Note that the two continuous arrows point to the same DC field values as in Figure 7a, to allow for a direct comparison between the two sets of data.

The choice of small $\mu_0 h_0$ values in these measurements aims at improving the surface sensitivity. It can be observed that the onset of the normal-to-superconductor transition does not vary significantly by increasing $\mu_0 h_0$ from 10 to 100 μT , for laser processed samples, but it shifts at slightly lower external DC fields for the reference sample. This indicates that both AC field amplitudes would provide good sensitivity to analyze near-surface regions. It should be underlined that, upon increasing $\mu_0 h_0$, the AC field will sense deeper into the sample so that the peak of the $\chi''(H)$ curve shifts towards lower fields [5]. More specifically, for the fs-laser treated samples, the peak shifts from 0.49–0.50 T for the $\mu_0 h_0 = 10 \mu\text{T}$ AC field down to the 0.45–0.46 T for the 100 μT AC field, when H is parallel to the y -axis (Figures 7 and 8). The behavior is similar in all laser treated samples, although the peak of the sample processed in argon appears at slightly higher fields. In the case of the non-irradiated sample, the observed shift is larger, as the $\chi''(H)$ peak moves from 0.60 T (at 10 μT AC field) down to 0.50 T (at 100 μT AC field). In all samples, these fields are well above the $\mu_0 H_{c2}$ field, thus clearly indicative of surface phenomena.

The surface critical fields, H_{c3} , derived from $\chi''(H)$ measurements at 5 K and AC fields of 10 Hz and amplitude 10 μT are plotted in Figure 9 for all analyzed samples presented in this study and for both DC field orientations. Note that the values H_{c3} obtained from $\chi'(H)$ curves, which are not displayed here for clarity purposes, show the same trends, but are slightly shifted towards lower magnetic fields than those corresponding to $\chi''(H)$. The estimated $\mu_0 H_{c3}$ values for external magnetic fields applied parallel to the surface nanostructures (y -axis) decrease from 0.84 T for the REF sample to about 0.54–0.58 T. That is, the r_{32} factor ($=H_{c3}/H_{c2}$) decreases from ≈ 2.4 for the as-rolled reference sample to 1.6–1.7 for fs-laser irradiated samples. Moreover, H_{c3} values are smaller when applying the magnetic field perpendicular to the nanostructures (x -axis). For this field orientation, we observe some changes depending on the processing atmosphere, with samples irradiated in argon and nitrogen having the smallest and the largest anisotropy, respectively. More precisely, for this field orientation, the transition of FS_N shifts slightly towards lower fields compared to the other irradiated samples (see Figure 7d), whereas the transitions of FS_air1 and FS_Ar are very similar for $\chi'/\chi'_{-1} > 0.06$, but differ on the onset of diamagnetism, which occurs at higher DC fields for FS_Ar, thus exhibiting a larger H_{c3} value. The reasons for the observed differences among the irradiated samples are still unknown. They are, in any case, small compared with those found between fs-laser irradiated and non-irradiated samples. It seems clear, however, that irradiation with fs-lasers, as used in this work, is sufficiently short in time to limit the chemical reaction between niobium and oxygen or nitrogen, thus resulting in very similar critical surface fields, independently of the atmosphere used during the irradiation process. Hence, this similarity points toward a topographic effect of the LIPSS here. Moreover, it was observed that the laser polarization orientation with respect to the rolling direction of the sample does not show a very important effect on the superconducting properties of the laser processed surface as the laser treatment diminishes rolling defects and both FS_air1 and FS_air2 samples exhibit a similar nanostructure and magnetic behavior.

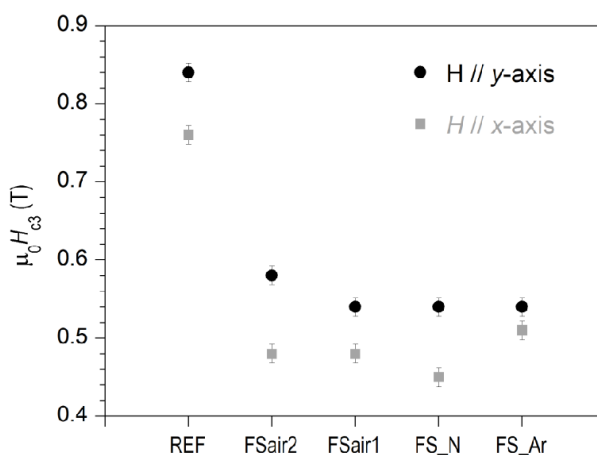


Figure 9. Critical surface fields, $\mu_0 H_{c3}$, of all analyzed samples derived from $\chi''(H)$ measurements at $T = 5$ K, $f = 10$ Hz and $\mu_0 h_0 = 10$ μT , with the external magnetic field applied parallel to the x - and y -axes.

Note that the effect of fs-laser processing on H_{c3} is similar to the effect of electropolishing and buffered chemical polishing of Nb wire reported by Sung et al. [11]. In that study, the authors observed a decrease of H_{c3} in all polished samples as compared with the as-drawn wires. For example, $\mu_0 H_{c3}$ at 5 K was reduced from ≈ 0.84 T (as-drawn) to ≈ 0.68 T after electropolishing for 3 h. They also found some differences in H_{c3} and r_{32} values by annealing (at 800 $^\circ\text{C}$) or by baking (at 120 $^\circ\text{C}$) the niobium samples. Following these results, it is thus worth further exploring the effect of different LIPSS topographies,

together with annealing and/or baking of the Nb samples, on the surface superconducting properties of niobium.

4. Conclusions

Laser-induced periodic surface structures (LIPSS) were generated on oppositely aligned (3–4) mm × (3–4) mm areas on the top and bottom surfaces of as-rolled commercial niobium foils using two different fs-laser systems under different atmospheres (air, argon, and nitrogen). After laser treatment, the surface roughness is very similar in all cases. The formed low spatial period LIPSS (LSFL) have similar modulation depths (peak-to-valley distance of about 200 nm) and are aligned perpendicular to the laser beam polarization. They are characterized by a spatial frequency that depends on the laser wavelength: 775 nm (std 68 nm) and 570 nm (std 35 nm), i.e., approximately 73–74% of the irradiation wavelengths of $\lambda = 1030$ and 790 nm, respectively. High spatial frequency LIPSS (HSFL) with periods between 50 and 80 nm, are also formed between the LSFL structures, in the perpendicular direction.

Chemical analyses by EDX and XPS indicated some laser-induced oxidation effects, with Nb₂O₅ being the dominating type of oxide. Upon fs-laser processing in ambient air, a thin surface oxide layer of a few tens of nanometers extent was detected through cross-sectional STEM/EDX analyses. When laser processing takes place under inert gases, however, the laser-induced oxide layer thickness of ~5 nm is similar to that found for the native oxide on the non-irradiated reference sample. A small nitrogen signal is observed by EDX and XPS on the surface of the laser irradiated sample under nitrogen, not being consistent with the definite presence of niobium nitrides.

The surface critical field, H_{c3} , was derived from AC susceptibility measurements as a function of the externally applied DC magnetic field, which was applied parallel to the surface and in both orientations with respect to the generated LIPSS. Clear effects of laser irradiation on the surface superconducting properties of the niobium foil samples have been shown. In particular, H_{c3} decreases for laser irradiated samples as compared to the non-irradiated reference sample. Laser irradiation also results in significantly narrower normal-superconductor transitions and lower $\chi''(H)$ peaks, whereas the upper critical field, H_{c2} , remains unaffected. The microstructural anisotropy of the fs-laser-generated LIPSS is clearly reflected on the surface superconducting properties of the samples, with higher H_{c3} when the external magnetic field is parallel to the LIPSS (LSFL). Nevertheless, the differences in the spatial periodicity of LIPSS between these samples do not affect significantly the H_{c3} values. Moreover, it seems clear that irradiation with ultra-short pulsed lasers, as used in this work (with pulse durations of 280 fs and 30 fs), is of sufficiently short interaction time to limit the chemical reaction between niobium and oxygen or nitrogen, thus resulting in similar critical surface fields independently of the irradiation atmosphere.

The observed behavior indicates that fs-laser processing is useful to control the surface superconducting properties of niobium and could be an alternative to some well-established procedures, such as electropolishing or buffered chemical polishing. This work demonstrates that surface modification associated with ultra-short pulse laser processing strongly affects surface superconductivity. In order to understand completely the interaction between the laser generated surface nanostructures and superconductivity, additional studies using different laser sources (wavelengths or longer pulse durations) should be necessary.

Supplementary Materials: The following are available online at <http://www.mdpi.com/2079-4991/10/12/2525/s1>, Figure S1: Comparison between $\chi'(H)$ and $\chi''(H)$ curves of two different non-irradiated samples, REF and REF(2), nominally identical. Magnetic fields were applied parallel to the y -axis and the measurements were performed at 5 K, 10 Hz and $\mu_0 h_0 = 10$ μ T with descending fields from the initial field of 1.5 T. Figure S2: $\chi''(H)$ for different samples at 5 K, 10 Hz and $\mu_0 h_0 = 100$ μ T, measured in descending DC fields from the initial magnetic field 1.5 T. AC and DC magnetic fields were applied parallel to the x -axis.

Author Contributions: Conceptualization, L.A.A., G.F.d.I.F., and E.M.; methodology, E.M., G.F.d.I.F., L.A.A., and J.B.; investigation, Á.C., E.M., G.F.d.I.F., and L.A.A.; formal analysis, Á.C., R.N., and E.M.; resources, G.F.d.I.F., L.A.A., H.L., J.K., and J.B.; writing—original draft preparation, E.M. and Á.C.; writing—review and editing, R.N.,

L.A.A., G.F.d.l.F., J.B., and J.K.; software, J.B.; project administration, L.A.A., E.M., G.F.d.l.F., J.K., and J.B. All authors have read and agreed to the published version of the manuscript.

Funding: This work was funded by project ENE2017-83669-C4-1-R (MCIU/AEI/FEDER, EU) and by the Gobierno de Aragón “Construyendo Europa desde Aragón” (research group T54_20R).

Acknowledgments: This paper is dedicated to the memory of Rafael Navarro. The authors acknowledge the use of Servicio General de Apoyo a la Investigación-SAI and Laboratorio de Microscopías Avanzadas, University of Zaragoza. The authors are extremely grateful to Agustín González-Elípe for very valuable discussions regarding the XPS measurements.

Conflicts of Interest: The authors declare no conflict of interest.

References

1. Dew-Hughes, D. The metallurgical enhancement of type II superconductors. *Rep. Prog. Phys.* **1971**, *34*, 821–873. [[CrossRef](#)]
2. Bean, C.P.; Livingston, J.D. Surface barrier in type-II superconductors. *Phys. Rev. Lett.* **1964**, *12*, 14–16. [[CrossRef](#)]
3. Zeldov, E.; Larkin, A.I.; Geshkenbein, V.B.; Konczykowski, M.; Majer, D.; Khaykovich, B.; Vinokur, V.M.; Shtrikman, H. Geometrical Barriers in high-temperature superconductors. *Phys. Rev. Lett.* **1994**, *73*, 1428–1431. [[CrossRef](#)] [[PubMed](#)]
4. van der Klein, C.A.M.; Kes, P.H.; van Beelen, H.; de Klerk, D. The effect of neutron irradiation damage on the magnetic behavior of superconducting niobium in stationary fields. *J. Low Temp. Phys.* **1974**, *16*, 169–191. [[CrossRef](#)]
5. Hopkins, J.R.; Finnemore, D.K. Surface superconductivity in niobium and niobium-tantalum alloys. *Phys. Rev. B* **1974**, *9*, 108–114. [[CrossRef](#)]
6. Mishra, P.K.; Ravikumar, G.; Sahni, V.C.; Koblischka, M.R.; Grover, A.K. Surface pinning in niobium and a high- T_c superconductor. *Physica C* **1996**, *269*, 71–75. [[CrossRef](#)]
7. Chen, D.-X.; Cross, R.W.; Sanchez, A. Effects of critical current density, equilibrium magnetization and surface barrier on magnetization of high temperature superconductors. *Cryogenics* **1993**, *33*, 695–702. [[CrossRef](#)]
8. Konczykowski, M.; Burlachkov, L.I.; Yeshurun, Y.; Holtzberg, F. Evidence of surface barriers and their effect on irreversibility and lower critical field measurements in Y-Ba-Cu-O crystals. *Phys. Rev. B* **1991**, *43*, 13707–13710. [[CrossRef](#)]
9. Saint-James, D.; de Gennes, P.G. Onset of superconductivity in decreasing fields. *Phys. Lett.* **1963**, *7*, 306–308. [[CrossRef](#)]
10. Casalbuoni, S.; Knabbe, E.A.; Kötzler, J.; Lilje, L.; von Sawilski, L.; Schmüser, P.; Steffen, B. Surface superconductivity in niobium for superconducting RF cavities. *Nucl. Instrum. Methods Phys. Res. Sect. A* **2005**, *538*, 45–64. [[CrossRef](#)]
11. Sung, Z.-H.; Dzyuba, A.; Lee, P.J.; Larbalestier, D.C.; Cooley, L.D. Evidence of incomplete annealing at 800 °C and the effects of 120 °C baking on the crystal orientation and the surface superconducting properties of cold-worked and chemically polished Nb. *Supercond. Sci. Technol.* **2015**, *28*, 075003. [[CrossRef](#)]
12. Aburas, M.; Pautrat, A.; Bellido, N. Change of surface critical current in the surface superconductivity and mixed states of superconducting niobium. *Supercond. Sci. Technol.* **2017**, *30*, 015009. [[CrossRef](#)]
13. Scola, J.; Pautrat, A.; Goupil, C.; Méchin, L.; Hardy, V.; Simon, C. Voltage noise and surface current fluctuation in the superconducting surface sheath. *Phys. Rev. B* **2005**, *72*, 012507. [[CrossRef](#)]
14. Grassallino, A.; Romanenko, A.; Sergatskov, D.; Melnychuk, O.; Trenikhina, Y.; Crawford, A.; Rowe, A.; Wong, M.; Khabiboulline, T.; Barkov, F. Nitrogen and argon doping of niobium for superconducting radio frequency cavities: A pathway to highly efficient accelerating structures. *Supercond. Sci. Technol.* **2013**, *26*, 102001. [[CrossRef](#)]
15. Lasagni, A.; Benke, D.; Kunze, T.; Bieda, M.; Eckhardt, S.; Roch, T.; Langheinrich, D.; Nerger, J. Bringing the Direct Laser Interference Patterning Method to Industry: A One Tool-Complete Solution for Surface Functionalization. *J. Laser Micro/Nanoeng.* **2015**, *10*, 340–344. [[CrossRef](#)]
16. Pronko, P.P.; Dutta, S.K.; Squier, J.; Rudd, J.V.; Du, D.; Mourou, G. Machining of sub-micron holes using a femtosecond laser at 800 nm. *Opt. Commun.* **1995**, *114*, 106–110. [[CrossRef](#)]

Surface Superconductivity Changes of Niobium Sheets by Femtosecond Laser-Induced Periodic Nanostructures

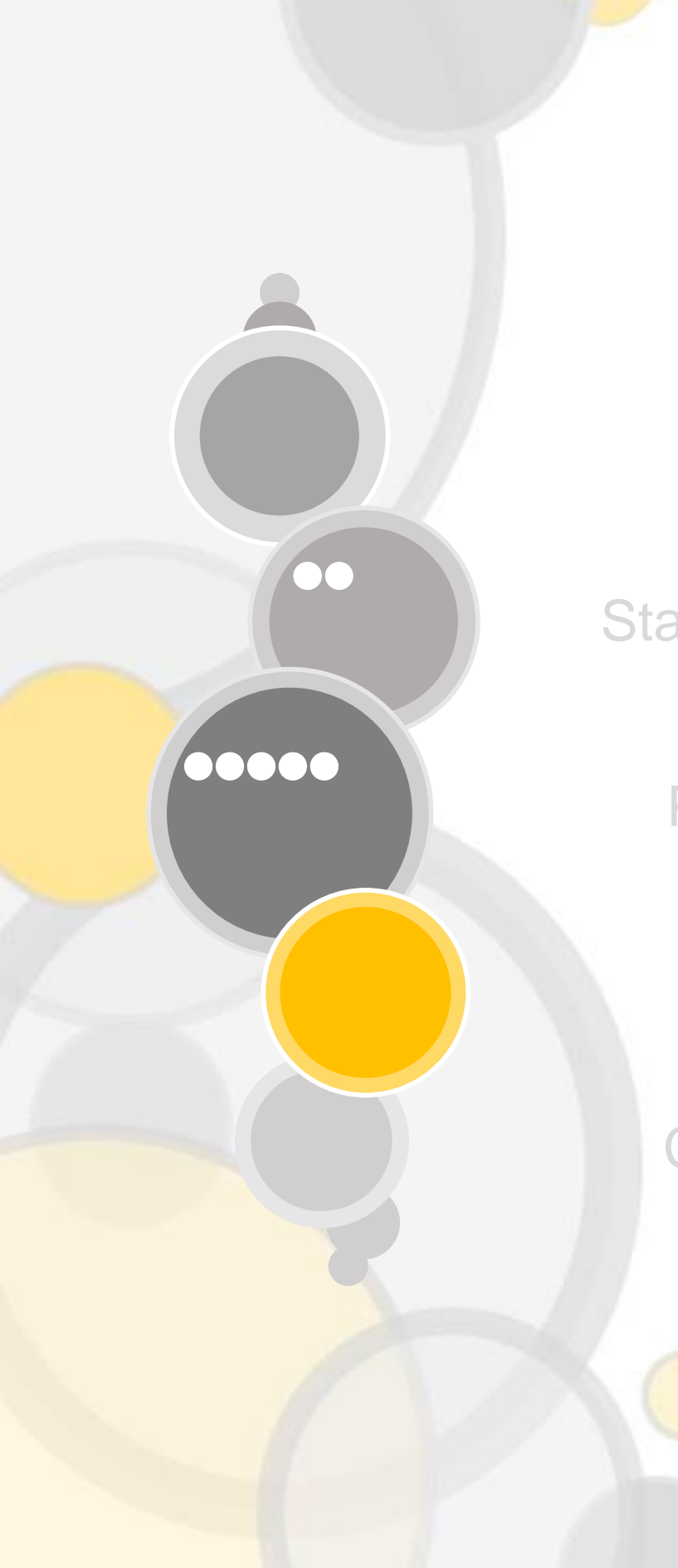
17. Bonse, J.; Höhm, S.; Kirner, S.V.; Rosenfeld, A.; Krüger, J. Laser-Induced Periodic Surface Structures—A Scientific Evergreen. *IEEE J. Sel. Top. Quantum Electron.* **2017**, *23*, 9000615. [[CrossRef](#)]
18. Cubero, A.; Martínez, E.; Angurel, L.A.; de la Fuente, G.F.; Navarro, R.; Legall, H.; Krüger, J.; Bonse, J. Effects of laser-induced periodic surface structures on the superconducting properties of Niobium. *Appl. Surf. Sci.* **2020**, *508*, 145140. [[CrossRef](#)]
19. Voisiat, B.; Gedvilas, M.; Indrišūnas, S.; Raciukaitis, G. Flexible microstructuring of thin films using multi-beam interference. *J. Laser Micro/Nanoeng.* **2011**, *6*, 185–190. [[CrossRef](#)]
20. Gedvilas, M.; Indrišūnas, S.; Voisiat, B.; Stankevičius, E.; Selskis, A.; Račiukaitis, G. Nanoscale thermal diffusion during the laser interference ablation using femto-, pico-, and nanosecond pulses in silicon. *Phys. Chem. Chem. Phys.* **2018**, *20*, 12166–12174. [[CrossRef](#)]
21. Bonse, J.; Kirner, S.V.; Krüger, J. Laser-Induced Periodic Surface Structures (LIPSS). In *Handbook of Laser Micro and Nano-Engineering*; Sugioka, K., Ed.; Springer: Cham, Switzerland, 2020.
22. Bonse, J.; Gräf, S. Maxwell Meets Marangoni—A Review of Theories on Laser-Induced Periodic Surface Structures. *Laser Photonics Rev.* **2020**, *14*, 2000215. [[CrossRef](#)]
23. Bonse, J. Quo Vadis LIPSS?—Recent and Future Trends on Laser-Induced Periodic Surface Structures. *Nanomaterials* **2020**, *10*, 1950. [[CrossRef](#)] [[PubMed](#)]
24. Okamuro, K.; Hashida, M.; Miyasaka, Y.; Ikuta, Y.; Tokita, S.; Sakabe, S. Laser fluence dependence of periodic grating structures formed on metal surfaces under femtosecond laser pulse irradiation. *Phys. Rev. B* **2010**, *82*, 165417. [[CrossRef](#)]
25. Hou, S.; Huo, Y.; Xiong, P.; Zhang, Y.; Zhang, S.; Jia, T.; Sun, Z.; Qiu, J.; Xu, Z. Formation of long-and short-periodic nanoripples on stainless steel irradiated by femtosecond laser pulses. *J. Phys. D* **2011**, *44*, 505401. [[CrossRef](#)]
26. Gecys, P.; Vinciunas, A.; Gedvilas, M.; Kasparaitis, A.; Lazdinas, R.; Raciukaitis, G. Ripple formation by femtosecond laser pulses for enhanced absorptance of stainless steel. *J. Laser Micro/Nanoeng.* **2015**, *10*, 129–133. [[CrossRef](#)]
27. Liu, J.M. Simple technique for measurements of pulsed Gaussian-beam spot sizes. *Opt. Lett.* **1982**, *7*, 196. [[CrossRef](#)] [[PubMed](#)]
28. Zemaitis, A.; Gaidys, M.; Brikas, M.; Gecys, P.; Raciukaitis, G.; Gedvilas, M. Advanced laser scanning for highly efficient ablation and ultrafast surface structuring: Experiment and model. *Sci. Rep.* **2018**, *8*, 17376. [[CrossRef](#)]
29. Golovashkin, A.I.; Leksina, I.E.; Motulevich, G.P.; Shubin, A.A. The optical properties of niobium. *Sov. Phys. JETP* **1969**, *29*, 27–34.
30. Raether, H. *Surface Plasmons on Smooth and Rough Surfaces and on Gratings*; Springer: Berlin/Heidelberg, Germany, 1988.
31. Derrien, T.J.Y.; Krüger, J.; Bonse, J. Properties of surface plasmon polaritons on lossy materials: Lifetimes, periods and excitation conditions. *J. Opt.* **2016**, *18*, 115007. [[CrossRef](#)]
32. Gedvilas, M.; Raciukaitis, G.; Regelskis, K. Self-organization in a chromium thin film under laser irradiation. *Appl. Phys. A* **2008**, *93*, 203–208. [[CrossRef](#)]
33. Kunz, C.; Bonse, J.; Spaltmann, D.; Neumann, C.; Turchanin, A.; Bartolomé, J.F.; Müller, F.A.; Gräf, S. Tribological performance of metal-reinforced ceramic composites selectively structured with femtosecond laser-induced periodic surface structures. *Appl. Surf. Sci.* **2020**, *499*, 143917. [[CrossRef](#)]
34. Pan, A.; Dias, A.; Gomez-Aranzadi, M.; Olaizola, S.M.; Rodriguez, A. Formation of laser-induced periodic surface structures on niobium by femtosecond laser irradiation. *J. Appl. Phys.* **2014**, *115*, 173101. [[CrossRef](#)]
35. Choudhury, T.; Saied, S.O.; Sullivan, J.L.; Abbot, A.M. Reduction of oxides of iron, cobalt, titanium and niobium by low-energy ion bombardment. *J. Phys. D Appl. Phys.* **1989**, *22*, 1185–1195. [[CrossRef](#)]
36. Dacca, A.; Gemme, G.; Mattera, L.; Parodi, R. XPS analysis of the surface composition of niobium for superconducting RF cavities. *Appl. Surf. Sci.* **1998**, *126*, 219–230. [[CrossRef](#)]
37. Yang, Z.; Lu, X.; Tan, W.; Zhao, J.; Yang, D.; Yang, Y. XPS studies of nitrogen doping niobium used for accelerator applications. *Appl. Surf. Sci.* **2018**, *439*, 1119–1126. [[CrossRef](#)]
38. Kirner, S.V.; Wirth, T.; Sturm, H.; Krüger, J.; Bonse, J. Nanometer-resolved chemical analyses of femtosecond laser-induced periodic surface structures on titanium. *J. Appl. Phys.* **2017**, *122*, 104901. [[CrossRef](#)]
39. Badrinarayanan, S.; Sinha, S. X-ray photoelectron spectroscopy studies of the reaction of N^{+2} -ion beams with niobium and tantalum metals. *J. Appl. Phys.* **1991**, *69*, 1141–1146. [[CrossRef](#)]

40. Prieto, P.; Galán, L.; Sanz, J.M. An XPS study of NbN_x prepared by ion implantation and the near-surface effects induced by Ar⁺ bombardment. *Surf. Sci.* **1991**, *251–252*, 701–705. [[CrossRef](#)]
41. van Gurp, G.J. The effect of structure on the superconducting properties of vanadium and niobium foils. *Philips Res. Rep.* **1967**, *22*, 10–35.
42. Finnemore, D.K.; Stromberg, T.F.; Swenson, C.A. Superconducting properties of high-purity niobium. *Phys. Rev.* **1966**, *149*, 231–243. [[CrossRef](#)]
43. Castel, X.; Guilloux-Viry, M.; Perrin, A.; Le Paven-Thivet, C.; Debuigne, J. Correlation between microwave surface resistance, AC susceptibility and in-plane ordering in YBa₂Cu₃O₇ thin films epitaxially grown on (100) MgO substrates. *Physica C* **1995**, *255*, 281–292. [[CrossRef](#)]

Publisher's Note: MDPI stays neutral with regard to jurisdictional claims in published maps and institutional affiliations.



© 2020 by the authors. Licensee MDPI, Basel, Switzerland. This article is an open access article distributed under the terms and conditions of the Creative Commons Attribution (CC BY) license (<http://creativecommons.org/licenses/by/4.0/>).



Objectives

State of the Art

Publications

Discussion

Conclusions

Global Discussion

During this thesis, several objectives have been accomplished. Along this chapter, the general overview and discussion of the main obtained results are discussed.

1. Thermal stability and electromagnetic behaviour of superconducting cables and coils

In the course of this work, thermal stability of different superconducting devices has been tested. Worth to mention that the required cryogenic operating regime in these cases is an important constrain and thermal analysis is very relevant. As a reminder, local temperature gradients above a certain value can induce a sudden transition to normal state. This can be caused by the existence of conductor defects or by the temporal application of overcurrents (currents above I_c), generating irreversible damages if the conductor is not appropriately stabilized.

1.1 MgB₂ Rutherford cables: Quench analysis

In this thesis, magnesium diboride conductors braided in Rutherford geometry have been analysed. This work has been done in collaboration with the group of Dr. Kováč in the Institute of Electrical Engineering in Bratislava (Slovakia), who manufactured the cables, using wires fabricated by HyperTech Inc. (USA) as strands. Our main work was to analyse the quench dynamics of these cables, which were new for MgB₂. The results have been published in **publication A** and presented in the EUCAS 2017 conference.

Referred cables are composed by 12 strands braided with a transposition length of ≈ 27 mm, without metallic core between the upper and lower layer, and have a rectangular cross-section with final dimensions on 2.7 mm width and 0.7 mm thickness. Filaments are surrounded by a niobium barrier to minimise chemical reaction between the precursor powders and the sheath during in situ formation of the MgB_2 phase. Two different cable configurations have been analysed, which differ on the type of wire used as strands, but have the same dimensions: First, a 6-filament strands, each sheathed with copper. And the second one, monofilament strands with a copper-nickel alloy sheath. **Figure I** shows the cross-sections of both mentioned Rutherford cables (**a-b**), together with a picture of the same cables with the installed heater, voltage taps and thermocouples to study their behaviour against quench (**c-d**). In order to minimise effects related with the cable ends (soldered to the current leads), the length of the measured cables was 25 cm and 11 cm for the Cu- and Cu10Ni-sheathed cables, respectively, because of the higher thermal and electrical conductivity of the former. In both cases, the cables were cooled by conduction from the ends.

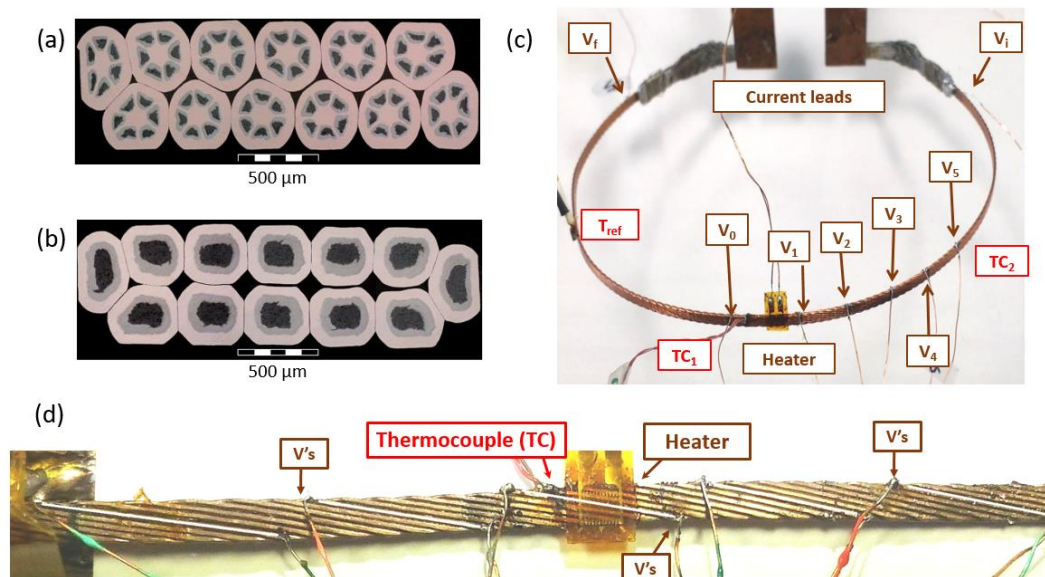


Figure I Analysed MgB_2 Rutherford cables. **(a)** Cross-section of the copper-sheathed multifilament configuration. **(b)** Cross-section of the monofilament cable with Cu10Ni alloy sheath. **(c)** Copper sheathed cable with soldered thermocouples (TC_i) and voltage taps (V_j). The heater is placed between V_0 and V_1 , separated 1 cm, and the distance between consecutive voltage taps V_2 to V_5 is 1.5 cm **(d)** Picture of a Cu10Ni-sheathed cable showing one of the used voltage tap configurations.

1. Thermal stability and electromagnetic behaviour of superconducting cables and coils

Unlike most monolithic conductors, such as wires or tapes, where the full cross section at a given position can be considered equipotential in a good approximation, for Rutherford cables this assumption may not be valid because of their braided geometry. The measured voltages may thus depend on the relative position of voltage taps between the strands. To facilitate the analysis of the quench dynamics across the strands and also along them, several voltage taps have been soldered to different strands to measure both inter- and intra-strand voltages. In addition, the cables have been instrumented with thermocouples to measure the conductor's temperature.

The analysis of the Cu-sheathed Rutherford cables consisted in their electrical characterization and the study of quenches induced by heat pulses. These cables showed an E versus J potential dependence with very low n -value of ≈ 2.5 (**Figure II (a)**). Due to this dependence and to the copper's high thermal and electrical conductivity, it was not possible to induce quenches on it. For every heat pulse (of different duration and power), recovery was always observed. As an example of this behaviour, during the heat pulse showed in **Figure II (b)** none of the voltages measured between strands (following configuration depicted in **Figure I (c)**) reached $10 \mu\text{V}$, being some positives and others negative as a result of the current redistribution among strands caused by the heat disturbance. During the pulse, the maximum temperature values registered by the thermocouples were 25.3 K and 21.4 K for TC_1 and TC_2 respectively, being the initial temperature of 18.3 K.

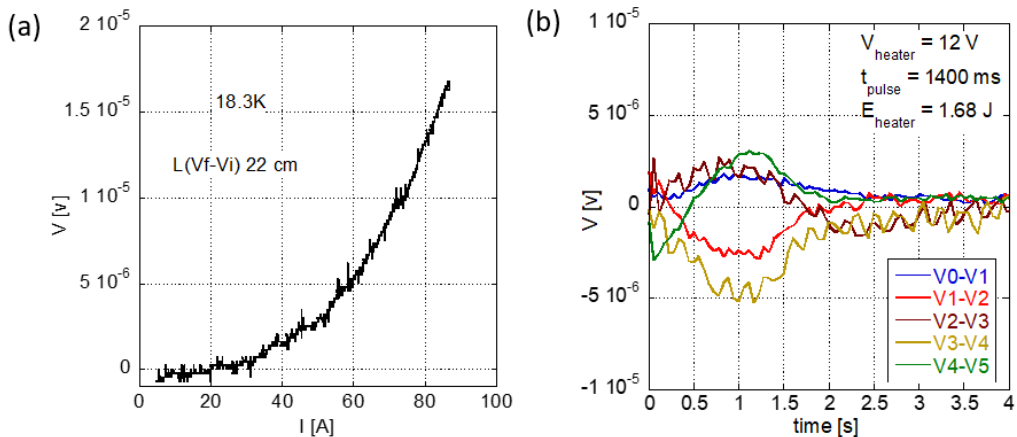


Figure II Copper-sheathed Rutherford cable characterization **(a)** Current-voltage dependence of the cable. **(b)** Time evolution of the voltage measured between different voltage taps during a heat pulse of 1.68 J that starts at $t = 0$ s.

For the cables made with Cu10Ni-sheathed strands, two types of test have been performed to induce quenches: External heat pulse to reproduce a hot-spot in the conductor, and overcurrents injected to the cable. Quenches induced by an external heater present two distinct stages in their propagation. During the first one, the minimum propagation zone (MPZ) is formed slowly, mainly by the strands in contact with the heater. Here, current-sharing phenomenon takes place between the superconductor core and the metallic sheath. Once the MPZ is developed, the quench propagates towards the ends of the cable, which is much faster. Voltages measured between separated strands could be negative due to unequal quenching of strand segments, causing local differences in $E(J)$ between them. Current redistribution and current transfer between strands can induce the transition from negative to positive of that voltage signal, so that eventually all strands transit to normal state.

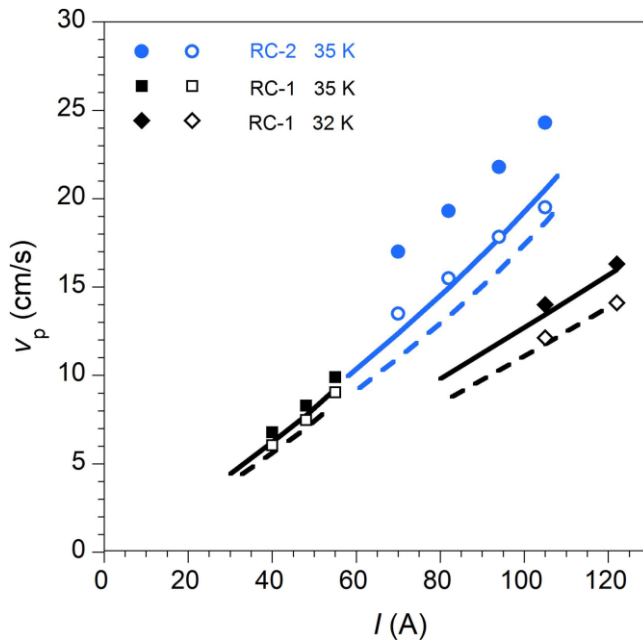


Figure III Quench propagation velocities in Cu10Ni-sheathed Rutherford cables (RC-1 and -2 are two different tested cables, names used in Publication A), as a function of the operating current and at different temperatures. Symbols correspond to experimental values using different criteria, as discussed in publication A: Solid symbols are values obtained with $V_{\Delta t} = 1$ mV criterion and open symbols with $V_{\Delta t} = V_{normal}/2$ criterion. Continuous lines draw Wilson’s model predictions and dashed lines Dresner’s ones.

During these hot-spot studies, quench propagation velocities along the cable have been analysed at different temperatures. The quench propagation velocities have been estimated from the time delay between the voltages measured in different strand

1. Thermal stability and electromagnetic behaviour of superconducting cables and coils

segments and the distance between the corresponding voltage taps. Two different criteria were used, as described in detail in **publication A**. The obtained experimental values are displayed in **Figure III**. They show relatively good agreement with those estimated by the one-dimensional predictions made by Wilson and Dresner models. However, the presence of inhomogeneities in the conductor, or some local differences in the E - J function along the cable, can cause those variations in the experimental values compared with the models.

On the other hand, overcurrents induce quenches almost simultaneously spread over the cable. Copper-nickel alloy (Cu10Ni) showed high electrical resistance producing not enough thermal stability along the cable under the studied cooling conditions. Hence, during high current operation, induced quenches can deteriorate the conductor, being advisable the introduction of higher conductive sheath in the strands to make the cables more robust, at least for applications where AC losses are not critical.

1.2 2G-HTS coil: Electromagnetic and thermal behaviour.

Publication B has been devoted to the study of the thermal and electromagnetic performance of a second generation high temperature superconductor double pancake (DP), wound continuously and without insulation between turns (NI-coil). After the winding of 30 turns per layer, the coil was impregnated with epoxy and then glued to a copper support plate. This plate was anchored to the cold finger of a cryocooler (i.e., the coil is conduction cooled). So, once the first challenge of building the coil was overcome, the next objective was to study its thermal and electromagnetic behaviour under high-current operating conditions.

Several thermal cycles (from room temperature to cryogenic operating temperature) have been performed without sensible degradation of the superconducting properties. The temperature gradient has been measured between the copper plate and the lower pancake coil and also between both, lower and upper pancake coils (**Figure IV (a-b)**). It has been found that the adhesion between the copper plate and the epoxy must be improved, since it is crucial to a proper coil thermalization, and after various tests, it was needed to re-glue again. As it is shown in **Figure IV (c)**, the coil performance improved in the fifth cycle, after the coil was re-glued. This has opened new research lines in which new epoxies have been explored and copper surface is being modified in order to improve mechanical and thermal properties of these junctions. Thanks to the lack of turn-to-turn insulation, thermal behaviour during regular (high current) operating regime was

satisfactory and temperature in the most adverse point (upper coil, the one further from the cold finger) slightly increased.

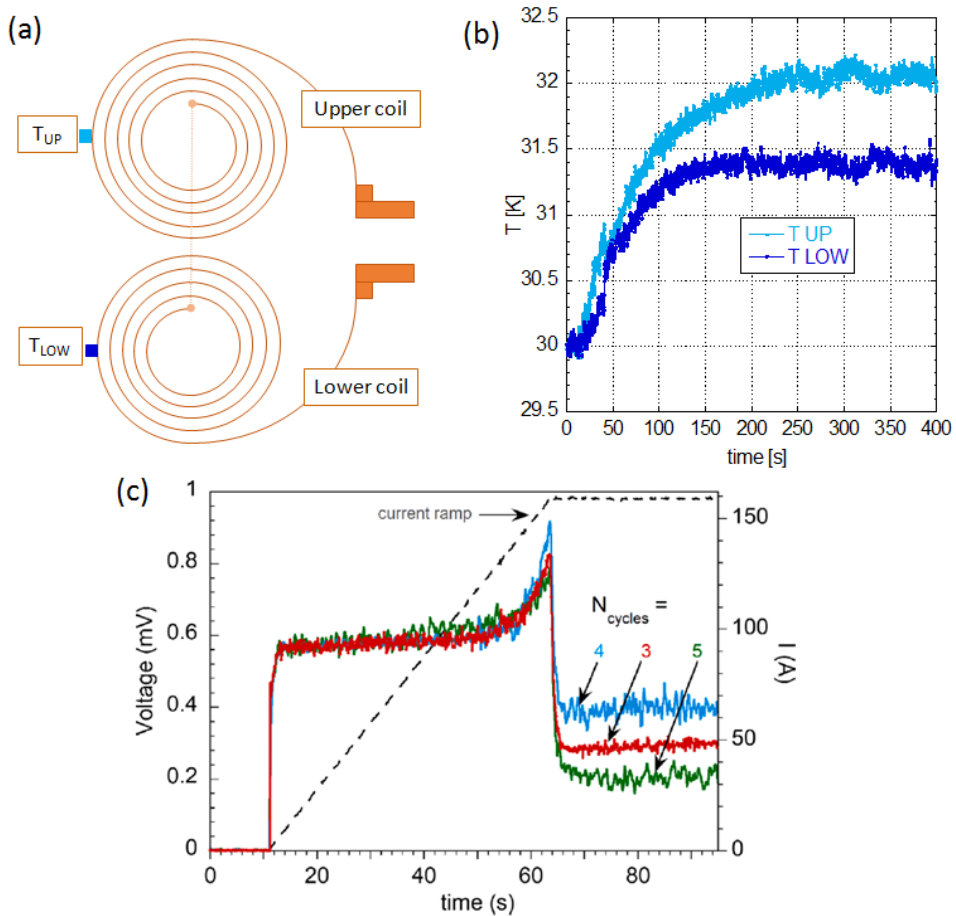


Figure IV (a) Schematic illustration of DP continuous coil connected to the current leads (orange L-shaped parts), indicating the position of the thermocouples. Lower coil was the one attached to the copper-support plate. **(b)** Time evolution of temperature in both coils with the copper plate set at 30 K after applying 0.08W power to a heater placed over the upper coil. Measured temperature increase was $\Delta T_{UP-Low} \approx 0.7$ K and $\Delta T_{Low-Copper\ plate} \approx 1.4$ K at steady conditions. **(c)** Time evolution of upper-coil's voltages during coil's charging ($T = 60$ K, current rate 3 A/s up to 159 A) in different thermal cycles 3, 4 and 5.

From the electromagnetic viewpoint, the coil has been studied during charge and discharge processes, with different current ramps rates and at diverse temperatures. Maximum current tested above coil's critical current has also been performed to analyse its thermal stability. This way, resistive voltages (inferior to 50 μ V in the lower coil and less than 350 μ V for the upper one) were hold without triggering a quench, a sign of the

1. Thermal stability and electromagnetic behaviour of superconducting cables and coils

coil good thermal behaviour. Besides, an analysis of the experimental data has been performed to estimate the different energy AC loss contributions during the current ramps. Thus, the contribution to AC losses of the induced currents in the radial direction between turns (as a consequence of the absence of insulation between neighbouring turns), and those related with the superconductor (magnetic losses) have been identified. Moreover, although turn-to-turn electrical contact resistance, R_t , depends on several factors (such as tape surface condition, winding tension, etc) it was calculated as $\approx 110 \mu\Omega \text{ cm}^2$ at 77K, similar value to the one reported by other groups. In addition, it should be remarked the good agreement between the experimentally obtained coils' critical currents and those calculated numerically using the modified load-line method and magnetic finite-element simulations.

Previous to the study of the coil's behaviour, thermal stability of the whole cryogenic system was analysed, and the results have been also included in **publication B**. High current injection (up to 400 A) in steady conditions is needed during this work, and that means a heat entrance to the superconducting device that has to be controlled. Current leads, through which the current flows from ambient temperature to the coil, have been designed with two intermediate heat sinks (HS2 and HS1, thermally attached at the liquid nitrogen vessel and at the first stage of the cryocooler, respectively). These have to be electrically insulated and with sufficient thermal conductance in their joints to avoid heat overloads both, in the leads and the coil. The solution proposed has been to design the appropriate copper pieces (contact areas of 17 and 20 cm^2) coated with plasma-sprayed alumina (Al_2O_3). Stable conditions with high working currents were achieved for more than 5 hours, thanks to thermal contact conductance values, h_j , which were estimated ≈ 1800 and $850 \text{ W m}^{-2} \text{ K}^{-1}$ at $\approx 80 \text{ K}$ and $\approx 35 \text{ K}$, respectively. In the course of the experiments, heat inputs are entering through the current leads via ohmic losses (current injection) and also via thermal conductance (since one side on the lead is at room temperature and the other end is working in cryogenic regime). With the maximum applied current, in comparison with no-current situation, the temperatures of the lead in contact with the sinks further increase by $\Delta T \approx 3 \text{ K}$ and $\approx 5.5 \text{ K}$ in HS2 and HS1, respectively. These values can be reduced by improving h_j values, meaning better contact conductance in the heat sink joints.

2. Laser melting techniques to improve thermal properties of alumina coatings

In order to further improve thermal behaviour of the alumina coatings mentioned above, especially at cryogenic temperatures, **publication C** analyses how laser technology enables remelting processes of the electrical insulation ceramic layer, increasing its density and controlling crack generation without detachment between the Al_2O_3 and the metallic support. A special setup, using a cryocooler, has been built, with both hot and cold focus, to measure the thermal conductance of the insulating layer in samples of 2 cm^2 surface contact at temperatures ranging from 10 to 77 K. Heat transfer via radiation and convection has been neglected because of the radiation shield installed and the high vacuum ($\approx 10^{-5}$ hPa) conditions that have been used during the experiments. To ensure good surface contact, Apiezon-N has been used as an intermediate layer between all surfaces in contact.

Pulsed near-infrared laser has been used to densify the plasma-sprayed alumina coating of around 150-micron thickness. Laser processing was done by the meandering laser beam scanning (MLBS) method, where the laser beam follows a meander-shaped path, covering this way the whole surface. Main laser processing parameters, such as average pulse fluence (F_p), irradiance (I_p), repetition frequency (f_{rep}), pulse duration (τ_p), laser beam scanning speed (v_L) and hatching distance between consecutive lines (d_s) were adjusted to control the melted front, to avoid the formation of holes in the surface and to minimize crack generation. All those parameters had to be precisely controlled to process the alumina coating without affecting excessively the copper substrate.

Figure V shows the evolution of surface topography during the optimization experiments of the laser process. The first sample **(a)** has been irradiated with a laser power of 35 W, using a τ_p value of just 20 ns ($F_p = 1.17 \text{ J/cm}^2$ and $I_p = 58.6 \text{ MW/cm}^2$). Such short pulses in combination with $v_L = 500 \text{ mm/s}$, ended in a flickering melting treatment over Al_2O_3 , not convenient for our purpose. The second one **(b)** has been treated with $\tau_p = 200 \text{ ns}$, but using $f_{rep} = 300 \text{ kHz}$. Since this sample has been irradiated with $F_p = 7 \text{ J/cm}^2$, v_L was set at 1000 mm/s. The result was a strong ablation, without appreciable remelting. The third sample **(c)** has been irradiated with $\tau_p = 200 \text{ ns}$, $f_{rep} = 900 \text{ kHz}$, $F_p = 1.17 \text{ J/cm}^2$ ($I_p = 5.86 \text{ MW/cm}^2$) with $v_L = 120 \text{ mm/s}$. Al_2O_3 was melted, but a large number of holes and cracks emerge after the treatment, which are not suitable for good thermal contact applications. **Figure V (d)** shows the result of appropriate relation of parameters ($\tau_p = 200 \text{ ns}$, $f_{rep} = 900$

2. Laser melting techniques to improve thermal properties of alumina coatings

kHz, $F_p = 0.91 \text{ J/cm}^2$, $I_p = 4.57 \text{ MW/cm}^2$ and $v_L = 50 \text{ mm/s}$) ending in a continuous and more homogenous melted surface, with minimized number and size of formed cracks during the processing.

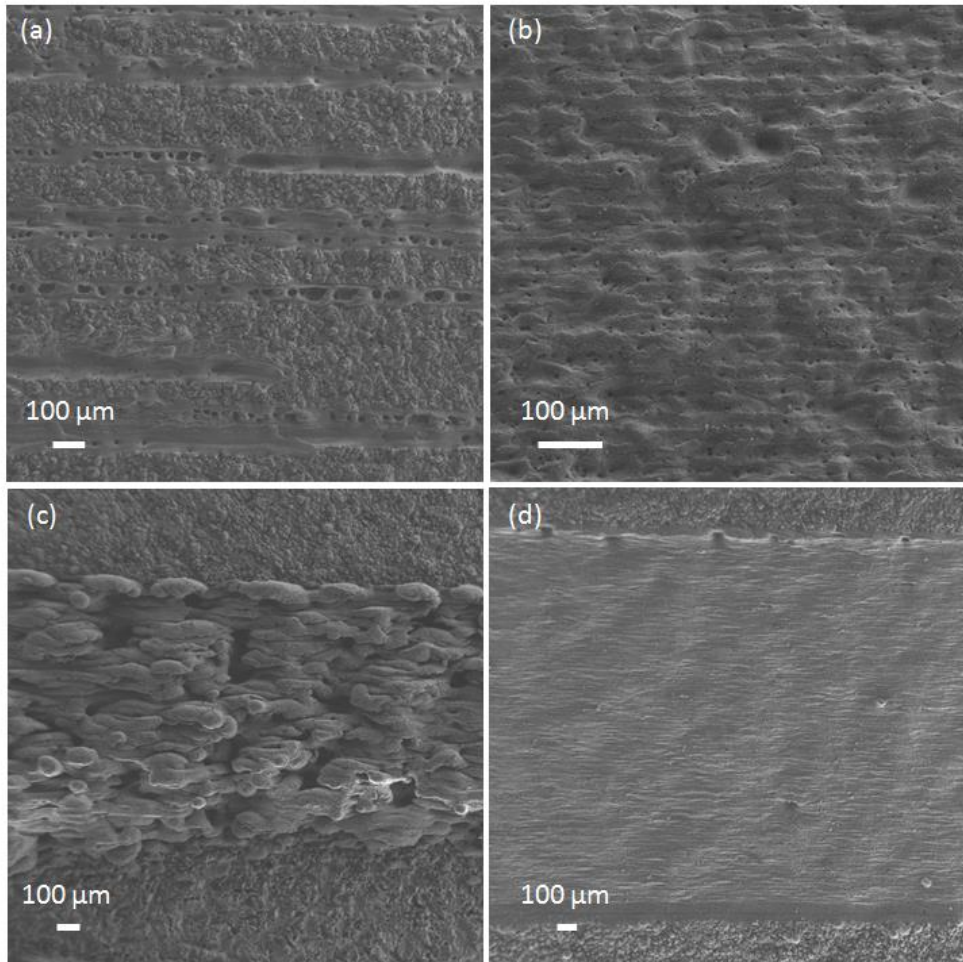


Figure V SEM images of alumina coatings after several treatment tests with parameters given in the text. In all of them with the laser beam scanning was horizontally. In (c) and (d) figures, untreated surfaces are shown above and below processed areas.

Final samples were irradiated with $I_p = 4.57 \text{ MW/cm}^2$, 900 kHz, $\tau_p = 200 \text{ ns}$ and v_L values between 50 and 80 mm/s with $d_s = 20 \mu\text{m}$, in order to measure their thermal behaviour. At these conditions, predominant metastable γ -alumina phase of as-sprayed coatings was turned to α -alumina (corundum).

Thermal measurements of those samples threw out an enhancement of the thermal contact conductance, especially in the range between 30 K and 77 K where an improvement factor larger than two was achieved (**Figure VI**). Values of thermal conductance of the as-sprayed coating samples presented in this work are slightly different from those calculated in **publication B**. There are several reasons that explain those differences. In one hand, the size of the samples is much smaller in the latter analysis, so that the contact pressure during the measurements have not been the same in both experiments due to the differences in the contact configurations. The optimization of bolted configurations, to achieve homogenous contact pressures for large contact areas, is the subject of ongoing research. On the other hand, the estimated h_j values presented in publication B, were calculated using the numerical calculated heat inleak in the heat sinks and the experimentally measured ΔT across the joint for different currents. However, experiments have shown that the real heat values were of the order but systematic higher than the numerical predictions, as explained in detail in **publication B**.

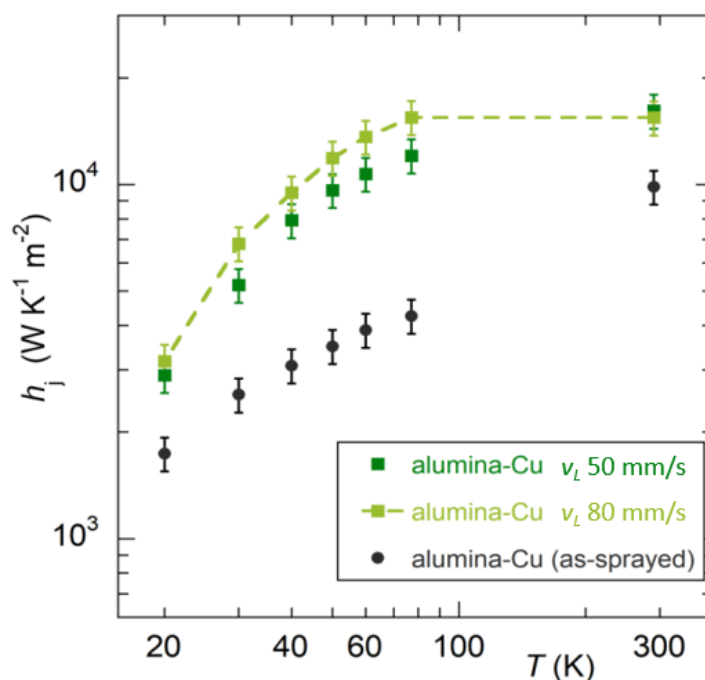


Figure VI Temperature dependence of the thermal contact conductance between copper and alumina, for the as-sprayed alumina coatings and laser processed coatings with two optimum laser processing conditions. Samples were processed with the same conditions except the scanning speeds values that were 80 and 50 mm/s, respectively.

3. Surface laser nanostructuring and superconducting properties

Laser technology can be a useful tool for surface processing, allowing, thus, a change of its properties. In this thesis, diverse lasers have been used to engineer superconducting material surfaces. Pulsed lasers, which pulse duration range from hundreds of picoseconds to tenths of femtoseconds, have been used to irradiate niobium surface. The use of ultrashort pulse lasers eases the formation of micro and nanostructures in quasi-periodic arrangements. These laser-induced periodic surface structures, known as LIPSS, may have diverse periodicities and shapes depending on the laser irradiation parameters and the material optical properties. This fact opens the path to investigate how structures with the size close to coherence length can affect the superconducting properties. Niobium has been chosen since is the pure metal with the highest critical temperature and critical magnetic field and has a large coherence length.

Publications D and E present the first studies about the effect of those nanostructures in the superconducting properties of niobium. Diverse laser processing treatments have been reported using three different lasers: An ultraviolet picosecond laser with repetition frequencies in the range of hundreds of kHz, and two different near-infrared femtosecond lasers (228 and 30 fs) irradiating with 1 kHz. All the analysed samples were treated on its top and bottom surfaces, in order to identify better any possible modification of their magnetic behaviour. The use of so different laser sources and processing parameters results in treatments whose irradiance values differ by three orders of magnitude (I_p ranges from 0.3 to 5000 GW/cm²). Surface morphology characterization has been performed by FESEM and AFM techniques, and EDX and XPS have been used for surface chemical analysis as well. Wide range of nano- and microstructures has been generated with different morphology, depth and spatial periodicity.

Initially, 1-mm thick samples of Nb were irradiated with the UV laser and rippled nanostructures were formed over the surface (**Figure VII (a)**). It is clearly observed that this ps-laser treatment has produced some changes in the superconducting properties of the processed sample compared to the reference one (**Figure VII (b)**), with a small reduction of the ΔM values at low magnetic fields, and an increase at magnetic fields above 0.6 T. Then, in order to increase the effect of surface superconductivity over the bulk (overall) contribution, thinner samples (25- μ m) have been processed with both femto- and picosecond near-IR lasers.

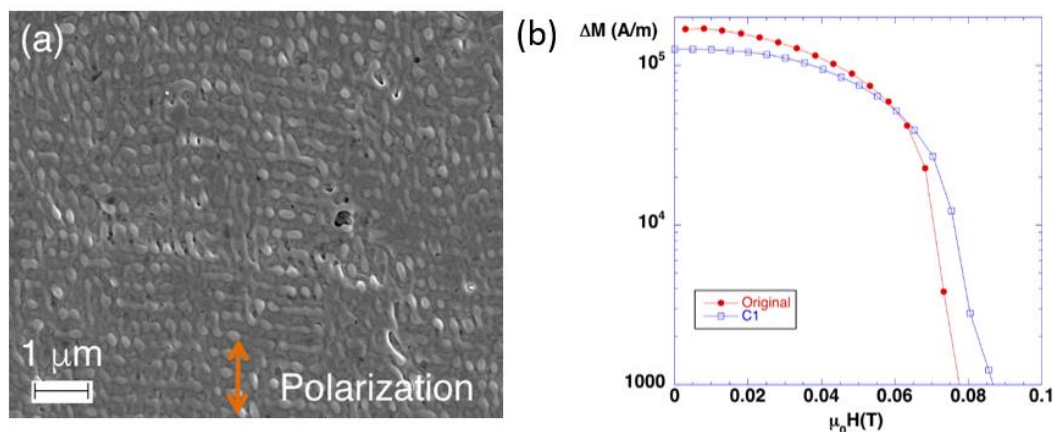


Figure VII (a) SEM image of 1- μm thick niobium sample irradiated with 300-ps UV laser under nitrogen atmosphere and group of parameters named C1 in publication D: $I_p = 0.45 \text{ GW/cm}^2$, $f_{\text{rep}} = 700 \text{ kHz}$, $v_L = 300 \text{ mm/s}$ and $d_s = 5 \mu\text{m}$. Orange arrow indicates laser polarization direction. **(b)** Magnetic field dependence, measured at $T = 8 \text{ K}$, of the width of hysteresis loop, $\Delta M(H)$, calculated as the difference between descending- and ascending-branch magnetization.

Surface nanostructures generated by both used fs-lasers are similar. These structures are named low spatial frequency LIPSS (LSFL) (see **Figure VIII (a)**), whose main orientation is perpendicular to the laser polarization and their observed periodicity (≈ 570 and $\approx 775 \text{ nm}$) is well-correlated with the laser incident wavelength (790 nm and 1030 nm, respectively), in agreement with reported results in literature. Those analysed structures show a peak-to-valley depth of $\approx 150 - 200 \text{ nm}$ and in between LSFL arrangements, also emerged high spatial frequency structures (HSFL type) parallel to polarization with spatial periods between 50 and 80 nm (**Figure VIII (b)**).

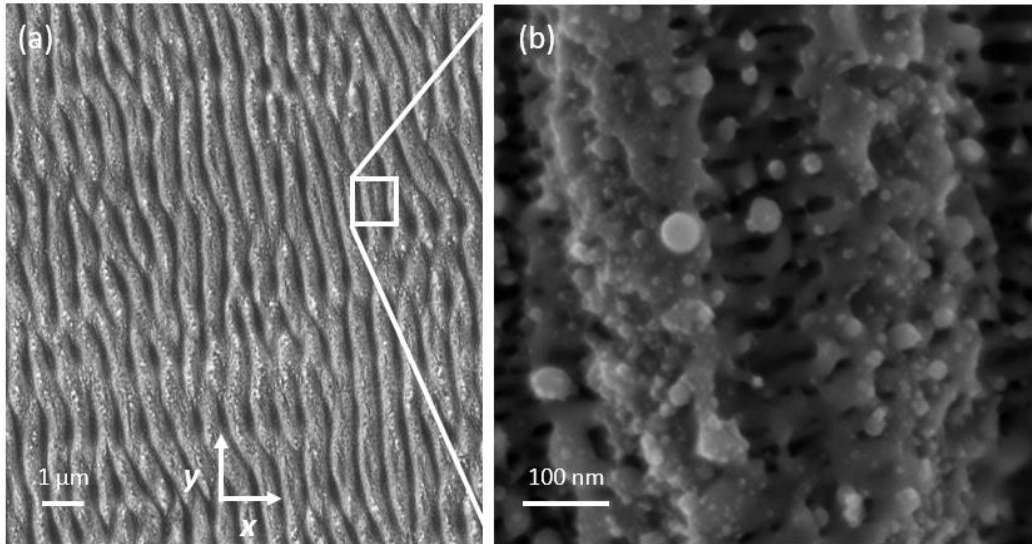


Figure VIII Niobium sheet surface irradiated with 30-fs n-IR laser of centre wavelength 790 nm. (This sample was named FS_air2 in publication E). LSFL are shown in the left image. HSFL are depicted in the zoom-in right image. Laser polarization is parallel to x-axis. Some horizontal macroscopic defects can be seen in the left image, which correspond to rolling process previous to laser treatment.

Samples treated with 300-ps UV laser have presented a wider range of structures: Less energetic treatments have originated ripples structures, sometimes with drop-like nanostructures over those arrangements (shown in **Figure IX (a-b)**). On the other hand, more aggressive irradiation processes (higher irradiance and larger number of pulses overlapped) have derived in protrusions separated by distances of around 1 micrometre (shown in **Figure IX (c-d)**). Low-fluence treatments have induced structures with spatial periodicity of ≈ 337 nm, very close to the laser wavelength, and AFM topographies showed a peak-to-valley distance less than 20 nm. Additionally, treatments with fluence values above $F_p \approx 0.3$ J/cm² have induced spike-type structures with less spatial homogeneity.

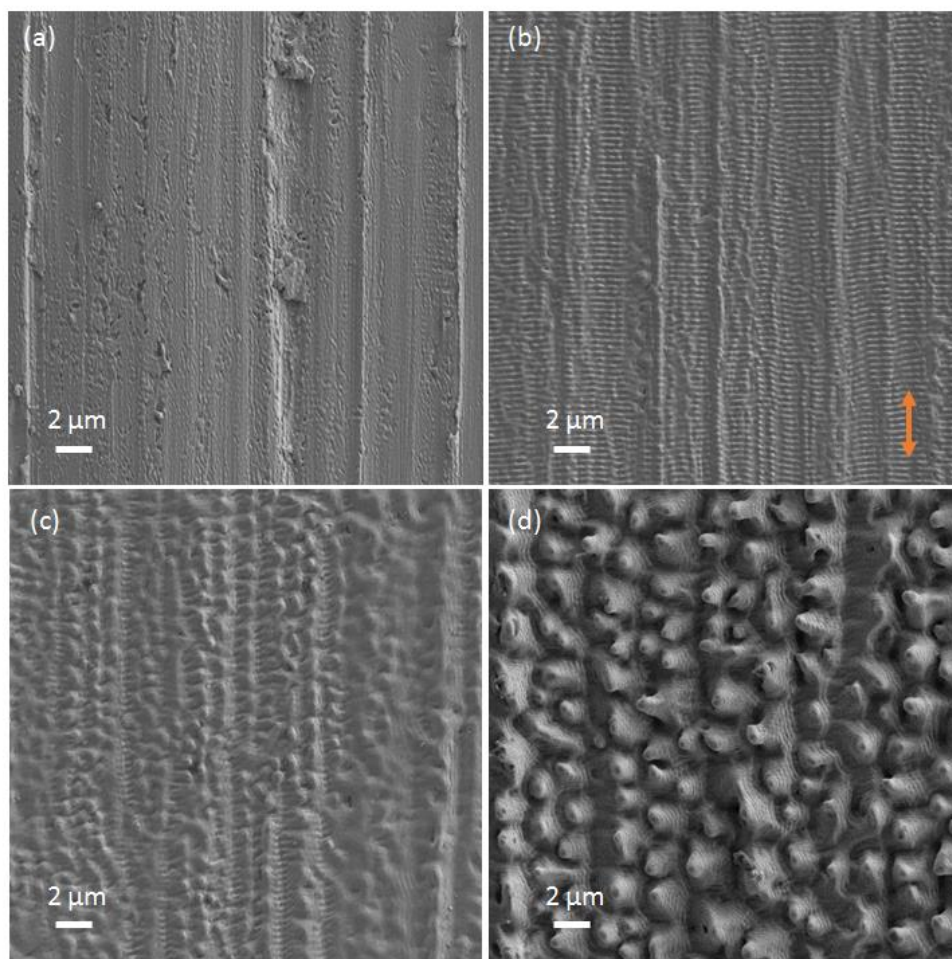


Figure IX Niobium sheet surfaces irradiated with 300-ps UV laser. Vertical macroscopic defects shown correspond to rolling process previous to any laser treatment. Orange arrow point the laser polarization direction. Different fluence values were employed: **(a)** 0.14 J/cm². **(b)** 0.23 J/cm². **(c)** 0.33 J/cm². **(d)** 0.59 J/cm².

Studied samples have been treated in different controlled atmospheres (air, argon and nitrogen). Surface chemical analysis has been performed to study the effect of the used atmosphere. Firstly, EDX analysis done over 1-mm thick Nb sample, irradiated with UV laser in N₂ atmosphere, has shown that the amount of oxygen in the sample surface was slightly reduced compared with non-treated surface. Niobium surfaces irradiated with fs-lasers under diverse atmospheres were analysed with both EDX and XPS, indicating that Nb₂O₅ is the dominating type of oxide near the surface. In air-treated samples, the laser-induced oxide layer has a thickness of few tens of nanometers, being thinner in surfaces irradiated under inert atmospheres. The latter case is comparable to the oxide layer of

non-treated samples. Referred irradiation under nitrogen induces a small signal of that element in chemical analysis but not consistent with the presence of niobium nitrides.

Regarding magnetic analysis performed in 25- μm thick samples, **publication D** presents a clear influence on the measured current density values in some magnetic field ranges, when the magnetic field is applied perpendicular to a sample's surfaces, previously irradiated with either UV and n-IR lasers. Moreover, **publication E**, shows magnetic measurements with external fields above H_{C2} (parallel to the samples) to analyse the effect of fs-laser irradiation on the surface superconductivity, which persists up to H_{C3} . Here, clear influences of the laser processing in the surface superconductivity have been found, compared to non-irradiated samples.

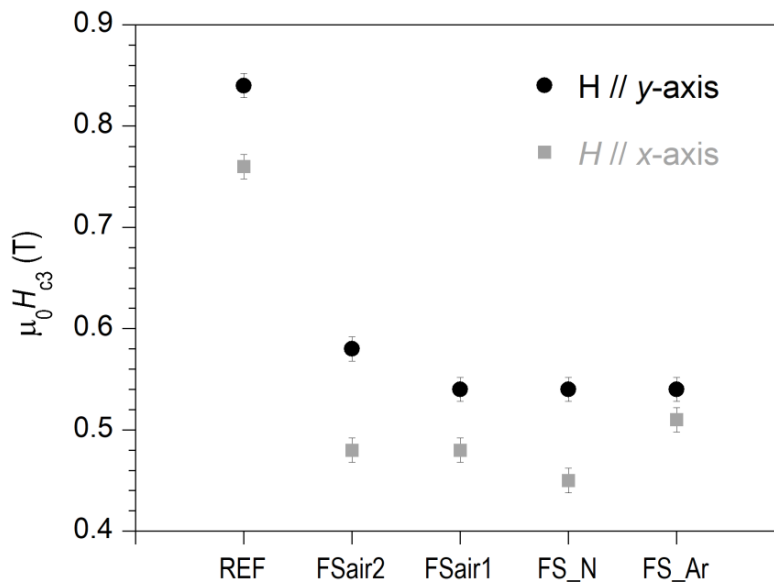


Figure X Critical surface fields, $\mu_0 H_{C3}$, of all analyzed samples derived from $\chi''(H)$ measurements at $T = 5$ K, $f = 10$ Hz and $\mu_0 h_0 = 10$ μT , with the external magnetic field applied parallel to the x - and y -axis. X - and Y -axis are plotted in **Figure VIII**.

As it can be observed in **Figure X**, H_{C3} values are lower for fs-irradiated samples (H_{C2} remains unaffected). It is worth to remark that the surface anisotropy generated by LSFL (LIPSS) derives in higher values of H_{C3} when the external magnetic field is applied parallel to the nanostructures main orientation. It is reported as well that a narrowing of the normal-superconductor transition takes place in irradiated samples. Different atmospheres used during fs-laser irradiation do not seem to have enough influence on

the modification of the surface superconducting properties, since the ultrafast laser-matter interaction does not trigger chemical reactions with oxygen or nitrogen.

In addition to the work described in publications **D** and **E**, a very extensive analysis of laser processes under several atmospheres and different laser sources have been done over niobium surfaces. In general, the used atmosphere (nitrogen, argon or vacuum) does not affect significantly the induced nanostructures on niobium, neither its magnetic properties. An exception of this behaviour is observed when niobium is irradiated with UV ps-laser in nitrogen atmosphere. In this case, there is a slight shift in H_{C2} towards higher values, as it can be seen in heat capacity measurements shown in **Figure XI**. Heat capacity is essentially a bulk property and is frequently used to define H_{C2} , so this result encourages us to continue with further analysis.

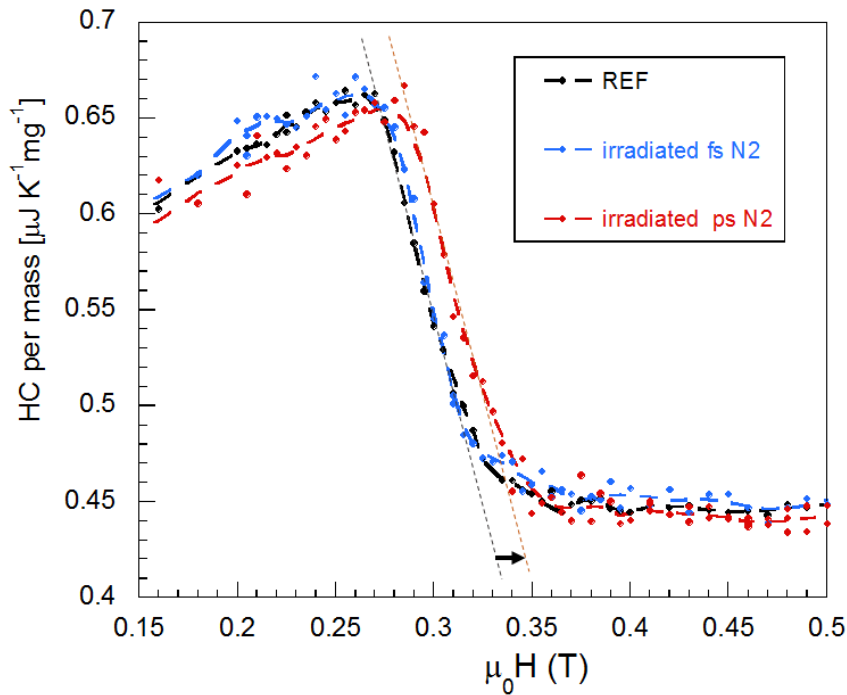
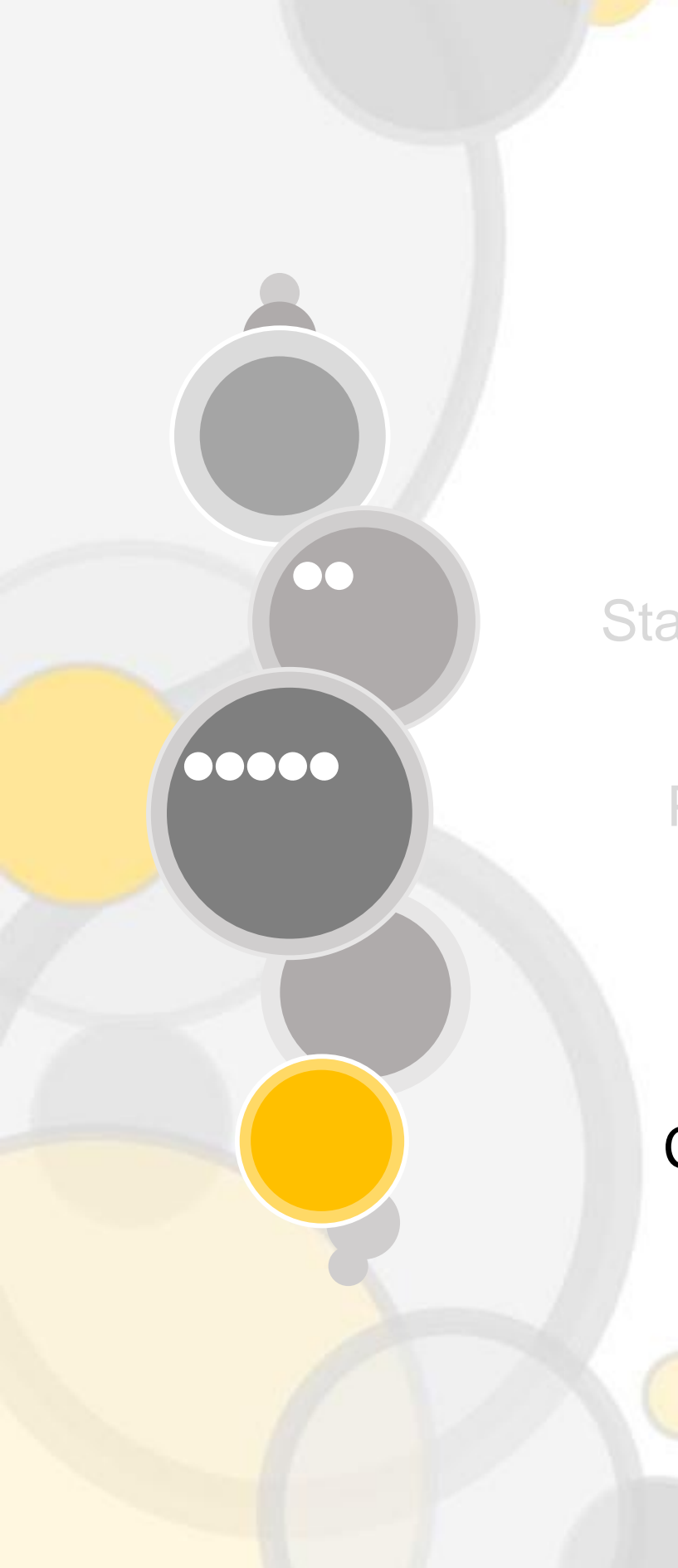


Figure XI Heat capacity measurements comparing non-irradiated Nb sheet (black, REF) with samples treated with 228-fs n-IR (blue) and 300-ps UV (red) lasers under nitrogen atmosphere. Black arrow just indicates the shift of grey dashed line (transition to normal) to the red one.

Finally, larger pulse duration ($\tau_p = 800$ ps) n-IR lasers have also been used to irradiate the same 25-micron thick niobium sheets under different atmospheres. Surface processing of metals with almost-nanosecond pulses in the infrared spectrum means more thermal treatments. This fact can induce chemical reactions, for example oxidation when the hot

metal is in contact with oxygen. It is worth to mention here that oxidation reaction is an exothermic process. Hence, powerful enough treatments trigger thermal avalanche-like mechanisms that end destroying any nanostructure and even bending the whole metallic sheet.

Based on the obtained results, it is fair to conclude that laser irradiation is an innovative, simple, dry and scalable method to tune superconductivity (both, surface and bulk components). Particularly, lasers irradiation could be an alternative to previous procedures like electropolishing or buffered chemical polishing.



Objectives

State of the Art

Publications

Discussion

Conclusions

Thesis Conclusions

Along this thesis several research lines have been explored and here are presented the conclusions of the work done within each one.

1. Thermal stability and electromagnetic behaviour of superconducting cables and coils

Different architectures of Rutherford MgB₂ cables have been analysed from the point of view of their thermal stability and their behaviour against quench phenomena. To study quench dynamics induced by local hot-spots and overcurrents, voltages inter- and intrastrands were measured.

In the case of cables formed by monofilament strands sheathed with a copper-nickel alloy, quench induced by local heat disturbance have shown two different time scales. During the first one, MPZ formation along the strands in contact with the heater takes place. The strand segments enter in the current-sharing regime, where the current is shared between the superconducting core and the metal sheath. This time interval is considerably longer than for single conductors. Once the MPZ has been formed, the quench propagates towards the ends of the cable in shorter times.

Quench propagation velocities have been estimated experimentally, showing good agreement with the predictions given by one-dimensional-geometry models. However, important local variations of the quench propagation velocities across the strands near the heater have been detected. This behaviour can be justified with the presence of

some inhomogeneities in the cable structure or local differences in $E(J)$ among strands or strand segments.

Same inhomogeneities have also been observed in quench processes induced by overcurrents. In this scenario, almost simultaneous nucleation of many normal strand segments surrounded by superconducting ones in different parts of the cable has been detected. Normal regions grew and collapsed resulting in the transition of the entire cable.

Cu10Ni alloy has high electrical resistance and together with the quasi-adiabatic conditions of the analysis, results in an insufficient thermal stability of the cables, which are prone to deteriorate if transition to normal state occurs during high current operation. So, higher conductive sheath involving the strands would be beneficial in order to make the cables more robust. This has been observed when similar experiments have been performed in wire with higher thermal and electrical conductivity metal sheaths.

A double pancake (DP) continuous coil has been fabricated with 2G-HTS tape without any turn-to-turn insulation. The coil has been epoxy impregnated after winding and subsequently glued with an epoxy resin to a copper support plate. In turn, this plate was anchored to the second stage of a cryocooler. The coil behaviour has been analysed between 5 K and 77 K under conduction-cooling conditions and high currents, above and below the coil critical current.

Charging and discharging tests have been performed and an electromagnetic analysis have been done in order to estimate turn-to-turn contributions and magnetization losses during the ramp, for different ramp rates, obtaining good correspondence with the observed coil heating. The derived turn-to-turn contact resistance $R_t \approx 100 \mu\Omega \text{ cm}^2$ at 77 K and about half at 5 K, are of the order of results reported by other groups in similar non-insulated 2G-HTS coils without epoxy resin impregnation.

Good correspondence between experimental coil critical currents and the estimated values using a modified load-line method to account for the tape anisotropy were found between 30 K and 70 K with almost identical temperature dependence, but with experimental values $\approx 10\%$ lower.

Currents above I_c ($I = 447 \text{ A}$) have been injected at 30 K, and resistive voltages above 250 μV during several seconds have been generated in the coil without triggering a quench. Additionally, the coil has been subjected to several thermal cycles from room

2. Laser melting techniques to improve thermal properties of alumina coatings

temperature to cryogenic operating temperatures without observing degradation of its superconducting properties. That indicates its electro-thermal robustness.

The thermal contact between the different parts of the DP coil (i.e., copper support plate, and lower and upper coils) has been analysed. It has been found that the joint between the coil and the support plate constitutes the weak-point of the coil cooling system. It has been detected that it is necessary to improve the adhesion properties between copper and epoxy.

Thermal stability of the whole cryogenic system has also been analysed, paying special attention to the current leads behaviour. These current leads were designed with two intermediate heat sinks with electrical insulation. A configuration, based on coating the copper plates with alumina, has been studied. These junctions show thermal contact conductance values, h_j , of ≈ 1800 and $850 \text{ W m}^{-2} \text{ K}^{-1}$ at $\approx 80 \text{ K}$ and $\approx 35 \text{ K}$ respectively. These values were obtained from the numerically calculated total heat inleak into the heat sink and the measured temperature difference across the whole joint in steady state conditions. The contact areas of both joints were 17 cm^2 and 20 cm^2 , respectively.

2. Laser melting techniques to improve thermal properties of alumina coatings

Laser melting techniques have been used to increase the density of the plasma-sprayed alumina coating in order to improve its thermal properties. Laser processing was done by the meandering laser beam scanning method, using a n-IR Ytterbium pulsed fibre laser, with central wavelength $\lambda = 1060\text{-}1070 \text{ nm}$, $1/e^2$ beam diameter $2r_b = 65 \mu\text{m}$, pulse repetition frequency of 900 kHz , and pulse duration of 200 ns . The effect of the main laser processing parameters, including pulse fluence (F_p), laser beam scanning velocity (v_L) and hatch distance between adjacent lines (d_s) has been reported. The optimum microstructures were obtained for $F_p \sim 0.9 \text{ J/cm}^2$, $d_s \sim 20 \mu\text{m}$ (corresponding to $d_s / r_b \sim 0.6$) and v_L between 50 and 80 mm/s .

Thermal contact conductance as a function of the temperature has been performed in samples selected on the basis of their better microstructural microstructure, characterized by a layer of dense recrystallized alumina in the upper part of the coating, near the surface, with a more porous layer near the copper substrate. An important improvement of the thermal behaviour was observed at all conditions, from cryogenic to ambient temperatures, as compared to the as-sprayed samples. The observed

differences become particularly marked in the range between 40 K and 77 K, where the thermal resistance R_H values of the laser treated samples were about 3 to 4 times lower than those corresponding to the plasma-sprayed samples. Values of the thermal contact conductance, h_j , as high as $0.95 \cdot 10^4$ and $1.55 \cdot 10^4 \text{ Wm}^{-2}\text{K}^{-1}$ at temperatures of 40 K and 77 K, respectively, were obtained for the optimized laser processed sample for contact areas of 2 cm^2 . These values include the contribution at the alumina/copper interface and across the alumina coating layer itself.

3. Surface laser nanostructuring and superconducting properties of Niobium samples

Different laser sources were used to nanostructure niobium sheet surfaces, differing in wavelengths (ultraviolet, UV, and near infrared, n-IR) and in pulse duration (pico- and femtosecond ranges). Laser induced periodic surface structures (LIPSS) were generated and characterized over areas around 20 mm^2 in $25\text{-}\mu\text{m}$ thick samples.

High irradiance processes, achieved with n-IR fs-lasers (with τ_p of 30 fs and 228 fs), have induced low spatial frequency LIPSS (LSFL) perpendicular to laser polarization with spatial periodicity between λ and $\lambda/2$, around 73% of λ , with a peak-to-valley distance about 200 nm. Also high spatial frequency LIPSS (HSFL) have been generated parallel to incident polarization with spatial periods between 50 and 80 nm.

On the other hand, UV ps-laser ($\tau_p = 300 \text{ ps}$) laser has been used to induce a variety of structures that range from ripples, with spatial periodicity similar but lower than λ and depth about 20 nm, to spike-shaped structures distanced about 1 micron.

Laser treatments have been performed at different atmospheres. Ambient air, pressurized argon and nitrogen, as well as vacuum conditions, have been tested and surface chemical analysis have been done. In samples irradiated with fs-lasers, XPS measurements have shown that laser treatments have generated very low oxidation effects, with Nb_2O_5 being the dominating type of oxide. Upon fs-laser processing in ambient air, a thin surface oxide layer of a few tens of nanometers extent was detected through cross-sectional STEM/EDX analyses. When fs-laser processing has taken place under inert gases the laser-induced oxide layer thickness of $\approx 5 \text{ nm}$ was similar to that found for the native oxide on the non-irradiated reference sample.

3. Surface laser nanostructuring and superconducting properties of Niobium samples

In samples irradiated with UV ps-laser under nitrogen atmosphere, EDX analysis has indicated that the amount of oxygen in the surface sample has slightly been reduced. The O/Nb ratio has changed from 0.41 to 0.34.

Changes in niobium superconducting properties induced by laser nanostructuring have been firstly reported. To perform magnetic measurements, samples were irradiated on the top and bottom surfaces. Treated samples showed modifications in magnetization hysteresis loops (directly related with critical current density) at certain applied magnetic fields below H_{C2} . These changes were observed also in a 1-mm thick sample irradiated with the UV ps-laser.

Clear effects of the laser irradiation on the surface superconducting properties have been shown. The surface critical field, H_{C3} , was derived from AC susceptibility measurements as a function of the externally applied DC magnetic field. H_{C3} values in all the laser nanostructured samples show a reduction in comparison with the non-treated samples. Narrower normal-superconductor transitions and lower $\chi''(H)$ peaks have been reported, while H_{C2} remained unaffected.

When fs-lasers have been used, generated LIPSS exhibit a high degree of orientation, generating a nanostructure with high anisotropy. This is also reflected in their superconducting properties. By performing experiments with the external magnetic field applied parallel or perpendicular to the LIPSS main orientation, it has been observed that H_{C3} reduction is stronger when the field is applied perpendicular to the LSFL orientation.

Laser treatments open the possibility to develop a scalable method for tuning superconductors at the manufacture level. In particular, fs- and ps-laser can be useful to control surface superconducting properties of niobium, and could be an alternative to some well-established procedures such as electropolishing or buffer chemical polishing.

Further studies should be necessary to completely understand the interaction of laser generated nanostructures and (surface) superconductivity.

4. Further, based on the former, research lines

All the previous discussed results and conclusions are part of the work accomplished during this PhD thesis, and each one of them opens the possibility to continue further investigations.

The collaboration with the group of Slovakia in the analysis of the thermal stability of MgB₂ Rutherford cables will continue with the study of new strand architectures with different metallic sheaths.

Following the work related with DP-coil manufacture and its analysis in **publication B**, it is planned to fabricate larger coils, with more layers. Also, an ongoing research is the study of modifying copper surfaces in order to improve the mechanical adhesion and enhance coil thermalization in junctions with epoxy. Derived from the use of 2G-HTS tape, low resistance joints are under study within the group, being necessary to connect coil layers or tapes. Part of this work is based on the irradiation of the stabilizer metallic layer of these tapes with sub-nanosecond lasers, aiming at providing better surface quality to the welding or soldering processes.

Remelting of plasma-sprayed alumina coatings by energetic pulse lasers to improve their thermal properties is an easily scalable process, but since relevant parameters need to be precisely chosen, more studies will be done in order to confirm and to scale the good results obtained in this thesis for larger areas.

Publications D and **E** have opened new possibilities, never studied before. The influence of LIPSS on surface superconductivity, are the first step of ongoing studies where other processing parameters can enhance niobium (or other superconductors) behaviour, as different laser sources (wavelengths and pulse duration) can be employed.

Conclusiones Generales

A continuación, se detallan las conclusiones generales de la tesis, resultado de las diferentes líneas de investigación que se han abordado a lo largo de este trabajo.

1. Cables y bobinas superconductoras: Estabilidad térmica y comportamiento electromagnético

Se han analizado distintas arquitecturas de cables de MgB_2 con geometría Rutherford, desde el punto de vista de su estabilidad térmica y su comportamiento frente al *quench*. Para realizar el estudio de la evolución de *quench* inducido por puntos calientes o por sobrecorrientes, se han instrumentalizado los cables para poder medir los voltajes a lo largo de un mismo hilo y los voltajes que se generan entre los diferentes hilos que componen el cable.

En el caso de los cables formados por hilos monofilamento recubiertos por $Cu_{10}Ni$, el *quench* inducido térmicamente evoluciona en dos escalas de tiempo. En la primera, se forma la zona mínima de propagación (MPZ) a lo largo de los hilos en contacto con el calentador. Esos segmentos de los hilos entran en régimen de *current-sharing* donde la transmisión de corriente se comparte entre el núcleo superconductor y el recubrimiento metálico. Este intervalo de tiempo es considerablemente más largo que en conductores tipo "monolítico". Una vez que se ha generado la MPZ, el *quench* se propaga mucho más rápido hacia los límites del cable.

Las velocidades de propagación del *quench* se han medido experimentalmente y los valores obtenidos concuerdan con las predicciones obtenidas utilizando modelos

unidimensionales. Sin embargo, se han detectado algunas variaciones en las velocidades de propagación en los hilos cercanos al calentador. Este comportamiento se puede justificar por la presencia de inhomogeneidades en la estructura del cable o por la generación de diferentes valores del campo eléctrico entre hilos en función de la densidad de corriente, $E(J)$.

Estas inhomogeneidades también se han observado cuando el *quench* se genera aplicando sobrecorrientes. En estos casos, se observan muchos segmentos de hilos en distintas partes del cable que pasan a la vez a estado normal, y que están rodeados por otras zonas aún superconductoras. Al final, las regiones en estado normal crecen y colapsan, generando así la transición de todo el cable a estado normal.

La aleación de cobre-níquel empleada en el recubrimiento de los hilos, Cu10Ni, tiene una alta resistencia eléctrica, que junto a las condiciones quasi-adiabáticas del ensayo, provoca que la estabilidad térmica de estos cables sea insuficiente. Esto hace que se puedan deteriorar fácilmente si la transición a estado normal ocurre en condiciones de operación con altas corrientes. Un recubrimiento metálico de los hilos con mayor conductividad térmica daría al cable mayor robustez. Esto se ha observado con experimentos similares en cables con recubrimientos metálicos con mayor conductividad eléctrica y térmica.

Se ha fabricado una bobina continua con configuración doble *pancake* con cinta 2G-HTS sin aislamiento entre vueltas. Después del bobinado, el conjunto se impregnó con resina tipo epoxi y posteriormente se pegó a un soporte de cobre que a su vez queda anclado térmicamente al dedo frío de un crio-refrigerador. De esta manera, se ha podido analizar el comportamiento térmico y electromagnético de la bobina, enfriada por conducción a temperaturas en el rango desde los 5 K hasta los 77 K, y siendo alimentada con altas corrientes (incluso por encima de su corriente crítica).

Se han realizado pruebas de carga y descarga y un posterior análisis para estimar, por ejemplo, las contribuciones vuelta a vuelta o las pérdidas asociadas con la magnetización durante las rampas de carga. La resistencia de contacto entre vueltas, R_t , es $\approx 100 \mu\Omega \text{ cm}^2$ a 77 K y aproximadamente la mitad a 5 K, lo que coincide con resultados de otros grupos que han estudiado bobinas similares.

Los valores de la corriente crítica de la bobina entre 30 y 70 K, obtenidos experimentalmente fueron muy similares a los calculados usando el método *load-line* modificado (que tiene en cuenta la anisotropía de la cinta) y con una dependencia de la

2. Procesado láser para la mejora de propiedades térmicas de los recubrimientos de alúmina

temperatura casi idéntica, siendo los valores experimentales aproximadamente un 10 % más bajos que los obtenidos con las simulaciones.

Para realizar estos experimentos, ha sido necesario utilizar corrientes eléctricas por encima del valor de la corriente crítica ($I = 447$ A) a 30 K, midiéndose voltajes por encima de 250 μ V sin desencadenar el *quench*. Además, la bobina fue sometida a varios ciclos térmicos desde temperatura ambiente hasta la temperatura criogénica de trabajo, sin observarse degradación de las propiedades superconductoras. Estos resultados muestran la robustez térmica y electromagnética de este tipo de bobinados.

Al analizarse el contacto térmico entre las distintas partes de la bobina (entre las dos capas de bobinado, así como entre la capa inferior y el soporte de cobre) se aprecia que el punto débil en el proceso de enfriamiento es la unión entre el soporte metálico y la bobina. Se ha detectado que es necesario mejorar la adhesión entre el cobre y la resina epoxi.

Se ha analizado también la estabilidad térmica de todo el sistema criogénico, prestando especial atención al comportamiento de las barras de corriente. Estas barras de corriente fueron diseñadas con dos disipadores de calor intermedios con aislamiento eléctrico. Para lograr ese aislamiento, pero manteniendo una buena conductividad térmica, la solución estudiada ha consistido en depositar un recubrimiento de alúmina sobre las piezas de cobre. Las uniones estudiadas, con áreas de contacto entre 17 y 20 cm^2 , mostraron unos valores de conductancia térmica de contacto, h_j , de ≈ 1800 y 850 $\text{W m}^{-2} \text{K}^{-1}$ a temperaturas de ≈ 80 K y ≈ 35 K respectivamente. Para obtener estos valores, se utilizó el valor de flujo de entrada de calor en cada unión obtenido numéricamente en el diseño de las barras, y la diferencia de temperatura medida experimentalmente a ambos lados de la unión una vez que se ha alcanzado el estado estacionario.

2. Procesado láser para la mejora de propiedades térmicas de los recubrimientos de alúmina

Se han utilizado técnicas de procesado láser para fundir (total o parcialmente) y densificar recubrimientos de alúmina para mejorar sus propiedades térmicas. Para ello se ha empleado un láser pulsado que emite en el infrarrojo cercano ($\lambda = 1060$ -1070 nm), con una duración del pulso de 200 ns, un tamaño de haz $2r_b = 65$ μ m y una frecuencia de repetición de 900 kHz. Con el haz láser barriendo toda la superficie, y estando la muestra

fija (movimiento bidireccional, describiendo meandros) se ha estudiado la influencia del resto de parámetros del procesado como son: fluencia (F_p), velocidad con la que el haz escanea la muestra (v_L), o la distancia entre las líneas de barrido (d_s). Las condiciones que generaron las mejores microestructuras fueron: $F_p \approx 0.9 \text{ J/cm}^2$, $d_s \approx 20 \text{ }\mu\text{m}$ (resultando un cociente $d_s / r_b \approx 0.6$) y valores de v_L entre 50 y 80 mm/s.

Utilizando dichas muestras para fabricar las uniones, con una capa densa de alúmina recristalizada y sin despegarse del sustrato de cobre, se caracterizó la conductancia térmica de contacto en función de la temperatura. Al comparar el comportamiento de estas uniones con otras fabricadas con el recubrimiento cerámico sin realizar el tratamiento láser se ha observado una notable mejoría en el comportamiento térmico a todas las temperaturas. La mejora es especialmente destacable entre 40 K y 77 K donde la resistencia térmica R_H de las muestras procesadas con láser es entre 3 y 4 veces menor. Las muestras (con una superficie de 2 cm^2) presentan valores de h_j de $0.95 \cdot 10^4$ y $1.55 \cdot 10^4 \text{ W m}^{-2} \text{ K}^{-1}$ a 40 K y 77 K, respectivamente. Estos valores incluyen la contribución de la interfase alúmina-cobre y la del propio recubrimiento de alúmina.

3. Procesado láser para la nanoestructuración de muestras de Nb y el estudio de sus propiedades superconductoras

Se han empleado distintos láseres para nanoestructurar superficies de aproximadamente 20 mm^2 de láminas de niobio de 25 micras de espesor. Para ello se han irradiado las muestras con un láser ultravioleta con pulsos de 300 ps y con dos láseres de infrarrojo cercano con pulsos en el rango de los femtosegundos.

Los procesos con alta irradiancia, conseguidos con láseres de fs, inducen estructuras periódicas en la superficie (*LIPSS*) con periodos del orden de la longitud de onda del láser incidente (aproximadamente 73% de λ), perpendiculares a la polarización del haz y con una altura pico-valle de alrededor de los 200 nm. También se observaron estructuras periódicas con mayor frecuencia espacial (periodos mucho menores que λ , entre 50 y 80 nm), *HSFL*, perpendiculares a la polarización.

Por otro lado, las muestras tratadas con el láser ultravioleta presentan una variedad de estructuras más amplia. Se inducen desde *ripples* con una periodicidad similar y ligeramente inferior a λ , hasta protrusiones con menor ordenación y separadas unas distancias próximas a la micra.

3. Procesado láser para la nanoestructuración de muestras de Nb y el estudio de sus propiedades superconductoras

Se han estudiado tratamientos láser en diferentes atmósferas: al aire, argón y nitrógeno, y en bajo vacío. Las superficies se han analizado químicamente mediante XPS. En las muestras tratadas con el láser de fs se aprecia muy poca oxidación, siendo Nb₂O₅ el óxido prevalente. Las imágenes de secciones transversales obtenidas por STEM/EDX muestran que los tratamientos al aire generan una capa de óxido de pocas decenas de nanómetros, y que en los tratamientos bajo atmósferas inertes la capa de óxido inducida por el láser tiene un espesor de ≈ 5 nm, un valor similar al medido en muestras no irradiadas.

Las muestras tratadas con el láser ultravioleta en atmósfera de nitrógeno presentaron una leve reducción en la cantidad de oxígeno en la superficie, tal y como se observa en los análisis de EDX, en los que se observa una reducción del cociente O/Nb desde 0.41 a 0.34.

Estos trabajos muestran por primera vez cambios en las propiedades superconductoras del niobio inducidas por nanoestructuración con láser. Para las medidas magnéticas, las láminas se trataron por ambas caras. Estas muestras presentan cambios en los ciclos de histéresis $M(H)$, en especial en ciertos rangos de campos magnéticos por debajo de H_{C2} , estando esta medida directamente relacionada con la densidad de corriente crítica. Estos cambios también se observaron en muestras de un milímetro de espesor procesadas con el láser ultravioleta de 300 ps.

Los efectos del tratamiento láser son también evidentes cuando se analiza la superconductividad superficial. El campo crítico superficial H_{C3} (derivado de medidas de susceptibilidad alterna en función de campos magnéticos externos) se redujo tras realizar los tratamientos láser. La transición desde el estado superconductor al estado normal se estrechó y se observaron picos $\chi''(H)$ más bajos mientras que H_{C2} no cambiaba al realizar el tratamiento láser.

Los LIPSS generados con los láseres de femtosegundos tienen una dirección preferencial (perpendicular a la polarización del láser), y esa anisotropía se ve reflejada también en sus propiedades superconductoras. Al aplicar el campo magnético orientado perpendicularmente a la dirección de las nanoestructuras, la reducción de H_{C3} es más acusada.

Estos tratamientos láser abren la posibilidad de implementar y escalar un método para modificar las propiedades superconductoras a nivel industrial. En particular, los láseres de pulsos ultracortos pueden ser muy útiles en el control de las propiedades asociadas a

la superconductividad superficial del niobio, siendo una alternativa a otros procedimientos más establecidos como el electropulido o el pulido químico.

4. Líneas y trabajos futuros

Todos los resultados anteriores y las conclusiones derivadas del trabajo realizado durante esta tesis generan la posibilidad de continuar diferentes líneas de investigación.

La colaboración con el grupo de Eslovaquia en el análisis de la estabilidad térmica de los cables de MgB_2 de geometría Rutherford va a continuar con el estudio de nuevas arquitecturas de hilos y diferentes recubrimientos metálicos.

El trabajo mostrado en la **publicación B** va a seguir con la fabricación de bobinas más grandes, con más capas. Además, un estudio que se está realizando en la actualidad, es la modificación de superficies de cobre para mejorar la adhesión de resinas tipo epoxi. De esta manera se podrá mejorar la termalización de las bobinas. Del trabajo relacionado con las cintas 2G-HTS se están estudiando procesos para mejorar las uniones entre cintas, con el fin de obtener bajos valores de resistencia eléctrica. Estas uniones serán necesarias para poder conectar, por ejemplo, las distintas capas de una bobina. Parte de este trabajo se basa en el uso de tecnologías láser para modificar la superficie de las capas estabilizadoras de las cintas con el objetivo de conseguir soldaduras de mejor calidad.

El re-fundido mediante láseres pulsados de recubrimientos de alúmina proyectados por plasma, y la mejora de sus propiedades térmicas, es un proceso escalable, pero necesitará de más estudios para ajustar los parámetros de procesado y confirmar esa mejoría en superficies más grandes.

Las **publicaciones D y E** han abierto una nueva línea de investigación. La influencia de la nanoestructuración en la superconductividad superficial es el primer paso de las investigaciones que se están realizando en el grupo actualmente, con el objetivo de mejorar el comportamiento del niobio (y otros superconductores) a través de otras estrategias de procesado o mediante el uso de otros tipos de láser (distinta longitud de onda o anchuras de pulso).

“Life is like a trumpet. If you don’t put anything into it, you don’t get anything out of it”

-William Christopher Handy. *“Father of blues”* (1873-1958)

Agradecimientos Y Recuerdos

Que hacer una tesis no es algo fácil, lo tenía claro. Que terminar de escribirla y poner todo el trabajo, experiencias y resultados en un mismo documento iba a costar, eso también lo tenía claro. Pero siempre hay cosas que se te vienen encima, y el año 2020 que dejamos atrás, desde luego, ha sido muy duro. En lo personal y en lo colectivo, muy duro.

Por esto, me gustaría agradecer y dedicar unas líneas (no todas las que se merecen) a toda esa gente sin la cual este trabajo no habría sido posible. Empezando, lógicamente, por las otras dos personas que firman este trabajo, Luis y Elena. Responsables últimos de que todos los temas que hemos tocado a lo largo de estos años hayan acabado en la redacción de esta tesis. Sé que también han pasado por mucho durante este tiempo, lo que le da aún más valor a toda la ayuda que me han brindado. Las jornadas de medida a ritmo de criostato, las muestras "*Frankenstein*" y, sobre todo, las reuniones a pie de escalera con cinco o seis temas en paralelo han acabado con esta memoria en depósito. Si esa barandilla hubiera tomado apuntes, está claro que compartía el doctorado con ella.

Antes de continuar, un paréntesis para agradecer también a las entidades públicas Ministerio y Gobierno de Aragón, por los fondos y los medios para hacer posible esta tesis englobando contrato predoctoral, ayuda para estancia y congresos varios. Me ha permitido, además de poder llevar a cabo nuestras investigaciones, viajar y conocer sitios que seguramente no hubiera visto si no es por esta experiencia científica. Así que gracias.

Siguiendo con el grupo, creo que merecen especial mención las reuniones de grupo y cómo, gracias a ellas, se han generado discusiones (en el buen sentido) que han llevado a buenos resultados. Buena parte de esas aportaciones, hay que agradecerse a Rafa. Hasta el final aportó y enseñó a todos los que estábamos cerca suyo de una manera que, sinceramente, no me lo hubiera imaginado cuando, allá por segundo de carrera, oí hablar de “campos y ondas con Navarro”. Mil gracias, allá donde estés. Y gracias también a Xermán, que poco a poco se ha ido convirtiendo en un *advisor* más, siempre aportando ideas y alternativas que han acabado siendo importantísimas en esta tesis.

No me quiero olvidar de Mario e Hippo con ese buen humor que les caracteriza y que siempre han estado ahí para lo que necesitase. Y especial dedicatoria a Carlos Borrel, que también ha peleado esta tesis. Con bici, con láseres, con hombro o sin él, ¡pon un Carlos en tu vida que te irá bien!

En el área de ciencia y tecnología de materiales y fluidos ha habido mucha gente importante en esta tesis: Macarena y Marisol, Celia, Isra y Jose Antonio. En mayor o menor medida, sin su ayuda y las charradas varias tampoco estaría escribiendo esto. Al igual que Michel, Anselmo, Pacho, Andrés y María, José Ángel o Rut que han tenido buenas palabras y gestos en momentos clave. La parte de apoyo docente ha sido también otra experiencia que apuntar en el cuaderno de cosas que suman, y sin ellos hubiera sido imposible. Quería hacer también un recordatorio especial a la gente del grupo “*de pilas*” porque, bueno, con algunos de ellos empezó esta aventura de la investigación hace unos cuantos años. Luego no hemos trabajado juntos, pero han estado ahí para todo: Jose Ignacio, Ángel, Patricia y, sobre todo, Miguel y Alodia que valen muchísimo.

En estos años en el departamento he compartido la sala de colaboradores con gente muy variada y, como digo, de todos te llevas algo: Desde Carlos, María, Laura, Jant, Castel o Cristian, pasando por Wei, los franceses, Ashiqur o Evan hasta Lorena, María, MariaJosé o Luis mucho más recientes. Muchas gracias por el apoyo, por las comidas/café/cerveza. En el mismo pack aunque de otro edificio toca meter a Adrián, la persona más maja de Ávila y parte del planeta, y a Jorge, que también estuvo ahí desde el principio y con el que queda pendiente algo de monte (a mi nivel, no al suyo que quiero volver de una pieza).

Siguiendo esa línea, Miguel (a.k.a “*su panameño preferido*”) y Héctor han llevado el término *afterwork* a otro nivel, siendo un apoyo clave en esta recta final. Y Ana, que estuvo al principio (cuando aún no tenía muy claro que era un *quenck*), durante (a modo

visita fugaz vía congreso) y al final con su propio sprint para cerrar con épica la tesis peleando contra fotocopadoras y todo lo que se pusiese por medio. Os debo una (o varias). Y un ¡gracias! bastante grande también a Jorge, el chico que volvía todas las navidades al departamento, también moviéndose en su salsa en los congresos y que ha acabado echándole un ojo a esta tesis.

Siguiendo en el departamento, no puedo pasar sin agradecer y recordar el medio millón (aproximadamente) de sesiones de microscopio con Cristina de charrada en charrada y nuestros sufrimientos varios con el Zaragoza. Igual que las Rosas, y más gente del SAI.

Also want to acknowledge people from BAM. It was a huge pleasure to spend three months there in Berlin, surrounded with really nice people: Jörg, Herbert, Simone, Christoph. Especial mention to Jörn, that not only teach me so many things about LIPSS, but also welcomed me and made things easy for me since the first day. As Javier Solis used to say: "Tiene un corazón que no le cabe en el pecho, y eso que mide 2 metros".

Y de esa experiencia alemana que salió genial también quiero nombrar aquí a gente que me lo puso muy fácil desde que llegue, mis compis en el *WG Ana*, Sarah e Irene. Y a los del *United*, por los partidos y los *späti* de después.

Dicho todo esto, no puedo pasar sin nombrar a mi familia, que a su modo también han estado ahí. Nos ha tocado vivir momentos muy amargos y rondar demasiado los hospitales, pero aun así eso también suma para conseguir acabar esta tesis. Y si esta tesis tiene una dedicatoria especial y quedará en el recuerdo, es para mi madre. Sin estar muy encima, supo apreciar (aunque nuestro trabajo nos costó) el esfuerzo que esto suponía. A mi padre y demás familia (corta), que no se preocupen, que celebraremos esto. Seguro.

Y en este sentido, agradecer también a los Domínguez García. Esa, también, familia (larga) que desde hace unos años me acogieron como uno más y me han apoyado en momentos realmente duros. Especialmente Carmen, Ángel, Silvia, Luis y ese sobrinazo majísimo Mario. Nombraría a todos, pero esta tesis tiene que tener un final, así que os lo diré en persona, jeje.

Y ese otro grupo de hermanos y hermanas. Esa gente que ha estado ahí a las buenas y a las malas y que han sido tan necesarios e importantes con los que me une algo más que amistad. Rosa, con su increíble capacidad para escuchar, superar problemas y sacar siempre la parte más divertida de todo. Guille, con esa proactividad y ganas de hacer cosas infinitas. Berni, que tiene un corazón gigante y siempre aporta esa calma que

necesito. Juan, ese otro hermano que cuento los días para tenerlo más cerca. Ricardo, con esa capacidad de simplificar, y de abrazar. Chema, que siempre ha estado también listo, incluso en momentos difíciles para él. Paúl, que aunque haya distancia, siempre está. Igual que Dani. Waldo, otro tío leal, que tiene ese toque del sur tan necesario. Raúl, y esa claridad con la que también ve las cosas. Reich, que también ha estado ahí para cafés, conciertos y lo que haga falta. Y Fer, esa navaja suiza en forma de músico – ingeniero/doctor – cineasta – karateka – ciclista – festivalero – y un largo etcétera, pero sobretodo amigo y compañero de fatigas. En esta gran familia entran también toda la cuadrilla de Pozuel, Carol, Patri, Urbano, Patri, Aurora, Mario, Alba, Andrea, Adrián, Pedro, Alba, Emilio (otro que es todo corazón y lealtad), Bea, Alex (Little Almazán), Mery, Gracia (“Dra. Mendoza”), Euge, Carmona, Anichu, Letona, Ani, Julen, Jano, Peña, Elisa, Edgar, Bebo, Silvia y seguro que me dejo a alguien. “Mucha Gente” “Buena gente”.

Un apartado especial para esa gente que sin darse cuenta (o sí) me ha servido de vía de escape, oyente, terapia o todo a la vez: Luis, Jorge y Manoli en la Badina (otro nido de buena gente), Carlos, Lili y Merry con la trompeta o el Submarino y LosFlapas con el fútbol. A todos ellos, también les dedico esta tesis porque sin ellos, hubiera sido imposible. La montaña, la bicicleta, la música, el deporte. Esas cosas, sin las que el equilibrio no sería posible.

Y he dejado para el final a la más importante y especial de todas las personas de mi alrededor. Marta ha sido la compañera de vida que me ha ayudado a llegar hasta aquí, que me ha sostenido y no me ha dejado caer. Una fuente de energía, sonrisas y apoyo inagotable. No creo que me equivoque si digo que es la mejor persona que conozco y que tengo la enorme suerte de compartir con ella pasado, presente y futuro.

He tenido el privilegio de conocer a mucha gente y de todo el mundo puedes aprender algo. Somos la suma de las personas que conocemos, las experiencias que vivimos y las decisiones que tomamos. Y el haber decidido tomar el camino de la investigación me ha llevado a vivir grandes momentos y conocer personas excepcionales. Es un gran mensaje que quiero llevarme de esta aventura llamada tesis.

Esto ha sido todo por hoy. Muchas gracias. Mañana más y mejor.

